Investigations towards more performing and more stable solution-processed hybrid perovskite solar cells

Zhelu Hu

Thèse de Doctorat

Doctoral School Physique et Chimie des Matériaux (ED 397)

Laboratoire de Physique et d'Etude des Matériaux (LPEM),

ESPCI-ParisTech/CNRS/Sorbonne Université

Investigations Towards More Performing and More Stable Solution-Processed Hybrid Perovskite Solar Cells

In order to obtain the title of Philosophiae Doctor of Sorbonne Université

Specialty: Materials Physics and Chemistry

By

Zhelu Hu

Directed by Zhuoying Chen and Lionel Aigouy

Publically defended on the 09/09/2020 in front of a jury composed by:

Mrs Christel Laberty-Robert	Member of the jury	Sorbonne Université
Mr Bernard Geffroy	Member of the jury	Ecole Polytechnique
Mr Bernard Ratier	Reviewer	Université de Limoges
Mrs Emmanuelle Deleporte	Reviewer	ENS Paris Saclay
Mr Lionel Aigouy	Ph.D. Supervisor	LPEM, ESPCI
Mrs Zhuoying Chen	Ph.D. Director	LPEM, ESPCI

Acknowledgements

To start with, I would like to sincerely thank my supervisors Dr. Lionel Aigouy and Dr. Zhuoying Chen, for their fantastic and patient tutoring and helping me achieve great progress in every aspect of my life. Due to their broad and deep scientific knowledge, they provide me countless fruitful suggestions and keep me have a great passion for my work. Moreover, I am also very grateful they give me large freedom to pursue my research interest, help me construct the completed scientific research system and build great academic habits.

Furthermore, I would like to express my great respect and gratitude to Prof. Danièle Fournier in Sorbonne Université, who I have a great pleasure of working with and also gives me a lot of support for my research. Meanwhile, I would like to show my hearty thanks to the collaboration group from Madrid, Prof. Antonio García-Martín, Dr. María Ujué González, Dr. José Miguel García-Martín, and Dr. Fernando Fresno provides me many samples and valuable discussion. If my research work without their help, my thesis would not go well smoothly. I want to thank Prof, Baoquan Sun and Dr. Yajuan Li for the professional research discussion and helpful measurement on my research work.

I would like to express my appreciation for the funding contribution from the China Scholarship Council, which made my Ph.D. work possible, and the science and technology resources sharing platforms from IPGG and ENS. I extend my gratitude to Dr. Olivier Lesage, who always gives me great help in gold evaporation and the patient training of the instruments in the IPGG platform. Besides, I want to greatly thank José Palomo from ENS, providing me a lot of help in using AFM, Dektak, Microscopy instruments. And I also very much appreciate the help from Bruno Bresson who always provides me powerful support on SEM measurement.

I also would like to take the opportunity here to thank my colleagues, Laurent Billot, Mathilde Schoenauer Sebag, Hengyang Xiang, Xiangzhen Xu, Tingting Niu, Cyrine Ernandes, Hungju Lin, Chenghao Xin, Corentin Paillassard, Mahima Chaudhary, Liangcai Xu, Jonathan Baptista, Sophie Demonchaux, Marie-Claude Theme, Francis Cassagne, Ricardo Lobo, Dimitri Roditchev, and all the others from LPEM, for their great contribution and kind friendship to my research and life.

I would like to thank all the friends in France, Dan Xu and Jiaqi Hou (who are my tennis partners); Wei Wang, Yishan Ye, Xiao Liu, Kankan Qin, Liqiong Yang and Teng Zhang (who are my badminton partners), Wenyi Wu, Mo Yang etc. Due to their selfless companionship and kind help, they make my life very exciting and interesting in Paris.

I would like to thank my family for their endless encouragement and warm support all the time.

Résumé en Français

Avec l'énorme demande mondiale en énergie et l'épuisement des combustibles fossiles, une crise énergétique se rapproche de plus en plus de nous. Les dispositifs photovoltaïques, qui peuvent convertir efficacement l'énergie solaire, inépuisable, en électricité, ont attiré beaucoup d'attention. Par conséquent, la recherche vers des dispositifs photovoltaïques efficaces et à faible coût devient plus importante que jamais. Au cours des dernières décennies, différents types de cellules solaires ont été proposés avec des progrès prometteurs en termes de performances. Ces dispositifs photovoltaïques comprennent des cellules solaires au silicium, des cellules solaires inorganiques en couche mince, des cellules solaires organiques, des cellules solaires sensibilisées aux colorants et des cellules solaires hybrides à base de pérovskite.

Parmi les dispositifs photovoltaïques de 3e génération fabriqués en solution, les cellules solaires hybrides en pérovskite d'halogénure organométallique ont fait l'objet d'énormément de recherches et d'intérêt industriel. Cela est principalement dû à leurs performances photovoltaïques exceptionnelles et à leur fabrication en solution adaptable à grande échelle dans une usine, et à faible coût. Jusqu'à présent, l'efficacité de conversion de puissance certifiée (PCE) des cellules solaires à base de pérovskite à jonction unique à la pointe de la technologie a dépassé 25%, ce qui suggère leur grand potentiel pour concurrencer les cellules solaires au silicium. Malgré l'excellente efficacité obtenue et les avantages de la fabrication en solution, des étapes importantes sont encore nécessaires pour que les cellules solaires à base de pérovskite atteignent l'industrialisation et donc un développement à grande échelle. Des recherches fondamentales sur les cellules solaires à base de pérovskite sont donc encore nécessaires pour bien comprendre leurs propriétés photovoltaïques et l'impact de la couche de transport, de la couche active et des interfaces sur leurs propriétés et sur leur stabilité.

Dans cette thèse de doctorat, je me suis concentré sur l'optimisation et les stratégies concernant la couche de transport d'électrons (ETL), la couche active à base de pérovskite hybride et leurs interfaces dans les cellules solaires fonctionnelles de pérovskite. En ce qui concerne l'étude des ETL, j'ai réalisé deux travaux: l'un porte sur la comparaison d'une architecture simplifiée de cellules solaires planaires à base de pérovskite sans ETL avec celle d'un ETL plan en TiO_2 (décrit au chapitre 2); un autre travail porte sur la comparaison des

cellules solaires à base de pérovskite avec des nanocolonnes de TiO_2 (NA) orientées à celles comportant simplement une ETL de TiO_2 plane et non nanostructurée (chapitre 3). Lors des recherches sur la couche active de pérovskite, la pérovskite à cations mixtes et aux halogénures mixtes a été utilisée dans trois axes de travail distincts. J'ai tout d'abord optimisé et maximisé la taille des grains de la couche active de pérovskite (chapitre 2). Ensuite, j'ai étudié des films de pérovskite hybride nano-structurés et leur amélioration au niveau de la collection de la lumière (Chapitre 6). J'ai aussi étudié les propriétés thermiques des films minces de pérovskite à cation mixte et j'ai notamment déterminé leur conductivité et leur diffusivité thermique. L'étude contribue à comprendre leur meilleure stabilité thermique par rapport aux perovskite à base d'iodure de plomb de méthylammonium ($MAPbI_3$) (voir chapitre 4). Enfin, j'ai étudié les méthodes de passivation pour atténuer la recombinaison de la charge interfaciale et pour améliorer la stabilité des cellules solaires de pérovskite (chapitre 5).

Comme décrit au chapitre 2, un dispositif typique de cellule solaire à base de pérovskite est formé d'un film mince de couche active de pérovskite hybride (l'absorbeur) pris en sandwich entre un ETL et une couche de transport de trous (HTL). Ces couches de transport jouent un rôle important pour collecter et transporter les porteurs de charges vers le circuit externe. Parmi les pérovskites hybrides à cations mixtes et à halogénures mixtes, $FA_{0.83}Cs_{0.17}Pb(I_{(1-x)}Br_x)_3$ (FA = formamidinium $[HC(NH_2)_2]$) est une pérovskite prometteuse dont la bande interdite convient à la réalisation de cellules en tandem avec Si. Des cellules solaires à jonction unique ont même utilisé une double ETL comprenant une couche de SnO_2 et une couche de PCBM (phényl-C60-butyrique acide méthyl ester). Bien que ces résultats soient très intéressants, il reste difficile de savoir si un tel transport d'électrons ou une double couche bloquant les trous est absolument nécessaire pour réaliser des cellules solaires à base de $FA_{0.83}Cs_{0.17}Pb(I_{(1-x)}Br_x)_3$ et dans quelle mesure leurs propriétés sont modifiées si une structure sans ETL est développée. D'un point de vue pratique, un dispositif dont la structure est simplifiée est logiquement souhaitable pour une fabrication à faible coût.

Bien que la structure du dispositif sans couche de blocage ait permis de fabriquer des cellules solaires hautes performances à base de $MAPbI_3$, cette approche n'a pas encore été explorée sur les cellules solaires à base de $FA_{0.83}Cs_{0.17}Pb(I_{(1-x)}Br_x)_3$ au moment où les travaux du chapitre 2 ont été réalisés. Par rapport aux structures des cellules solaires habituelles, les

structures simplifiées sans ETL peuvent offrir des avantages intéressants comme une recombinaison de surface réduite (entre l'électrode et l'ETL), la possibilité de séparer l'étude du mécanisme de croissance de la pérovskite grâce à la fabrication de l'ETL et à la fabrication à basse température adaptable aux substrats polymères flexibles. En particulier, dans les cellules solaires sans ETL, la morphologie de la pérovskite est particulièrement importante car tout contact direct entre l'oxyde d'étain dopé au fluor (FTO) et le HTL peut entraîner une réduction néfaste des performances photovoltaïques.

C'est dans ce contexte que j'ai réalisé les travaux du chapitre 2 sur la fabrication de cellules solaires planaires efficaces sans ETL à base de cations et d'halogénures mixtes $FA_{0.83}Cs_{0.17}Pb(I_{(1-x)}Br_x)_3$ directement sur des substrats FTO. Étant donné que la qualité de la couche active de pérovskite dans la structure de ce dispositif est particulièrement importante, en faisant varier la concentration molaire du précurseur, nous avons optimisé les conditions de dépôt de la couche active conduisant à une épaisseur ajustable et compacte de films minces de pérovskite $FA_{0.83}Cs_{0.17}Pb(I_{(1-x)}Br_x)_3$ avec une grande taille de grain allant jusqu'à 12 microns. En utilisant les conditions optimales de dépôt de la couche active sur la structure du dispositif planaire avec et sans ETL en TiO_2, nous avons obtenu des cellules solaires pérovskites à base de $FA_{0.83}Cs_{0.17}Pb(I_{0.6}Br_{0.4})_3$ planaires, fonctionnelles, sans ETL et avec une PCE et un hystérésis comparables à ceux ayant un ETO en TiO_2. Ces résultats sont très encourageants pour la fabrication à grande échelle de cellules solaires à base de $FA_{0.83}Cs_{0.17}Pb(I_{0.6}Br_{0.4})_3$.

Malgré les résultats intéressants obtenus sur des cellules solaires fonctionnelles à base de pérovskite sans ETL au chapitre 2, les performances des dispositifs restent modestes. Dans le chapitre 3, nous avons cherché à obtenir des cellules solaires plus stables et plus performantes en étudiant l'influence d'une ETL formée d'un réseau de nanocolonnes en TiO_2 sur $Cs_{0.05}(FA_{0.83}MA_{0.17})_{0.95}Pb(I_{0.83}Br_{0.17})_3$ en considérant 3 types de cellules solaires avec $FA^+ = CH_5N_2^+$ et $MA^+ = CH_3NH_3^+$. Par rapport aux ETL planaires, les non-planaires, tels que les ETL mésoporeux, semblent être plus adaptés pour obtenir une efficacité et une stabilité plus élevée et moins d'hystérésis. Néanmoins, de tels échafaudages à base de nanoparticules de TiO_2 présentent certains inconvénients tels que l'existence de nombreux grains / défauts structurels, des difficultés de remplissage des pores par le précurseur de la pérovskite et une perturbation de la croissance des grains de pérovskite. En comparaison, les réseaux de nanotiges / nanofils / nanotubes TiO_2 unidimensionnels (1-D) orientés dans une direction

représentent une stratégie prometteuse, présentant moins de défauts de surface et de joints de grains et facilitant le remplissage des pores par le précurseur. Les matrices de TiO_2 1D peuvent ainsi fournir des chemins conducteurs directs permettant d'extraire et de transporter efficacement les porteurs générés par la couche de pérovskite. En termes de stratégies de collection de la lumière, les matériaux non métalliques à haute permittivité peuvent aussi améliorer les processus d'absorption optique et de fluorescence. En raison de l'absence d'absorption optique dans le domaine du spectre visible et de ses excellentes propriétés de transport d'électrons, les nanoarrays de TiO_2 1D devraient être d'excellents 'booster' électronique et optique sur ce type de cellules solaires à base de pérovskite.

Dans ce contexte, comme décrit dans le chapitre 3, des matrices de nanocolonnes 1D en TiO_2 alignées verticalement ont été intentionnellement fabriquées sur une moitié de substrats de FTO compacts recouverts d'un film de TiO_2. La technique de dépôt est le GLAD (glacing angle deposition) dans lequel il y a un angle de dépôt et le substrat tourne simultanément. Cette technique permet de générer des nanorods inorganiques orientés de façon régulière avec des dimensions uniformes sur des substrats. L'évaporation s'effectue par dépôt physique en phase vapeur (PVD). Des caractérisations structurales, spectroscopiques et optiques ont ensuite été réalisées sur ces nanoarrays de TiO_2 et comparées avec une structure sans nanocolonnes à base de TiO_2 compact (cp-TiO_2) présente sur le même substrat. En particulier, par microscopie optique en champ proche (SNOM), nous avons observé une forte localisation et concentration de la lumière (champs électromagnétiques) à des endroits précis sur les nanocolonnes. Des cellules solaires à base de pérovskite à triple cation basées sur $Cs_{0.05}(FA_{0.83}MA_{0.17})_{0.95}Pb(I_{0.83}Br_{0.17})_3$ ont ensuite été fabriquées sur ces structures, dont la moitié est couverte par les nanocolonnes en TiO_2 couche (ETL) et l'autre moitié par du cp-TiO_2 ETL. Par rapport aux cellules solaires construites sur un ETP cp-TiO_2 planaire du même substrat FTO, les cellules solaires avec des réseaux de nanocolonnes de TiO_2 présentent une augmentation de 5% de son courant de court-circuit et une amélioration de 7% de son efficacité de conversion de puissance. Elles présentent aussi une durée de vie considérablement prolongée. Par spectroscopie d'impédance électrochimique, nous avons observé que la structure ayant un réseau de nanocolonnes de TiO_2 possède une résistance au transport de charge plus faible et une résistance à la recombinaison de charge plus élevée, contribuant à l'amélioration des performances photovoltaïques observées. De plus, de tels réseaux de nanocolonnes en TiO_2 présentent une absorption optique plus importante dans le

domaine spectral UV par rapport à son homologue planaire. Les nanocolonnes semblent constituer un écran UV partiel améliorant la stabilité de la cellule solaire. Les caractérisations structurales, spectroscopiques, photovoltaïques et optiques combinées présentées ici constituent une analyse détaillée des origines physiques et du rôle bénéfique des réseaux de nanocolonnes 1D en TiO_2 dans les cellules solaires hybrides à base de pérovskite.

Par rapport aux cellules solaires en silicium qui ont généralement une durée de vie de 25 ans, les cellules solaires hybrides à pérovskite se dégradent relativement rapidement en fonctionnement, ce qui pose de sérieux problèmes limitant leur développement à grande échelle. Il est donc essentiel d'effectuer des recherches fondamentales sur les mécanismes de dégradation et notamment les mécanismes de dégradation thermique des cellules solaires à base de pérovskite. Sur les halogénures de plomb de méthylammonium ($MAPbX_3$, X = Cl, Br, I), les conductivités thermiques ont été mesurées par différents groupes par différentes méthodes expérimentales et théoriques. En comparaison, bien que les composés à base de pérovskite hybride à cations et halogénures mixtes tels que $Cs_{0.05}(FA_{0.83}MA_{0.17})_{0.95}Pb(I_{0.83}Br_{0.17})_3$ présentent une stabilité thermique améliorée par rapport à celle formées de $MAPbI_3$, leurs propriétés thermiques n'ont toujours pas été bien étudiées.

Dans ce contexte, au chapitre 4, nous avons mesuré la conductivité thermique et la diffusivité thermique sur une série de couches minces de $Cs_{0.05}(FA_{0.83}MA_{0.17})_{0.95}Pb(I_{0.83}Br_{0.17})_3$, d'épaisseur différente mais de morphologie similaire dans une configuration de cellule solaire réelle, par la technique de microscopie à thermoréflectance modulée. La conductivité thermique et la diffusivité thermique sont des paramètres cruciaux pour prédire à quelle vitesse et avec quelle efficacité la chaleur se dissipera dans la couche active et vers le substrat. Sur nos échantillons, nous avons mesuré une conductivité thermique k de 0.26 ± 0.03 $W.m^{-1}.K^{-1}$ et une diffusivité thermique D_{per} de $3.5 \times 10^{-7} \pm 0.5$ $m^2.s^{-1}$. Nos mesures indiquent que la conductivité thermique de ces composés à cations mixtes et halogénures mixtes n'est que légèrement inférieure à celle des pérovskites à base de MA trouvées dans la littérature, montrant que la substitution de MA^+ par FA^+ et Cs^+ a une influence très limitée sur les propriétés des pérovskites hybrides. Ainsi, la stabilité thermique améliorée des pérovskites $Cs_{0.05}(FA_{0.83}MA_{0.17})_{0.95}Pb(I_{0.83}Br_{0.17})_3$ par rapport à $MAPbI_3$ provient probablement d'une origine chimique.

Outre les propriétés thermiques mentionnées ci-dessus, la cristallinité et la morphologie de la couche active de pérovskite et les interfaces pérovskite / couche de transport jouent ensemble des rôles critiques sur l'optimisation des performances photovoltaïques et sur la stabilité du dispositif. En particulier, les joints de grains, les impuretés et les défauts situés dans la masse ou aux interfaces peuvent faciliter la migration des ions et agir comme sites de recombinaison des porteurs de charges, conduisant à une perte d'efficacité et à une dégradation du dispositif. Différentes stratégies sont actuellement à l'étude pour contrôler avec précision la cristallinité et la morphologie de la couche de pérovskite et ses interfaces avec les couches de transport visant à obtenir une couche hautement cristalline, compacte et lisse à gros grains cristallins. En particulier, sur les pérovskites à triple cation avec une composition du type $Cs_{0.05}(FA_{0.83}MA_{0.17})_{0.95}Pb(I_{0.83}Br_{0.17})_3$, il est récemment devenu très courant de changer légèrement la concentration en PbI_2/iodure de méthylammonium (MAI) par rapport au rapport stoechiométrieque (de 1) pour améliorer les performances photovoltaïques. Néanmoins, le véritable rôle de l'excès de PbI_2 reste très controversé, faute de consensus sur son effet sur la masse et sur les propriétés d'interface de la cellule solaire en pérovskite.

À la lumière des résultats apparemment contradictoires de la littérature, nous présentons dans le chapitre 5 une étude sur le rôle controversé de l'excès de PbI_2 dans les cellules solaires à base de pérovskite. Plus précisément, sur la base de cellules solaires pérovskites $Cs_{0.05}(FA_{0.83}MA_{0.17})_{0.95}Pb(I_{0.83}Br_{0.17})_3$, nous avons fourni une comparaison expérimentale du le comportement photovoltaïque et de la stabilité des cellules solaires sous un éclairage solaire continu entre des échantillons avec un léger excès de PbI_2 n'ayant pas réagi (en vrac et à l'interface) et des échantillons avec un excès de PbI_2 volontairement retiré à l'interface pérovskite / HTL. En combinant des mesures structurales, optiques et photovoltaïques, nous avons constaté qu'en retirant l'excès de PbI_2 de l'interface pérovskite / HTL en traitant la surface de la pérovskite avec une solution saline organique, non seulement l'efficacité, mais aussi la stabilité des cellules solaires peuvent être améliorées. L'amélioration de l'efficacité est associée à une résistance au transport considérablement réduite et à une résistance à la recombinaison accrue des échantillons traités par l'AMI, sondés par spectroscopie d'impédance. Plus important encore, sous un éclairage solaire continu, les cellules solaires non encapsulées dans lesquelles l'excès de PbI_2 a été retiré de l'interface pérovskite / HTL ont maintenu respectivement 81% et 86% traitées par la solution MAI et FAI de leur PCE initial (contre 64% pour la cellule solaire avec un excès de PbI_2) après cent heures de dégradation.

Nos résultats montrent que l'élimination du PbI_2 à l'interface pérovskite / HTL est très bénéfique à la fois pour l'efficacité et la stabilité des dispositifs de pérovskite et peut être facilement mise en œuvre au cours de leur processus de fabrication.

Enfin, dans le chapitre 6, nous avons étudié une stratégie pour améliorer la collection de la lumière par optimisation de la couche de $Cs_{0.05}(FA_{0.83}MA_{0.17})_{0.95}Pb(I_{0.83}Br_{0.17})_3$, en visant à étendre la réponse spectrale de la structure. Pour cela, nous voulons incorporer des nanoparticules contenant des ions de terres rares et permettant de faire de l'up-conversion. De plus, pour booster encore plus les effets d'up-conversion, nous avons aussi nanostructuré la couche de pérovskite $Cs_{0.05}(FA_{0.83}MA_{0.17})_{0.95}Pb(I_{0.83}Br_{0.17})_3$ pour modifier sur ses propriétés optiques locales. Pour cela, la surface de la pérovskite a été gravée par un faisceau ionique focalisé pour former des réseaux de rainures unidimensionnelles. Nous avons ensuite caractérisé les surfaces de pérovskite gravée par un SNOM. L'échantillon est excité en mode transmission par un faisceau laser focalisé modulé à $\lambda exc = 975$ nm et sa surface est scannée par une pointe de microscopie à force atomique (AFM) à l'extrémité de laquelle est collée une nanoparticule possédant des propriétés d'up-conversion : il s'agit d'un cristal de KY_3F_{10} co-dopé aux ions Er^{3+} et Yb^{3+}. Les cartographies de fluorescence obtenues montrent un réseau de franges brillantes et sombres orientées dans une direction parallèle aux rainures. En scannant les structures en fonction de la profondeur des sillons, allant de 100 nm à 200 nm, nous avons observé une augmentation de fluorescence 3 fois plus importante pour une profondeur de sillon de 200 nm par rapport à celle de 100 nm. La fluorescence s'est révélée être améliorée entre les rainures, pas à l'intérieur, quelles que soient la profondeur des rainures et la direction de polarisation incidente. De plus, nous avons également étudié l'influence des inhomogénéités de la couche de pérovskite et nous avons observé que la rugosité pouvait localement modifier l'intensité des franges et perturber légèrement leur alignement. Cette étude indique que la position idéale pour l'insertion de nanocristaux à up-conversion est entre les rainures. Les résultats expérimentaux sont en accord avec les simulations numériques. Ce travail fournit donc des informations intéressantes pour la conception et d'un film de pérovskite nanostructuré permettant une extension de la collection de la lumière dans le domaine spectral du proche infrarouge à l'aide de nano-cristaux possédant des propriétés d'up-conversion.

Au cours de cette thèse de doctorat, j'ai effectué des investigations dans plusieurs domaines, couvrant des aspects comprenant diverses structures de dispositifs, l'optimisation des matériaux, les méthodes de passivation interfaciales, les propriétés thermiques et les stratégies de récupération de la lumière, pour développer des cellules solaires à base de perovskite plus performantes et plus stables. Les connaissances fondamentales acquises ici contribueront, je l'espère, à des développements importants dans ce domaine.

Mots-clés: cellules solaires pérovskites; la stabilité; couches de transport d'électrons; Nanocolonnes de TiO_2; conductivité thermique; diffusivité thermique; nanostructuration

English Abstract

With the tremendous global demand for energy and the depletion of fossil fuel, an energy crisis is closer and closer to us. Photovoltaic devices, which can efficiently convert the inexhaustible solar energy to electricity, have attracted much attention. Therefore, research towards efficient and low-cost of photovoltaic devices becomes more important than any time before. In the past decades, various types of solar cells were proposed with promising progress in performance achieved. These photovoltaic devices include silicon solar cells, inorganic thin-film solar cells, organic solar cells, dye-sensitized solar cells, and hybrid perovskite solar cells.

Among the solution-processed 3rd-generation photovoltaic devices, hybrid organometal halide perovskite solar cells have drawn enormous research and industrial attention. This is mainly due to their outstanding photovoltaic performance and their solution-processed fabrication adaptable to large-scale and low-cost manufactory. Up to now, the certified power conversion efficiency (PCE) of state-of-the-art single-junction perovskite solar cells has exceeded 25%, suggesting their great potential to compete with silicon solar cells. Despite the excellent efficiency achieved and the advantages in solution-processed fabrication, important steps are still need for perovskite solar cells to reach industrialization and large-scale application. Fundamental research in perovskite solar cells is thus still needed in order to fully understand their photovoltaic properties, and the impact of transport layer, the active layer, and the interfaces on device properties and stability.

In this Ph.D. thesis, I have been focused to investigate optimizations and strategies concerning the electron transport layer (ETL), the hybrid perovskite active layer, and their interfaces in functional perovskite solar cells. On the investigation of ETLs, I have performed two works: One is on the comparison of a simplified ETL-free planar perovskite solar cells architecture to that with a planar TiO_2 ETL (described in Chapter 2); Another work is on the comparison of perovskite solar cells with well-oriented one-dimension TiO_2 nanocolumn (NA) ETL to those with a planar TiO_2 ETL (Chapter 3). On the investigations of the perovskite active layer, mixed-cation and mixed-halide perovskite was applied into three relevant works: (1) I optimized and maximized the grain size of the perovskite active layer (Chapter 2); (2) I studied nano-structured hybrid perovskite films and their light-harvesting enhancement

(Chapter 6): (3) I investigated the thermal properties of mixed-cation perovskite thin films to understand their improved thermal stability compared to methylammonium lead iodide ($MAPbI_3$) perovskite (Chapter 4). In addition, I studied passivation methods to alleviate the interfacial charge recombination and to improve the stability of perovskite solar cells (Chapter 5).

As will be described in Chapter 2, a typical perovskite solar cell device comprises a hybrid perovskite active layer (the absorber) thin film sandwiched between an ETL and a hole-transport layer (HTL). These transport layers play an important role to collect and transport charge carriers to the external circuit. On mixed-cation and mixed-halide hybrid perovskite $FA_{0.83}Cs_{0.17}Pb(I_{(1-x)}Br_x)_3$ (FA = formamidinium $[HC(NH_2)_2]$), a promising tunable-bandgap perovskite suitable for tandem perovskite/Si applications, state-of-the-art single junction solar cells applied even a double ETL involving a layer of SnO_2 and a layer of PCBM (phenyl-C60-butyric acid methyl ester). While these results are highly interesting, it remains unclear whether such an electron transport or hole-blocking double layer is absolutely necessary for $FA_{0.83}Cs_{0.17}Pb(I_{(1-x)}Br_x)_3$ -based solar cells and to what extent their properties are modified if an ETL-free device structure are applied. From a practical point of view, a more simplified device structure should be in principle desirable towards low-cost fabrication.

While the blocking layer-free device structure can enable high-performance solar cells based on $MAPbI_3$, this approach has not been explored yet on solar cells based on $FA_{0.83}Cs_{0.17}Pb(I_{(1-x)}Br_x)_3$ at the time when the work of Chapter 2 was carried out. Compared to standard solar cell structures, the simplified ETL-free structures may offer opportunities such as reduced surface recombination (between the electrode and the ETL), the possibility to decouple the study of the perovskite growth mechanism and the device batch-to-batch differences due to the fabrication of ETL, and low-temperature fabrication adaptable to flexible polymer substrates. In particular, in ETL-free solar cells, the perovskite morphology was found to be of particular importance because any direct contact between the fluorine doped tin oxide (FTO) and the HTL can lead to detrimental reduction of photovoltaic performance.

It was under this context that I carried out the work of Chapter 2 on the realization of ETL-free efficient planar solar cells based on mixed cation and mixed halide $FA_{0.83}Cs_{0.17}Pb(I_{(1-x)}Br_x)_3$ perovskite grown directly onto FTO substrates. As the quality of the

perovskite active layer in this device structure is particular important, by varying the precursor molar concentration, we optimized the deposition conditions of the active layer leading to thickness-tunable and compact $FA_{0.83}Cs_{0.17}Pb(I_{0.6}Br_{0.4})_3$ perovskite thin films with a large grain size up to 12 microns. By employing the optimized active layer deposition conditions on to the planar device structure with and without a TiO_2 ETL, we obtained functional planar ETL-free $FA_{0.83}Cs_{0.17}Pb(I_{0.6}Br_{0.4})_3$ perovskite solar cells with PCEs and hysteresis comparable to those with a TiO_2 ETL. These results are highly encouraging for the future large-scale simplified fabrication of $FA_{0.83}Cs_{0.17}Pb(I_{0.6}Br_{0.4})_3$-based solar cells.

Despite the interesting results were obtained on functional ETL-free perovskite solar cells in Chapter 2, the device performance remains modest. In Chapter 3, we sought to achieve more stable and more performing solar cells by investigating the effect of a series of TiO_2 nanocolumn photonic ETLs on $Cs_{0.05}(FA_{0.83}MA_{0.17})_{0.95}Pb(I_{0.83}Br_{0.17})_3$-based perovskite solar cells (where $FA^+ = CH_5N_2^+$ and $MA^+ = CH_3NH_3^+$). By comparison to the planar ETLs, non-planar ones, such as mesoporous ETLs, appear to be more advantageous for perovskite solar cells to achieve higher efficiency, higher stability, and less hysteresis. Nevertheless, such straightforward TiO_2 nanoparticle-based scaffolds have some drawbacks such as the existence of numerous grain boundaries/structural defects, difficulty of pore-filling by the perovskite precursor, and perturbation to the growth of perovskite grains. By comparison, well-oriented one-dimension (1-D) TiO_2 nanorods/nanowires/nanotubes arrays represent a promising strategy, exhibiting less surface defects and grain boundaries and facilitating precursor pore-filling. 1D TiO_2 arrays can thus provide a direct physical conductive paths to extract and transport efficiently carriers generated by the perovskite layer. In terms of light-harvesting strategies, non-metal materials with high permittivity are alternative choices for nanoantenna enhancing the optical absorption and fluorescence processes at their surroundings. Due to the absence of optical absorption in the visible spectrum and its excellent electron transporting properties, 1D TiO_2 nanoarrays should be an excellent electronic and optical booster for perovskite solar cells.

Under this context, in Chapter 3, vertically aligned 1D TiO_2 nanocolumn arrays are intentionally fabricated onto half of the compact TiO_2-coated FTO substrates by the glancing angle deposition (GLAD), a method capable to generate well-oriented inorganic nanorods with uniform dimensions on substrates when using physical vapor deposition (PVD).

Structural, spectroscopy and optical characterizations were then performed on these TiO_2 nanoarrays by comparison to the compact TiO_2 (cp-TiO_2) counterpart of the same substrate. In particular, by scanning near-field optical microscopy (SNOM), the light-management capability of these nanoarrays is studied in detail, revealing strong concentration of electromagnetic fields at the surroundings of the nanoarrays. Functional triple-cation lead perovskite halide solar cells based on $Cs_{0.05}(FA_{0.83}MA_{0.17})_{0.95}Pb(I_{0.83}Br_{0.17})_3$ are then built onto the above-mentioned substrates, half of which covered by TiO_2 nanocolumn electron transport layer (ETL) and the other half covered by cp-TiO_2 ETL. By comparison to the solar cells built on only a planar cp-TiO_2 ETL of the same FTO substrate, solar cells with TiO_2 nanocolumn arrays exhibit a 5% increase in its short-circuit current and a 7% enhancement in its power conversion efficiency, together with a significantly prolonged shelf-life. Revealed by electrochemical impedance spectroscopy, the application of TiO_2 nanocolumn arrays leads to a lower charge transport resistance and a higher charge recombination resistance in the solar cell, both contributing to the observed enhanced photovoltaic performance. In addition, such TiO_2 nanocolumn arrays exhibit a more significant optical absorption in the UV spectrum by comparison to the planar counterpart, capable to perform partial UV-screening boosting the stability of the perovskite solar cell. The combined structural, spectroscopic, photovoltaic and optical characterizations presented herein provide a detail analysis on the physical origins of the beneficial roles of 1D TiO_2 nanocolumn arrays in hybrid perovskite solar cells.

By comparison to silicon solar cells which typically have a life-span of 25 years, hybrid perovskite solar cells degrade relatively rapidly under operating conditions, so far posing serious issues limiting their large-scale applications. It is thus essential to perform fundamental research on the thermal management and thermal degradation mechanisms of perovskite solar cells, which may be closely related to the device lifetime. On methylammonium lead halides ($MAPbX_3$, X=Cl, Br, I), their thermal conductivities have been studied by different groups by various experimental and theoretical methods. By comparison, while mixed-cation and mixed-halide hybrid perovskite compounds such as $Cs_{0.05}(FA_{0.83}MA_{0.17})_{0.95}Pb(I_{0.83}Br_{0.17})_3$ exhibit enhanced thermal stability than $MAPbI_3$, their thermal property is still not well-studied.

Under this context, in Chapter 4, we measured the thermal conductivity and thermal diffusivity on a series of $Cs_{0.05}(FA_{0.83}MA_{0.17})_{0.95}Pb(I_{0.83}Br_{0.17})_3$ perovskite thin films, of

different thickness but similar morphology in a real solar cell configuration, by the technique of modulated thermoreflectance microscopy. The thermal conductivity and thermal diffusivity are crucial parameters to predict how fast and how efficiently heat will dissipate in the active layer and toward the substrate. On our samples we measured a thermal conductivity k of 0.26 ± 0.03 $W.m^{-1}.K^{-1}$ and a thermal diffusivity D_{per} of $3.5 \times 10^{-7} \pm 0.5$ $m^2.s^{-1}$. Our measurements indicate that thermal conductivity of such mixed-cation and mixed-halide compounds is only slightly smaller than that of MA-based perovskites found in the literature, showing that the substitution of MA^+ by FA^+ and Cs^+ has a very limited influence on the thermal properties of hybrid perovskites. Rather, the enhanced thermal stability of $Cs_{0.05}(FA_{0.83}MA_{0.17})_{0.95}Pb(I_{0.83}Br_{0.17})_3$ perovskites by comparison to $MAPbI_3$ likely comes from a chemical origin.

A part from the above-mentioned thermal property, the crystallinity and the morphology of the perovskite active layer and the perovskite/transport-layer interfaces play together critical roles on the optimization of the photovoltaic performance and device stability. In particular, the grain boundaries, impurities, and defects located either in the bulk or at interfaces can facilitate ion migration and act as charge carrier recombination sites, leading to efficiency loss and device degradation. Various strategies are currently under extensive investigation in order to precisely control the crystallinity and the morphology of the perovskite layer and its interfaces with the transport layers aiming to obtain a highly crystalline, compact and smooth layer with large crystalline grains. In particular, on the triple-cation perovskites with the composition of $Cs_{0.05}(FA_{1-x}MA_x)_{0.95}Pb(I_{1-y}Br_y)_3$, recently it becomes very common to apply a slight deviation of the PbI_2/methylammonium iodide (MAI) concentration ratio above the stoichiometric ratio (of 1) aiming for improved photovoltaic performance. Nevertheless, the true role of the excess PbI_2 remains highly controversial, lacking consensus on its effect on the bulk and interface properties of the perovskite solar cell.

In light of the seemingly contradicting results from the literature, in Chapter 5 we propose an investigation on the controversial role of the excess PbI_2 in perovskite solar cells. Specifically, based on $Cs_{0.05}(FA_{0.83}MA_{0.17})_{0.95}Pb(I_{0.83}Br_{0.17})_3$ perovskite solar cells, we provided an experimental comparison on the photovoltaic behavior and the solar cell stability under continuous solar illumination between samples with a slight excess of unreacted PbI_2 (in the bulk and at the interface) and samples with the excess PbI_2 intentionally removed at the

perovskite/HTL interface. By combining a series of structural, optical, and photovoltaic characterization methods, we found that upon removing the excess PbI_2 from the perovskite/HTL interface by treating the perovskite surface with an organic salt solution, not only the efficiency, but also the stability of triple-cation perovskite solar cells can be enhanced. The improvement in efficiency is associated with a significantly reduced transport resistance and an increased recombination resistance of the organic salt solution -treated samples as probed by impedance spectroscopy. More importantly, under continuous solar illumination, the unencapsulated solar cells in which the excess PbI_2 was removed from the perovskite/HTL interface maintained respectively 81% and 86% treated by the MAI and FAI solution of their initial PCE (*v.s.* 64% for the solar cell with excess PbI_2) after 100 hours of degradation. Our results show that eliminating PbI_2 at the perovskite/HTL interface is highly beneficial for both the efficiency and stability of perovskite devices and can be easily implemented during their fabrication process.

Finally, in Chapter 6, we explored a light-harvesting strategy by optical optimization on $Cs_{0.05}(FA_{0.83}\ MA_{0.17})_{0.95}Pb(I_{0.83}Br_{0.17})_3$ perovskite solar cells, aiming for an extended photovoltaic spectral response when coupled with rare-earth-doped upconversion nanoparticles. Specifically, we investigated nanostructuring the $Cs_{0.05}(FA_{0.83}\ MA_{0.17})_{0.95}Pb(I_{0.83}Br_{0.17})_3$ perovskite layer and its effect on its local optical properties. For this, the perovskite surface was engraved by a focused ion beam to form gratings of one-dimensional grooves. We then characterized the surfaces of engraved perovskite by a home-built SNOM where the sample was excited in a transmission mode by a modulated focused laser beam at λ_{exc} = 975 nm with its surface scanned by a sharp atomic force microscopy (AFM) tip glued with a Er^{3+} and Yb^{3+} co-doped KY_3F_{10} upconversion nanoparticle. The obtained fluorescence maps showing a clear fringe pattern oriented in a direction parallel to the grooves. By scanning structures as a function of the grooves depth, ranging from 100 nm to 200 nm, we observed that a 3-fold fluorescence enhancement for a groove depth of 200 nm by comparison to that of 100 nm. The near-field fluorescence was found to be enhanced between the grooves, not inside them, whatever the groove depth and the incident polarization direction. In addition, we also studied the influence of the inhomogeneities of the perovskite layer and we observed that the roughness could locally modify the intensity of the fringes and to distort their alignment. This study indicates that the ideal position for the upconversion nanocrystal insertion is between the grooves. With the

experimental results well agreed with numerical simulations, this work provides fundamental insights for the design and application of nanostructured perovskite film towards enhanced light harvesting and spectral response extension.

In a brief summary, through this PhD thesis I performed a multi-domain investigations, covering aspects including various device structures, material optimization, interfacial passivation methods, thermal properties, and light-harvesting strategies, all towards more performing and more stable solution-processed hybrid perovskite solar cells. The fundamental knowledge obtained here will contribute strongly to the further development of this field.

Keywords: perovskite solar cells; stability; electron-transport layers; TiO_2 nanocolumns; thermal conductivity; thermal diffusivity; nanostructuration

Table of Contents

Chapter 1. Introduction

1.1. Structure and Properties of Perovskite Materials and the Evolution of PSCs

1.1.1. Structure and Properties of Perovskite Materials

In 1839, the calcium titanium oxide ($CaTiO_3$, abbreviated as ABX_3 formula) compound was first discovered by German mineralogist Gustav Rose in the Ural Mountains of Russia. Since then, the term "perovskite" refers to any kind of materials owning the same type of the crystal structure of $CaTiO_3$, to be the honor of Russian mineralogist Lev Perovski.[1] In 1978, Weber et al., first reported that the introduction of methylamine ions into perovskite crystal structure formed an organic-inorganic halide perovskite materials with a three-dimension structure.[2]

Since the typical molecular formula of perovskite material is ABX_3; here, A represents a monovalent cation (like $CH_3NH_3^+$, $CH(NH_2)_2^+$, Cs^+); B represents a divalent metal cation (such as Pb^{2+}, Sn^{2+}, Ge^{2+}) and X is a halogen anion (like Cl^-, Br^-, I^-).[3,4] In an ideal perovskite featuring cubic-symmetry or octahedral structure, the small-sized B cation is coordinated with the 6-fold X halogen anion, forming an octahedron BX_6; while large-sized A cation is in 12-fold X halogen anion, constituting a cubic octahedral structure AX_{12} shown in **Figure 1**.[5]

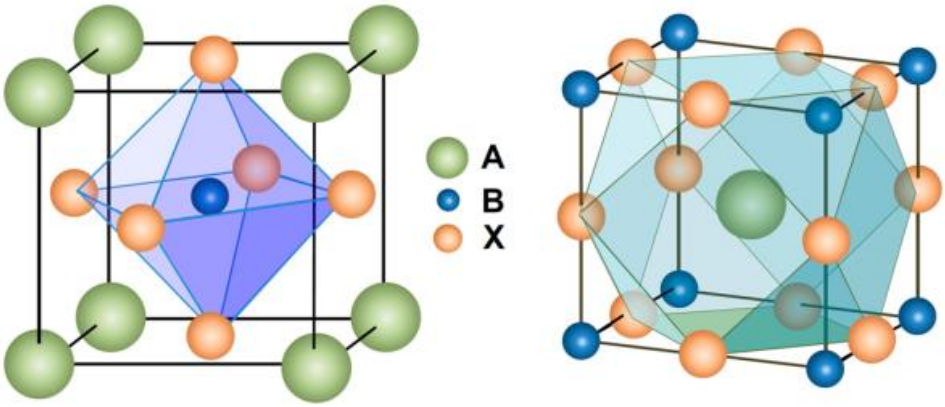

***Figure 1**. ABX_3 perovskite structure showing (left) BX_6 octahedral and (right) AX_{12} cuboctahedral geometry.*[5]

Therefore, the perovskite crystal structure is described as a three-dimensional network of a corner-sharing octahedral BX_6 unit, and with A cation located in the octahedral interstices. The stability of the perovskite structure based on the three A, B, X ions can be analyzed by using Goldschmidt's tolerance factor (*t*), the corresponding equation is listed below:

$$t=\frac{R_A+R_X}{(R_B+R_X)\sqrt{2}} \qquad (1\text{-}1\text{-}1\text{-}1)$$

where R_A, R_B, and R_X are the radius of corresponding A, B, X site elements. To maintain the special perovskite crystal structure, the value of the *t* factor should be kept in the range of about $0.81 < t < 1.11$ (as shown in **Figure 2**).

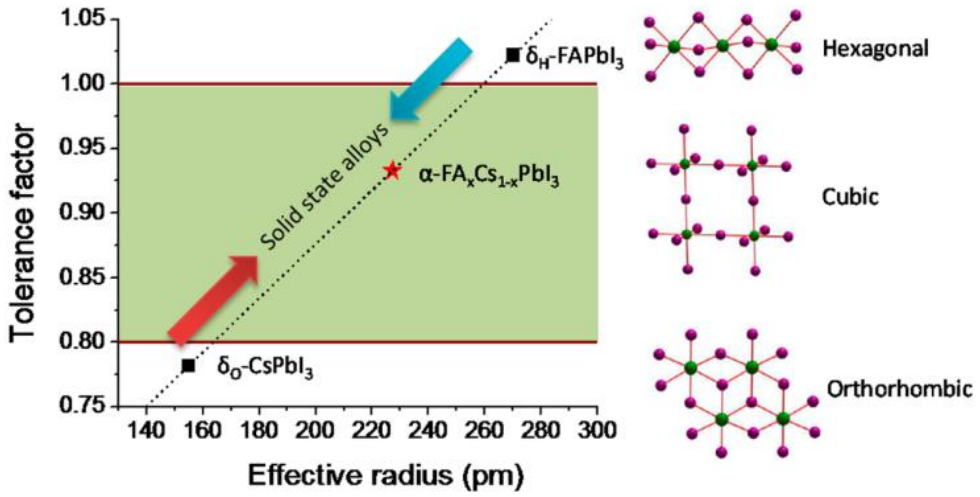

Figure 2. *Correlations between tolerance factor and the crystal structure of perovskite materials.*[6]

When the tolerance factor is close to 1, the likely cubic structure of perovskite materials is more stable based on these three mentioned above ions.[7] In contrast, when the *t* factor is a bit far away from 1.0, the ideal crystal structure of ABX_3 perovskite material would change correspondingly. Simultaneously, if the A ions own small radius or the B ions have large size, it would result in the *t* factor <1, which is favorable for the formation of orthogonal, trigonal, or tetragonal structures.[6,8] If the radius of the A ions is too large or B cation is too small, it is beneficial for the constitution of two-dimensional (2D) structure and even one-dimensional materials.[9] As a consequence, the related physical properties of perovskite material, such as electronic, optical, magnetic properties would be affected.

However, for some types of perovskites, the tolerance factor is not sufficient to predict the stability of the structure. Because the *t* factor is calculated based on the related ion radius, which is considered as a rough estimation. Therefore, the octahedral factor (μ) was introduced to complement the analysis of the stability of the perovskite crystal structure based on ABX_3, which is defined by the corresponding equation listed below:

$$\mu = \frac{R_B}{R_X} \qquad (1\text{-}1\text{-}1\text{-}2)$$

Generally, for the halide perovskite materials (X=Cl, Br, I) with a likely cubic structure, the tolerance factor range is $0.81 < t < 1.11$, also require an octahedral factor between $0.44 < \mu < 0.90$.[10,11]

1.1.2. Photoelectric Properties of Perovskite Materials

Up to now, numerous hybrid organic-inorganic halide perovskite materials have been developed as the light harvesting layer. In particular, $CH_3NH_3PbI_3$ ($MAPbI_3$) perovskite material has been widely studied due to its inherent excellent photoelectric properties, which are mainly listed as follows:

(1) Wide absorption range

The bandgap of the $MAPbI_3$ perovskite material is around 1.5 eV (approaching to Schotty barrier theory), which can absorb the entire visible region (from 300 nm to 800 nm) and meanwhile present high efficiency of sunlight utilization, resulting in a high photo-generated current.[12,13]

(2) High absorption coefficient

The high absorption coefficient is an important pre-condition to achieve the prominent performance of PSCs because it can effectively reduce the required thickness of the light absorption layer and increase the efficiency of harvesting photo-generated carriers. $MAPbI_3$ perovskite materials are well-known direct semiconductor, so the absorption coefficient of perovskite material is much higher than that of the silicon material.[14,15]

(3) Long exciton diffusion length

Compared to the exciton diffusion length organic semiconductor (approximately 10 nm), the exciton diffusion length of polycrystalline $MAPbI_3$ materials reaches around 100 nm by

transient photoluminescence measurement.[16] While the exciton diffusion length of the mixed halogen $MAPbI_{3-x}Cl_x$ has exceeded 1 μm.[17] Recently, Dong et al. have proved that exciton diffusion length in a single $MAPbI_3$ perovskite crystal reaches 175 μm, due to the single crystal with fewer defects, higher carrier mobility, and longer lifetime. It means that the exciton recombination possibility can be efficiently reduced during the transmission process, thereby improving the power conversion efficiency of the PSCs.[18]

(4) Fast carrier mobility

The perovskite materials present bipolar carrier transport properties, which can transfer both electrons and holes.[19] This bi-functional performance greatly enriches the structure of the devices. It found that the hole and electron mobility of $MAPbI_3$ were 12.5-66 and 7.5 cm^2/Vs, respectively, leading to rapid separation action between the photo-generated electrons and holes, thereby the negative carrier recombination can be suppressed.[20]

(5) Low exciton binding energy

It is reported that the $MAPbI_3$ perovskite material has an exciton binding energy of approximately 19 meV. When exposed to light, the exciton produced can be spontaneously separated into a large number of free electrons and holes at room temperature, contributing to the following photoabsorption.[21]

(6) Tunable bandgap

Another advantage of perovskite materials is that the bandgap can be tuned by ion (cation or anion) doping and replacement, resulting in acquiring expected photoelectronic properties. For the $MAPbI_3$ perovskite materials, Br^- or Cl^- can be applied instead of I^- and then to prepare $MAPbBr_3$ and $MAPbCl_3$ perovskite material with different bandgaps (shown in **Figure 3**).[22,23] The colorful perovskite devices can be significantly designed by this strategy. While, MA^+ ($CH_3NH_3^+$) can be replaced by FA^+ $(CH(NH)_2)_2^+$ with a slightly larger ionic radius, which presents more stable photovoltaic performance.[24] The bandgap of $FAPbI_3$ is around 1.45-1.52 eV, compared with $MAPbI_3$ (1.59 eV). Moreover, if using Sn^{2+} to replace Pb^{2+}, the bandgap of $MASnI_3$ is around 1.3 eV, extending the absorption range to 1100 nm (infrared light).[25]

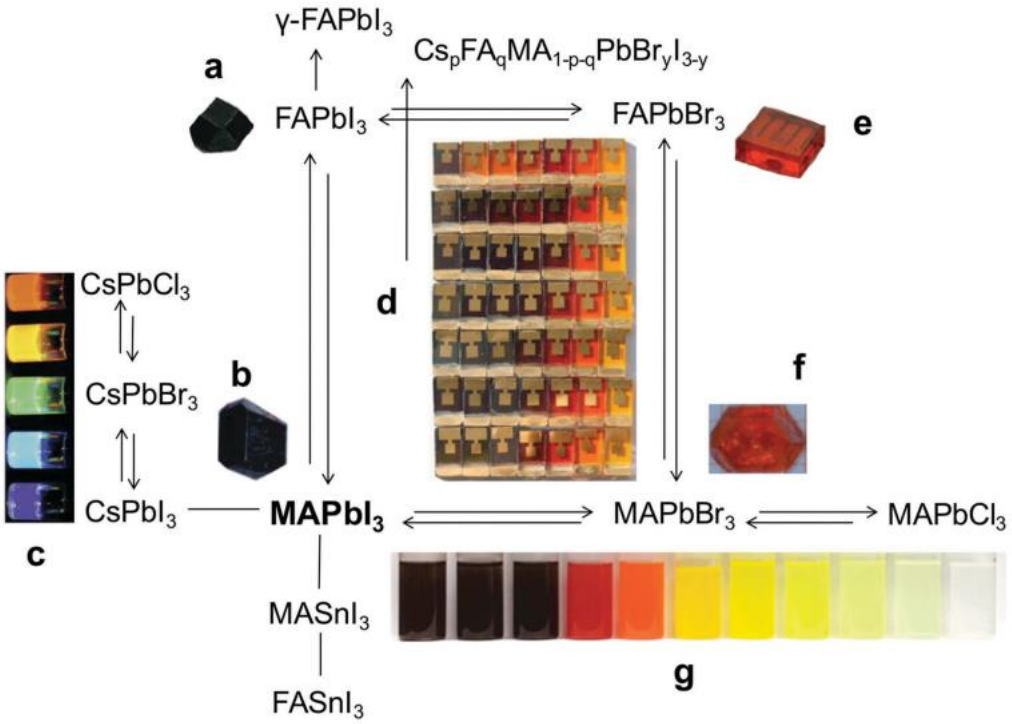

Figure 3. *The versatility of hybrid perovskite materials and their absorption tunability. Schematics of some investigated perovskites closely related to* $MAPbI_3$*. The insets show (a) single crystal of* $FAPbI_3$*, (b) single crystal of* $MAPbI_3$*, (c) colloidal solutions of* $CsPbX_3$ *(X = Cl, Br, I) perovskites, (d) solar cells of different compositions in the MA/FA-Pb-Br/I compositional space, (e) single crystal of* $FAPbBr_3$*, (f) single crystal of* $MAPbBr_3$*, and (g) colloidal nanocrystals of* $MAPbX_3$ *(X = Cl, Br, I) perovskites.*[22]

1.1.3. Photovoltaic Evolution of PSCs

Hybrid organic-inorganic perovskite solar cells have attracted huge attention due to their excellent photovoltaic performance and low-cost solution processing characteristics. Up to now, the certified power conversion efficiency (PCE) of PSCs has rapidly increased from the initial 3.8% to 25.2% as shown in **Figure 4**. The perovskite solar cells have great potential in the area of solar cells, comparable to the traditional silicon solar cells.

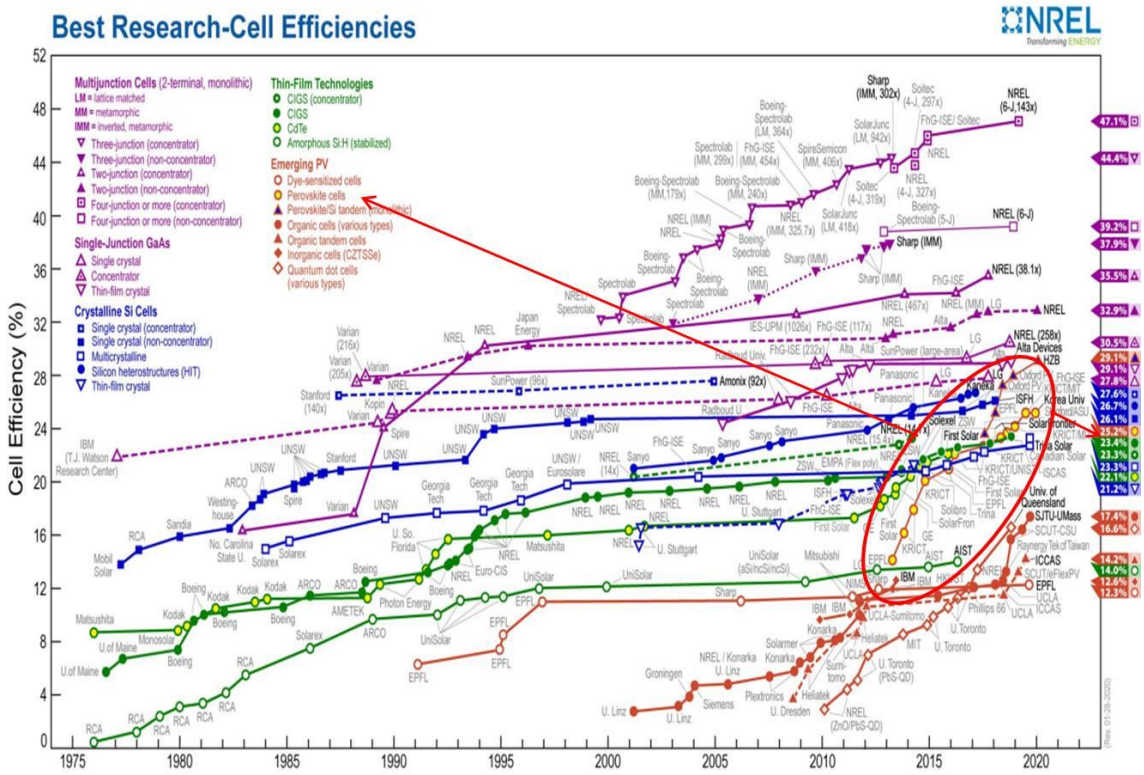

Figure 4. *Best research-cell efficiency chart of perovskite solar cells (https://www.nrel.gov/pv/cell-efficiency.html).*

In 2009, Miyasaka et al., first reported that the dye-sensitized solar cells (DSSCs) with TiO_2 mesoporous structure, using perovskite material ($MAPbI_3$) as dye sensitizer. It was found that the PCE of the corresponding solar cells can reach 3.8%, unfortunately within poor stability.[26] In 2011, Park et al., deposited a layer of perovskite quantum dots with a diameter of about 2.5 nm on the surface of TiO_2 ETLs, using similar device structure as former work as shown in **Figure 5**. The PCE of the solar cells was 6.5%.[27] Although the perovskite quantum dots present better absorption than the standard N719 dye sensitizer, it was prone to dissolve in the electrolyte and then led to device degradation rapidly. In 2012, Park and Grätzel groups collaborated to use organic hole transport layer Spiro-OMeTAD instead of liquid electrolytes to fabricate a more stable solid-state solar cell with a PCE of 9.7%, exceeding that of the traditional solid-state DSSCs.[28]

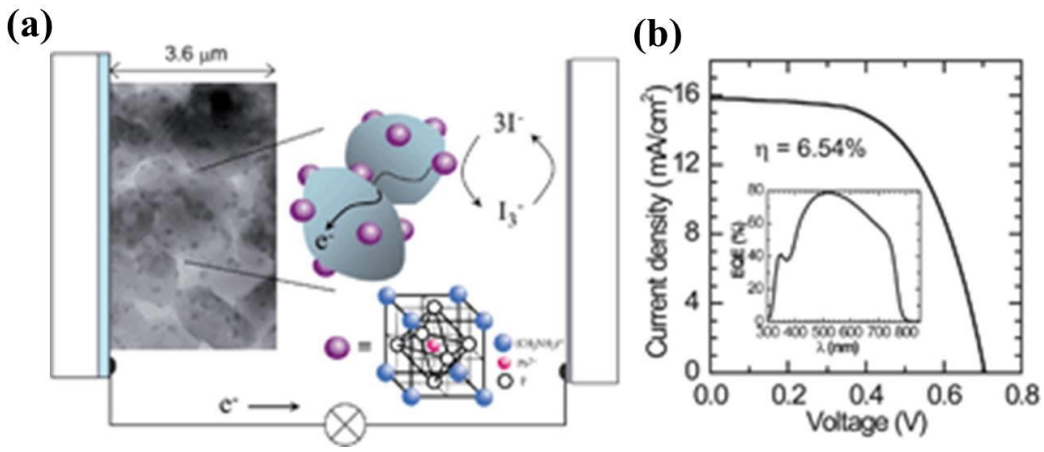

Figure 5*. (a) the sketch of the perovskite quantum-dot-sensitized solar cell. (b) Photocurrent–voltage curve and EQE for the perovskite (CH_3NH_3)PbI_3 QD-sensitized TiO_2 film.*[27]

In the same year, Snaith et al., reported that the $MAPbI_{3-x}Cl_x$ was used as a light active layer deposited by spin-coating method into a mesoporous Al_2O_3 framework, and the Spiro-OMeTAD was also used hole transport material with a PCE of 10.9% shown in **Figure 6**.[29] Since then, all-solid-state hybrid organic-inorganic perovskite solar cells have attracted worldwide attention, promoting the rapid development of the PSCs. In 2013, Grätzel's group developed a two-step iodide deposition method, which improved the quality of the perovskite morphology and reached a PCE of 15%.[30] And the same year, Snaith's group prepared the high-quality $MAPbI_{3-x}Cl_x$ perovskite film based on the planar structure by dual-source thermal evaporation, achieving a PCE of 15.4%.[31]

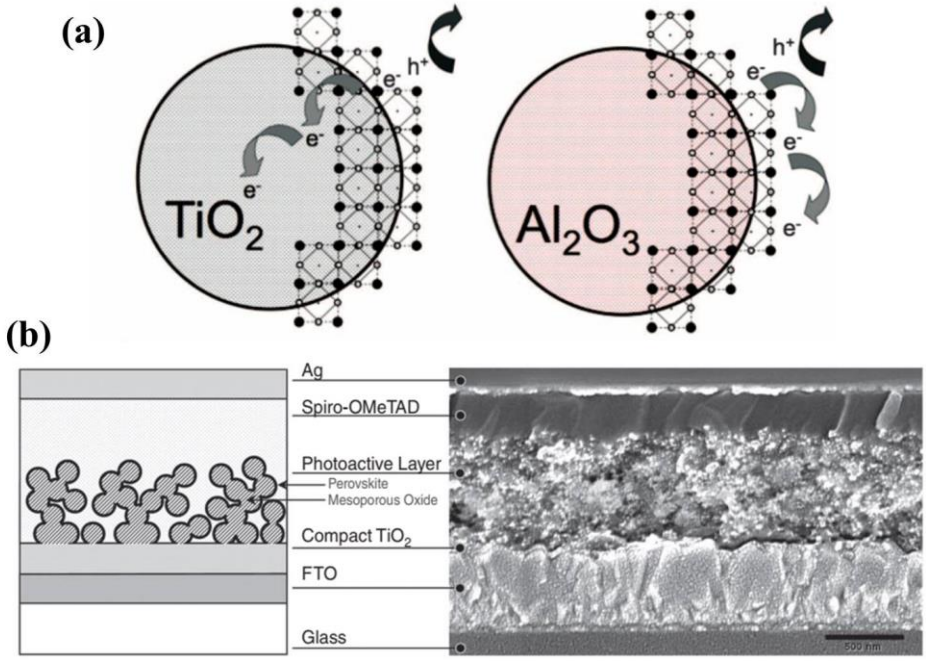

Figure 6. *(a) Schematic illustrating the charge transfer and charge transport in a perovskite-sensitized TiO_2 solar cells (left) and a noninjecting Al_2O_3-based solar cells. (b) Left: Schematic representation of full device structure, where the mesoporous oxide is either Al_2O_3 or anatase TiO_2. Right: Cross-sectional SEM image of a full device incorporating mesoporous Al_2O_3.*[29]

In 2014, Yang Yang's group used yttrium-doped TiO_2 as an ETL and combined the optimized perovskite deposition technique, reaching a PCE of 19.3%.[32] In 2017, Seok's group reported that the introduction of additional iodide ions into the perovskite precursor solution is the benefit of obtaining high-quality perovskite film, with a certified PCE of 22.1% in small cells and 19.7% in 1 cm^2 PSCs.[33] In 2019, You's group found that the perovskite solar cells based on mixed cation $FAMAPbI_3$ passivated by phenethylammonium iodide (PEAI) can efficiently reduce the defects and suppress non-radiative recombination, with a certified PCE soared up to 23.32% shown in **Figure 7**.[34] And in 2019, the latest perovskite solar cell certification efficiency has reached to 25.2%.

Furthermore, with the high development of the PSCs, a series of other perovskite solar cells with novel device structures have begun to be derived. At present, researchers do not just focus on improving the PCE of the perovskite device, and they begin to shift their attention to

solve the drawbacks, such as device stability, toxicity, flexible device, and large area efficiency.

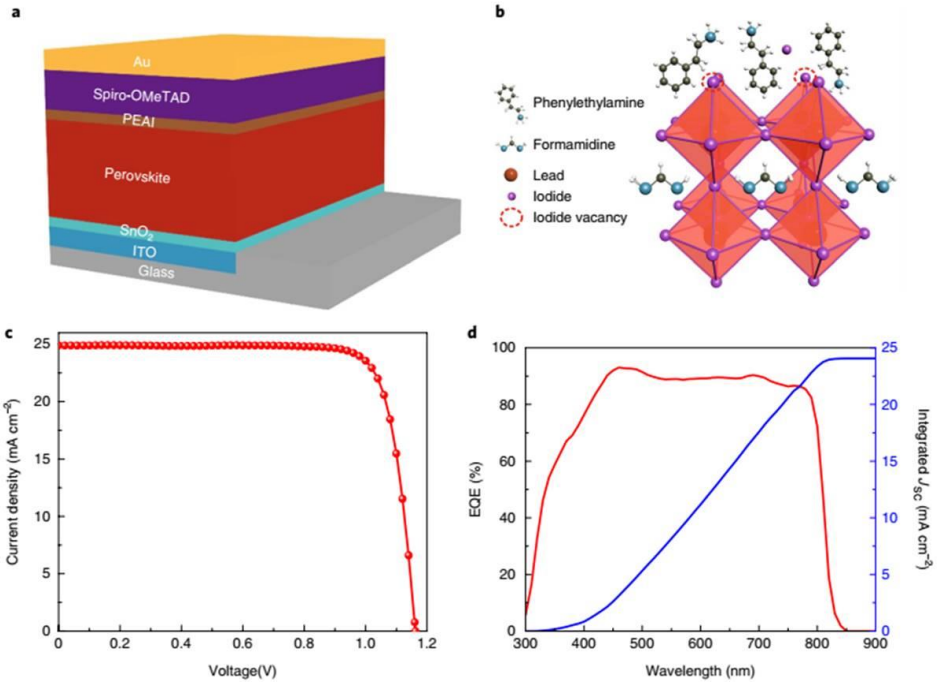

Figure 7. *(a) The schematic structure of PSCs. (b) possible passivation mechanism of the PEAI layer for perovskite film. (c) Photocurrent–voltage curve and (d) EQE for the best perovskite solar cells.*[34]

1.2. Components of Typical PSCs

1.2.1. Working Electrode

The requests of the electrode substrate for the perovskite solar cells are with good planarity, proper work function, high electrical conductivity, and high light transmittance. Generally, the square resistance of the electrode should be around 10-20 ohms. At present, the substrate is mainly fluorine-doped tin oxide (FTO) and indium tin oxide (ITO). Although the conductivity of the ITO substrate is higher than that of the FTO substrate, the thermal stability of the ITO substrate is not as good as FTO. Before using the conductive glass substrate, it is commonly cleaned with soap detergent, deionized water, acetone, ethanol, and ozone treatment.

1.2.2. Electron Transport Layer (ETLs)

Electron transport layer refers to the material applied to receive electrons from the perovskite absorption layer and transport the electrons to the photoanode, with high electron mobility, and appropriate conduction band energy level, and an outstanding light transmittance and stability. [35] Commonly, the electron transport layer can be divided into a compact layer and a mesoporous layer. At present, TiO_2 is epidemically used as an electron in PSCs. The main roles of the compact TiO_2 layer are to collect electrons and block holes. The functions of the mesoporous TiO_2 layer is ***i)*** to behave as a scaffold and ***ii)*** to transport electrons. The thickness of the mesoporous layer determines the thickness of the perovskite active layer, which greatly influences the open-circuit voltage of the PSCs.[36] For the planar perovskite solar cells, the ETL has only consisted of the dense TiO_2 layer. While for the mesoporous perovskite solar cells, electron transport layers contains the compact and mesoporous TiO_2 structure. Besides, because the growth of the perovskite film is restricted by the mesoporous layer, the morphology of the perovskite film is relatively repeatable, compared to the perovskite layer with planar structure.

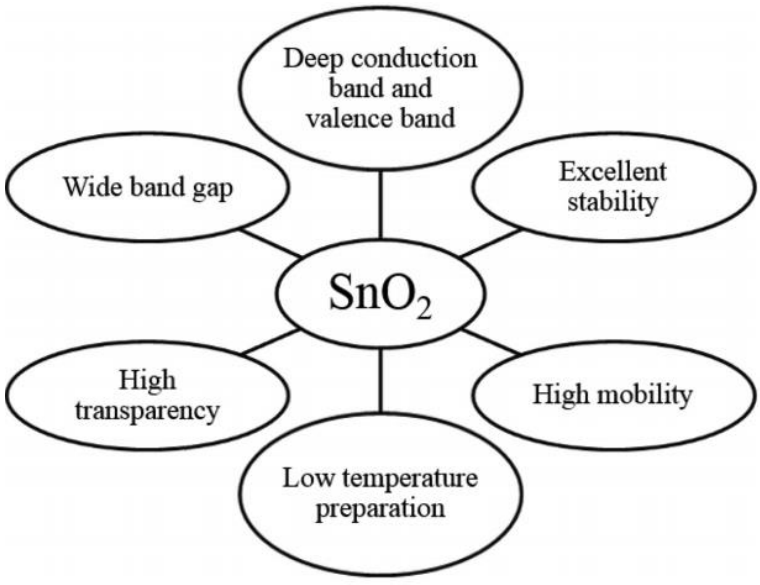

Figure 8. *Unique and favorable advantages of SnO_2 as ETLs in PSCs.*[37]

However, the shortcomings of the TiO_2 ETL are also obvious. The electron mobility of TiO_2 ETL (0.1-0.2 cm^2/Vs) is relatively low.[38] And there are a large number of oxygen-deficient states in the TiO_2 film, leading to strong photocatalytic degradation action and then influence

the long-term stability of the PSCs.[39] Therefore, researchers have studied other n-type semiconductor materials such as ZnO, SnO_2 (advantages listed in **Figure 8**) and CdS to replace TiO_2 ETL and also have obtained some excellent results.[37,40,41] Except for using inorganic semiconductor as ETL, more and more organic semiconductor materials including fullerenes and fullerene derivations are widely used as ETL into the perovskite device.[42] Because such organic materials can be deposited by a simple solution process method and present good electronic conductivity.

1.2.3. Perovskite Absorber Layer

As the key component of PSCs, the development of the perovskite thin films determines the progress of the perovskite solar cells. Researchers mainly improve the stability and power conversion efficiency of PSCs by modulating the composition of perovskite materials, regulating the grain size of perovskite crystal, and optimizing the interface of the perovskite layer.[43,44] In particular, the typical hybrid organic-inorganic perovskite materials ($MAPbI_3$) have been intensively studied into the PSCs, presenting excellent photovoltaic performance. According to Goldschmidt's tolerance factor theory, organic FA^+ ($CH(NH)_2^+$) not only can replace the MA^+ to form $FAPbI_3$ perovskite material with a slightly narrower bandgap but also can keep the required cubic perovskite structure.[45] Pellet et al. first used the mixed MA^+ and FA^+ cations in the A position of the ABX_3 perovskite material. By adjusting the varied ratio of MA^+ and FA^+, the absorption edge extends to approximately 810 nm. As a result, the short-circuit of the PSCs with the mixed cations has been improved, compared to the device with a single MA^+ cation.[46] Although the efficiency and stability of the perovskite ($MAPbI_3$) device have been improved after interacting with FA^+ cation, the stability of the mixed cation perovskite solar cells still does not reach to the commercial requirements. To further improve the stability of the device, two-dimensional (2D) halide perovskite materials have shown great advantages. Compared to three dimensional (3D) hybrid perovskite materials, layered 2D hybrid perovskite material (such as monommoniums PEA^+, phenylethylammonium BA^+, n-butylammonium EDA^{2+}) owns bulkier a more hydrophobic organic cations and possess superior moisture stability shown in **Figure 9**.[47] Bai et al., reported that the perovskite device using Quai-2D $MAPbI_3$-$PEA_2Pb_2I_4$ as light active layer lead to an ultrahigh V_{oc} at 1.17 V and significantly improved their thermal stability.[48]

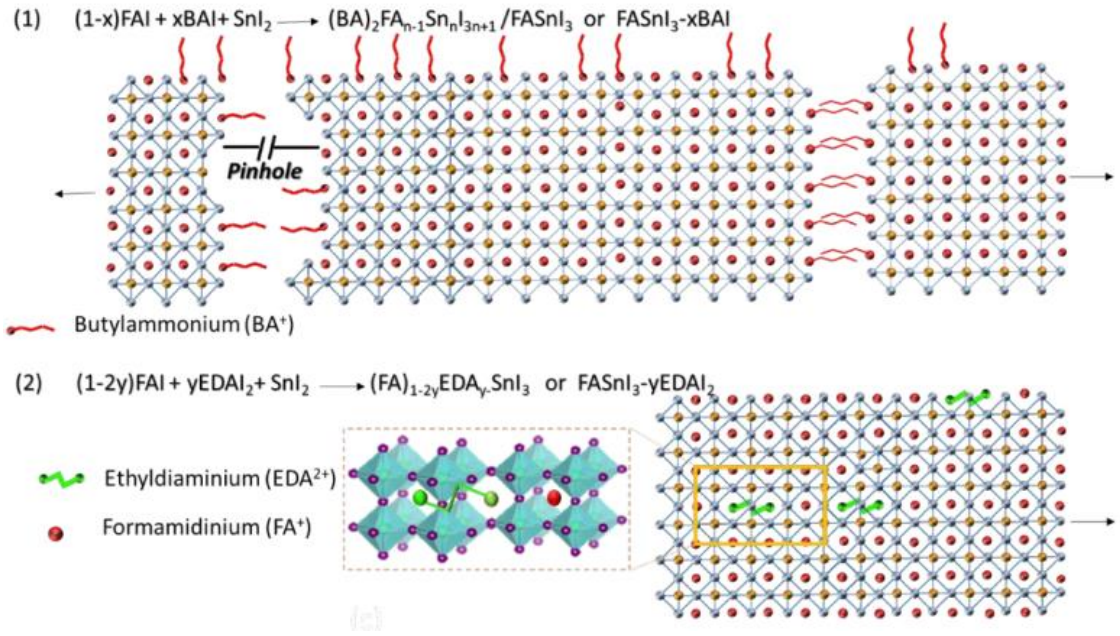

Figure 9. *Schematic representations of perovskite crystals in the presence of BAI and $EDAI_2$ additives.*[47]

It is well known that the stability of inorganic perovskite solar cells is more stable, compared to organic perovskite solar cells. In the inorganic lead halide perovskite field, the cubic (α) $CsPbI_3$ is considered as perfect materials for the photovoltaic applications with a bandgap of 1.73 eV. Unfortunately, the $CsPbI_3$ perovskite material presents a stable non-perovskite orthorhombic (δ) phase (E_g=2.82 eV) at room temperature and only can transfer to cubic perovskite phase at high temperature.[49] Although the inorganic perovskite materials suffer from poor phase stability, they have become one of the most appealing research pots and achieved some huge progress in the latest 3 years. In 2005, Snaith's group first studied the novel inorganic $CsPbI_3$ perovskite device with a PCE of 2.9% by using hydriodic acid (HI) to optimize the grain size of the perovskite crystals.[50] In 2018, the certified PCE of inorganic PSCs was over 18%, showing its great potential in the photovoltaic area.[51]

So far, the high PCE and stable perovskite solar cells contain the heavy metal lead (toxic element to nerve system), which may cause a serious environmental pollution problem and threatens the health of human beings. As for PSCs, how to solve the lead pollution issue is a big challenge. Some research groups successively reported that many non-lead materials, such as $MASnI_3$, $FASnI_3$, and $MASnBr_3$, etc. exhibit exciting photovoltaic behavior.[52–54] However, the Sn^{2+} ions are not stable in the ambient environment with oxygen, which is very easy to be

oxidized and then leads to non-perovskite phase. In addition, halide double perovskites $A_2BB'X_6$ (e.g.$Cs_2AgBiBr_6$, $Cs_2Ag(Bi_{0.625}Sb_{0.375})Br_6$) have attracted much attention due to their proper bandgap for perovskite device.[55] However, due to a crystal structure defect at B-site, the PCE of halide double perovskite solar cells is relatively low. And the Ge-based PSCs, Cu-based PSCs, Bi-based PSCs, and Sb-based PSCs present highly stable performance, while also show a similar low-efficiency problem. Therefore, these free-lead perovskite materials may be a good choice for future perovskite devices, but there is still a long way to go before realizing the commercial application.

Simultaneously, to obtain high quality of perovskite film, researchers have developed various preparation methods for the PSCs, such as one-step spin-coating method, a two-step spin-coating method, two-step deposition method, a dual-sources evaporation method, etc.[56–59]

1.2.4. Hole Transport Layers (HTLs)

Hole transport layer refers to the material applied to receive holes from the perovskite absorption layer and transport the holes to the photocathode, with high hole mobility, and appropriate valence band energy level, and good stability. Currently, the organic Spiro-OMeTAD (**Figure 10**) is widely used HTL with some additives, such as lithium salt (Li-TFSI) and 4-tert-butylpyridine (4-TBP).[60] However, the price of the Spiro-OMeTAD is very expensive, which greatly increases the cost of the PSCs. Meanwhile, the additives are volatile and hygroscopic, which seriously impact the stability of PSCs. Therefore, it is very meaningful to deplore new low-cost and dopant-free HTL, to further promote the commercial process of PSCs. In, Han et al., first reported using the tetrathiafulvalene derivative TTF-A small organic molecule as dopant-free HTL for the PSCs with a PCE of 11.03%, comparable to the perovskite device base on doped Spiro-OMeTAD (11.4%).[61] Besides the small organic molecule, the polymeric compounds are also commonly used in PSCs as HTL, which present suitable carrier mobility, low-cost, compatible with perovskite material. Poly-3-hexylthiophene (P3HT) polymer without any additive is the most widely used in PSCs, showing good photovoltaic performance.[62] Another low-cost and commonly used polymer is PEDOT: PSS, due to its tunable conductivity and high optical transmittance.[63]

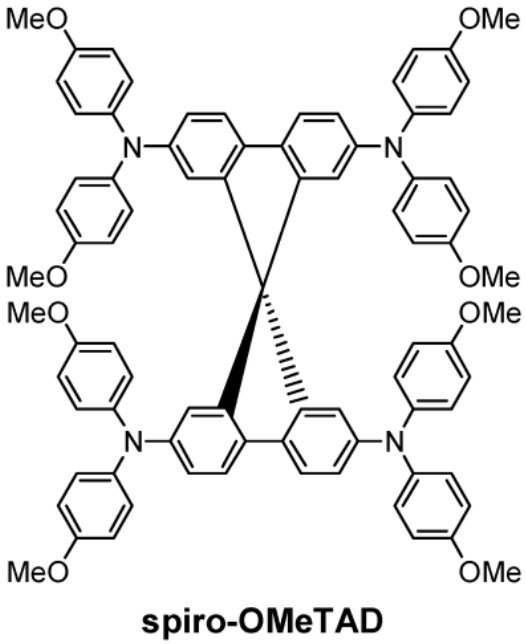

***Figure 10**. The structure of Spiro-OMeTAD.*[60]

As an alternative to organic HTLs, the inorganic p-type semiconductors have attracted more and more attention because of their low-cost, simple fabrication, and great stability. p-type NiO_x compound with a large bandgap is widely used in the inverted perovskite solar cells. With the rapid development of NiO_x HTL, the photovoltaic performance of the PSCs reached beyond 19%.[64] Besides NiO_x, CuI, and Cu_2O are also considered as suitable HTL, due to showing good energy level alignment with the HOMO level of perovskite materials.[65,66] As a consequence, the free-dopant organic and inorganic p-type materials have presented great promising and can be used into PSCs in the future commercial perovskite devices.

1.2.5. Contact Electrode

For PSCs, the counter electrode should have a high work function with small ohmic contact resistance. The role of the counter electrode is to rapidly collect and transport the carrier. At present, the intensively used metal electrodes are Au, Ag, Cu, and Al electrodes.[67] However, these metal electrodes are prone to be oxidized in the air ambient to form insulating oxides, which will increase the contact resistance during the photovoltaic test. In addition, these metal electrodes may react with the diffused halogen to form a halide barrier layer, impacting the PCE and stability of the perovskite devices. The work function of the carbon materials (-5.0 eV) is similar to Au (-5.1 eV), and the carbon materials have great stability and

hydrophobicity. Therefore, in 2014, Han's group first used the carbon materials as a counter electrode into PSCs without HTL, reaching a PCE of 12.8%, comparable to the perovskite device based on the Au electrode (**Figure 11**).[68] Since then, the carbon electrode is very popular in the PSCs.

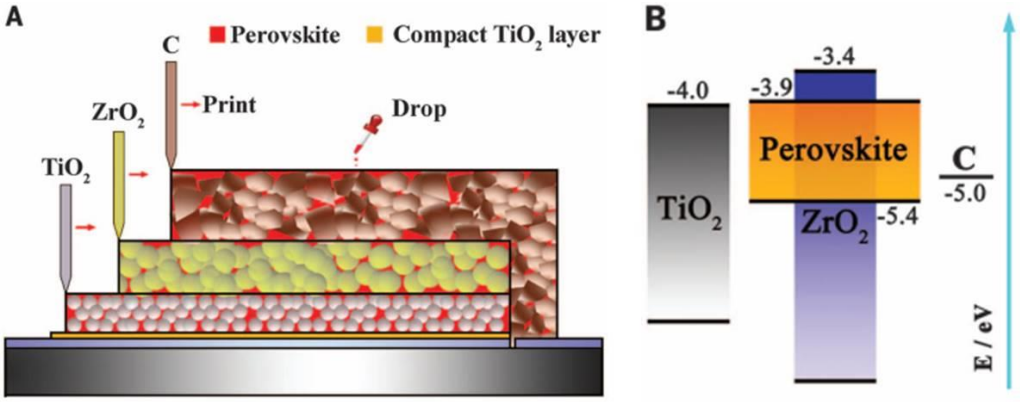

Figure 11. *(A) Schematic drawing showing the cross section of the triple-layer perovskite–based fully printable mesoscopic solar cell. (B) Energy band diagram of the triple-layer device. Energies are expressed in electron volts, using the electron energy in vacuum as a reference.*[68]

1.3. Perovskite Device Architectures and Working Principles

The architecture of PSCs can be divided into two types of structures, depending on the underlying materials on the side of the transport electrode: forward architecture structure (n-i-p); inverted architecture structure (p-i-n). Meanwhile, whether the perovskite device contains a mesoporous scaffold structure, it can be separated into the mesoporous n-i-p structure and mesoporous p-i-n structure. The mesoporous structure originated from the DSSCs; the planar structure derived from organic solar cells. In the following content, the specific classification details will be introduced.

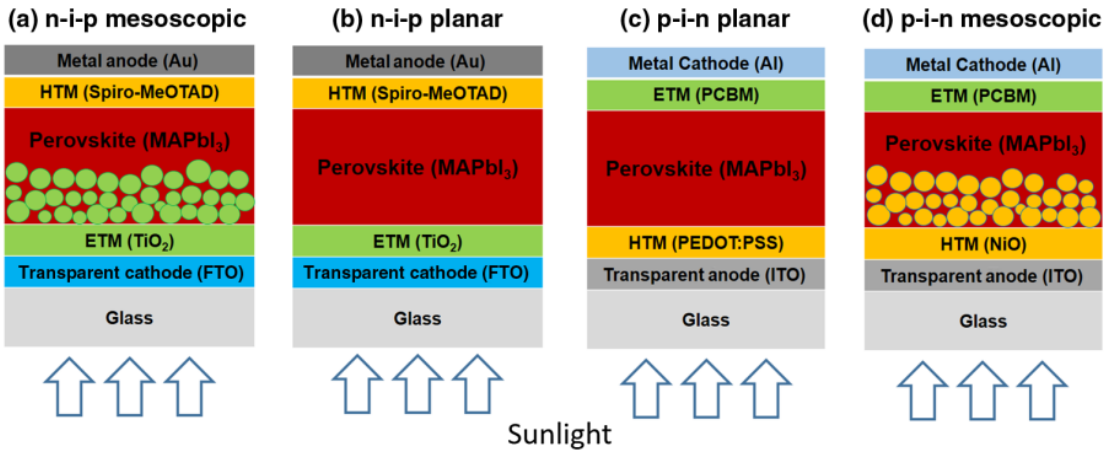

Figure 12. *Schematic diagrams of perovskite solar cells in the (a) n-i-p mesoscopic, (b) n-i-p planar, (c) p-i-n planar, and (d) p-i-n mesoscopic structures.*[69]

1.3.1. n-i-p Planar and Mesoporous Structures

Generally, for the n-i-p planar structure, the PSCs own a sandwich structure as shown in **Figure 12**.[69] including an electron transport layer, a perovskite absorption layer, and a hole transport layer with the two electrodes in the ends. The TiO_2 ETL is most intensively ETL for the perovskite device because the PSCs are developed with reference to DSSCs. The compact TiO_2 layer commonly is prepared by thermal spraying or spin-coating method, and then is annealed at a high temperature of about 500 ℃ to ensure the electrical properties of TiO_2 (**Figure 12b**). After TiO_2 annealing treatment, the perovskite precursor solution deposits on the surface of the ETL to form the light-harvesting layer with antisolvent treatment. Next, some small molecular materials (Spiro-OMeTAD) and organic conjugated polymer materials are covered onto the perovskite film as the hole transport layer. In the end, a 100 nm Au electrode is deposited by vacuum evaporation.

For the n-i-p mesoporous structure, after completing the compact preparation, the mesoporous TiO_2 precursor solution is spun onto the compact TiO_2 surface and then the obtained mesoporous TiO_2 film is annealed for the second time (**Figure 12a**). The other fabrication steps are the same as the above-mentioned details. Although the high PCE and more stable PSCs are based on mesoporous structures, the complex preparation structure needs high-temperature annealing for several times and seriously blocks the PSCs to be used onto a flexible substrate, which may be detrimental to its commercial development.

1.3.2. p-i-n Planar and Mesoporous Structures

Compared with the traditional n-i-p structure, when the hole transport layer is deposited on a transparent electrode (FTO or ITO glass), the perovskite devices own an inverted architecture structure shown in **Figure 12(c-d)**. For the preparation process, the inverted perovskite solar cells do not demand a high annealing temperature, compared to the n-i-p PSCs. It has attracted more and more attention due to its simple fabrication process and its high PCE for devices without obvious hysteresis. For the p-i-n planar structure, organic (PEDOT:PSS, PTAA, P3HT et al) hole transport materials are commonly used onto the FTO glass surface as HTL, the growth of perovskite is on the HTL, and then fullerene derivative $PC_{61}BM$ is deposited onto the perovskite absorption layer. Finally, Au, Al, or Cu metals are deposited on the $PC_{61}BM$ ETL as a counter electrode shown in **Figure 12c**. For the p-i-n mesoporous structure, the inverted perovskite solar cells are expected to have the compact HTL but also to have the mesoporous inorganic (NiO_x) hole transport materials as a scaffold, the rest parts of the device is the same as the above-mentioned structure shown in **Figure 12d**. In 2013, Jeng et al., first reported the p-i-n PSCs with ITO/PEDOT: PSS/$MAPbI_3$/C_{60}/BCP/Al structure and its PCE reached 3.9% (shown in **Figure 13**).[70] At present, with the rapid development of the p-i-n inverted PSCs, the PCE has significantly improved and have exceeded 20%.[71]

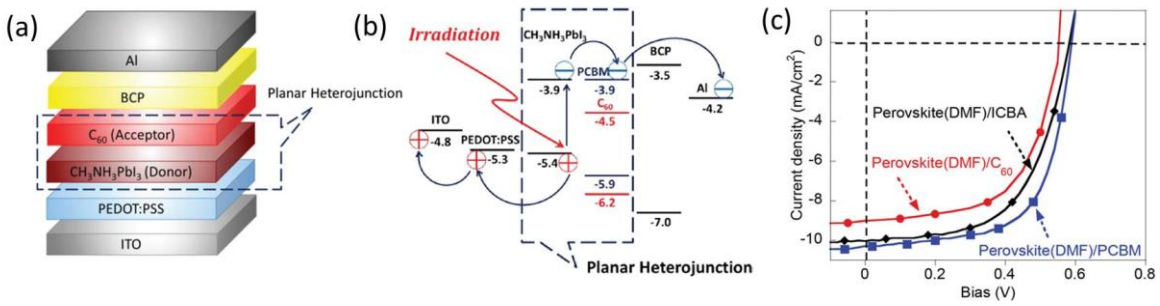

Figure 13. *(a) Configuration of the hybrid solar cell in this study. (b) Scheme of the energy levels of each layer in the device. (c) J–V curves of $CH_3NH_3PbI_3$ perovskite (DMF)/C_{60} or C_{60}-derivative hybrid solar cells under standard 1 sun AM 1.5 simulated solar irradiation.*[70]

1.3.3. Perovskite Device without ETL or HTL Architecture

Compared to the n-i-p or p-i-n structure of PSCs, the architecture of the perovskite devices without the electron transport layer or hole transport layer is much simple, by removing the high temperature processed TiO_2 ETL or NiO_x HTL.[72,73] In particular, for the commercial

application of PSCs, it is crucial to simplify the device preparation process to low cost and meanwhile maintain the excellent photovoltaic performance, comparable to the conventional silicon solar cells. To date, the PSCs without ETL or HTL have obtained unprecedented progress, reaching relatively high PCE and stable behavior.[72,73] The specific detail information will be discussed as follows:

For the perovskite devices without ETL, some literature has reported that the electron transport layer (TiO_2, ZnO, SnO_2, et al.) is not an indispensable part for the PSCs, in contrast, these ETLs may introduce the negative oxygen vacancies induced by ultraviolet photocatalytic degradation, resulting in severe hysteresis for the PSCs. Simultaneously, the popularly used TiO_2 ETL of the perovskite device need high-temperature annealing process, which makes the device fabrication more complex and impedes the development of the flexible perovskite devices.[74] In 2014, Liu et al proposed the new type PSCs without a compact free layer, exhibiting high PCE up to 13.5%, which is very close to that of the perovskite device with ZnO ETL and the corresponding architecture shown in **Figure 14**.[75] Since then, the new type perovskite device without ETL has attracted tremendous attention and experienced rapid evolution. In 2019, Huang et al used the tetramethylammonium hydroxide (TMAH) small molecule to modify the surface and electrical properties of the FTO electrode in the PSCs, with a high PCE over 20%. Therefore, the new type of perovskite solar cells provide a new approach to promote flexible perovskite photovoltaic applications.[76]

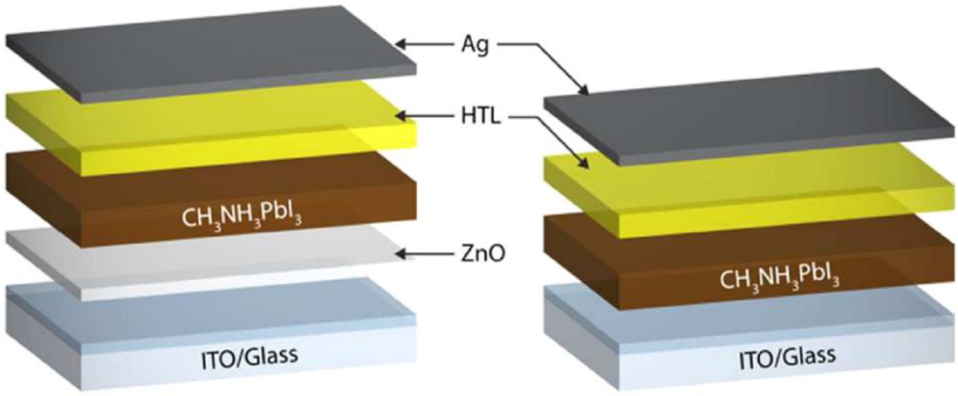

Figure 14. *Device architecture of the perovskite solar cells with and without a ZnO ETL; the HTL is either P3HT or Spiro-OMeTAD.*[75]

As we know, the traditional organic hole transport layer (Spiro-OMeTAD, PTAA) seriously increases the cost of the perovskite devices and also results in poor stability of perovskite solar cells. To accelerate the commercialization process, researchers begin to pay more attention to replacing the expensive organic HTL by low-cost inorganic HTL (NiO_x, Cu_2O, CuI) or directly removing the HTL of PSCs.[77] So far, inverted hole-transport-free PSCs have achieved huge progress, which not only lows the cost of the perovskite device but also presents remarkable performance. In 2018，Wu et al prepared the inverted hole-transport-free perovskite device with the blade coating method, and they optimize the interface between the FTO/perovskite layer via interface molecular engineering, obtaining a high PCE over 20%.[78] Meanwhile, the stability of the perovskite device also has been improved. This new structure of the PSCs provides an available method to boost the scalable and simple fabrication process.

1.3.4. Nanostructure of Perovskite Layer

Up to now, except for the various strategies to optimize the architecture of PSCs as above mentioned content, the crucial perovskite light harvesting layer also has undergone many improvements by the composition modulation methods, morphology passivation engineerings, and many different novel preparation techniques.[79] Because the high quality of the perovskite layer is the prerequisite for reaching good photovoltaic performance, it contributes to absorbing more incident sunlight with lower recombination current.[80] However, the photocurrent density of the reported PSCs is still lower than the theoretical value (~26 mA cm^{-2})[81], implying that there is a quiet part of the incident light remains unemployed for the photocurrent generation.

To further improve the photocurrent density, some researchers proposed that the nanopatterned structure of the perovskite layer may be a good choice to optimize the optoelectronic properties of perovskite crystals in their related photovoltaic devices. Since the light-trapping schemes can increase the internal scattering effect and intensity of absorption of the incident light, resulting in high photocurrent.[82] Therefore, how to more efficiently design nanopatterned lead halide perovskite crystals has become a hot topic in the past few years. For instance, in 2017, Kim et al reported that the simply pressing polyurethane stamps with hexagonal nanodot arrays can be applied to prepare the nanopatterned perovskite layer (shown in **Figure 15**), achieving well preferred-orientation and enlarged perovskite grains. As

a consequence, the PCE of both inverted-planar PSCs and normal PSCs based on the pressure-induced perovskite crystals were dramatically improved.[83] And in 2019, Schmager et al used the thermal nanoimprint lithography to obtain nanophotonic perovskite layers as light harvesting layer, with a 2% increase in PCE compared to the control planar devices.[84] Therefore, by introducing some nanopatterned perovskite schemes into perovskite devices, the light absorption efficiency can be efficiently optimized. It provides an available way to further improve the J_{sc}, approaching the theoretical value.

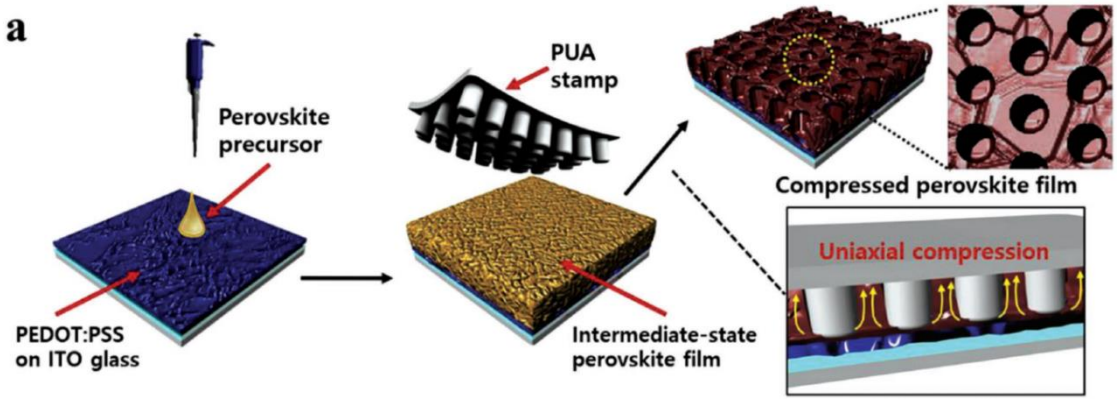

Figure 15. *Surface and vertical columnar morphology of compressed perovskite films. a) Schematic of the compression process on the perovskite film with nanoimprinting stamps.*[83]

1.3.5. Working Theory of the PSCs

The **Figure 13b** shows the energy level matching diagram of the materials from different components of the perovskite device. To achieve the excellent PCE of the device, the energy level of each layer should be a good match. The main working principle of perovskite solar cells can be summarized as the following four steps.[85]

(1) Photon absorption: under the sunlight illumination, the perovskite light active layer absorbs the numerous photons and then generates many excitons (e.g. electron-hole pairs).

(2) Exciton diffusion: The photo-generated electrons transition to the excited LUMO level, while the holes remain at the HOMO level.

(3) Charge carrier separation: After the irradiation, a built-in electric field is generated inside the perovskite device, and then the excitons are separated at the interface of the perovskite/ETL and perovskite/HTL under the drive of the built-in field.

(4) Charge carrier transportation and collection: Under the successive action of the built-in electric field, the electrons are transported and collected to the cathode, and the holes are transported and collected to the anode.

Finally, the electrons and holes are collected into an external circuit to form a closed loop, which generates the photocurrent.

1.4. Challenges in Perovskite Solar Cells

1.4.1 Shockley Queisser Limit

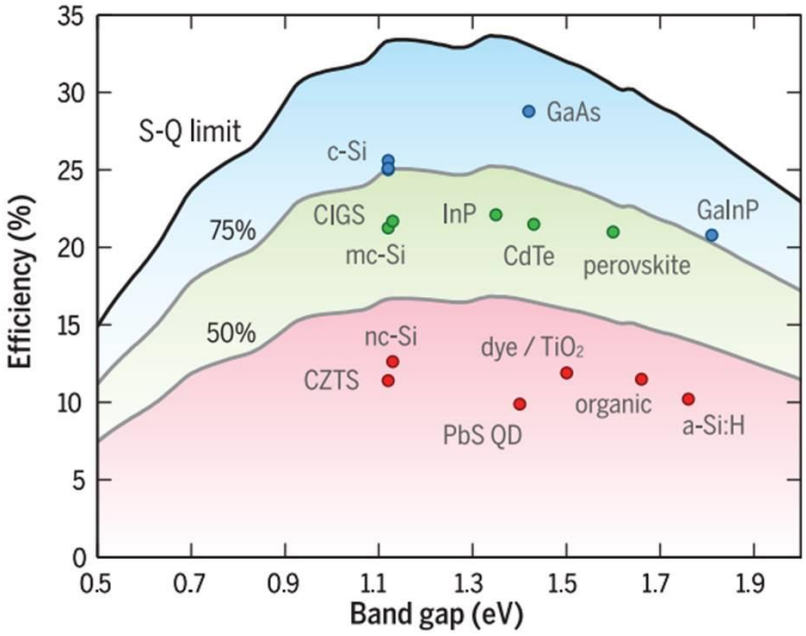

Figure 16. *Theoretical Shockley-Queisser detailed-balance efficiency limit as a function of bandgap (black line) and 75% and 50% of the limit (gray lines).The record efficiencies for different materials are plotted for the corresponding bandgaps.*[86]

In the Shockley-Queisser (Q-S) theory[87] (reported in 1961), it is well known that the maximum power conversion efficiency of a single-junction under the standard AM 1.5 solar spectrum with "one-sun" illumination (100 mW/cm^2) is 33.7%, at an ideal bandgap of 1.34 eV. According to the Q-S theory analysis, the incident photons owing fewer energies than the bandgap of semiconductor material cannot be absorbed, whereas the photons with larger energies above the bandgap of the light-harvesting layer cannot be fully absorbed and

converted to the electrical energy, due to the thermalization of charge carrier. The record efficiencies for different photovoltaic technologies with corresponding bandgaps shown in **Figure 16**.[86]

The limitation of open-circuit voltage (V_{oc})

Even in an ideal solar cell, the V_{oc} is always lower than the bandgap energy of the light active layer because the thermodynamic detailed balance needs the solar cell to spontaneously radiate heat to achieve an equilibrium with its environment (**Figure 17B**). It implies that there is an energy loss process by the light emission from the cell.[86] The dark current of devices can be generated by the corresponding radiative charge carrier recombination, leading to the V_{oc} to be considerably lower than the bandgap voltage. Furthermore, the Auger recombination, band tail recombination, and recombination at bulk, interface and surface defects also reduce the S-Q V_{oc} values.[88]

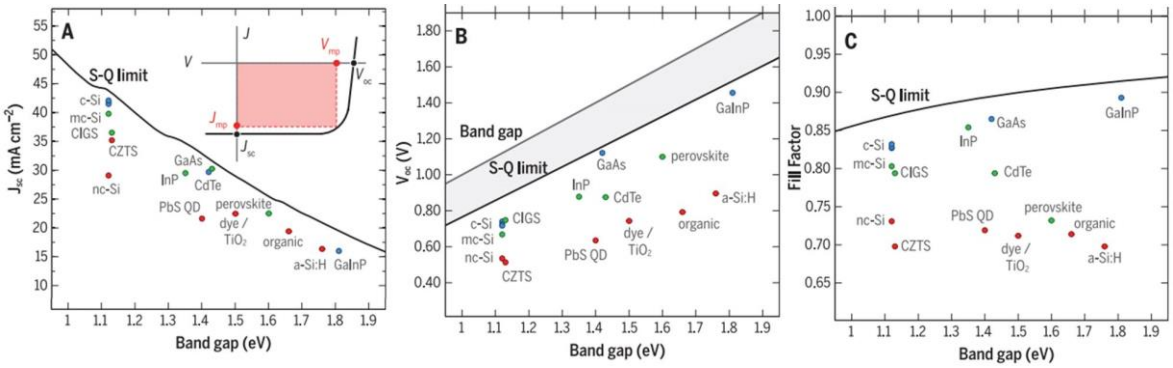

Figure 17. *Single-junction solar cell parameters are shown as a function of bandgap energy according to the Shockley-Queisser limit (solid lines) and experimental values for record efficiency cells. (A) Short-circuit current J_{sc}. (B) Open-circuit voltage V_{oc}. The voltage corresponding to the bandgap is shown for reference, with the voltage gap V_g-VSQ indicated by the gray shaded region. (C) Fill factor FF.*[86]

The limitation of short-circuit current (J_{sc})

In any ideal photovoltaic devices, the J_{sc} is always less than the ideal maximum value that can be obtained from the bandgap of the corresponding semiconductor (shown in **Figure 17A**).[86] This is because the incident sunlight is not entirely absorbed, so not all the photo-generated charge carriers are converted and transported.

Compared to the conventional inorganic semiconductors, the $MAPbI_3$ perovskite material is an ideal photovoltaic semiconductor material, presenting many excellent photovoltaic properties, such as long charge carrier diffusion length, good charge carrier mobility, tunable bandgap, etc. The bandgap of the $MAPbI_3$ is around 1.6 eV, which can be adjusted by doping bromide or chloride. According to the Q-S model, the optical bandgap value is 1.1-1.5 eV under the simulated one sun illumination (AM 1.5G). Therefore, the $MAPbI_3$ perovskite material with a direct bandgap is considered as a good light absorber material for the next-generation solar cells.

1.4.1. Hysteresis Effect

Although the PCE of perovskite solar cells has improved significantly during the last decade, there are still some issues that need to be solved. Hysteresis effect that one of the major confusing problems limits the advancement of PSCs.[89,90] In recent years, researchers have found that the various scan directions and scan rates of the external bias voltage significantly affect the efficiency of the perovskite device during the testing process. The efficiency of perovskite devices executed at reverse sweeping (from open-circuit voltage to short circuit current) is much higher, compared to the PCE of perovskite devices performed at forward scanning (from short-circuit current to open-circuit voltage). Moreover, researchers also found that the various structures of perovskite devices also affect the forward and reverse scanning efficiency of the devices, and seriously impact the correct evaluation of the efficiency of PSCs.[91]

In order to understand exactly what causes the hysteresis effect of PSCs, many possible explanations have been proposed and investigated, such as capacitance effect, ferroelectricity, ion migration, and charge trap, etc.[92–95]

(1) Capacitance Effect

During the voltage scanning of perovskite devices, the steady-state photocurrent and non-steady-state photocurrent are generated. The value of the steady-state photocurrent depends on the extraction and recombination rate of the photogenerated carrier charge of the diode response characteristics. While the non-steady-state photocurrent is decided by the scanning process of the applied voltage. In the slow voltage sweeping process, the capacitor with charging and discharging current will generate an unsteady state photocurrent (capacitance), resulting in a J-V hysteresis shown in **Figure 18**.[96] When the applied voltage

scan speed is relatively slow, in the range of seconds to milliseconds, such a dynamic photovoltage change will produce a large dielectric constant and a corresponding large capacitance induced by light. Under forward scanning with an increased bias, the capacitor discharge process generates a negative non-steady-state photocurrent.[97] The direction of non-steady-state photocurrent is opposite to the direction of the output current, resulting in a measured photocurrent owned smaller value than the steady-state. On the other hand, during reverse scanning with the voltage gradually decreasing, a forward non-steady-state photocurrent is generated, which causes the measured value of photocurrent to be larger than the steady-state photocurrent.

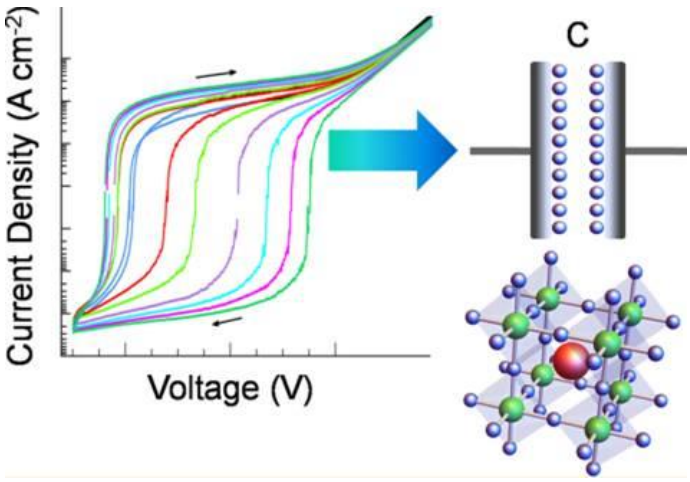

Figure 18. *J-V curves at different scan rates as indicated with logarithmic scaled currents.*[96]

(2) Ferroelectricity

The ferroelectricity is a possible reason but is not a perfect explanation for the J-V hysteresis phenomenon. If the ferroelectricity effect exists in perovskite material ($MAPbI_3$), the interface energy band will be changed, due to the shift of ions in the perovskite crystal away from their corresponding lattice point or different polarized characteristics as shown in **Figure 19**.[94] It results in different PCE of perovskite devices at forward and reverse scanning. By forward scanning, the PSCs based on a ferroelectric p-FE-n structure are negatively polarized. So the $MAPbI_3$ film owns a built-in electric field opposite to the polarized electric field to prevent the carrier charge separation and then impact the photovoltaic performance. By forward sweeping (from short-circuit current to open-circuit voltage), the initial polarized electric field weakens the built-in electric field, so it will suppress the charge extraction and collection.[98]

Meanwhile, by reverse scanning (from open-circuit voltage to short circuit current), the opposite polarization effect of the perovskite devices generates a consistent polarized electric field with the built-in electric field, which benefits to promote the separation and collection of the photogenerated carriers. However, according to the recent research reports suggest that the perovskite materials are not ferroelectric at room temperature, and the observed ferroelectric performance may be due to piezoelectric or electrochemical behavior.[99,100]

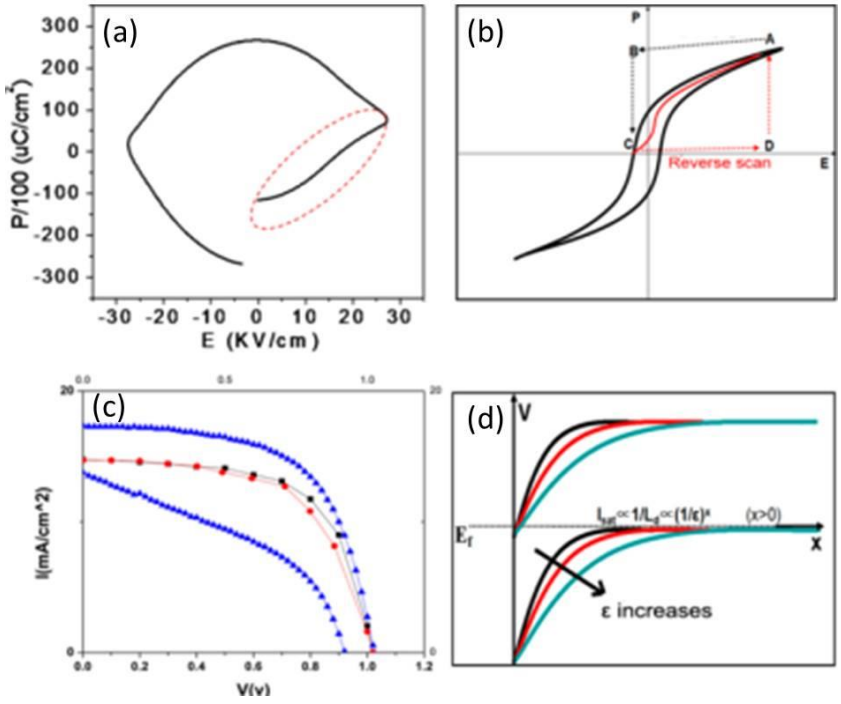

Figure 19. *(a) E−P measurement plot of Al_2O_3 on perovskite (b) Schematic diagram of the relationship between polarization P as a function of E in ferroelectric materials; path A−B−C indicates the forward scan under a moderate scan velocity, and path C−D−A indicates the reverse scan. (c) Current−voltage measurements of the stable-state scan and transient scan (scan velocity: 250 mV/s) in forward and reverse scans. (d) Schematic diagram of the space charge region distributed in perovskite, showing that the depletion region length is strongly dependent on ε.*[94]

(3) Ion Migration

Another possible cause of the J-V hysteresis effect is ion migration, shown on a schematic diagram of ion migration in **Figure 20**.[101] When the perovskite device is under an external electric field, the positive and negative ions accumulated near electrodes will accelerate or

suppress ion migration to the corresponding sides of the device, building space regions close to the electrode interfaces.[102] In addition, the bending of the energy band caused by ion migration affects the transportation and collection of electrons and holes, impacting the photovoltaic performance of the PSCs. Such ion migration has also been demonstrated in polarization-switchable perovskite devices, where the direction of photocurrent can be switched by changing the voltage scanning direction.[103] Under the external electric field, the slow-moving ion distribution process induces the J-V hysteresis effect.[92] Therefore, decreasing the density of mobile ions or carrier charge defects inside the perovskite light absorber layer and at the interfaces may suppress the hysteresis effect.

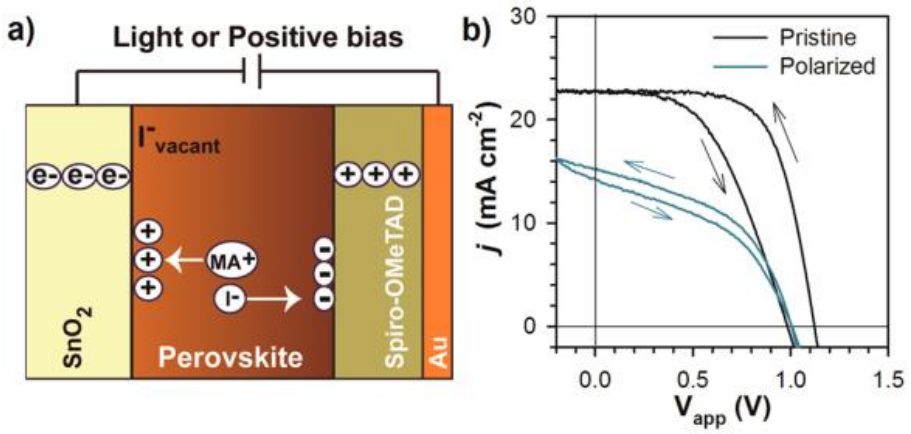

Figure 20. *(a) Diagram representing the ion migration under either light conditions or positive bias. (b) j−V curves of a representative pristine device.* [101]

(4) Defect State Theory

In addition to the above-mentioned possible hysteresis reasons, currently the defect state theory is also considered as another possible major cause of device hysteresis. Because at present, the perovskite materials are mainly prepared by the solution process method, and then a large number of defects exist in the formed thin film, and these defects will capture the carrier charge, leading to the unexpected hysteresis effect shown in **Figure 21**.[104] Huang's group reported that if a perovskite film is modified by fullerene, the surface and interface defect states of perovskite film were efficiently passivated, which can effectively suppress the perovskite hysteresis phenomenon.[105]

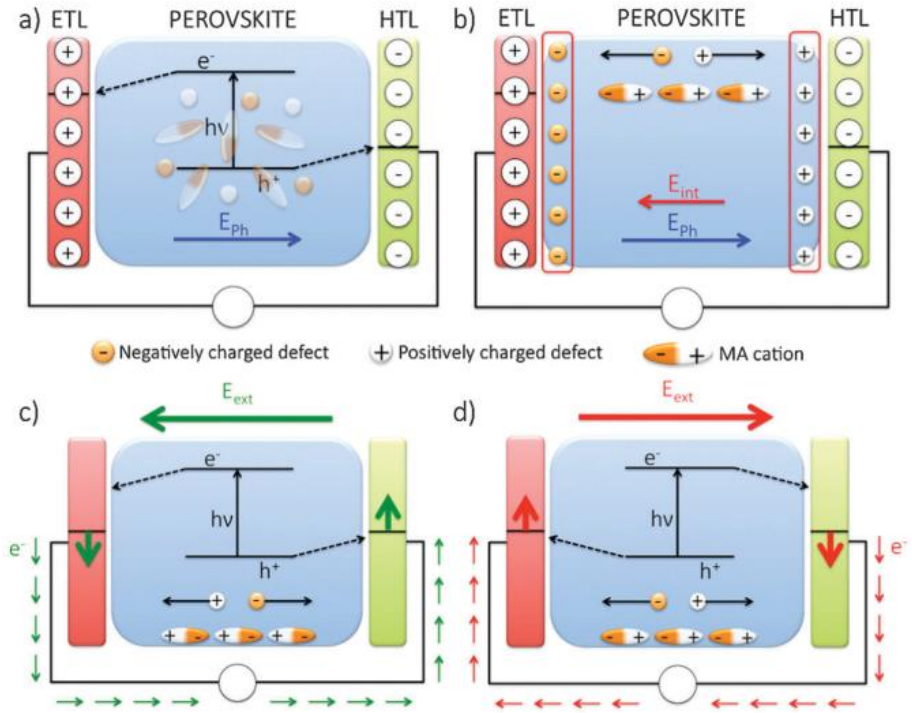

Figure 21. *Sketch of defect migration and their impact on the PSC operational mechanism. (a) shows the separation of the charge carriers driven by the photogenerated potential (EPh), along with the even distribution of the point defects and the random orientation of the MA cations; (b) depicts the migration of the point defects and the reorientation of the MA cations in response to the photogenerated field (EPh), and the internal potential developed as a consequence (Eint); (c) and (d) show the switchable current as a function of the applied external field (poling).*[104]

1.4.2. Stability of the Perovskite Devices

Although the perovskite solar cells present high power conversion efficiency and tremendous prospect for commercial applications, the extremely poor stability of perovskite devices limits their development in practical applications. Due to their unique structure and properties, perovskite materials are prone to decompose in the environment of moisture, oxygen, ultraviolet, etc. and present poor long-term stability.[106–108] So it is very important to deeply understand the degradation mechanism of perovskite materials in different atmospheres.

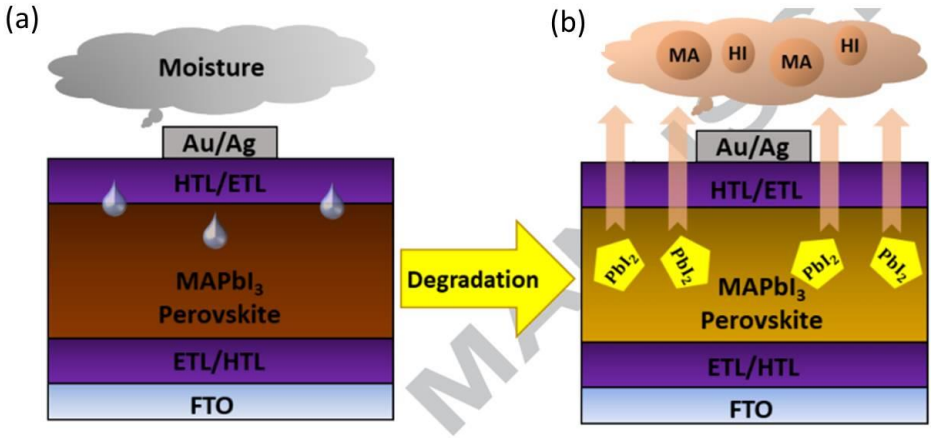

Figure 22. *Degradation of PSCs configurations before (a) and after (b) in the contact with moisture environment.*[109]

(1) Moisture

The degradation of PSCs in a humid environment is a big challenge because the organic part of the $MAPbI_3$ perovskite materials easily absorbs water molecules to decompose the perovskite materials into CH_3NH_2, PbI_2, and HI molecules as shown in **Figure 22**.[109,110] However, water molecules do not always decompose the perovskite film. Wu et al., found that the prepared perovskite film presents a longer carrier lifetime and better crystallization with doping H_2O molecules, reaching a PCE over 20%.[111] Nevertheless, when the ambient humidity is high, the perovskite film will suffer from serious degradation. The following reaction process elaborated the mechanism of perovskite decomposition[112,113]:

$$CH_3NH_3PbI_3 + H_2O \leftrightarrow CH_3NH_3PbI_3 \bullet H_2O \quad (1\text{-}4\text{-}2\text{-}1)$$

$$4(CH_3NH_3PbI_3 \bullet H_2O) \leftrightarrow (CH_3NH_3)_4PbI_6 \bullet 2H_2O + 3PbI_2 + 2H_2O \quad (1\text{-}4\text{-}2\text{-}2)$$

$$(CH_3NH_3)_4PbI_6 \bullet 2H_2O \rightarrow 4CH_3NH_3I + PbI_2 + 2H_2O \quad (1\text{-}4\text{-}2\text{-}3)$$

At the beginning of the reaction, when perovskite materials are exposed to the moisture ambient, the $CH_3NH_3PbI_3 \bullet H_2O$ phase of monohydrate will be initially formed through hydrogen bonding (shown in formula 1-4-2-1). In this phase state, the bond between $CH_3NH_3^-$ and I^- ions become weaker, in contrast, the combination bond between $CH_3NH_3^-$ and H_2O molecules presents stronger.[112,113] However, it is a reversible process. Water molecules absorbed on the surface of perovskite film can be removed by heating, vacuuming or nitrogen

drying. As the amount of H_2O molecules absorbed on the surface of the perovskite layer increases, the perovskite material further combines with water to form a dihydrate material ($(CH_3NH_3)_4PbI_6 \cdot 2H_2O$) and begins to decompose to PbI_2, as shown in formula (1-4-2-2).[112,113] This reaction process is also a reversible process. By regulating the external environment and reducing the concentration of water molecules combined with perovskite material, the decomposition process of the perovskite materials can be suppressed. However, when the perovskite materials continue to react with water molecules, the water molecules will continue to destroy the perovskite crystal structure, causing the perovskite materials to gradually decompose into CH_3NH_3I, PbI_2, and H_2O, as shown in formula (1-4-2-3).[112,113] Through the above process, water molecules in the air gradually attack the perovskite film, causing the attenuations of the perovskite film and device in humid ambient, which restricts the application of perovskite devices in the moisture environments.

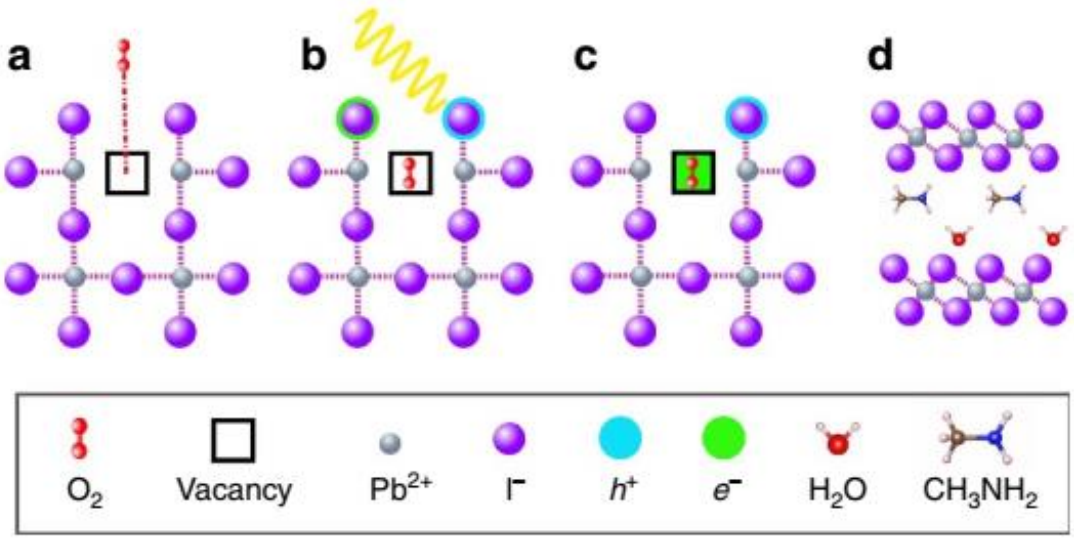

Figure 23. *Oxygen-induced photo-degradation. Schematic representation of the reaction steps of O_2 with $CH_3NH_3PbI_3$. (a) Oxygen diffusion and incorporation into the lattice, (b) photoexcitation of $CH_3NH_3PbI_3$ to create electrons and holes (c) superoxide formation from O_2, and (d) reaction and degradation to layered PbI_2, H_2O, I_2 and CH_3NH_2.*[114]

(2) Oxygen

Aristidou et al., combined experimental research and theoretical simulation to investigate the role of oxygen on perovskite thin film.[114] They found that when the perovskite layer is exposed to oxygen, O_2 molecules will diffuse into the perovskite material lattice and

preferentially absorbs on the iodine vacancy defects inside perovskite materials as shown in **Figure 23**. After the sunlight illumination, the photo-generated electrons of perovskite film can by captured by O_2 molecules, and then be transferred to O_2^-, and finally O_2^- reacts with photo-oxidized $CH_3NH_3PbI_3$ to form PbI_2, I_2, H_2O, and CH_3NH_2, resulting in decomposition of the perovskite materials. The reaction is as follows:

$$4CH_3NH_3PbI_3 + O_2^- \rightarrow 4PbI_2 + 2I_2 + 2H_2O + 4CH_3NH_2\,(g) \qquad (1\text{-}4\text{-}2\text{-}4)$$

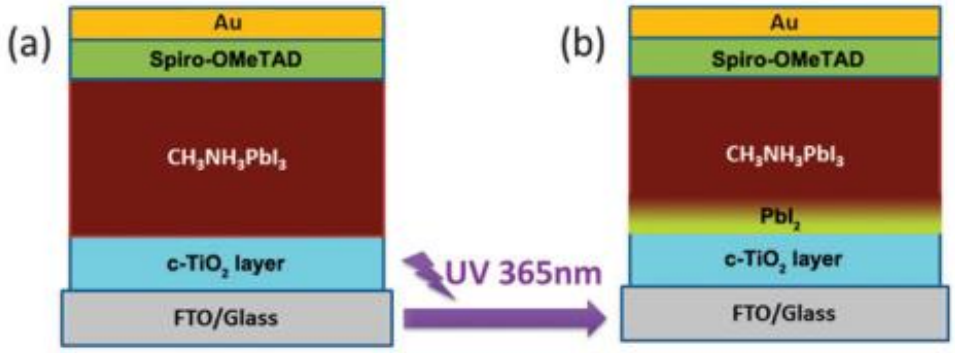

Figure 24. *Schematic illustration of the control perovskite solar cell (a) before and (b) after UV irradiation.*[43]

(3) Ultraviolet Illumination

As organic solar cells and dye-sensitized solar cells, UV irradiation can cause degradation of PSCs, leading to poor photovoltaic performance. Under the standard sunlight (AM 1.5 G), there is approximately 5% UV light. The TiO_2 materials are most widely used as an electron transport layer into the PSCs. Due to the photocatalytic properties of titanium dioxide materials, the TiO_2 layer absorbs the ultraviolet light and then generates electron-hole pairs shown in **Figure 24**.[43] Photogenerated holes are highly oxidizing, which will induce the perovskite materials to decompose into I_2, CH_3NH_2 and HI. Moreover, it will cause the change of the local electric field and cause the migration of iodine ions in the perovskite. The chemical reaction under the light is as follows[115]:

$$2I^- \leftrightarrow I_2 \qquad (1\text{-}4\text{-}2\text{-}5)$$

$$3CH_3NH_3^+ \leftrightarrow 3CH_3NH_2\,(g) + 2H^+ \qquad (1\text{-}4\text{-}2\text{-}6)$$

$$I^- + I_2 + 3H^+ + 2e^- \leftrightarrow 3HI\,(g) \qquad (1\text{-}4\text{-}2\text{-}7)$$

(4) Thermal Stability

Although the above-mentioned external factors have a serious influence on the stability of perovskite devices, it is possible to solve this problem by isolating H_2O and O_2 through suitable device package techniques. The temperature has a great influence on the crystal structure and phase transition of organic-inorganic mixed perovskite materials. When the perovskite materials are under high temperature, organic-inorganic perovskite materials will undergo thermal degradation. For $MAPbI_3$ perovskite materials, at a temperature of 54-56 ℃, the perovskite material with a tetragonal phase (non-perovskite phase) begins to transfer to a cubic phase (perovskite phase).[116] According to the test standard of international solar cells, the thermal stability of solar cells modules must be exposed to a high-temperature environment at 85 ℃ to complete the test. McGehee et al., found the perovskite materials are prone to decompose into PbI_2 when the perovskite devices were heated at 85 ℃ for 24 h in a nitrogen ambient shown in **Figure 25**.[117] In order to avoid high-temperature degradation, the utilization of heat-resistant materials might be an appropriate choice, on. The FA^+ cation has been used to partly instead of MA^+ or replaces MA^+ cation into PSCs, which have efficiently improved the thermal stability of the PSCs.[118] At present, some researchers found that two-dimensional perovskite materials also can be used to enhance the thermal stability of perovskite devices.[119]

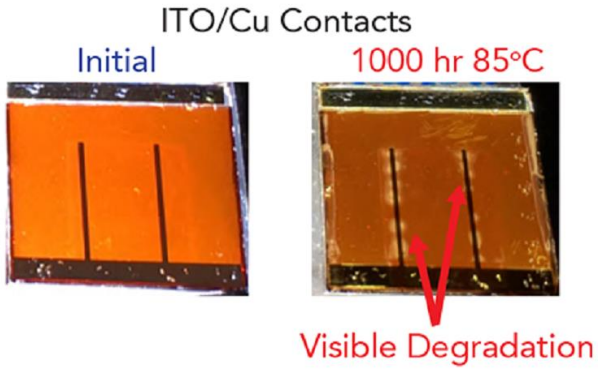

Figure 25. *$FA_{0.83}Cs_{0.17}Pb(I_{0.83}Br_{0.17})_3$ cell with Cu contacts before and after heating for 1000 h at 85 °C in N_2 in the dark.*[117]

To further improve the thermal management of the perovskite device, first, it is critical to understand the intrinsic thermal properties and thermal loss mechanism of perovskite materials. Since a large part of the solar radiation is converted into heat, which is highly related to the lifetime and optimal performance of the perovskite device.[120] Besides that, it is

also beneficial for investigating the thermally activated decomposition issue of the perovskite materials. In 2014, Pisoni et al reported the thermal conductivity (K) of the corresponding large single-crystalline and polycrystalline organometallic perovskite $MAPbI_3$ samples. The thermal conductivity value of the single crystals and polycrystals is 0.5 W/(Km) and 0.3 W/(Km) at room temperature, respectively. Such a low K resists the rapid spread of the light deposited heat, which will severely limit the lifetime of the perovskite devices.[120] In 2016, Wang et al analyzed the thermal conductivity of $MAPbI_3$ with various phases (cubic, tetragonal, and orthorhombic) via equilibrium molecular dynamics simulations, achieving similar scale thermal conductivity values.[121] In 2017, Heiderhoff et al investigated the thermal conductivity of a series of single-crystal and films of methylammonium lead halide perovskite materials ($CH_3NH_3PbX_3$, X=I, Br, and Cl) shown in **Figure 26**, with scanning near-field thermal microscopy.[122]

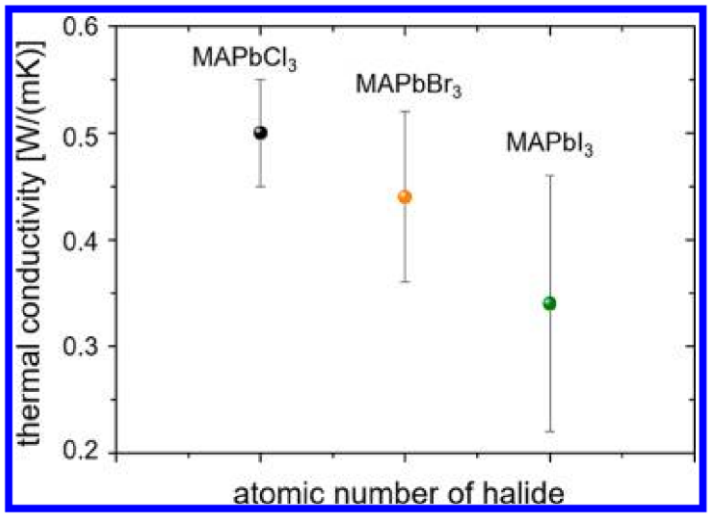

Figure 26. *Perovskites with decreasing atomic number of the halide possess slight higher average thermal conductivities and less inhomogeneity (reflected by smaller error bars).*[122]

However, up to now, only a few research have been proposed about the thermal properties of perovskite materials. The understanding of the thermal conductivity attributes of the various perovskite materials is not still enough and clear, and the obtained knowledge of the thermal conductivity knowledge to direct and manage the thermal decomposition of perovskite devices is still limited.

1.5. Device Photovoltaic Parameters

1.5.1. Reference Solar Spectrum

In order to achieve consistent and comparable J-V measurement results, researchers test their perovskite solar cells under one standard AM 1.5 G sunlight simulator with 100 mW/cm^2 power density. The standard sunlight spectrum is shown in **Figure 27**.[123] A small part of the sunlight spectrum (from 350 to 800 nm) can be absorbed by the perovskite light-harvesting layer. While a substantial part of the sunlight spectrum cannot be used for electricity generation. Researchers have attempted various strategies to extend the absorption range of PSCs and improve the incident light-harvesting efficiency.

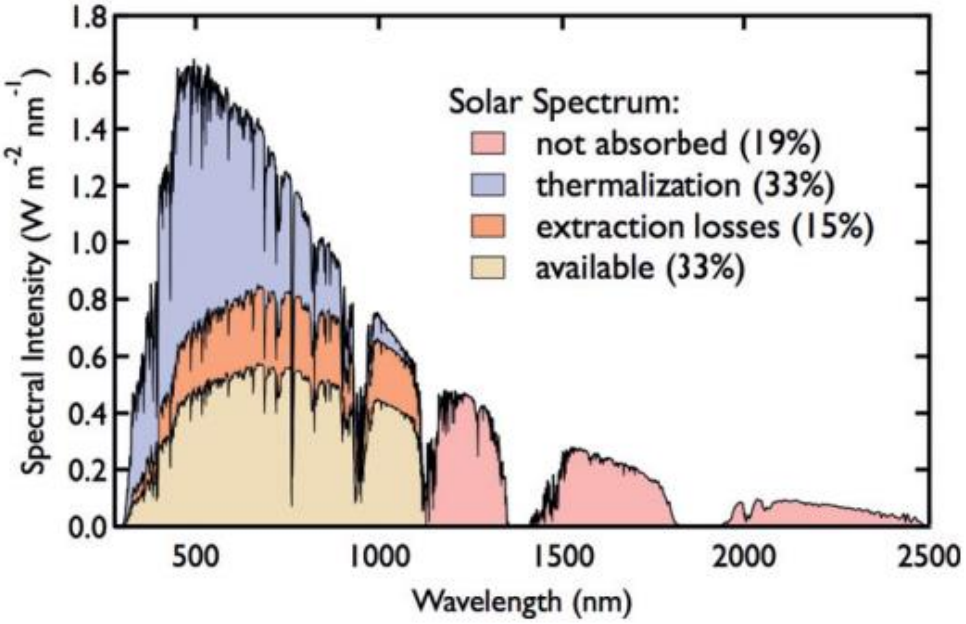

Figure 27. *Spectral analysis of the minimum losses for a silicon solar cell (bandgap = 1.1 eV). These are the losses accounted for in the Shockley-Queisser limit and represent an upper limit for solar cells made from single-junction bulk semiconductors.*[123]

1.5.2. External Quantum Efficiency (EQE) Measurement

Quantum efficiency including internal quantum efficiency (IQE) and external quantum efficiency (EQE) exhibits the ratio of collected charge to the incident photons by a solar cell. The EQE is also noted as IPCE, for incident photon-to-electron conversion efficiency. The EQE is defined as the ratio of the number of electrons (N_e) generated in an external circuit to

the number of photons (N_p) of incident monochromatic light per unit time. The value of the EQE can represent the light capture efficiency and also can represent the efficiency of converting the absorbed light into electricity. Therefore, EQE is an important indicator for measuring the photovoltaic performance of PSCs. The specific formula can be defined as follows:

$$\text{EQE} = \frac{Ne}{Np} = \frac{1240 * I_{sc}}{\lambda * P_{in}} \quad (1\text{-}5\text{-}2\text{-}1)$$

where I_{sc} is the short-circuit current of PSCs, λ is the wavelength of the incident monochromatic light, and P_{in} is the power of the incident monochromatic light.

1.5.3. J-V Characterization

The current-voltage curve (I-V) measurement of solar cells is a necessary test to evaluate the photovoltaic performance of the solar cells shown in **Figure 28**.[124] The current density (J, mA/cm^2) defined by the ratio of current to solar cell area is commonly used to present the volt-ampere characteristic curve. The main related factors include: short circuit current (J_{sc}), open-circuit voltage (V_{oc}), fill factor (FF), and power conversion efficiency (PCE).

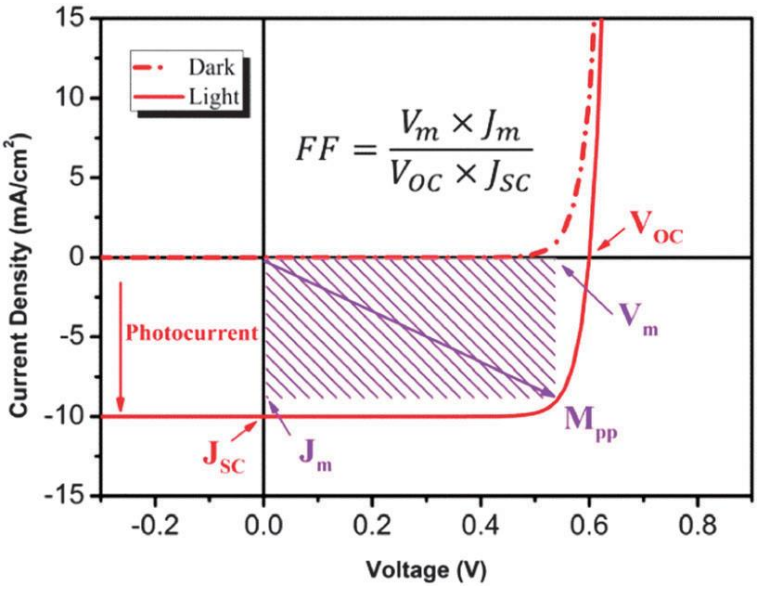

Figure 28. *Typical current–voltage characteristics for dark and light current in a solar cell illustrating the important parameters for such devices: J_{SC} is short-circuit current density, V_{OC} is open-circuit voltage, J_m and V_m are the current density and voltage at the maximum power point (M_{pp}), and FF is the fill factor.*[124]

Short Circuit Current (J_{sc})

Under short-circuit conditions, the output current of solar cells refers to short-circuit current (J_{sc}), with 0 V output voltage. As shown in **Figure 28**, it is the intercept of the vertical axis from the J-V curve. The short-circuit current is related to the number of photons absorbed by the perovskite light active layer. It can be defined as the integral of the entire solar spectrum, as shown in the following formula[125]:

$$J_{sc}=\int IPCE\ (\lambda)Isun(\lambda)d\lambda \qquad (1\text{-}5\text{-}3\text{-}1)$$

Theoretically, the bandgap of the perovskite materials determines the value of J_{sc}, which is an important factor to deep understand the properties of PSCs.

Open-Circuit Voltage (V_{oc})

Under the open-circuit conditions, the output voltage of the solar cells refers to open-circuit voltage (V_{oc}), with 0 mA output current. As shown in **Figure 28**, it is the intercept of the horizontal axis from the J-V curve. It is generally believed that the open-circuit voltage of the PSCs is determined by the difference between the lowest electron unoccupied orbit (LUMO) of the electron transport layer and the highest electron occupied orbit (HOMO) of the hole transport layer.[126] But, according to some literature, when the bandgap of perovskite material is adjusted, the corresponding V_{oc} of the perovskite devices will also be affected. In addition, improving the quality of the perovskite layer and passivating the surface and interfaces of perovskite films can also influence the open-circuit voltage of the perovskite devices.[127]

Fill Factor (FF)

The Fill factor is another important parameter that affects the performance of PSCs. Every perovskite device has the best operating point, presenting the maximum output power density (P_{max}). The ratio of the product of corresponding output current density and voltage (based on the best operating point) to the product of the J_{sc} and V_{oc} is defined as the fill factor. The formula is shown as follows:

$$FF = \frac{P_{max}}{J_{sc}*V_{oc}} = (J_{max}\times V_{max})/(J_{sc}\times V_{oc}) \qquad (1\text{-}5\text{-}3\text{-}2)$$

Power Conversion Efficiency (PCE)

The power conversion efficiency of PSCs is determined by the short-circuit current, open-circuit voltage, fill factor and the incident light power (P_{in}). The specific formula is as follows:

$$PCE = P_m/P_{in} = J_{sc}\times V_{oc}\times FF/P_{in} \quad (1\text{-}5\text{-}3\text{-}3)$$

1.6. References

1. Yan, Y., Yin, W. J., Shi, T., Meng, W. & Feng, C. Defect physics of CH3NH3PbX3 (X=I, Br, Cl) perovskites. Organic-Inorganic Halide Perovskite Photovoltaics: From Fundamentals to Device Architectures (2016). doi:10.1007/978-3-319-35114-8_4
2. Weber, D. & Perovskite, C. CH3NH3SnBrI(x = 0-3), ein Sn (II) -System mit kubischer Perowskitstruktur. *Zeitschrift für Naturforsch. B* **33**, 862–865 (1978).
3. Wang, K. *et al.* Metal Cations in Efficient Perovskite Solar Cells: Progress and Perspective. *Adv. Mater.* **31**, 1–17 (2019).
4. Wang, Z., Shi, Z., Li, T., Chen, Y. & Huang, W. Stability of Perovskite Solar Cells: A Prospective on the Substitution of the A Cation and X Anion. *Angew. Chemie - Int. Ed.* **56**, 1190–1212 (2017).
5. Kim, H. S., Im, S. H. & Park, N. G. Organolead halide perovskite: New horizons in solar cell research. *J. Phys. Chem. C* **118**, 5615–5625 (2014).
6. Li, Z. *et al.* Stabilizing Perovskite Structures by Tuning Tolerance Factor: Formation of Formamidinium and Cesium Lead Iodide Solid-State Alloys. *Chem. Mater.* **28**, 284–292 (2016).
7. Travis, W., Glover, E. N. K., Bronstein, H., Scanlon, D. O. & Palgrave, R. G. On the application of the tolerance factor to inorganic and hybrid halide perovskites: A revised system. *Chem. Sci.* **7**, 4548–4556 (2016).
8. Qiao, H. W. *et al.* A Gradient Heterostructure Based on Tolerance Factor in High-Performance Perovskite Solar Cells with 0.84 Fill Factor. *Adv. Mater.* **31**, 1–6 (2019).
9. Cohen, B. El, Wierzbowska, M. & Etgar, L. High efficiency quasi 2D lead bromide perovskite solar cells using various barrier molecules. *Sustain. Energy Fuels* **1**, 1935–1943 (2017).
10. Green, M. A., Ho-Baillie, A. & Snaith, H. J. The emergence of perovskite solar cells. *Nat. Photonics* **8**, 506–514 (2014).
11. Charles, B., Dillon, J., Weber, O. J., Islam, M. S. & Weller, M. T. Understanding the stability of mixed A-cation lead iodide perovskites. *J. Mater. Chem. A* **5**, 22495–22499 (2017).
12. Sum, T. C. & Mathews, N. Advancements in perovskite solar cells: Photophysics behind the photovoltaics. *Energy Environ. Sci.* **7**, 2518–2534 (2014).
13. Wang, Q. *et al.* Large fill-factor bilayer iodine perovskite solar cells fabricated by a low-temperature solution-process. *Energy Environ. Sci.* **7**, 2359–2365 (2014).

14. Ono, L. K. *et al.* Pinhole-free hole transport layers significantly improve the stability of MAPbI3-based perovskite solar cells under operating conditions. *J. Mater. Chem. A* **3**, 15451–15456 (2015).

15. Even, J., Pedesseau, L., Jancu, J. M. & Katan, C. Importance of spin-orbit coupling in hybrid organic/inorganic perovskites for photovoltaic applications. *J. Phys. Chem. Lett.* **4**, 2999–3005 (2013).

16. Xing, G. *et al.* Long-range balanced electron-and hole-transport lengths in organic-inorganic CH3NH3PbI3. *Science (80-.).* **342**, 344–347 (2013).

17. Lu, C. *et al.* Well-grown low-defect MAPbI3–xClx films for perovskite solar cells with over 20% efficiency fabricated under controlled ambient humidity conditions. *Electrochim. Acta* **326**, 134950 (2019).

18. Dong. Electron-Hole diffusion length >175 nm. *Sci. express* **43210**, 1–8 (2015).

19. Lian, J., Wang, Q., Yuan, Y., Shao, Y. & Huang, J. Organic solvent vapor sensitive methylammonium lead trihalide film formation for efficient hybrid perovskite solar cells. *J. Mater. Chem. A* **3**, 9146–9151 (2015).

20. Sum, T. C., Chen, S., Xing, G., Liu, X. & Wu, B. Energetics and dynamics in organic-inorganic halide perovskite photovoltaics and light emitters. *Nanotechnology* **26**, (2015).

21. Jodlowski, A. D. *et al.* Large guanidinium cation mixed with methylammonium in lead iodide perovskites for 19% efficient solar cells. *Nat. Energy* **2**, 972–979 (2017).

22. Correa-Baena, J. P. *et al.* The rapid evolution of highly efficient perovskite solar cells. *Energy Environ. Sci.* **10**, 710–727 (2017).

23. Sendner, M. *et al.* Optical phonons in methylammonium lead halide perovskites and implications for charge transport. *Mater. Horizons* **3**, 613–620 (2016).

24. Pang, S. *et al.* NH2CH=NH2PbI3: An alternative organolead iodide perovskite sensitizer for mesoscopic solar cells. *Chem. Mater.* **26**, 1485–1491 (2014).

25. Yu, Y. *et al.* Thermally evaporated methylammonium tin triiodide thin films for lead-free perovskite solar cell fabrication. *RSC Adv.* **6**, 90248–90254 (2016).

26. Kojima, A., Teshima, K., Shirai, Y. & Miyasaka, T. Organometal Halide Perovskites as Visible-Light Sensitizers for Photovoltaic Cells. *J. Am. Chem. Soc.* **131**, 6050–6051 (2009).

27. Im, J. H., Lee, C. R., Lee, J. W., Park, S. W. & Park, N. G. 6.5% Efficient Perovskite Quantum-Dot-Sensitized Solar Cell. *Nanoscale* **3**, 4088–4093 (2011).

28. Kim, H. S. *et al.* Lead iodide perovskite sensitized all-solid-state submicron thin film mesoscopic solar cell with efficiency exceeding 9%. *Sci. Rep.* **2**, 1–7 (2012).

29. Podolsky, B. *et al.* References and Notes 1. **338**, 643–648 (2012).

30. Burschka, J. *et al.* Sequential deposition as a route to high-performance perovskite-sensitized solar cells. *Nature* **499**, 316–319 (2013).

31. Liu, M., Johnston, M. B. & Snaith, H. J. Efficient planar heterojunction perovskite solar cells by vapour deposition. *Nature* **501**, 395–398 (2013).

32. Nicholson, B., Verma, S., Med, P. & S, S. R es e a rc h. (2014).

33. Yang, W. S. *et al.* Iodide management in formamidinium-lead-halide–based perovskite layers for efficient solar cells. *Science (80-.).* **356**, 1376 LP – 1379 (2017).

34. Jiang, Q. *et al.* Surface passivation of perovskite film for efficient solar cells. *Nat. Photonics* **13**, 460–466 (2019).

35. Zhou, Y. *et al.* Review on methods for improving the thermal and ambient stability of perovskite solar cells. *J. Photonics Energy* **9**, 1 (2019).

36. Abdi-Jalebi, M. *et al.* Impact of a Mesoporous Titania-Perovskite Interface on the Performance of Hybrid Organic-Inorganic Perovskite Solar Cells. *J. Phys. Chem. Lett.* **7**, 3264–3269 (2016).

37. Xiong, L. *et al.* Review on the Application of SnO2 in Perovskite Solar Cells. *Adv. Funct. Mater.* **28**, 1–18 (2018).

38. Solehudin, Diantoro, M., Sa'Adah, U. & Hidayat, A. Effect of SnO2 Nanoparticles on Band Gap Energy of x(SnO2)-y(Ag)-β-Carotene/FTO Thin Film. *J. Phys. Conf. Ser.* **1093**, (2018).

39. Li, Y. *et al.* Defective TiO2 with high photoconductive gain for efficient and stable planar heterojunction perovskite solar cells. *Nat. Commun.* **7**, 1–7 (2016).

40. Dunlap-Shohl, W. A., Younts, R., Gautam, B., Gundogdu, K. & Mitzi, D. B. Effects of cd diffusion and doping in high-performance perovskite solar cells using CdS as electron transport layer. *J. Phys. Chem. C* **120**, 16437–16445 (2016).

41. Zhang, P. *et al.* Perovskite Solar Cells with ZnO Electron-Transporting Materials. *Adv. Mater.* **30**, 1–20 (2018).

42. Gatti, T. *et al.* The Renaissance of fullerenes with perovskite solar cells. *Nano Energy* **41**, 84–100 (2017).

43. Li, W. *et al.* Enhanced UV-light stability of planar heterojunction perovskite solar cells with caesium bromide interface modification. *Energy Environ. Sci.* **9**, 490–498 (2016).

44. Chiang, C. H. & Wu, C. G. Film Grain-Size Related Long-Term Stability of Inverted Perovskite Solar Cells. *ChemSusChem* **9**, 2666–2672 (2016).

45. Yao, D. *et al.* Hindered Formation of Photoinactive δ-FAPbI3 Phase and Hysteresis-Free Mixed-Cation Planar Heterojunction Perovskite Solar Cells with Enhanced Efficiency via Potassium Incorporation. *J. Phys. Chem. Lett.* **9**, 2113–2120 (2018).

46. Pellet, N. *et al.* Mixed-organic-cation perovskite photovoltaics for enhanced solar-light harvesting. *Angew. Chemie - Int. Ed.* **53**, 3151–3157 (2014).

47. Jokar, E. *et al.* Slow surface passivation and crystal relaxation with additives to improve device performance and durability for tin-based perovskite solar cells. *Energy Environ. Sci.* **11**, 2353–2362 (2018).

48. Bai, Y. *et al.* Dimensional Engineering of a Graded 3D–2D Halide Perovskite Interface Enables Ultrahigh Voc Enhanced Stability in the p-i-n Photovoltaics. *Adv. Energy Mater.* **7**, 1–8 (2017).

49. Li, B. *et al.* Surface passivation engineering strategy to fully-inorganic cubic CsPbI3 perovskites for high-performance solar cells. *Nat. Commun.* **9**, 1–8 (2018).

50. Eperon, G. E. *et al.* Inorganic caesium lead iodide perovskite solar cells. *J. Mater. Chem. A* **3**, 19688–19695 (2015).

51. Wang, Y. *et al.* Thermodynamically stabilized b-CsPbI3–based perovskite solar cells with efficiencies >18%. *Science (80-.).* **365**, 591–595 (2019).

52. Coduri, M. *et al.* Band Gap Engineering in MASnBr3 and CsSnBr3 Perovskites: Mechanistic Insights through the Application of Pressure. *J. Phys. Chem. Lett.* **10**, 7398–7405 (2019).

53. Ke, W. *et al.* Enhanced photovoltaic performance and stability with a new type of hollow 3D perovskite {en}FASnI3. *Sci. Adv.* **3**, 1–10 (2017).

54. Ke, W. *et al.* Efficient Lead-Free Solar Cells Based on Hollow {en}MASnI3 Perovskites. *J. Am. Chem. Soc.* **139**, 14800–14806 (2017).

55. Wu, C. *et al.* The Dawn of Lead-Free Perovskite Solar Cell: Highly Stable Double Perovskite Cs2AgBiBr6 Film. *Adv. Sci.* **5**, 2–9 (2018).

56. Zhu, X. *et al.* Superior stability for perovskite solar cells with 20% efficiency using vacuum co-evaporation. *Nanoscale* **9**, 12316–12323 (2017).

57. Ko, H. S., Lee, J. W. & Park, N. G. 15.76% efficiency perovskite solar cells prepared under high relative humidity: Importance of PbI2 morphology in two-step deposition of CH3NH3PbI3. *J. Mater. Chem. A* **3**, 8808–8815 (2015).

58. Xu, Y. *et al.* Efficient hybrid mesoscopic solar cells with morphology-controlled CH3NH3PbI3-xClx derived from two-step spin coating method. *ACS Appl. Mater. Interfaces* **7**, 2242–2248 (2015).

59. Wang, Q. *et al.* Stabilizing the α-Phase of CsPbI3 Perovskite by Sulfobetaine Zwitterions in One-Step Spin-Coating Films. *Joule* **1**, 371–382 (2017).

60. Hsu, C. Y., Chen, Y. C., Lin, R. Y. Y., Ho, K. C. & Lin, J. T. Solid-state dye-sensitized solar cells based on spirofluorene (spiro-OMeTAD) and arylamines as hole transporting materials. *Phys. Chem. Chem. Phys.* **14**, 14099–14109 (2012).

61. Liu, J. *et al.* A dopant-free hole-transporting material for efficient and stable perovskite solar cells. *Energy Environ. Sci.* **7**, 2963–2967 (2014).

62. Di Giacomo, F. *et al.* High efficiency CH3NH3PbI(3-x)Cl x perovskite solar cells with poly(3-hexylthiophene) hole transport layer. *J. Power Sources* **251**, 152–156 (2014).

63. Sun, K., Li, P., Xia, Y., Chang, J. & Ouyang, J. Transparent Conductive Oxide-Free Perovskite Solar Cells with PEDOT:PSS as Transparent Electrode. *ACS Appl. Mater. Interfaces* **7**, 15314–15320 (2015).

64. Mali, S. S., Patil, J. V., Kim, H., Luque, R. & Hong, C. K. Highly efficient thermally stable perovskite solar cells via Cs:NiOx/CuSCN double-inorganic hole extraction layer interface engineering. *Mater. Today* **26**, 8–18 (2019).

65. Lin, L., Jiang, L., Li, P., Fan, B. & Qiu, Y. A modeled perovskite solar cell structure with a Cu2O hole-transporting layer enabling over 20% efficiency by low-cost low-temperature processing. *J. Phys. Chem. Solids* **124**, 205–211 (2019).

66. Cao, J. *et al.* Copper-copper iodide hybrid nanostructure as hole transport material for efficient and stable inverted perovskite solar cells. *Sci. China Chem.* **62**, 363–369 (2019).

67. Giuliano, G. *et al.* Nonprecious Copper-Based Transparent Top Electrode via Seed Layer–Assisted Thermal Evaporation for High-Performance Semitransparent n-i-p Perovskite Solar Cells. *Adv. Mater. Technol.* **4**, 1–12 (2019).

68. Mei, A. *et al.* A hole-conductor-free, fully printable mesoscopic perovskite solar cell with high stability. *Science (80-.).* **345**, 295–298 (2014).

69. Song, Z., Watthage, S. C., Phillips, A. B. & Heben, M. J. Pathways toward high-performance perovskite solar cells: review of recent advances in organo-metal halide perovskites for photovoltaic applications. *J. Photonics Energy* **6**, 022001 (2016).

70. Jeng, J. Y. *et al.* CH3NH3PbI3 perovskite/fullerene planar-heterojunction hybrid solar cells. *Adv. Mater.* **25**, 3727–3732 (2013).

71. Yang, D. *et al.* Achieving 20% Efficiency for Low-Temperature-Processed Inverted Perovskite Solar Cells. *Adv. Funct. Mater.* **29**, 1–6 (2019).

72. Zhou, Z. & Pang, S. Highly efficient inverted hole-transport-layer-free perovskite solar cells. *J. Mater. Chem. A* **8**, 503–512 (2020).

73. Liao, J. F. *et al.* Understanding of carrier dynamics, heterojunction merits and device physics: Towards designing efficient carrier transport layer-free perovskite solar cells. *Chem. Soc. Rev.* **49**, 354–381 (2020).

74. Huang, L. & Ge, Z. Simple, Robust, and Going More Efficient: Recent Advance on Electron Transport Layer-Free Perovskite Solar Cells. *Adv. Energy Mater.* **9**, 1–31 (2019).

75. Liu, D., Yang, J. & Kelly, T. L. Compact layer free perovskite solar cells with 13.5% efficiency. *J. Am. Chem. Soc.* **136**, 17116–17122 (2014).

76. Huang, C. *et al.* Facile fabrication of highly efficient ETL-free perovskite solar cells with 20% efficiency by defect passivation and interface engineering. *Chem. Commun.* **55**, 2777–2780 (2019).

77. Saki, Z., Sveinbjörnsson, K., Boschloo, G. & Taghavinia, N. The Effect of Lithium Doping in Solution-Processed Nickel Oxide Films for Perovskite Solar Cells. *ChemPhysChem* **20**, 3322–3327 (2019).

78. Wu, W. Q. *et al.* Molecular doping enabled scalable blading of efficient hole-transport-layer-free perovskite solar cells. *Nat. Commun.* **9**, 1–8 (2018).

79. Li, Y. *et al.* A review on morphology engineering for highly efficient and stable hybrid perovskite solar cells. *J. Mater. Chem. A* **6**, 12842–12875 (2018).

80. Wang, Y. *et al.* Patterned Wettability Surface for Competition-Driving Large-Grained Perovskite Solar Cells. *Adv. Energy Mater.* **9**, 1–8 (2019).

81. Ahn, N. *et al.* Highly Reproducible Perovskite Solar Cells with Average Efficiency of 18.3% and Best Efficiency of 19.7% Fabricated via Lewis Base Adduct of Lead(II) Iodide. *J. Am. Chem. Soc.* **137**, 8696–8699 (2015).

82. Xiao, Z. & Yan, Y. Progress in Theoretical Study of Metal Halide Perovskite Solar Cell Materials. *Adv. Energy Mater.* **7**, 1–20 (2017).

83. Kim, W. *et al.* Oriented Grains with Preferred Low-Angle Grain Boundaries in Halide Perovskite Films by Pressure-Induced Crystallization. *Adv. Energy Mater.* **8**, 1–10 (2018).

84. Schmager, R. *et al.* Light coupling to quasi-guided modes in nanoimprinted perovskite solar cells. *Sol. Energy Mater. Sol. Cells* **201**, 110080 (2019).

85. Berhe, T. A. *et al.* Organometal halide perovskite solar cells: Degradation and stability. *Energy Environ. Sci.* **9**, 323–356 (2016).

86. Polman, A., Knight, M., Garnett, E. C., Ehrler, B. & Sinke, W. C. Photovoltaic materials: Present efficiencies and future challenges. *Science (80-.).* **352**, (2016).

87. Shockley, W. & Queisser, H. J. Detailed balance limit of efficiency of p-n junction solar cells. *J. Appl. Phys.* **32**, 510–519 (1961).

88. Chen, J. & Park, N. G. Causes and Solutions of Recombination in Perovskite Solar Cells. *Adv. Mater.* **31**, 1–56 (2019).

89. Kim, H. S. & Park, N. G. Parameters affecting I-V hysteresis of CH3NH3PbI3 perovskite solar cells: Effects of perovskite crystal size and mesoporous TiO2 layer. *J. Phys. Chem. Lett.* **5**, 2927–2934 (2014).

90. Snaith, H. J. *et al.* Anomalous hysteresis in perovskite solar cells. *J. Phys. Chem. Lett.* **5**, 1511–1515 (2014).

91. Hu, L. *et al.* Inverted Planar Perovskite Solar Cells with a High Fill Factor and Negligible Hysteresis by the Dual Effect of NaCl-Doped PEDOT:PSS. *ACS Appl. Mater. Interfaces* **9**, 43902–43909 (2017).

92. Van Reenen, S., Kemerink, M. & Snaith, H. J. Modeling Anomalous Hysteresis in Perovskite Solar Cells. *J. Phys. Chem. Lett.* **6**, 3808–3814 (2015).

93. Calado, P. *et al.* Evidence for ion migration in hybrid perovskite solar cells with minimal hysteresis. *Nat. Commun.* **7**, 1–10 (2016).

94. Wei, J. *et al.* Hysteresis analysis based on the ferroelectric effect in hybrid perovskite solar cells. *J. Phys. Chem. Lett.* **5**, 3937–3945 (2014).

95. Chen, B. *et al.* Impact of Capacitive Effect and Ion Migration on the Hysteretic Behavior of Perovskite Solar Cells. *J. Phys. Chem. Lett.* **6**, 4693–4700 (2015).

96. Almora, O. *et al.* Capacitive dark currents, hysteresis, and electrode polarization in lead halide perovskite solar cells. *J. Phys. Chem. Lett.* **6**, 1645–1652 (2015).

97. Chen, B., Yang, M., Priya, S. & Zhu, K. Origin of J-V Hysteresis in Perovskite Solar Cells. *J. Phys. Chem. Lett.* **7**, 905–917 (2016).

98. Zhang, C. C. *et al.* Electric-field assisted perovskite crystallization for high-performance solar cells. *J. Mater. Chem. A* **6**, 1161–1170 (2018).

99. Coll, M. *et al.* Polarization switching and light-enhanced piezoelectricity in lead halide perovskites. *J. Phys. Chem. Lett.* **6**, 1408–1413 (2015).

100. Fan, Z. *et al.* Ferroelectricity of CH3NH3PbI3 perovskite. *J. Phys. Chem. Lett.* **6**, 1155–1161 (2015).

101. Correa-Baena, J. P. *et al.* Changes from Bulk to Surface Recombination Mechanisms between Pristine and Cycled Perovskite Solar Cells. *ACS Energy Lett.* **2**, 681–688 (2017).

102. Xiao, Z. *et al.* Giant switchable photovoltaic effect in organometal trihalide perovskite devices. *Nat. Mater.* **14**, 193–197 (2015).

103. Bergmann, V. W. *et al.* Real-space observation of unbalanced charge distribution inside a perovskite-sensitized solar cell. *Nat. Commun.* **5**, (2014).

104. Azpiroz, J. M., Mosconi, E., Bisquert, J. & De Angelis, F. Defect migration in methylammonium lead iodide and its role in perovskite solar cell operation. *Energy Environ. Sci.* **8**, 2118–2127 (2015).

105. Shao, Y., Xiao, Z., Bi, C., Yuan, Y. & Huang, J. Origin and elimination of photocurrent hysteresis by fullerene passivation in CH3NH3PbI3 planar heterojunction solar cells. *Nat. Commun.* **5**, 1–7 (2014).

106. Leijtens, T. *et al.* Towards enabling stable lead halide perovskite solar cells; Interplay between structural, environmental, and thermal stability. *J. Mater. Chem. A* **5**, 11483–11500 (2017).

107. Leijtens, T. *et al.* Stability of metal halide perovskite solar cells. *Adv. Energy Mater.* **5**, 1–23 (2015).

108. Niu, G., Guo, X. & Wang, L. Review of recent progress in chemical stability of perovskite solar cells. *J. Mater. Chem. A* **3**, 8970–8980 (2015).

109. Byranvand, M. M., Kharat, A. N. & Taghavinia, N. Moisture stability in nanostructured perovskite solar cells. *Mater. Lett.* **237**, 356–360 (2019).

110. Smith, I. C., Hoke, E. T., Solis-Ibarra, D., McGehee, M. D. & Karunadasa, H. I. A Layered Hybrid Perovskite Solar-Cell Absorber with Enhanced Moisture Stability. *Angew. Chemie - Int. Ed.* **53**, 11232–11235 (2014).

111. Chiang, C. H., Nazeeruddin, M. K., Grätzel, M. & Wu, C. G. The synergistic effect of H2O and DMF towards stable and 20% efficiency inverted perovskite solar cells. *Energy Environ. Sci.* **10**, 808–817 (2017).

112. de Holanda, M. S. *et al.* In Situ 2D Perovskite Formation and the Impact of the 2D/3D Structures on Performance and Stability of Perovskite Solar Cells. *Sol. RRL* **3**, 1900199 (2019).

113. Koh, T. M., Thirumal, K., Soo, H. Sen & Mathews, N. Multidimensional Perovskites: A Mixed Cation Approach Towards Ambient Stable and Tunable Perovskite Photovoltaics. *ChemSusChem* **9**, 2541–2558 (2016).

114. Aristidou, N. *et al.* Fast oxygen diffusion and iodide defects mediate oxygen-induced degradation of perovskite solar cells. *Nat. Commun.* **8**, 1–10 (2017).

115. Ito, S., Tanaka, S., Manabe, K. & Nishino, H. Effects of surface blocking layer of Sb2S3 on nanocrystalline TiO2 for CH3NH3PbI3 perovskite solar cells. *J. Phys. Chem. C* **118**, 16995–17000 (2014).

116. Targhi, F. F., Jalili, Y. S. & Kanjouri, F. MAPbI 3 and FAPbI 3 perovskites as solar cells: Case study on structural, electrical and optical properties. *Results Phys.* **10**, 616–627 (2018).

117. Boyd, C. C. *et al.* Barrier Design to Prevent Metal-Induced Degradation and Improve Thermal Stability in Perovskite Solar Cells. *ACS Energy Lett.* **3**, 1772–1778 (2018).

118. Yi, C. *et al.* Entropic stabilization of mixed A-cation ABX3 metal halide perovskites for high performance perovskite solar cells. *Energy Environ. Sci.* **9**, 656–662 (2016).

119. Lee, J. W. *et al.* 2D perovskite stabilized phase-pure formamidinium perovskite solar cells. *Nat. Commun.* **9**, 1–10 (2018).

120. Pisoni, A. *et al.* Ultra-low thermal conductivity in organic-inorganic hybrid perovskite CH3NH3PbI3. *J. Phys. Chem. Lett.* **5**, 2488–2492 (2014).

121. Wang, M. & Lin, S. Anisotropic and Ultralow Phonon Thermal Transport in Organic–Inorganic Hybrid Perovskites: Atomistic Insights into Solar Cell Thermal Management and Thermoelectric Energy Conversion Efficiency. *Adv. Funct. Mater.* **26**, 5297–5306 (2016).

122. Heiderhoff, R. *et al.* Thermal Conductivity of Methylammonium Lead Halide Perovskite Single Crystals and Thin Films: A Comparative Study. *J. Phys. Chem. C* **121**, 28306–28311 (2017).

123. Semonin, O. E., Luther, J. M. & Beard, M. C. Quantum dots for next-generation photovoltaics. *Mater. Today* **15**, 508–515 (2012).

124. Qi, B. & Wang, J. Fill factor in organic solar cells. *Phys. Chem. Chem. Phys.* **15**, 8972–8982 (2013).

125. Teng, N. W., Yang, S. S. & Chen, F. C. Plasmonic-Enhanced Organic Photovoltaic Devices for Low-Power Light Applications. *IEEE J. Photovoltaics* **8**, 752–756 (2018).

126. Yang, W., Yao, Y. & Wu, C. Q. Origin of the high open circuit voltage in planar heterojunction perovskite solar cells: Role of the reduced bimolecular recombination. *J. Appl. Phys.* **117**, (2015).

127. Edri, E., Kirmayer, S., Cahen, D. & Hodes, G. High open-circuit voltage solar cells based on organic-inorganic lead bromide perovskite. *J. Phys. Chem. Lett.* **4**, 897–902 (2013).

Chapter 2. Simplify the Conventional Perovskite Structure

In this chapter, we represent electron transport layer-free (ETL-free) efficient planar solar cells based on mixed cation and mixed halide $FA_{0.83}Cs_{0.17}Pb(I_{0.6}Br_{0.4})_3$ perovskite grown directly onto fluorine doped tin oxide (FTO) substrates. Crystalline $FA_{0.83}Cs_{0.17}Pb(I_{0.6}Br_{0.4})_3$ with a large lateral grain size up to 12 microns was deposited by spin-coating of a precursor solution of an optimized molar concentration and subsequent annealing. With grain size- and thickness-optimized compact $FA_{0.83}Cs_{0.17}Pb(I_{0.6}Br_{0.4})_3$ perovskite thin films, the best-performing planar ETL-free $FA_{0.83}Cs_{0.17}Pb(I_{0.6}Br_{0.4})_3$ perovskite solar cell exhibited a PCE of 13.80% and prolonged stability.

2.1. Introduction

Organic-inorganic hybrid lead halide perovskites have been considered as one of the most promising contenders for emerging solution-processed photovoltaics (PVs).[1] These materials are made of ABX_3 perovskite-type structure where the A site cation is typically an organic molecule such as methylammonium or formamidinium, the B site cation is a metal such as Pb^{2+} or Sn^{2+}, and the X site anion is a halide (such as I^-, Br^- or Cl^-). They have been applied in a variety of solid-state structures, including mesoporous[2] or planar[3] *p-i-n* cells, by various chemical and physical deposition techniques.[4–10] Micron-scale carrier diffusion length has been identified in metylammonium lead iodide perovskites and free charges are believed to form within a few picoseconds upon photoabsorption.[11,12] Global research effort on this topic has led to a substantial increase of power-conversion efficiency (PCE) for single junction perovskite solar cells, from 3.8% in 2009[13] to the current record of 22.1% in 2016.[14,15] Such a rapid increase of PCE suggests a huge potential for hybrid halide perovskites to enter the PV market.

One promising strategy for perovskite solar cells to enter the PV market is to apply them on a mature technology such as a silicon (Si) "bottom cell" to create a "tandem junction".[16] Such a strategy ideally requires a halide perovskite "top cell" component with a bandgap of ~ 1.75 eV to current-match the crystalline Si bottom cell with a bandgap of 1.1 eV.[17] Toward this objective, a series of mixed-cation lead mixed-halide perovskites based on

$FA_{0.83}Cs_{0.17}Pb(I_{(1-x)}Br_x)_3$ (FA = formamidinium [$HC(NH_2)_2$]) were synthesized with a tunable bandgap by controlling the value of x.[16,18] The partial substitution of Cs^+ in the A site cation promotes photo- and moisture stability[19,20] and the partial substitution of I^- by Br^- enables a monotonic tunability of bandgap. In particular, when x = 0.4, $FA_{0.83}Cs_{0.17}Pb(I_{0.6}Br_{0.4})_3$ exhibits an optimal optical bandgap of ~ 1.74 eV favorable for the above-mentioned tandem strategy together with highly competitive PCEs ranging from 14.7 to 17%.[16,18] These PCEs were achieved by a planar device structure with the perovskite absorber sandwiched between a *n*-type electron transport double layer (SnO_2 together with phenyl-C60-butyric acid methyl ester ($PC_{60}BM$)) and a *p*-type hole-transport polymer layer (HTL, 2′-7,7′-tetrakis(*N*,*N*-di-*p*-methoxyphenylamine)-9,9′-spirobifluorene, Spiro-OMeTAD). While these results are highly interesting, it remains unclear whether such an electron transport (or hole-blocking) double layer is necessary for $FA_{0.83}Cs_{0.17}Pb(I_{(1-x)}Br_x)_3$-based solar cells. A more simplified device structure should be in principle desirable towards low-cost fabrication. While the blocking layer-free device structure can enable high-performance solar cells based on methylammonium lead iodide,[21–25] this approach has not been explored yet on $FA_{0.83}Cs_{0.17}Pb(I_{(1-x)}Br_x)_3$, to our best knowledge. Compared to standard solar cell structures, the simplified electron transport layer-free (ETL-free) structures offer opportunities such as reduced surface recombination (between electrode and ETL),[25] the possibility to decouple the study of perovskite growth mechanism and that of the ETL,[23] and low-temperature fabrication adaptable to flexible polymer substrates.[26] In particular, the perovskite morphology was found to be of particular importance for ETL-free structures because any direct contact between the FTO and the HTL can lead to detrimental reduction of photovoltaic performance.[21]

In this work, we report on the realization of ETL-free efficient planar solar cells based on mixed cation and mixed halide $FA_{0.83}Cs_{0.17}Pb(I_{0.6}Br_{0.4})_3$ perovskite grown directly onto fluorine doped tin oxide (FTO) substrates. In particular, by controlling the precursor molar concentration, we optimized both the film thickness and morphology of $FA_{0.83}Cs_{0.17}Pb(I_{0.6}Br_{0.4})_3$ which have important impacts on the final photovoltaic performance of the ETL-free solar cells. We applied solution-processed pinhole-free $FA_{0.83}Cs_{0.17}Pb(I_{0.6}Br_{0.4})_3$ on a simple planar FTO/perovskite/Spiro-OMeTAD/gold device structure. A comparison of devices built with and without a single planar *n*-type TiO_2 ETL are carried out to investigate the necessity of such a layer. Optimized ETL-free planar solar cells based on $FA_{0.83}Cs_{0.17}Pb(I_{0.6}Br_{0.4})_3$ exhibited a PCE of 13.80 % and an open-circuit voltage

(V_{oc}) of 1.04 V under the reverse voltage scan. Our results therefore demonstrate that the molar concentration of the perovskite precursor can be an effective tool to control both the thickness and the film morphology of mixed cation and mixed halide perovskites and to improve the photovoltaic performance of ETL-free planar solar cells based on them.

2.2. Results and Discussion

2.2.1. Morphology and Crystal Grain Size Distribution of Perovskite Films

Highly crystalline and compact $FA_{0.83}Cs_{0.17}Pb(I_{0.6}Br_{0.4})_3$ perovskite films fully covering the substrate (oxygen plasma-treated FTO) were achieved by a simple spin-coating of perovskite precursor and a post-spin-coating annealing procedure. No solvent dripping during spin-coating was necessary. The precursor solution contains a mixture of four chemicals, FAI, CsI, $PbBr_2$ and PbI_2 in a stoichiometric proportion according to the target perovskite composition of $FA_{0.83}Cs_{0.17}Pb(I_{0.6}Br_{0.4})_3$, dissolved in anhydrous dimethylformamide (DMF) solution. We first applied the molar concentration (0.95M) optimized by McMeekin et al.[16] By this condition a perovskite film with a thickness of about 330 nm was obtained on FTO exhibiting complete surface coverage with grains ranging from a few hundred nanometers to about 2-3 microns large (**Figure 1a**). Such a perovskite absorber layer may be too thin for a fully optimized solar cell.[22] We therefore experimented a series of precursor solutions of higher molar concentration. Together with the increase of film thickness, grain coarsening was observed when the precursor concentration increases (**Figure 1f)**. By the intercept procedure[27] we analyzed the average grain size of $FA_{0.83}Cs_{0.17}Pb(I_{0.6}Br_{0.4})_3$ films obtained from different precursor concentrations (**Figure 1f**). Films made from 1.25M precursor exhibited particularly large grains of a lateral dimension up to 12 microns (**Figure 1c** and **Figure 2f**). When further concentrated precursor solution (1.40M and 1.55M) were applied, the final perovskite films started to exhibit some sparse pinholes (**Figure 1d** and **1e**). And the low magnification SEM images based on different perovskite precursor concentrations are presented in **Figure 2(a-e)**, respectively.

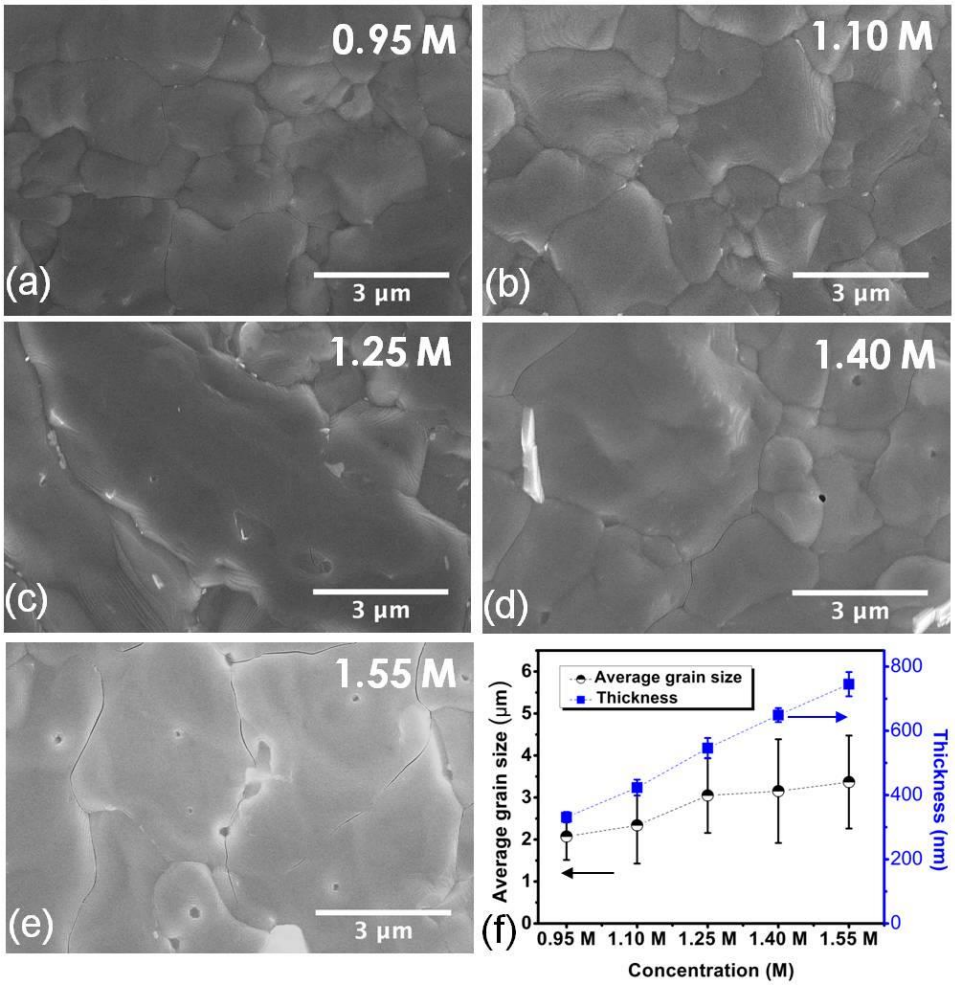

Figure 1. *Scanning electron microscope (SEM) images of the* $FA_{0.83}Cs_{0.17}Pb(I_{0.6}Br_{0.4})_3$ *perovskite thin films deposited from a precursor of (a) 0.95M, (b) 1.10M, (c) 1.25M, (d) 1.40M, and (e) 1.55M concentration. (f) Summary of the average grain size and the film thickness corresponding to each precursor concentration. Error bars represent the one standard deviation from* ≥ 28 *and* ≥ 4 *measurements on grain size and film thickness respectively.*

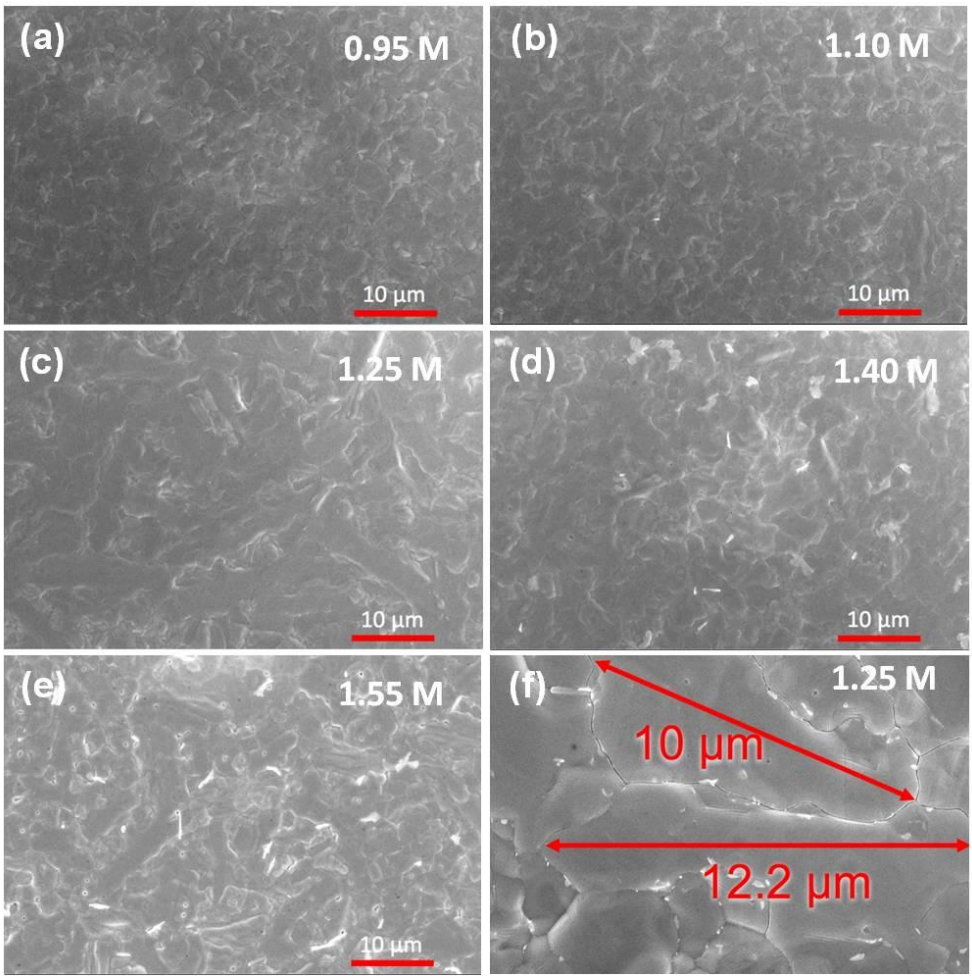

Figure 2. *(a-e) Low-magnification (3 500x) scanning electron microscope (SEM) images of the* $FA_{0.83}Cs_{0.17}Pb(I_{0.6}Br_{0.4})_3$ *perovskite thin films deposited from a precursor solution of 0.95M, 1.10M, 1.25M, 1.40M, and 1.55M concentration. (f) High magnification (15 000x) SEM image of a* $FA_{0.83}Cs_{0.17}Pb(I_{0.6}Br_{0.4})_3$ *perovskite thin film deposited from a 1.25M precursor solution exhibiting large grains with a lateral dimension up to 12 microns.*

2.2.2. X-ray Diffraction Spectrum and Optical Properties of Perovskite Materials

XRD patterns of the above-mentioned $FA_{0.83}Cs_{0.17}Pb(I_{0.6}Br_{0.4})_3$ films on FTO indicate that all films are well-crystalline into the cubic phase α-$FAPbI_3$ structure[28] (**Figure 3**). XRD results are in good agreement with previous reports on this family of perovskites.[16,18] In addition, the perovskite films of this work are highly textured in the (001) direction. It is worth to note that the crystallization of the current $FA_{0.83}Cs_{0.17}Pb(I_{0.6}Br_{0.4})_3$ perovskite is a much slower process than that of $CH_3NH_3PbI_3$ perovskites. For $CH_3NH_3PbI_3$ perovskites, crystallization is

typically complete after spin-coating as indicated by the appearance of brownish-dark color of the film.[29] By comparison, for $FA_{0.83}Cs_{0.17}Pb(I_{0.6}Br_{0.4})_3$ perovskite, right after spin-coating the film still remained of yellow color. The XRD spectrum of a film at this stage (before annealing) revealed only limited perovskite formation (**Figure 4**). Full crystallization with film color-change from yellow to dark occurred after a thermal annealing step at 185°C for 90 minutes, during which further nucleation, growth and grain coarsening happened. The current observation of textured grain growth and larger grains on thicker films is similar to that observed in oxide thin films deposited by sol-gel routes.[30,31] The (001) oriented perovskite should be a result of preferential grain growth (vertical mode perpendicular to the substrate) to minimize the substrate-film interfacial energy and surface free energy. Lateral growth mode (resulting in larger grains) is more important for thicker films due to the decrease of strain within the film.[31]

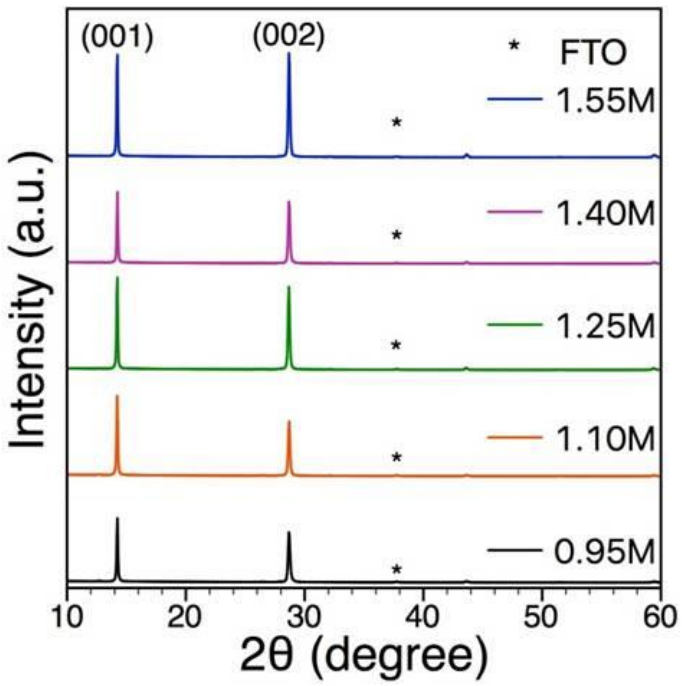

Figure 3. *XRD patterns of $FA_{0.83}Cs_{0.17}Pb(I_{0.6}Br_{0.4})_3$ perovskite thin films on FTO/glass substrates deposited from precursor solution of five different concentrations.*

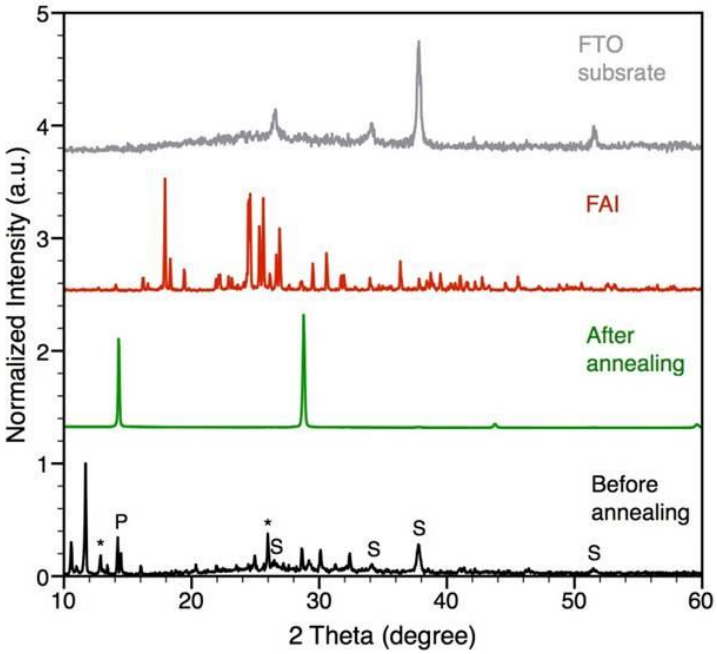

Figure 4. *The XRD spectrum of a spin-coated sample by a 1.25M* $FA_{0.83}Cs_{0.17}Pb(I_{0.6}Br_{0.4})_3$ *perovskite precursor solution before 185 ℃ annealing (black curve), presented together with the XRD spectra of the same sample after 185 ℃ annealing (green curve), FAI (red curve), and a bare FTO/glass substrate (grey curve). "P" indicates diffractions possibly from the early formation of perovskite phase. "S" indicates diffractions from the FTO substrate. "*" indicates diffractions from* PbI_2 *and/or* $PbBr_2$*.*

Precursor solutions of different concentrations resulted in $FA_{0.83}Cs_{0.17}Pb(I_{0.6}Br_{0.4})_3$ perovskite films of similar absorbance and photoluminescence (PL) with an optical bandgap of ~ 1.72 eV determined by a Tauc plot (**Figure 5** and **6**, Tauc plot in **Figure 7**) which is in reasonable agreement with previous reports.[16,18]

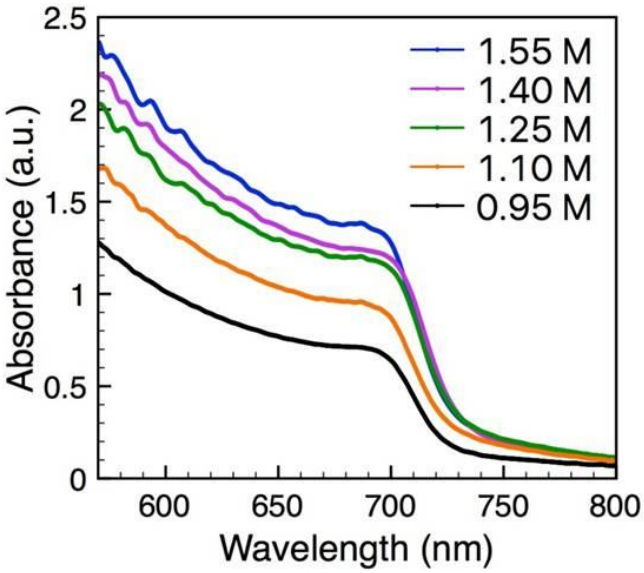

Figure 5. *Absorbance PL spectra of $FA_{0.83}Cs_{0.17}Pb(I_{0.6}Br_{0.4})_3$ perovskite thin films on FTO/glass substrates deposited from precursor solution of five different concentrations.*

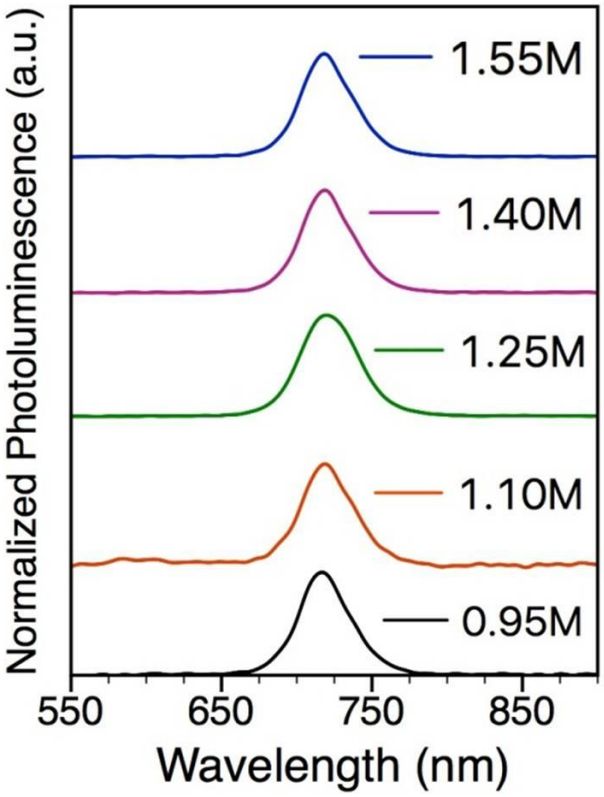

Figure 6. *Normalized PL spectra of $FA_{0.83}Cs_{0.17}Pb(I_{0.6}Br_{0.4})_3$ perovskite thin films on FTO/glass substrates deposited from precursor solution of five different concentrations.*

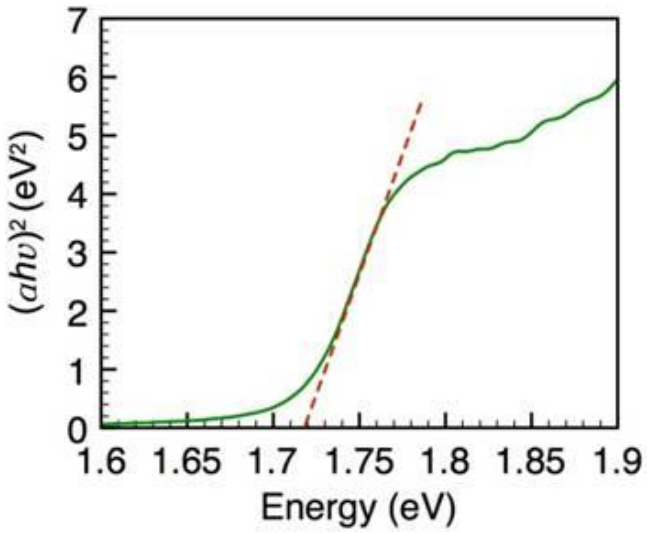

Figure 7. *Tauc plot of $FA_{0.83}Cs_{0.17}Pb(I_{0.6}Br_{0.4})_3$ assuming direct bandgap allowing the determination of its optical bandgap from intercept to be ~1.72 eV.*

2.2.3. Photovoltaic Performance of PSCs with/without ETLs

$FA_{0.83}Cs_{0.17}Pb(I_{0.6}Br_{0.4})_3$ perovskite films grown directly onto FTO were then applied to build ETL-free planar solar cells. The cross-sectional SEM image of a typical device is shown in **Figure 8a**, where different layers composing the solar cell can be clearly distinguished. Coherent with the planar SEM observation (**Figure 1c**), large areas without grain boundary of a few microns large can be observed in the cross-sectional layer. No lateral grain boundaries perpendicular to the substrate were observed suggesting that the vertical charge transport and collections mainly occur within a single grain. The measured current-voltage (*J-V*) characteristics under reversed voltage scans of ETL-free $FA_{0.83}Cs_{0.17}Pb(I_{0.6}Br_{0.4})_3$ perovskite solar cells fabricated on the same day and deposited from different precursors are shown in **Figure 8b** and summarized in **Table 1**. As the precursor concentration increases from 0.95M to 1.25M, accompanied with the increase of average grain size and thickness, there is a monotonic increase of photovoltaic parameters including short-circuit current (J_{sc}), open-circuit voltage (V_{oc}), fill-factor (FF) and therefore PCE. This observed improvement of photovoltaic performance can be a combined consequence of the increased absorber thickness towards its optimal value and of the reduced charge recombination due to larger grain size. At further higher precursor concentration starting from 1.40M, however, despite the appearance of large grain size we started to observe a deterioration of photovoltaic performance due to the

reduction in both V_{oc} and FF. The reduction of FF can be attributed to the increased thickness of the absorber layer: As it increases beyond the optimal value, photogenerated carriers cannot be collected efficiently, therefore leading to an increased recombination loss. In addition, pinholes started to appear on perovskite films deposited from high concentration precursor solution (**Figure 1**). Pinholes in these cases can lead to a direct contact between the HTL and the FTO substrate resulting in losses in both V_{oc} and FF.

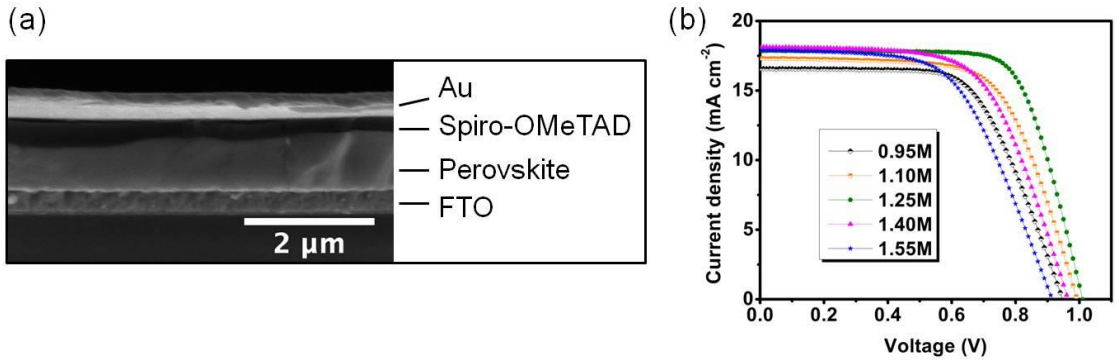

Figure 8. *(a) Cross-sectional SEM image of a completed ETL-free planar perovskite solar cell based on $FA_{0.83}Cs_{0.17}Pb(I_{0.6}Br_{0.4})_3$.The perovskite layer was deposited by a 1.25 M precursor solution. (b) Forward bias to short-circuit J-V characteristics under AM1.5G illumination (100 mW cm^{-2}) of planar ETL-free $FA_{0.83}Cs_{0.17}Pb(I_{0.6}Br_{0.4})_3$ perovskite solar cells fabricated on the same day and deposited by precursors of different concentrations.*

Table 1. *Photovoltaic parameters of the ETL-free perovskite solar cells fabricated on the same day. Error bars represent one standard deviation from ≥ 7 devices.*

Precursor concentration	J_{sc} (mA cm^{-2})	V_{oc} (V)	FF (%)	PCE (%)
0.95 M	16.61±0.51	0.96±0.05	0.63±0.03	10.05±0.59
1.10 M	17.09±0.21	0.99±0.02	0.64±0.02	10.85±0.56
1.25 M	17.84±0.06	1.02±0.02	0.69±0.03	12.39±0.27
1.40 M	17.93±0.09	0.97±0.02	0.62±0.01	10.81±0.35
1.55 M	17.92±0.18	0.93±0.02	0.59±0.02	9.88±0.47

The optimal precursor concentration is therefore found to be at 1.25M, by which a compact perovskite layer of relatively large lateral grain dimension and an optimal thickness of ~ 500 nm can be achieved. By this precursor concentration the best performing ETL-free $FA_{0.83}Cs_{0.17}Pb(I_{0.6}Br_{0.4})_3$ perovskite solar cell exhibited, under reversed (and forward) voltage scan, a J_{sc} of 18.54 (18.54) mA cm^{-2}, V_{oc} of 1.04 (1.04) V, FF of 71.57 (69.39) % and PCE of 13.80 (13.38) % (**Figure 9**). The integrated current density under AM1.5G illumination from the EQE spectrum was 18.41 mA cm^{-2}, which is in reasonable agreement with the measured J_{sc}. While the origin of hysteresis in perovskite solar cells is still a subject of debate, it is typically more pronounced on devices with a planar and blocking-layer-free structure likely linked to the compromised charge extraction.[22,32] The current observed ratio of PCE between forward and reversed voltage scans (~ 0.97) is comparable to reported optimized results obtained on ETL- free planar methylammonium lead halide solar cells.[21] The ETL-free $FA_{0.83}Cs_{0.17}Pb(I_{0.6}Br_{0.4})_3$ solar cells from this work is nevertheless highly encouraging due to factors such as (i) the simplified fabrication, (ii) the lack of high-temperature annealing step (e.g. ~ 450°C required for compact TiO_2), and (iii) the elimination of device degradation paths inherent to the blocking layer applied (e.g. SnO_2 and $PC_{60}BM$). Unencapsulated ETL-free $FA_{0.83}Cs_{0.17}Pb(I_{0.6}Br_{0.4})_3$ perovskite solar cells kept under room light and argon exhibited only small PCE decrease of ~ 5% from the original value over 552 hours (23 days) (**Figure 10**).

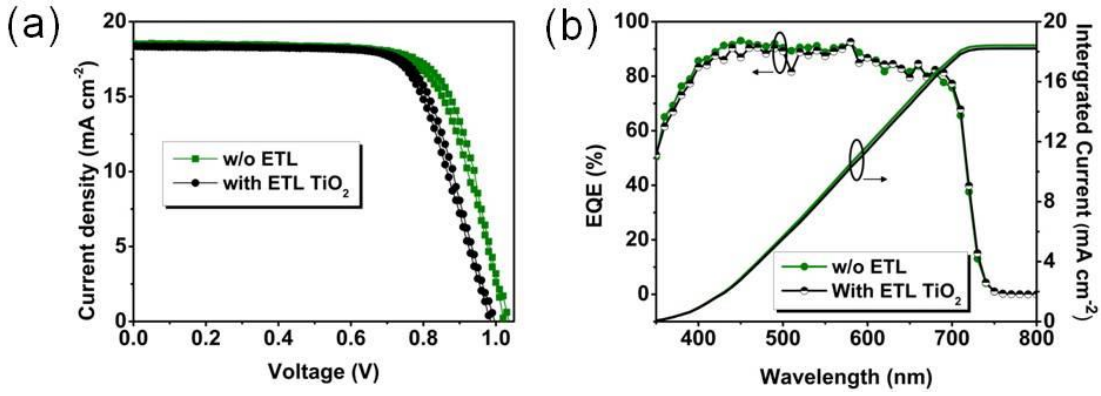

Figure 9*. (a) J-V characteristics under AM1.5G illumination (100 mW* cm^{-2}*) and (b) EQE spectra of the best-performing planar* $FA_{0.83}Cs_{0.17}Pb(I_{0.6}Br_{0.4})_3$ *perovskite solar cells with and without a layer of cp-*TiO_2 *as the ETL. Arrows indicate the measurement scan direction.*

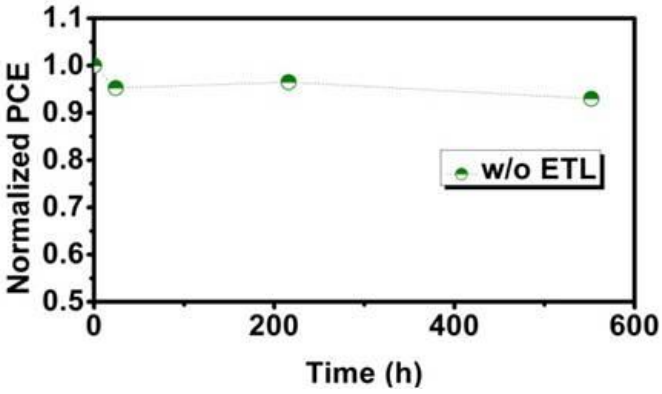

***Figure 10**. Normalized PCE versus time of an unencapsulated planar ETL-free $FA_{0.83}Cs_{0.17}Pb(I_{0.6}Br_{0.4})_3$ solar cells kept under argon and room light.*

We further investigated whether the application of a 50-nm-thick compact TiO_2 (cp-TiO_2) ETL layer can improve the $FA_{0.83}Cs_{0.17}Pb(I_{0.6}Br_{0.4})_3$ solar cell performance. We found that it is more difficult to form compact $FA_{0.83}Cs_{0.17}Pb(I_{0.6}Br_{0.4})_3$ perovskite with complete substrate coverage on cp-TiO_2/FTO compared to bare FTO substrates (**Figure 11**). While it is difficult to completely eliminate all perovskite pinholes on cp-TiO_2/FTO, by controlling the precursor concentration, on cp-TiO_2 we obtained $FA_{0.83}Cs_{0.17}Pb(I_{0.6}Br_{0.4})_3$ perovskite films with a thickness of ~ 500 nm and average grain size of ~ 2.5 microns on (**Figure 11**). Time-resolved PL measurements of $FA_{0.83}Cs_{0.17}Pb(I_{0.6}Br_{0.4})_3$ revealed a shorter mean carrier lifetime (~ 36 ns versus 183 ns) on cp-TiO_2/FTO compared to FTO, suggesting a slight improvement of charge extraction associated with the use of cp-TiO_2 ETL (**Figure 12**). The photovoltaic performance of planar $FA_{0.83}Cs_{0.17}Pb(I_{0.6}Br_{0.4})_3$ solar cells with cp-TiO_2 ETL is comparable to that of ETL-free devices with only a slightly compromised V_{oc} (1.00 V instead of 1.04 V, **Figure 9a**). The appearance of perovskite pinholes on cp-TiO_2 may lead to the observed compromised V_{oc}. This suggests that the insertion of high-temperature-annealed cp-TiO_2 ETL layer in planar $FA_{0.83}Cs_{0.17}Pb(I_{0.6}Br_{0.4})_3$ perovskite solar cells may not be advantageous unless the perovskite morphology issues on cp-TiO_2 can be eliminated.

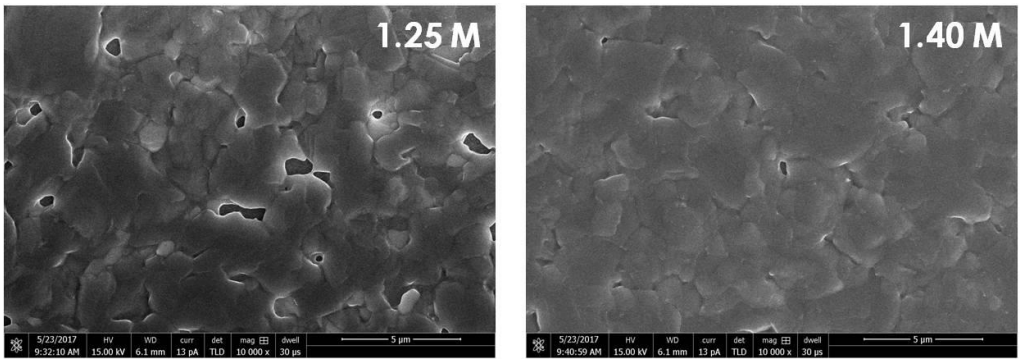

Figure 11. *SEM image of $FA_{0.83}Cs_{0.17}Pb(I_{0.6}Br_{0.4})_3$ thin films deposited on a cp-TiO_2/FTO substrate from a precursor solution of 1.25M (left image) and 1.40M (right image) concentration.*

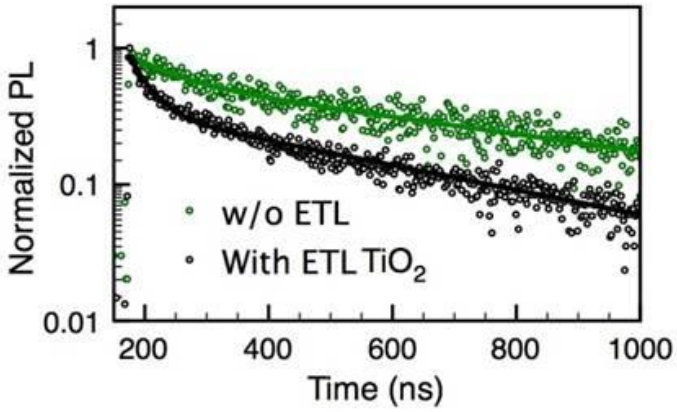

Figure 12*. (d) PL decay of $FA_{0.83}Cs_{0.17}Pb(I_{0.6}Br_{0.4})_3$ perovskite films on FTO (w/o ETL) and cp-TiO_2/FTO substrates. Solid lines are the bi-exponential fit of the decay data.*

2.3. Conclusion

In summary, thickness-tunable compact $FA_{0.83}Cs_{0.17}Pb(I_{0.6}Br_{0.4})_3$ perovskite thin films with large grain size up to 12 microns were achieved by controlling the concentration of the perovskite precursor. Applying grain size- and thickness-optimized compact $FA_{0.83}Cs_{0.17}Pb(I_{0.6}Br_{0.4})_3$ perovskite thin films grown directly onto FTO substrates, we fabricated functional solar cells with a simplified planar device structure without electron-transport layers. The best-performing planar ETL-free $FA_{0.83}Cs_{0.17}Pb(I_{0.6}Br_{0.4})_3$ perovskite solar cell exhibited a PCE of 13.80% and prolonged stability. $FA_{0.83}Cs_{0.17}Pb(I_{0.6}Br_{0.4})_3$ perovskite is a highly promising candidate due to the possibility of

its immediate application on Si solar cells through a tandem strategy. The current results on morphology and thickness control together with a simplified device structure are highly encouraging towards its future large-scale fabrication.

2.4. References

1. Correa-Baena, J. P. *et al.* The rapid evolution of highly efficient perovskite solar cells. *Energy Environ. Sci.* **10**, 710–727 (2017).
2. Lee, M. M., Teuscher, J., Miyasaka, T., Murakami, T. N. & Snaith, H. J. Efficient Hybrid Solar Cells Based on Meso-Superstructured Organometal Halide Perovskites. *Science (80-.).* **338**, 643–647 (2012).
3. Liu, M., Johnston, M. B. & Snaith, H. J. Efficient planar heterojunction perovskite solar cells by vapour deposition. *Nature* **501**, 395–398 (2013).
4. Malinkiewicz, O. *et al.* Perovskite solar cells employing organic charge-transport layers. *Nat. Photonics* **8**, 128–132 (2013).
5. Eperon, G. E., Beck, C. E. & Snaith, H. J. Cation exchange for thin film lead iodide perovskite interconversion. *Mater. Horiz.* **3**, 63–71 (2016).
6. Sutherland, B. R. *et al.* Perovskite thin films via atomic layer deposition. *Adv. Mater.* **27**, 53–58 (2015).
7. Barrows, A. T. *et al.* Efficient planar heterojunction mixed-halide perovskite solar cells deposited via spray-deposition. *Energy Environ. Sci.* **7**, 2944 (2014).
8. Xiao, Z. *et al.* Efficient, high yield perovskite photovoltaic devices grown by interdiffusion of solution-processed precursor stacking layers. *Energy Environ. Sci.* **7**, 2619 (2014).
9. Noh, J. H., Im, S. H., Heo, J. H., Mandal, T. N. & Seok, S. Il. Chemical Management for Colorful, Efficient, and Stable Inorganic–Organic Hybrid Nanostructured Solar Cells. *Nano Lett.* **13**, 1764–1769 (2013).
10. Chen, Q. *et al.* Planar Heterojunction Perovskite Solar Cells via Vapor-Assisted Solution Process. *J. Am. Chem. Soc.* **136**, 622–625 (2013).
11. Stranks, S. D. *et al.* Electron-Hole Diffusion Lengths Exceeding 1 Micrometer in an Organometal Trihalide Perovskite Absorber. *Science (80-.).* **342**, 341–344 (2013).
12. Xing, G. *et al.* Long-Range Balanced Electron- and Hole-Transport Lengths in Organic-Inorganic CH3NH3PbI3. *Science (80-.).* **6960**, 498–500 (2013).
13. Kojima, A., Teshima, K., Shirai, Y. & Miyasaka, T. Organometal Halide Perovskites as Visible-Light Sensitizers for Photovoltaic Cells. *J. Am. Chem. Soc.* **131**, 6050–6051 (2009).
14. National Renewable Energy Laboratory (NREL). Best Research-Cell Efficiencies. (2017).
15. Yang, W. S. *et al.* High-performance photovoltaic perovskite layers fabricated through intramolecular exchange. *Science (80-.).* **348**, 1234–1237 (2015).

16. McMeekin, D. P. *et al.* A mixed-cation lead mixed-halide perovskite absorber for tandem solar cells. *Science (80-.).* **351**, 151–155 (2016).

17. Shah, A., Torres, Tscharner, Wyrsch & Keppner. Photovoltaic technology: the case for thin-film solar cells. *Science* **285**, 692–8 (1999).

18. Yu, Y. *et al.* Synergistic Effects of Lead Thiocyanate Additive and Solvent Annealing on the Performance of Wide-Bandgap Perovskite Solar Cells. *ACS Energy Lett.* 1177–1182 (2017). doi:10.1021/acsenergylett.7b00278

19. Lee, J.-W. *et al.* Formamidinium and Cesium Hybridization for Photo- and Moisture-Stable Perovskite Solar Cell. *Adv. Energy Mater.* **5**, 1501310 (2015).

20. Choi, H. *et al.* Cesium-doped methylammonium lead iodide perovskite light absorber for hybrid solar cells. *Nano Energy* **7**, 80–85 (2014).

21. Huang, L. *et al.* Toward Revealing the Critical Role of Perovskite Coverage in Highly Efficient Electron-Transport Layer-Free Perovskite Solar Cells: An Energy Band and Equivalent Circuit Model Perspective. *ACS Appl. Mater. Interfaces* **8**, 9811–9820 (2016).

22. Ke, W. *et al.* Efficient hole-blocking layer-free planar halide perovskite thin-film solar cells. *Nat. Commun.* **6**, 6700 (2015).

23. Zheng, E. *et al.* PbI 2 -Based Dipping-Controlled Material Conversion for Compact Layer Free Perovskite Solar Cells. *ACS Appl. Mater. Interfaces* **7**, 18156–18162 (2015).

24. Zhu, Q. *et al.* Compact Layer Free Perovskite Solar Cells with a High-Mobility Hole-Transporting Layer. *ACS Appl. Mater. Interfaces* **8**, 2652–2657 (2016).

25. Liu, D., Yang, J. & Kelly, T. L. Compact layer free perovskite solar cells with 13.5% efficiency. *J. Am. Chem. Soc.* **136**, 17116–17122 (2014).

26. Xu, X. *et al.* Working Mechanism for Flexible Perovskite Solar Cells with Simplified Architecture. *Nano Lett.* **15**, 6514–6520 (2015).

27. ASTM. ASTM E112-13: Standard test methods for determining average grain size. *ASTM Int.* 1–28 (2013). doi:10.1520/E0112-13.1.4

28. Saidaminov, M. I., Abdelhady, A. L., Maculan, G. & Bakr, O. M. Retrograde solubility of formamidinium and methylammonium lead halide perovskites enabling rapid single crystal growth. *Chem. Commun.* **51**, 17658–17661 (2015).

29. Xiao, M. *et al.* A fast deposition-crystallization procedure for highly efficient lead iodide perovskite thin-film solar cells. *Angew. Chemie - Int. Ed.* **53**, 9898–9903 (2014).

30. Xu, L., Li, X., Chen, Y. & Xu, F. Structural and optical properties of ZnO thin films prepared by sol-gel method with different thickness. *Appl. Surf. Sci.* **257**, 4031–4037 (2011).

31. Sharma, M. & Mehra, R. M. Effect of thickness on structural, electrical, optical and magnetic properties of Co and Al doped ZnO films deposited by sol-gel route. *Appl. Surf. Sci.* **255**, 2527–2532 (2008).

32. Yu, H. *et al.* Large Grain-Based Hole Blocking Layer Free Planar-type Perovskite Solar Cell with Best Efficiency of 18.20 %. *ACS Appl. Mater. Interfaces* acsami.6b15710 (2017). doi:10.1021/acsami.6b15710

Chapter 3. Well-Oriented One-Dimension (1-D) TiO_2 to Improve the Performance of PSCs

In this chapter, we present vertically aligned 1D TiO_2 nanocolumn arrays intentionally fabricated onto half of the compact TiO_2-coated fluorine-doped tin oxide (FTO) substrates by glancing angle deposition with magnetron sputtering, a method particularly suitable for industrial applications due to its high reliability and reduced cost when coating large areas. By near-field optical microscopy (SNOM), the light-management capability of these nanoarrays is studied in detail, revealing strong concentration of electromagnetic fields on the of the nanoarrays. By comparison to the solar cells built on only a planar cp-TiO_2 ETL of the same FTO substrate, solar cells with TiO_2 nanocolumn arrays exhibit a 5% increase in its short-circuit current and a 7% enhancement in its power conversion efficiency, together with a significantly prolonged shelf-life.

3.1. Introduction

A typical PSC architecture consists of three components, including a perovskite absorber layer, sandwiched between an electron transport layer (ETL) and a hole transport layers (HTL), all of which co-determine the final performance of a PSC. Concerning ETLs, their critical roles are to transport photogenerated electrons and at the same time to block holes from the perovskite absorber. In order to achieve high power conversion efficiency, the electron collection must be efficient otherwise severe carrier recombination can occur at the ETL/perovskite interface.[1] So far, ETLs based on various semiconductor metal oxides (such as TiO_2, ZnO, SnO_2 ...) and *n*-type molecules have been investigated in PSCs to optimize the ETL/perovskite interface, as well as the improve the growth of perovskite layer.[2–5]

By comparison to the planar ETLs, mesoporous ETLs appear to be more advantageous for perovskite solar cells to achieve higher efficiency, higher stability, and less hysteresis.[1,6] For example, mesoporous scaffolds can be formed by depositing TiO_2 nanoparticles, which transport electrons while providing a large ratio of surface area for the nucleation of perovskite absorber.[1] Nevertheless, such straightforward TiO_2 nanoparticle-based scaffolds have some drawbacks such as the existence of numerous grain boundaries/structural defects,

difficulty of pore-filling by the perovskite precursor, and perturbation to the growth of perovskite grains.[7–9]

As a result, compromised charge transport efficiency and severe charge recombination at the perovskite/ETL interface was observed.[10] By comparison, well-oriented one-dimension (1-D) TiO_2 nanorods/nanowires/nanotubes arrays represent a promising strategy,[6,10,19–22,11–18] exhibiting less surface defects and grain boundaries and facilitating precursor pore-filling. 1D TiO_2 arrays can thus provide a direct physical conductive paths to extract and transport efficiently carriers generated by the perovskite layer. In terms of synthetic methods, 1D TiO_2 arrays for perovskite solar cells have been demonstrated through anodization,[11,14,17] block-copolymer template,[18] and solvothermal methods.[6,10,12,13,15,16,19,20] While the majority of these studies focused on the electronic contribution of the TiO_2 nanoarrays in perovskite solar cells (in terms of charge transport and carrier recombination), their optical contribution has not been well-characterized. While some studies observed the enhanced perovskite solar cell stability associated with the application of TiO_2 1D arrays,[6,11,15,21,22] the origins of such observations remain unclear. In addition, one of the important issues in this field concerns how to compare fairly the devices with the 1D array inserted and the devices without. The additional fabrication steps involved to generate the 1D arrays can introduce some source of differences between the device containing 1D arrays and the device without. Together with the possible batch-to-batch solar cell fabrication differences, it is therefore not straightforward to attribute the observed enhancement in solar cell characteristics directly to the inserted 1D arrays.

In terms of light-harvesting strategies, various nanostructures have been proposed for perovskite solar cells including textured absorber layer,[23,24] textured substrates,[25,26] SiO_2 prism arrays,[27] polymer micolens,[28] indium tin oxide (ITO) nanocone arrays,[29] metallic plasmonic nanoparticles,[30,31] microstructure composite hole transport layer,[32] TiO_2 nanoparticles,[33] and TiO_2 nano-dome and nano-void arrays.[34] While many of these studies focused only on simulations and optical measurements,[28,29,34] experimental studies applying textures,[23–26] SiO_2 prisms,[27] metallic plasmonic nanoparticles,[30,31] microstructure composites,[32] and TiO_2 nanoparticles[33] have indeed demonstrated functional and more performing perovskite solar cells owning to such light-harvesting strategies. By comparison to the popular metallic plasmonic structures, non-metal materials with high permittivity are alternative choices for nanoantenna enhancing the optical absorption and fluorescence

processes at their surroundings.[35–37] In particular, TiO_2 nanostructures such as nanodisks, owing to their large refractive index, have been shown to localize light and enhance the fluorescence of a nearby fluorescent nanoparticle.[38] In the context of perovskite solar cells, due to the absence of optical absorption in the visible spectrum and its excellent electron transporting properties, 1D TiO_2 nanoarrays should be an excellent electronic and optical booster.

In this work, vertically aligned 1D TiO_2 nanocolumn arrays are intentionally fabricated onto half of the compact TiO_2-coated fluorine-doped tin oxide (FTO) substrates by the glancing angle deposition (GLAD), a method capable to generate well-oriented inorganic nanorods with uniform dimensions on substrates when using physical vapor deposition (PVD).[21,39–41] Although the most common PVD technique in the scientific literature to perform GLAD is thermal evaporation, from an applied point of view the most interesting one is magnetron sputtering (MS), which is widely used in many industrial applications due to its high reliability and reduced cost when coating large areas.[42,43] Thus, our approach to fabricate the aligned 1D TiO_2 nanocolumn arrays is GLAD with magnetron sputtering. Structural, spectroscopy and optical characterizations were then performed on these TiO_2 nanoarrays by comparison to the compact TiO_2 (cp-TiO_2) counterpart of the same substrate. In particular, by near-field optical microscopy (SNOM), the effect of the nanostructuration of the TiO2 layer is studied in detail, revealing strong concentration of electromagnetic fields on the nanoarrays.

Functional triple-cation lead perovskite halide solar cells based on $Cs_{0.05}(FA_{0.83}MA_{0.17})_{0.95}Pb(I_{0.83}Br_{0.17})_3$ are then built onto the above-mentioned substrates, half of which covered by TiO_2 nanocolumn electron transport layer (ETL) and the other half covered by cp-TiO_2 ETL. By comparison to the solar cells built on only a planar cp-TiO_2 ETL of the same FTO substrate, solar cells with TiO_2 nanocolumn arrays exhibit a 5% increase in its short-circuit current and a 7% enhancement in its power conversion efficiency, together with a significantly prolonged shelf-life. Revealed by electrochemical impedance spectroscopy, the application of TiO_2 nanocolumn arrays leads to a lower charge transport resistance and a higher charge recombination resistance in the solar cell, both contributing to the observed enhanced photovoltaic performance. In addition, such TiO_2 nanocolumn arrays exhibit a more significant optical absorption in the UV spectrum by comparison to the planar counterpart, capable to perform partial UV-screening boosting the stability of the perovskite solar cell. The combined structural, spectroscopic, photovoltaic and optical characterizations

presented herein provide a detail analysis on the physical origins of the beneficial roles of 1D TiO_2 nanocolumn arrays in hybrid perovskite solar cells.

3.2. Results and Discussion

3.2.1. Top-View and Cross-Section SEM Measurements of Perovskite Films

The TiO_2 nanocolumn arrays obtained by glancing angle deposition composed of dense TiO_2 nanocolumns uniformly aligned perpendicular to the substrate (**Figure 1**). These nanocolumns exhibit an average diameter of 89 ± 18 nm and an average length of 254 ± 27 nm. For hole-blocking purpose, a thin layer of cp-TiO_2 ETL with a thickness of about 50 nm was applied before the deposition of the TiO_2 nanocolumn arrays onto half of the substrate surface. No observable change on the morphology nor on the RMS roughness of the FTO and the cp-TiO_2 ETL was induced by fabrication process of the TiO_2 nanocolumn arrays (**Figure 2 and 3**). The average root mean square (rms) roughness for FTO was 15.0 nm initially and 15.6 nm after the oxidation, whereas for cp-TiO_2 was 9.5 nm before and 9.4 nm after the treatment. And the corresponding XRD spectrum and SEM images of as-deposited Ti nanocolumns (a) and of the resulting TiO_2 nanocolumns after the thermal treatment (b) are presented in **Figure 4 and 5.** Despite the distinctively different microstructure of the nanocolumn sample by comparison to the cp-TiO_2 sample, the perovskite layers deposited on top of both samples exhibit similar morphology, grain size and surface roughness (**Figure 1d and e, Figure 6**). Cross-sectional SEM characterizations showed clearly the different sub-layers on both the control (without nanocolumns) and the nanocolumn sample (**Figure 1f and g**). The perovskite thin film deposited on top of the cp-TiO_2 layer exhibited a thickness of about 450 nm. By comparison, the perovskite thin film deposited on top of the nanocolumns is slightly thinner, reaching about 350 nm in thickness. Nevertheless, as shown in the cross-sectional SEM image, the perovskite precursor solution infiltrates well in between the nanocolumns forming a dense layer of perovskite in tight contact with each nanocolumn. This is coherent with a previous study on tilted 1D TiO_2 nanocolumn arrays prepared by GLAD but with thermal evaporation where excellent infiltration of the perovskite was also achieved.[22] Combining the infiltrated part and the part above the nanocolumns, there was

likely a more important amount of perovskite crystallites on the nanocolumn sample compared to the planar sample.

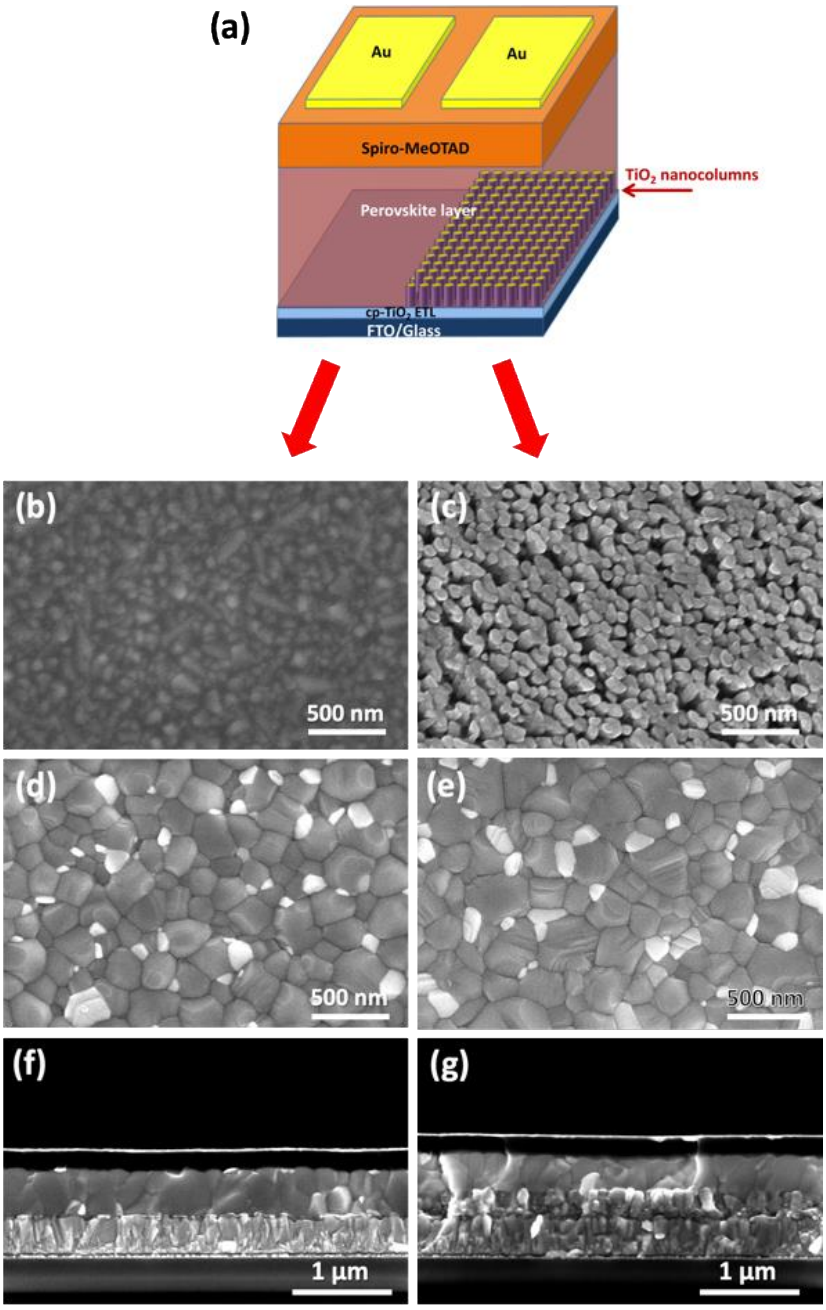

Figure 1. *(a) Schematics of the perovskite solar cell architecture with half of its interface covered by cp-TiO_2 ETL and the other half covered by TiO_2 nanocolumn arrays; (b, c) Top-view scanning electron microscopy (SEM) images of the cp-TiO_2 layer (b) and the TiO_2 nanocolumn arrays (c); (d, e) The SEM image of the perovskite film deposited on a cp-TiO_2 ETL (d) and on TiO_2 nanocolumn arrays (e); (f, g) Cross-sectional SEM image after the*

deposition of hole-transport polymer on the part of the sample with only a cp-TiO_2 ETL (without nanocolumns, f) and the part of the sample with TiO_2 nanocolumn arrays (g).

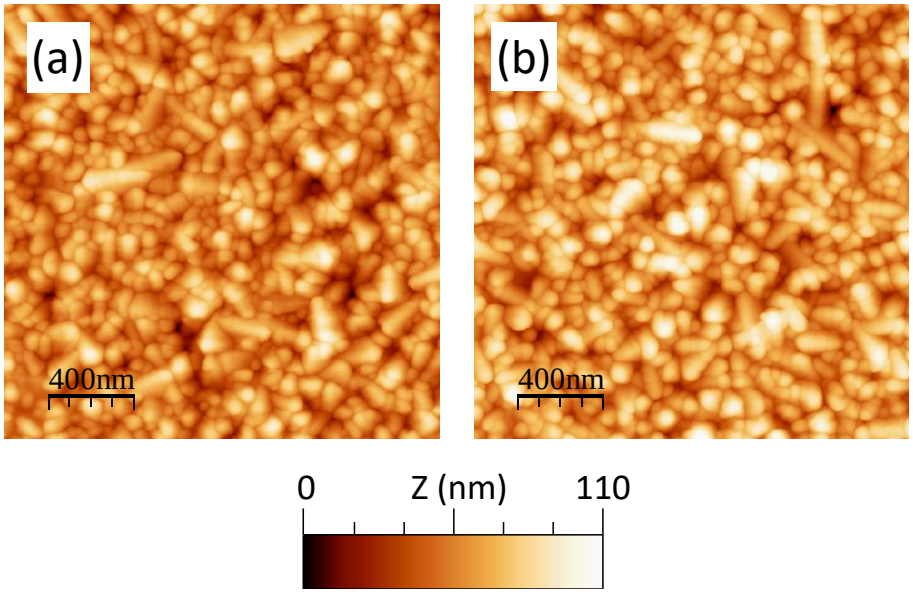

Figure 2: *Representative AFM images of a bare FTO before (a) and after (b) the thermal treatment.*

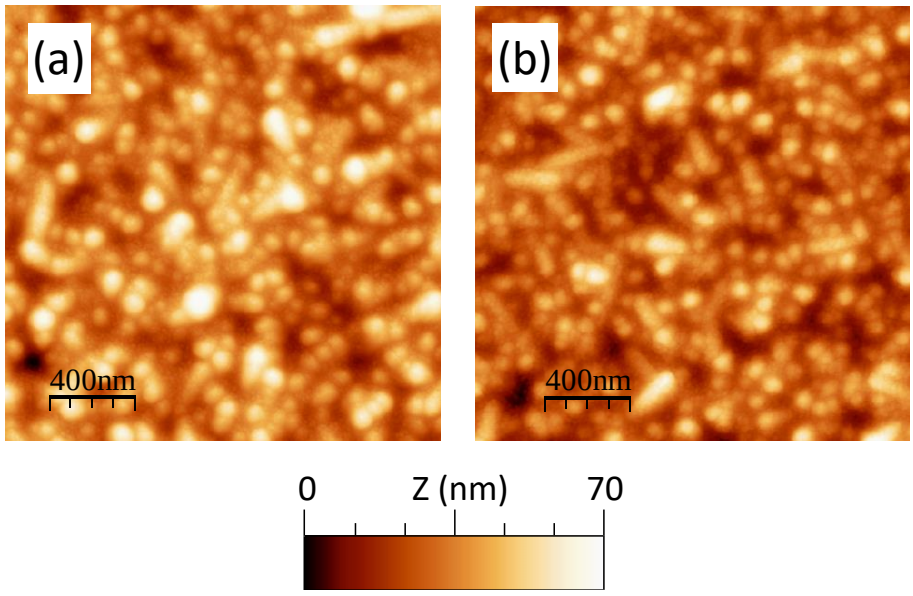

Figure 3: *Representative AFM images of cp-TiO_2 before (a) and after (b) the thermal treatment.*

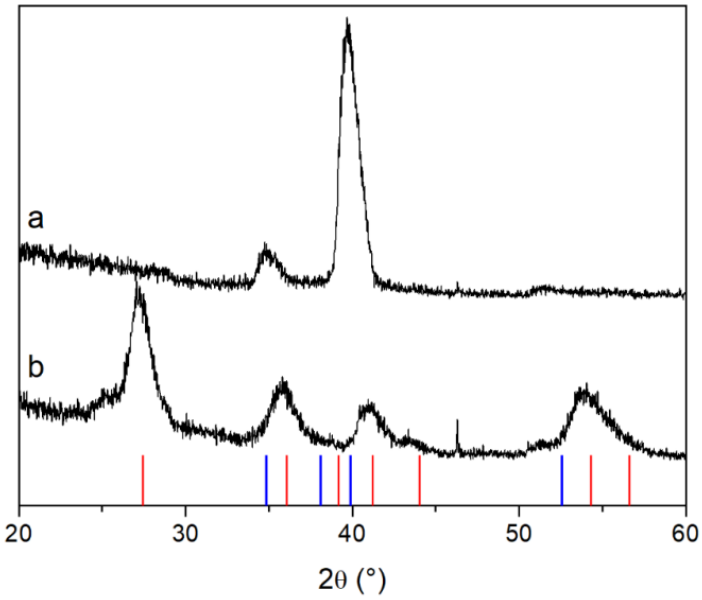

Figure 4: *X-ray diffractograms of the nanocolumn arrays before (a) and after (b) the thermal oxidation treatment. Bars correspond to the reflections of Ti metal (blue, ICDD PDF # 01-071-4632) and rutile TiO_2 (red, ICDD PDF # 01-072-1148).*

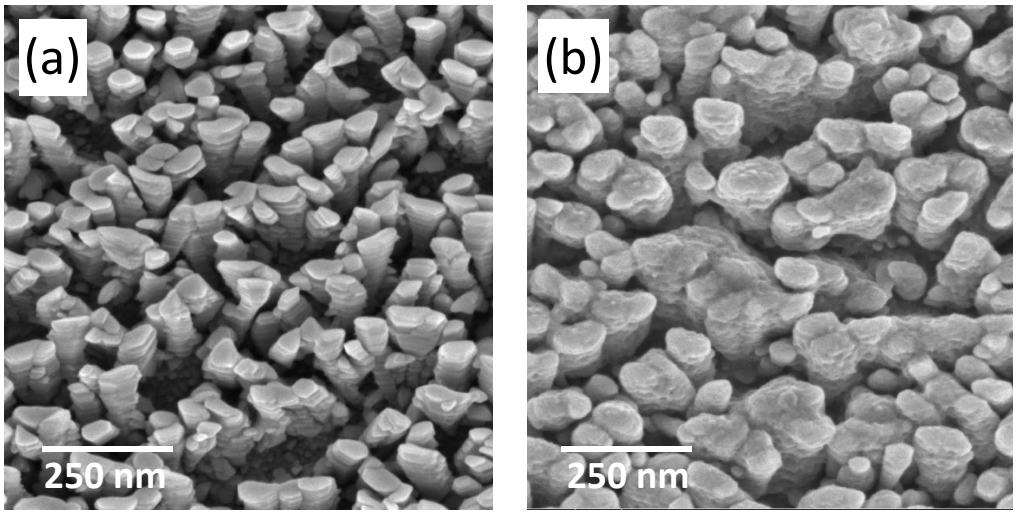

Figure 5: *Representative SEM images of as-deposited Ti nanocolumns (a) and of the resulting TiO_2 nanocolumns after the thermal treatment (b).*

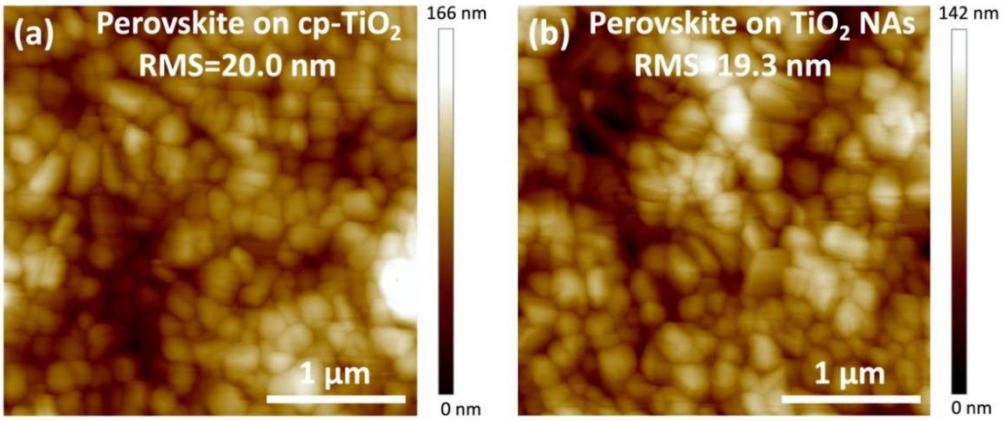

Figure 6: *Representative AFM images of the perovskite layer deposited on the cp-TiO_2 (a) and on TiO_2 nanocolumns (b).*

3.2.2. XPS and XRD Measurements of Perovskite Films

X-ray photoelectron spectroscopy (XPS) was applied to compare the surface chemistry of the nanocolumn array part and the planar cp-TiO_2 (control) part of the sample (**Figure 7**). As shown in **Figure 7a**, for the nanocolumn arrays, the doublet of Ti $2p_{3/2}$ and Ti $2p_{1/2}$ arising from the spin orbit-splitting are located at binding energies of 465.2 and 459.4 eV, respectively. Almost identical Ti 2p peaks were observed on the control part of the sample except for a 0.2 eV shift to lower binding energy. The binding energies and the shapes of these Ti 2p peaks are consistent with Ti^{4+} in a TiO_2 lattice.[44] The O 1s spectrum from both sample areas are also very similar (**Figure 7b**). For the nanocolumn arrays, it can be fitted with two peaks at binding energy of 530.7 and 532.2 eV, attributed to the lattice oxygen in TiO_2 and non-lattice oxygen species (such as -OH groups and/or oxygen vacancies),[45,46] respectively. Nearly identical O 1s spectrum was found on the control cp-TiO_2 area except also for a 0.2 eV shift to lower binding energy. Such a 0.2 eV shift in binding energy was observed in the C 1s spectrum recorded from the two sample areas. Combining the similar peak shape/position of Ti 2p and O 1s spectra observed, we conclude that the surface chemistry of both the nanocolumn arrays and the cp-TiO_2 are nearly identical even though a slight difference of conductivity may exist between them leading to the small shift of binding energy observed.

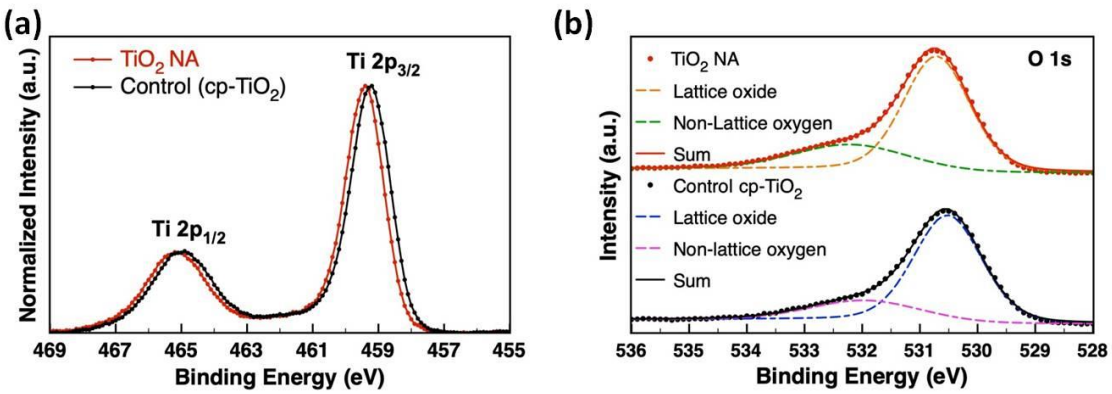

Figure 7. *(a) XPS spectra of Ti 2p regions of the TiO_2 nanocolumn (NA) sample and the planar cp-TiO_2 (control) sample; (b) XPS spectra of O 1s regions of the TiO_2 NA sample and control sample. Dash lines represent the fits and solid lines represent the sums of the two fitted peaks.*

After the deposition of the perovskite absorber layer onto one of the above-mentioned substrates, the substrate was cut into half separating the nanocolumn part and the cp-TiO_2 part in order to perform XRD characterizations. The perovskite films deposited on both the nanocolumn arrays and on the control cp-TiO_2 exhibited strong Bragg diffraction peaks which can be indexed according to the $Cs_{0.05}(FA_{0.83}MA_{0.17})_{0.95}Pb(I_{0.83}Br_{0.17})_3$ "black" (α) perovskite phase,[47] while more intense diffractions were observed on the perovskite/nanocolumn sample (**Figure 8**). This is coherent with the SEM observation, likely due to infiltration of perovskite precursor solution in between the nanocolumns leading to the existence of more perovskite crystallites on the nanocolumns compared to the control planar cp-TiO_2. In addition, by comparison to the planar TiO_2, the nanocolumns may offer more nucleation sites facilitating perovskite crystallization. Such observation is similar as those previously observed on other mesoporous ETLs.[1,48] Diffraction peak corresponding to the (001) diffraction of PbI_2 was also observed on both samples. This is due to the 10% mole excess of PbI_2 from the perovskite precursor solution. Here, an excess of PbI_2 was intentionally added into the perovskite precursor solution to optimize the solar cell performance according to previous reports to passivate the grain boundary of the mixed cation perovskite films aiming to benefit the charge transport and to reduce charge recombination.[49,50] The UV-Vis optical absorbance spectra on these perovskite films revealed an about 1.3-fold increase of optical absorption on the nanocolumns compared to the perovskite film deposited on the control planar cp-TiO_2 (**Figure 9**). Such an increase of optical absorbance can be a direct consequence of the more

perovskite materials deposited on the nanocolumns due to precursor infiltration as well as the light harvesting effect of the nanocolumns (which will be discussed below).

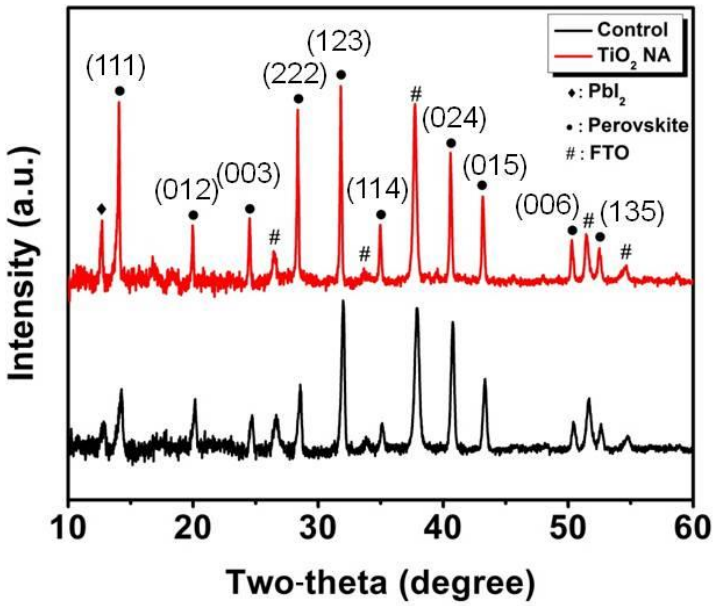

Figure 8. *X-ray diffraction (XRD) patterns of the perovskite film deposited on cp-TiO_2/FTO glass substrate and on TiO_2 NA/cp-TiO_2/FTO glass substrate, respectively.*

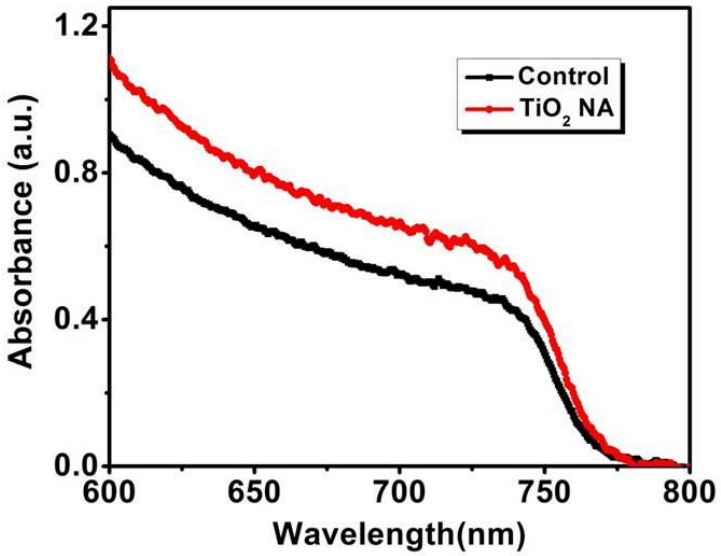

Figure 9. *Absorbance spectra of the perovskite film deposited on cp-TiO_2/FTO glass substrate and on TiO_2 NA/cp-TiO_2/FTO glass substrate, respectively.*

3.2.3. Scanning Near-field Optical Microscopy (SNOM) Characterization of ETLs

Scanning near-field optical microscopy (SNOM) was applied to characterize the potential light-harvesting capability of TiO_2 nanocolumns for their application in a perovskite solar cell. SNOM has been widely used in the past to characterize biological samples and optoelectronic devices,[51–53] capable to reveal the distribution of electromagnetic fields at the vicinity of a nano-object/nanostructure. Here, we used a fluorescent nanoparticle to probe the local optical properties of the TiO_2 nanocolumns by comparison to the planar cp-TiO_2 part situated on the same substrate. The measured fluorescence intensity of such a nanoparticle at a specific sample position can thus indicate the intensity of the local electromagnetic field. The schematic of the current SNOM experiment is shown in **Figure 10**. During the SNOM experiment, a sharp tungsten atomic force microscope (AFM) tungsten tip on which an upconversion fluorescent nanoparticle (KY_3F_{10}/YF_3:Er/Yb) is glued is scanned above the illuminated sample. The nanoparticle absorbs the near-field at the laser wavelength (λ = 650 nm) and re-emits it in the green-yellowish spectral zone (λ = 520-550 nm). The sample was illuminated in a transmission mode, from its rear face. By scanning the tip (with the nanoparticle) over the TiO_2 sample surface and simultaneously recording fluorescence signal at each scan position, both a topographic map of the sample and a map of the upconversion fluorescence (at λ = 550 nm) from the nanoparticle can be obtained. In order to keep the same measurement condition without any alteration of the probe, all the scanning experiments were performed with the same AFM tip.

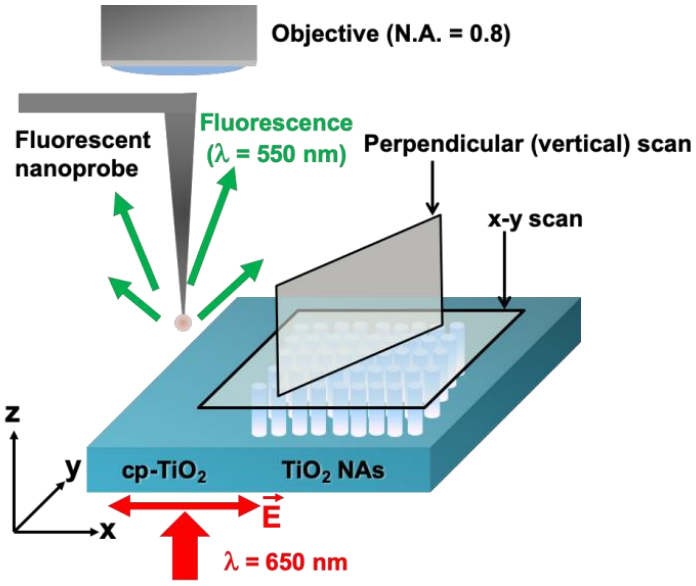

Figure 10. *Schematic of the illumination configuration and the scanning mode of the current scanning near-field optical microscopy (SNOM) experiments. TiO_2 nanocolumns (NAs) were fabricated onto half of the cp-TiO_2-coated FTO substrate surface so that AFM/SNOM measurements on the surface of TiO_2 nanocolumns and on cp-TiO_2 can be performed on the same substrate.*

From the AFM topography mapping presented in **Figure 11a** and **11d**, both surfaces of the cp-TiO_2 and TiO_2 nanocolumn arrays are very homogeneous, providing a uniform area for the growth of perovskite materials. In contrast to the topography mapping, the fluorescence mappings obtained on them revealed distinctively different features (**Figure 11b** and **11e**). Comparing to the two fluorescence mapping figures, one can observe on the surface of TiO_2 nanocolumns more inhomogeneity of the fluorescence signal from the nanoparticle glued on the AFM tip, indicating strong variations and a localization of electromagnetic field on the nanocolumn surface. In order to visualize the effect of the TiO_2 nanocolumns on the modulation of the incident light, two randomly selected line profiles from the fluorescence mapping obtained on the cp-TiO_2 and the TiO_2 nanocolumns were exhibited in **Figure 11c** and **11f**. Comparing these line profiles, one can observe enormous variations of the fluorescence intensity on TiO_2 nanocolumns by comparison to the planar cp-TiO_2. This indicates that TiO_2 nanocolumns perturb the incident field and create zones on which light is strongly enhanced compared to others. A vertical fluorescence scan in the out-of-plane direction was performed from the surface of TiO_2 nanocolumns to 1 µm above the surface

(**Figure 11g**). The intensity of fluorescence is strongest with a clear in-plane modulation when the AFM tip and the glued fluorescent nanoparticle are close to the surface of the TiO_2 nanocolumns. By comparison, when the distance between the tip and the nanocolumns increases, the observed fluorescence signal becomes weaker together with less in-plane modulation, indicating a smaller and less localized electromagnetic field when the AFM probe is far away from the TiO_2 nanocolumns. Similar as the above observed enhanced fluorescence process, in a perovskite solar cell configuration, the existence of TiO_2 nanocolumns and their resultant localization of electromagnetic field can lead to a more efficient light absorption by the perovskite absorber around the nanocolumns, leading to more photons available to be converted to electrons.

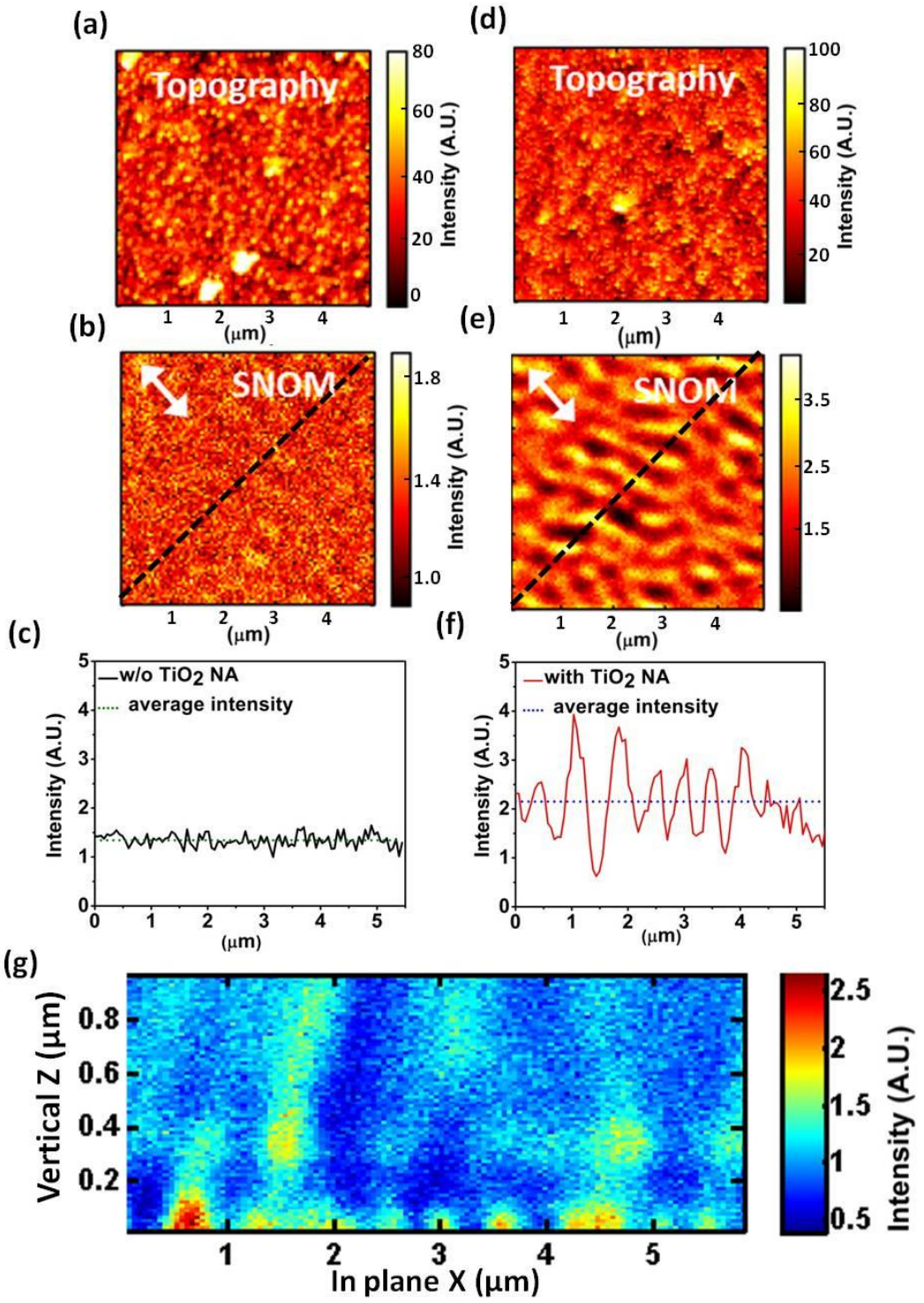

Figure 11. *AFM topography of planar cp-TiO_2 (a) and TiO_2 nanocolumns (NA) (d). Fluorescence maps of cp-TiO_2 layer (b) and TiO_2 NA (d). (c) and (f) exhibit the line profiles of the fluorescence map obtained on cp-TiO_2 (black dash line shown in (b)) and on TiO_2 NAs*

(black dash line shown in (e)). (g) The vertical fluorescence map obtained from the surface of TiO_2 NAs to 1 μm above the surface.

3.2.4. Photovoltaic Performance of PSCs with/without TiO_2 Nanocolumn Arrays

Functional perovskite solar cells were fabricated on both TiO_2 nanocolumn ETL and planar cp-TiO_2 ETL located on the same FTO substrate according to the device architectures shown in **Figure 1.** The current-voltage (*J-V*) characteristics, measured under 100 mW cm^{-2} AM 1.5G simulated illumination, of the best-performing perovskite solar cells from the same FTO substrate are shown in **Figure 12.** By comparison to the perovskite solar cell built on a planar cp-TiO_2 ETL, the incorporation of TiO_2 nanocolumn ETL leads to a slight increase of the solar cell short circuit photocurrent density (J_{sc}), from 19.27 mA/cm^2 to 20.19 mA/cm^2, and the fill-factor (FF), from 73.59% to 75.14%. The combination of both lead to an about 7% increase in the power conversion efficiency (PCE) in the solar cell with nanocolumns compared to the one with only a planar cp-TiO_2 ETL. The photovoltaic characteristics of these perovskite solar cells built onto the *same* substrate are listed in **Table 1** (the standard distribution of photovoltaic performance measured on different substrates were presented in **Table 2**). Their external quantum efficiencies (EQEs) are shown in **Figure 13**. The short-circuit current densities for the solar cell built on cp-TiO_2 ETL and on TiO_2 nanocolumns obtained from integrating their EQE spectra with the AM 1.5G spectrum are 19.10 and 20.03 mA/cm^2, respectively, which are in agreement with the J_{sc} measured in the *J-V* curves. The observation that the solar cell with TiO_2 nanocolumns shows a higher EQE value in the wavelength range of 450-600 nm than that of the cell without TiO_2 nanocolumns is qualitatively coherent with the optical absorbance spectra of the perovskite film deposited onto these substrates (**Figure 14**). The larger observed J_{sc} on the solar cell built on TiO_2 nanocolumns is coherent with the results obtained by SEM, UV-Vis absorption and SNOM. It is likely a combined consequence from both more perovskite materials deposited on top of the TiO_2 nanocolumns and the light-concentration effects of the TiO_2 nanocolumns.

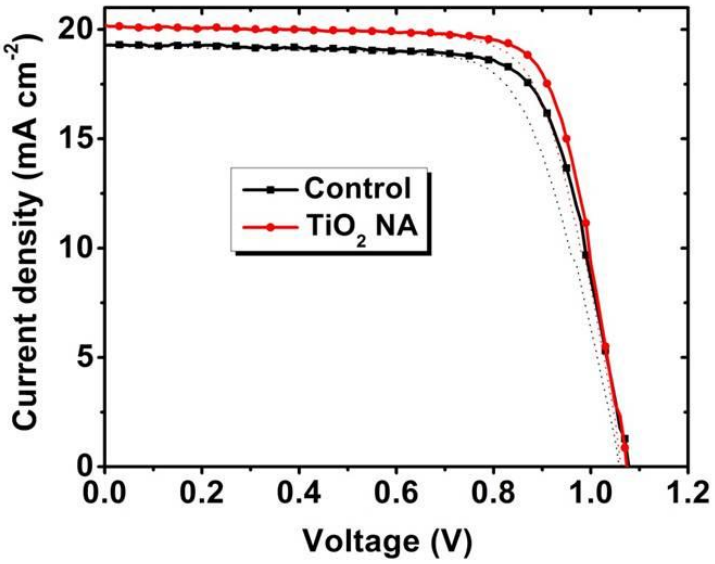

Figure 12. *(a) Current density-voltage (J-V) photovoltaic characteristics measured on the perovskite solar cells built on a cp-TiO_2 ETL (control) and on TiO_2 nanocolumn (NA) ETL of the same FTO substrate, under 100 mW cm^{-2} AM 1.5G illumination. Solid dots and lines indicate results from the reverse voltage scan (from V_{oc} to 0 V) and dotted lines indicate results from forward voltage scan (from 0 V to V_{oc}).*

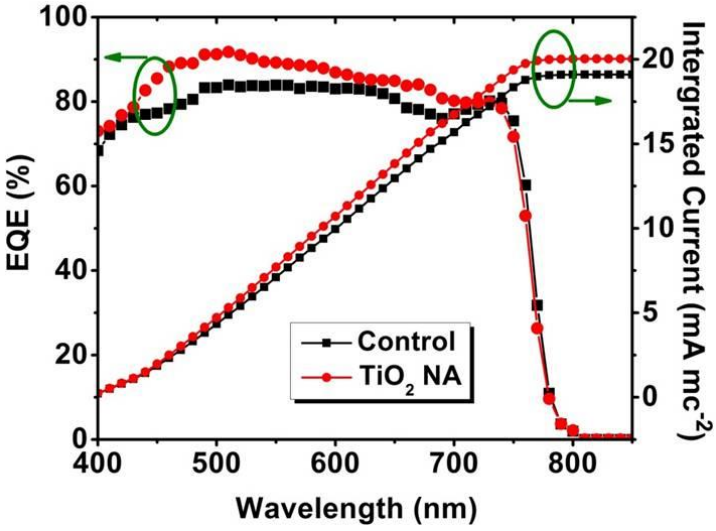

Figure 13. *The EQE spectra for the perovskite solar cells shown in* ***Figure 12*** *and the corresponding integrated J_{sc} of the devices.*

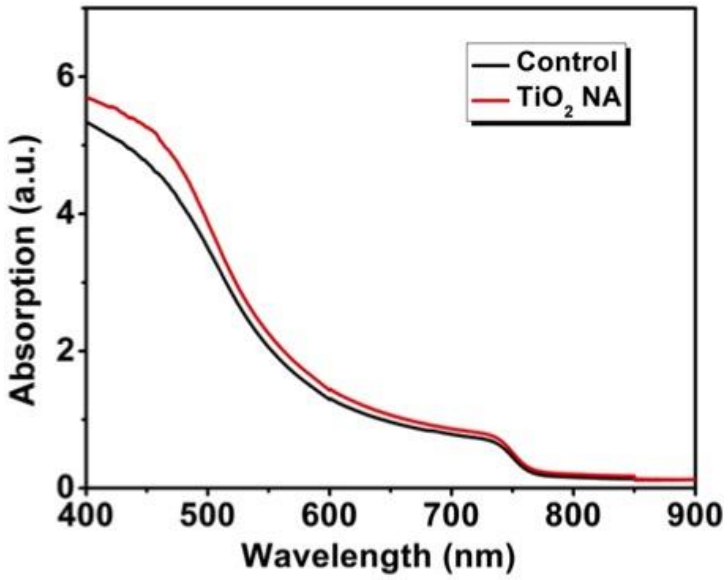

***Figure 14**: The optical absorbance spectra of the perovskite film deposited on a cp-TiO_2/FTO glass substrate (control sample) and on a TiO_2 NA/cp-TiO_2/FTO glass substrate, respectively.*

***Table 1.** The summary of the photovoltaic characteristics of the perovskite solar cells built on a cp-TiO_2 ETL (control) and on TiO_2 nanocolumn (NA) ETL of the same FTO substrate. Results are presented together with the parameters (inner series resistance R_s, charge transport resistance R_{tr}, and recombination resistance R_{rec}) obtained from fitting the electrochemical impedance spectroscopy results. J_{sc}: short-circuit current density; V_{oc}: open-circuit voltage; FF: fill-factor; PCE: power-conversion efficiency.*

ETL	J_{sc} (mA/cm^2)	V_{oc} (V)	*FF* (%)	*PCE* (%)	R_s (Ω)	R_{tr} (Ω)	R_{rec} (Ω)
cp-TiO_2	19.27	1.08	73.59	15.31	10.05	20.02	2085
TiO_2 NA	20.19	1.08	75.14	16.38	10.08	13.52	4410

Table 2. *Photovoltaic parameters with standard distribution of the perovskite solar cells built onto different substrates. Each substrate contains half of it covered by cp-TiO_2 ETL another half covered by TiO_2 nanocolumn arrays. Each error bar was obtained from eight solar cells fabricated and measured by the same conditions.*

ETL	J_{sc} (mA/cm^2)	V_{oc} (V)	*FF* (%)	*PCE* (%)
cp-TiO_2	19.43 ± 0.22	1.06 ± 0.02	72.90 ± 0.86	14.96 ± 0.28
TiO_2 NA	20.13 ± 0.21	1.07 ± 0.02	74.41 ± 1.27	15.97 ± 0.33

3.2.5. Electrochemical Impedance Spectroscopy (EIS) of the PSCs

Electrochemical impedance spectroscopy (EIS) was performed onto these solar cells to probe the charge transfer and recombination process at the interface between the ETL and perovskite absorber. **Figure 15** shows the Nyquist plots of the two perovskite solar cells built on the cp-TiO_2 ETL and the TiO_2 nanocolumn ETL of the same FTO substrate, measured in dark with an external bias holding at their respective V_{oc} and in the frequency range from 20 Hz to 2 MHz. The obtained EIS spectra can be fitted well with the equivalent electrical circuit model commonly used on perovskite solar cells.[54,55] The equivalent circuit is shown in the inset of **Figure 15** and the inner series resistance (R_s), charge transport resistance (R_{tr}), and the recombination resistance (R_{rec}) obtained from fitting are listed in Table 1. The whole set of fitting parameters are listed in the supporting information **Table 3**. When the nanocolumn ETL was applied, the charge transport resistance R_{tr} was reduced from 20 Ω to 13.5 Ω and the recombination resistance was substantially increased from 2085 Ω to 4410 Ω. Coherent with the enhanced fill-factor observed in the *J-V* characteristics, the current EIS results indicated that charge transport is more efficient in the TiO_2 nanocolumn ETL compared to the cp-TiO_2 ETL and the carrier recombination is less severe in the former case. These results suggest that, besides the optical benefits mentioned above, by comparison to the planar cp-TiO_2, TiO_2 nanocolumn ETL exhibits electronic benefits in terms of charge transport and recombination suppression.

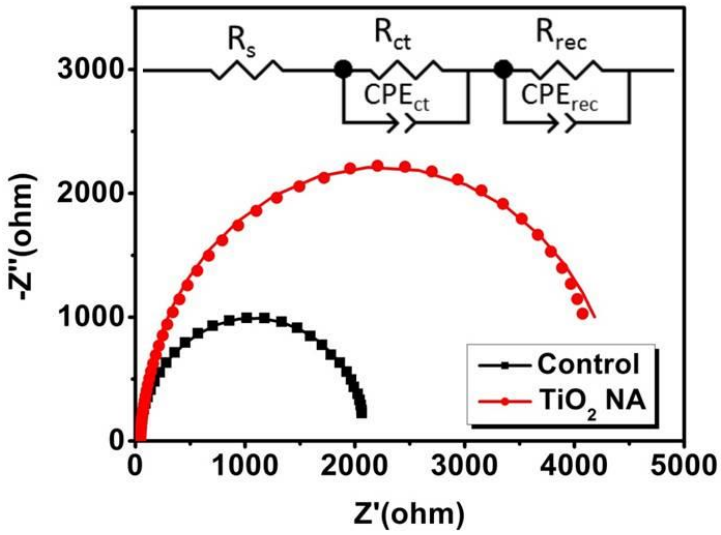

Figure 15. *The typical Nyquist plots (symbols) obtained from the perovskite solar cells shown in* ***Figure 12*** *tested in dark and at their V_{oc}. Solid lines represent the fits obtained by applying the equivalent circuit shown in the inset.*

Table 3. *EIS parameters for the perovskite solar cells with TiO_2 nanocolumn (NA) ETL and cp-TiO_2 ETL.*

ETL	R_s (Ω)	R_{tr} (Ω)	R_{rec} (Ω)	CPE_{ct}-T (F)	CPE_{ct}-P	CPE_{rec}-T (F)	CPE_{rec}-P
cp-TiO_2	10.05	20.02	2085	2.71×10^{-9}	1.08	1.44×10^{-8}	0.97
TiO_2 NA	10.08	13.52	4410	1.85×10^{-8}	1.35	8.08×10^{-7}	1.00

3.2.6. Stability of the Perovskite Devices

In addition to the above-mentioned optical and electrical benefits, it was observed that the application of TiO_2 nanocolumns significantly enhanced the shelf life of these perovskite solar cells. **Figure 16** presents the normalized PCE of the unencapsulated perovskite solar cells built on a cp-TiO_2 ETL and on a TiO_2 nanocolumn ETL of the same FTO substrate as a function of the storage time. When stored in argon, the perovskite solar cell built on TiO_2 nanocolumns maintained ~ 93.6 % of its initial PCE value after 126 days of storage, whereas under identical conditions the perovskite solar cell built on cp-TiO_2 exhibited only ~ 80.5 %

of its original PCE. When stored in air (with ~ 11% of humidity), the solar cell with the application of TiO_2 nanocolumns maintained ~ 75.3 % of its initial PCE value after 91 days of storage, which represents a more than 3.8-fold enhancement by comparison to the solar cell without nanocolumns (on cp-TiO_2) that maintained only ~ 19.8 % of its initial PCE under the same conditions. Under constant UV illumination, the perovskite solar cells built on TiO_2 nanocolumns also showed superior stability by comparison to the one built on the cp-TiO_2 ETL of the same substrate (**Figure 17**). After 95 hours of constant UV illumination (3 mW cm^{-2}) at λ = 365 nm in argon atmosphere, the perovskite solar cell with nanocolumns still maintained 92.4% of its initial PCE while the one without nanocolumns exhibited only 50.1% of its initial PCE. As observed from their optical images (inset of **Figure 16a**), after 91 days of air storage, there was inhomogeneous color with plenty of transparent spots visible as well as a transparent area surrounding the edge of the top electrode on the perovskite solar cell without nanocolumns, suggesting perovskite absorber decomposition. This is in clear contrast with the perovskite solar cell built on nanocolumns from the same substrate, where homogeneous perovskite absorber was still observed in the optical image. These observations are similar to the enhanced perovskite solar cell stability reported in previous studies with the application of 1D TiO_2 arrays,[6,11] while the physical origins accounting for the enhanced stability remain not well understood. To shed light on this, we compared the optical absorption from an identical area (by placing an aperture with a transmission diameter of 6 mm) between three sample conditions: a bare FTO/glass substrate, a cp-TiO_2-coated area on a FTO/glass substrate, and a TiO_2 nanocolumn-coated area on the same above-mentioned cp-TiO_2-coated FTO/glass substrate. As shown in **Figure 16b** (black symbols), the optical absorption contributed from the planar cp-TiO_2 is very small due to its limited thickness (50 nm). By comparison, the optical absorption contribution from the TiO_2 nanocolumns is much more significant (red symbols, **Figure 16b**), in particular in the wavelength range between 300 nm and 370 nm. Such optical absorption in the UV spectrum from the TiO_2 nanocolumns is thus beneficial for perovskite solar cells minimizing UV degradation occurred during each *J-V* measurements. While a much thicker cp-TiO_2 planar ETL should in principle be able to achieve the similar optical contribution as TiO_2 nanocolumns in the UV spectrum, a thicker cp-TiO_2 film may lead to a significantly increased solar cell series resistance, worse charge transport properties, and more carrier recombination events. These results underlined the

unique advantages of TiO_2 nanocolumns in perovskite solar cells, capable to perform partial UV screening without scarifying the electronic properties of ETL.

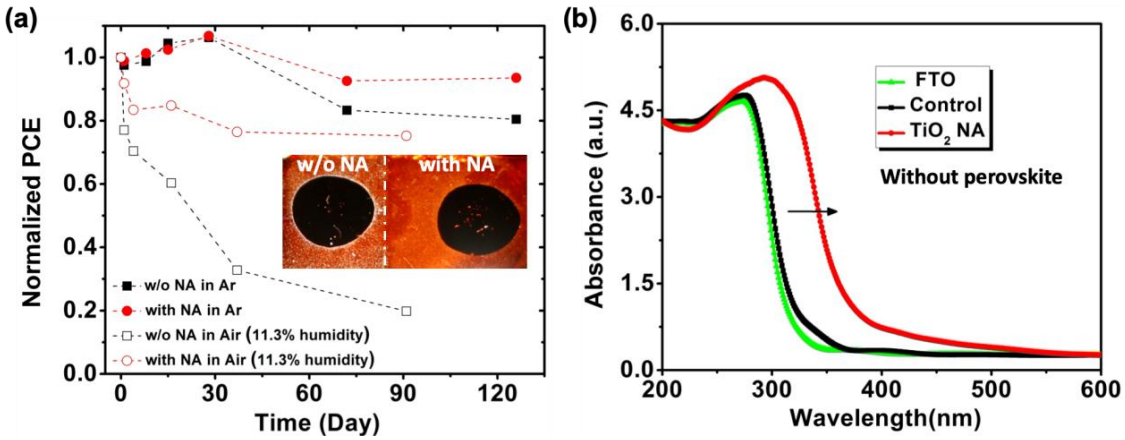

Figure 16 *(a) The evolution of power conversion efficiency (PCE) of perovskite solar cells with and without TiO_2 nanocolumn (NA) ETL built on the same FTO substrate over storage time. These solar cells were stored either in argon or in air (humidity at 11.3%), at 25 ℃ in dark. Insets exhibit the optical images of the area around the top electrode of the two solar cells built on the same FTO substrate after 91 days of degradation in air. The white dash line indicates the separation between the NA-coated part and part without NAs. The diameter of these top electrodes is 3.55 mm. (b) The comparison of optical absorption before perovskite deposition from an identical area (by placing a 6-mm-diameter aperture) from: a bare FTO/glass substrate (FTO), a cp-TiO_2-coated area on a FTO/glass substrate (control condition), and a TiO_2 NA-coated area from the same cp-TiO_2-coated FTO/glass substrate as the control condition.*

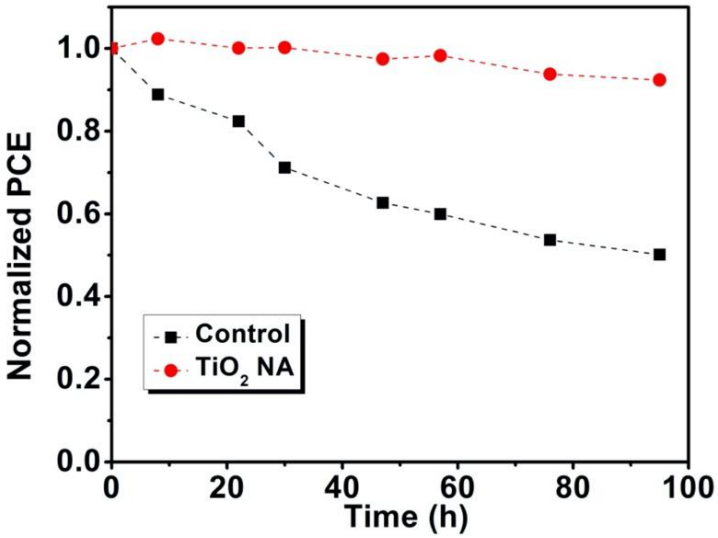

Figure 17: *The evolution of the power conversion efficiency (PCE) under constant UV illumination (λ = 365 nm, 3 mW cm^{-2}) in argon atmosphere measured on the perovskite solar cells built on the cp-TiO_2 ETL (control condition) and on TiO_2 nanocolumns arrays of the same substrate.*

3.3. Conclusion

In summary, vertically-aligned 1-D TiO_2 nanocolumn arrays were realized by glancing angle deposition and they were subsequently applied as the ETL to fabricate functional triple-cation lead perovskite halide solar cells based on $Cs_{0.05}(FA_{0.83}MA_{0.17})_{0.95}Pb(I_{0.83}Br_{0.17})_3$. By comparison to solar cells built on planar cp-TiO_2 of the same FTO substrate, solar cells built on a TiO_2 nanocolumn ETL exhibit a 5% increase of short-circuit current and a 7% enhancement in its power conversion efficiency together with a significantly prolonged shelf-life. Various macroscopic and microscopic characterization methods were combined to identify the physical origins of the observed enhanced photovoltaic property. Identified from SEM characterization, SNOM, and UV-vis absorption, TiO_2 nanocolumn ETL led to enhanced perovskite optical absorption, higher solar cell short-circuit currents, and better device stability by providing numerous precursor infiltration paths, near-field light concentration, and partial UV screening. In addition to these optical advantages, electrochemical EIS analysis showed that TiO_2 nanocolumn ETL is also superior to planar cp-TiO_2 in terms of charge transport and the reduction of recombination losses. These findings thus provide mechanistic insights on how 1D TiO_2 nanocolumns affect the performance of perovskite halide solar cells in terms of the

charge transport, light-harvesting, and stability, knowledge necessary for the future design of more-performing and more-stable perovskite solar cells.

3.4. References

(1) Haque, M. A.; Sheikh, A. D.; Guan, X.; Wu, T. Metal Oxides as Efficient Charge Transporters in Perovskite Solar Cells. *Adv. Energy Mater.* **2017**, *7*, 1602803. https://doi.org/10.1002/aenm.201602803.

(2) Liu, M.; Johnston, M. B.; Snaith, H. J. Efficient Planar Heterojunction Perovskite Solar Cells by Vapour Deposition. *Nature* **2013**, *501* (7467), 395–398. https://doi.org/10.1038/nature12509.

(3) Bai, Y.; Yu, H.; Zhu, Z.; Jiang, K.; Zhang, T.; Zhao, N.; Yang, S.; Yan, H. High Performance Inverted Structure Perovskite Solar Cells Based on a PCBM:Polystyrene Blend Electron Transport Layer. *J. Mater. Chem. A* **2015**, *3*, 9098–9102. https://doi.org/10.1039/C4TA05309E.

(4) Jiang, Q.; Zhang, L.; Wang, H.; Yang, X.; Meng, J.; Liu, H.; Yin, Z.; Wu, J.; Zhang, X.; You, J. Enhanced Electron Extraction Using SnO2 for High-Efficiency Planar-Structure HC(NH2)2PbI3-Based Perovskite Solar Cells. *Nat. Energy* **2017**, *2* (1), 16177. https://doi.org/10.1038/nenergy.2016.177.

(5) Liu, D.; Kelly, T. L. Perovskite Solar Cells with a Planar Heterojunction Structure Prepared Using Room-Temperature Solution Processing Techniques. *Nat. Photonics* **2014**, *8* (2), 133–138. https://doi.org/10.1038/nphoton.2013.342.

(6) Fakharuddin, A.; Di Giacomo, F.; Palma, A. L.; Matteocci, F.; Ahmed, I.; Razza, S.; D'Epifanio, A.; Licoccia, S.; Ismail, J.; Di Carlo, A.; Brown, T. M.; Jose, R. Vertical TiO2 Nanorods as a Medium for Durable and High Efficiency Perovskite Solar Modules. *ACS Nano* **2015**, *9* (8), 8420–8429. https://doi.org/10.1021/acsnano.5b03265.

(7) Wei, D.; Ji, J.; Song, D.; Li, M.; Cui, P.; Li, Y.; Mbengue, J. M.; Zhou, W.; Ning, Z.; Park, N. G. A TiO2 Embedded Structure for Perovskite Solar Cells with Anomalous Grain Growth and Effective Electron Extraction. *J. Mater. Chem. A* **2017**. https://doi.org/10.1039/c6ta10418e.

(8) Grancini, G.; Marras, S.; Prato, M.; Giannini, C.; Quarti, C.; De Angelis, F.; De Bastiani, M.; Eperon, G. E.; Snaith, H. J.; Manna, L.; Petrozza, A. The Impact of the Crystallization Processes on the Structural and Optical Properties of Hybrid Perovskite Films for Photovoltaics. *J. Phys. Chem. Lett.* **2014**. https://doi.org/10.1021/jz501877h.

(9) Giordano, F.; Abate, A.; Correa Baena, J. P.; Saliba, M.; Matsui, T.; Im, S. H.; Zakeeruddin, S. M.; Nazeeruddin, M. K.; Hagfeldt, A.; Graetzel, M. Enhanced Electronic Properties in Mesoporous TiO2 via Lithium Doping for High-Efficiency Perovskite Solar Cells. *Nat. Commun.* **2016**, *7*, 1–6. https://doi.org/10.1038/ncomms10379.

(10) Wu, W. Q.; Chen, D.; Cheng, Y. B.; Caruso, R. A. Three-Dimensional Titanium Oxide Nanoarrays for Perovskite Photovoltaics: Surface Engineering for Cascade Charge Extraction and Beneficial Surface Passivation. *Sustain. Energy Fuels* **2017**, *1* (9), 1960–1967. https://doi.org/10.1039/C7SE00377C.

(11) Qin, P.; Paulose, M.; Dar, M. I.; Moehl, T.; Arora, N.; Gao, P.; Varghese, O. K.; Grätzel, M.; Nazeeruddin, M. K. Stable and Efficient Perovskite Solar Cells Based on Titania Nanotube Arrays. *Small* **2015**, *11* (41), 5533–5539. https://doi.org/10.1002/smll.201501460.

(12) Jiang, Q.; Sheng, X.; Li, Y.; Feng, X.; Xu, T. Rutile TiO 2 Nanowire-Based Perovskite Solar Cells. *Chem. Commun.* **2014**, *50* (94), 14720–14723. https://doi.org/10.1039/C4CC07367C.

(13) Wu, S.; Chen, C.; Wang, J.; Xiao, J.; Peng, T. Controllable Preparation of Rutile TiO 2 Nanorod Array for Enhanced Photovoltaic Performance of Perovskite Solar Cells . *ACS Appl. Energy Mater.* **2018**, *1* (4), 1649–1657. https://doi.org/10.1021/acsaem.8b00106.

(14) Yang, H.-Y.; Rho, W.-Y.; Lee, S.; Kim, S.; Hahn, Y.-B. TiO2 Nanoparticles/Nanotubes for Efficient Light Harvesting in Perovskite Solar Cells. *Nanomaterials* **2019**, *9* (3), 326. https://doi.org/10.3390/nano9030326.

(15) Cui, Q.; Zhao, X.; Lin, H.; Yang, L.; Chen, H.; Zhang, Y.; Li, X. Improved Efficient Perovskite Solar Cells Based on Ta-Doped TiO2 Nanorod Arrays. *Nanoscale* **2017**, *9* (47), 18897–18907. https://doi.org/10.1039/c7nr05687g.

(16) Liu, C.; Zhu, R.; Ng, A.; Ren, Z.; Cheung, S. H.; Du, L.; So, S. K.; Zapien, J. A.; Djurišić, A. B.; Lee Phillips, D.; Surya, C. Investigation of High Performance TiO2 Nanorod Array Perovskite Solar Cells. *J. Mater. Chem. A* **2017**, *5* (30), 15970–15980. https://doi.org/10.1039/c7ta03710d.

(17) Gao, X.; Li, J.; Gollon, S.; Qiu, M.; Guan, D.; Guo, X.; Chen, J.; Yuan, C. A TiO 2 Nanotube Network Electron Transport Layer for High Efficiency Perovskite Solar Cells. *Phys. Chem. Chem. Phys.* **2017**, *19* (7), 4956–4961. https://doi.org/10.1039/c6cp07733a.

(18) Seo, M. S.; Jeong, I.; Park, J. S.; Lee, J.; Han, I. K.; Lee, W. I.; Son, H. J.; Sohn, B. H.; Ko, M. J. Vertically Aligned Nanostructured TiO2 Photoelectrodes for High Efficiency Perovskite Solar Cells: Via a Block Copolymer Template Approach. *Nanoscale* **2016**, *8* (22), 11472–11479. https://doi.org/10.1039/c6nr01010e.

(19) Zhong, D.; Cai, B.; Wang, X.; Yang, Z.; Xing, Y.; Miao, S.; Zhang, W.-H.; Li, C. Synthesis of Oriented TiO2 Nanocones with Fast Charge Transfer for Perovskite Solar Cells. *Nano Energy* **2015**, *11*, 409–418. https://doi.org/10.1016/j.nanoen.2014.11.014.

(20) Li, X.; Dai, S. M.; Zhu, P.; Deng, L. L.; Xie, S. Y.; Cui, Q.; Chen, H.; Wang, N.; Lin, H. Efficient Perovskite Solar Cells Depending on TiO2 Nanorod Arrays. *ACS Appl. Mater. Interfaces* **2016**, *8* (33), 21358–21365. https://doi.org/10.1021/acsami.6b05971.

(21) Salado, M.; Oliva-Ramirez, M.; Kazim, S.; González-Elipe, A. R.; Ahmad, S. 1-Dimensional TiO2 Nano-Forests as Photoanodes for Efficient and Stable Perovskite Solar Cells Fabrication. *Nano Energy* **2017**, *35*, 215–222. https://doi.org/10.1016/j.nanoen.2017.03.034.

(22) Ramos, F. J.; Oliva-Ramirez, M.; Nazeeruddin, M. K.; Grätzel, M.; González-Elipe, A. R.; Ahmad, S. Nanocolumnar 1-Dimensional TiO 2 Photoanodes Deposited by PVD-OAD for Perovskite Solar Cell Fabrication. *J. Mater. Chem. A* **2015**, *3*, 13291–13298. https://doi.org/10.1039/C5TA02238J.

(23) Zheng, L.; Ma, Y.; Chu, S.; Wang, S.; Qu, B.; Xiao, L.; Chen, Z.; Gong, Q.; Wu, Z.; Hou, X. Improved Light Absorption and Charge Transport for Perovskite Solar Cells with Rough Interfaces by Sequential Deposition. *Nanoscale* **2014**, *6* (14), 8171–8176. https://doi.org/10.1039/C4NR01141D.

(24) Pascoe, A. R.; Meyer, S.; Huang, W.; Li, W.; Benesperi, I.; Duffy, N. W.; Spiccia, L.; Bach, U.; Cheng, Y.-B. Enhancing the Optoelectronic Performance of Perovskite Solar Cells via a Textured CH 3 NH 3 PbI 3 Morphology. *Adv. Funct. Mater.* **2016**, *26* (8), 1278–1285. https://doi.org/10.1002/adfm.201504190.

(25) Shi, B.; Liu, B.; Luo, J.; Li, Y.; Zheng, C.; Yao, X.; Fan, L.; Liang, J.; Ding, Y.; Wei, C.; Zhang, D.; Zhao, Y.; Zhang, X. Enhanced Light Absorption of Thin Perovskite Solar Cells Using Textured Substrates. *Sol. Energy Mater. Sol. Cells* **2017**, *168*, 214–220. https://doi.org/10.1016/j.solmat.2017.04.038.

(26) Jošt, M.; Albrecht, S.; Kegelmann, L.; Wolff, C. M.; Lang, F.; Lipovšek, B.; Krč, J.; Korte, L.; Neher, D.; Rech, B.; Topič, M. Efficient Light Management by Textured Nanoimprinted Layers for Perovskite Solar Cells. *ACS Photonics* **2017**, *4* (5), 1232–1239. https://doi.org/10.1021/acsphotonics.7b00138.

(27) Wang, D.-L.; Cui, H.-J.; Hou, G.-J.; Zhu, Z.-G.; Yan, Q.-B.; Su, G. Highly Efficient Light Management for Perovskite Solar Cells. *Sci. Rep.* **2016**, *6* (1), 18922. https://doi.org/10.1038/srep18922.

(28) Peer, A.; Biswas, R.; Park, J.-M.; Shinar, R.; Shinar, J. Light Management in Perovskite Solar Cells and Organic LEDs with Microlens Arrays. *Opt. Express* **2017**, *25* (9), 10704. https://doi.org/10.1364/OE.25.010704.

(29) Wang, H.; Cai, B.; Yuan, X. Significant Light Absorption Improvement in Perovskite/CIGS Tandem Solar Cells with Dielectric Nanocone Structures. *J. Phys. Conf. Ser.* **2017**, *844*, 012004. https://doi.org/10.1088/1742-6596/844/1/012004.

(30) Luo, Q.; Zhang, C.; Deng, X.; Zhu, H.; Li, Z.; Wang, Z.; Chen, X.; Huang, S. Plasmonic Effects of Metallic Nanoparticles on Enhancing Performance of Perovskite Solar Cells. *ACS Appl. Mater. Interfaces* **2017**, *9* (40), 34821–34832. https://doi.org/10.1021/acsami.7b08489.

(31) Ginting, R. T.; Kaur, S.; Lim, D.-K.; Kim, J.-M.; Lee, J. H.; Lee, S. H.; Kang, J.-W. Plasmonic Effect of Gold Nanostars in Highly Efficient Organic and Perovskite Solar Cells. *ACS Appl. Mater. Interfaces* **2017**, *9* (41), 36111–36118. https://doi.org/10.1021/acsami.7b11084.

(32) Long, M.; Chen, Z.; Zhang, T.; Xiao, Y.; Zeng, X.; Chen, J.; Yan, K.; Xu, J. Ultrathin Efficient Perovskite Solar Cells Employing a Periodic Structure of a Composite Hole Conductor for Elevated Plasmonic Light Harvesting and Hole Collection. *Nanoscale* **2016**, *8* (12), 6290–6299. https://doi.org/10.1039/C5NR05042A.

(33) Yin, J.; Qu, H.; Cao, J.; Tai, H.; Li, J.; Zheng, N. Light Absorption Enhancement by Embedding Submicron Scattering TiO 2 Nanoparticles in Perovskite Solar Cells. *RSC Adv.* **2016**, *6* (29), 24596–24602. https://doi.org/10.1039/C6RA01894G.

(34) Haque, S.; Mendes, M. J.; Sanchez-Sobrado, O.; Águas, H.; Fortunato, E.; Martins, R. Photonic-Structured TiO2 for High-Efficiency, Flexible and Stable Perovskite Solar Cells. *Nano Energy* **2019**, *59*, 91–101. https://doi.org/10.1016/j.nanoen.2019.02.023.

(35) Caldarola, M.; Albella, P.; Cortés, E.; Rahmani, M.; Roschuk, T.; Grinblat, G.; Oulton, R. F.; Bragas, A. V.; Maier, S. A. Non-Plasmonic Nanoantennas for Surface Enhanced Spectroscopies with Ultra-Low Heat Conversion. *Nat. Commun.* **2015**, *6* (1), 7915. https://doi.org/10.1038/ncomms8915.

(36) Albella, P.; Poyli, M. A.; Schmidt, M. K.; Maier, S. A.; Moreno, F.; Sáenz, J. J.; Aizpurua, J. Low-Loss Electric and Magnetic Field-Enhanced Spectroscopy with Subwavelength Silicon Dimers. *J. Phys. Chem. C* **2013**, *117* (26), 13573–13584. https://doi.org/10.1021/jp4027018.

(37) Cambiasso, J.; Grinblat, G.; Li, Y.; Rakovich, A.; Cortés, E.; Maier, S. A. Bridging the Gap between Dielectric Nanophotonics and the Visible Regime with Effectively Lossless Gallium Phosphide Antennas. *Nano Lett.* **2017**, *17* (2), 1219–1225. https://doi.org/10.1021/acs.nanolett.6b05026.

(38) Lin, H.-J.; de Oliveira Lima, K.; Gredin, P.; Mortier, M.; Billot, L.; Chen, Z.; Aigouy, L. Fluorescence Enhancement near Single TiO 2 Nanodisks. *Appl. Phys. Lett.* **2017**, *111* (25), 251109. https://doi.org/10.1063/1.4994311.

(39) Deniz, D.; Lad, R. J. Temperature Threshold for Nanorod Structuring of Metal and Oxide Films Grown by Glancing Angle Deposition. *J. Vac. Sci. Technol. A Vacuum, Surfaces, Film.* **2011**, *29* (1), 011020. https://doi.org/10.1116/1.3525882.

(40) Cansizoglu, M. F.; Engelken, R.; Seo, H. W.; Karabacak, T. High Optical Absorption of Indium Sulfide Nanorod Arrays Formed by Glancing Angle Deposition. *ACS Nano* **2010**, *4* (2), 733–740. https://doi.org/10.1021/nn901180x.

(41) Waita, S. M.; Aduda, B. O.; Mwabora, J. M.; Granqvist, C. G.; Lindquist, S. E.; Niklasson, G. A.; Hagfeldt, A.; Boschloo, G. Electron Transport and Recombination in Dye Sensitized Solar Cells Fabricated from Obliquely Sputter Deposited and Thermally Annealed TiO2 Films. *J. Electroanal. Chem.* **2007**, *605* (2), 151–156. https://doi.org/10.1016/j.jelechem.2007.04.001.

(42) Bräuer, G.; Szyszka, B.; Vergöhl, M.; Bandorf, R. Magnetron Sputtering – Milestones of 30 Years. *Vacuum* **2010**, *84*, 1354–1359. https://doi.org/10.1016/j.vacuum.2009.12.014.

(43) Anders, A. Plasma and Ion Sources in Large Area Coating: A Review. *Surf. Coatings Technol.* **2005**, *200*, 1893–1906. https://doi.org/10.1016/j.surfcoat.2005.08.018.

(44) Sanjinés, R.; Tang, H.; Berger, H.; Gozzo, F.; Margaritondo, G.; Lévy, F. Electronic Structure of Anatase TiO 2 Oxide. *J. Appl. Phys.* **1994**, *75* (6), 2945–2951. https://doi.org/10.1063/1.356190.

(45) Ma, S.; Ahn, J.; Oh, Y.; Kwon, H.-C.; Lee, E.; Kim, K.; Yun, S.-C.; Moon, J. Facile Sol–Gel-Derived Craterlike Dual-Functioning TiO 2 Electron Transport Layer for High-Efficiency Perovskite Solar Cells. *ACS Appl. Mater. Interfaces* **2018**, *10* (17), 14649–14658. https://doi.org/10.1021/acsami.8b00549.

(46) Bharti, B.; Kumar, S.; Lee, H.-N.; Kumar, R. Formation of Oxygen Vacancies and Ti3+ State in TiO2 Thin Film and Enhanced Optical Properties by Air Plasma Treatment. *Sci. Rep.* **2016**, *6* (1), 32355. https://doi.org/10.1038/srep32355.

(47) Wang, Y.; Wu, J.; Zhang, P.; Liu, D.; Zhang, T.; Ji, L.; Gu, X.; David Chen, Z.; Li, S. Stitching Triple Cation Perovskite by a Mixed Anti-Solvent Process for High

Performance Perovskite Solar Cells. *Nano Energy* **2017**, *39* (July), 616–625. https://doi.org/10.1016/j.nanoen.2017.07.046.

(48) Bera, A.; Sheikh, A. D.; Haque, M. A.; Bose, R.; Alarousu, E.; Mohammed, O. F.; Wu, T. Fast Crystallization and Improved Stability of Perovskite Solar Cells with Zn 2 SnO 4 Electron Transporting Layer: Interface Matters. *ACS Appl. Mater. Interfaces* **2015**, *7*, 28404–28411. https://doi.org/10.1021/acsami.5b09182.

(49) Saliba, M.; Matsui, T.; Seo, J. Y.; Domanski, K.; Correa-Baena, J. P.; Nazeeruddin, M. K.; Zakeeruddin, S. M.; Tress, W.; Abate, A.; Hagfeldt, A.; Grätzel, M. Cesium-Containing Triple Cation Perovskite Solar Cells: Improved Stability, Reproducibility and High Efficiency. *Energy Environ. Sci.* **2016**, *9* (6), 1989–1997. https://doi.org/10.1039/c5ee03874j.

(50) Chen, Q.; Zhou, H.; Song, T.-B.; Luo, S.; Hong, Z.; Duan, H.-S.; Dou, L.; Liu, Y.; Yang, Y. Controllable Self-Induced Passivation of Hybrid Lead Iodide Perovskites toward High Performance Solar Cells. *Nano Lett.* **2014**, *14* (7), 4158–4163. https://doi.org/10.1021/nl501838y.

(51) Zhang, H.; Li, Y.; Ivanov, I. A.; Qu, Y.; Huang, Y.; Duan, X. Plasmonic Modulation of the Upconversion Fluorescence in NaYF 4: Yb/Tm Hexaplate Nanocrystals Using Gold Nanoparticles or Nanoshells. *Angew. Chemie - Int. Ed.* **2010**, *49* (16), 2865–2868. https://doi.org/10.1002/anie.200905805.

(52) Wang, P. H.; Li, Z. Q.; Salcedo, W. J.; Sun, Z.; Huang, S. M.; Brolo, A. G. Surface Plasmon Enhanced Up-Conversion from NaYF4:Yb/Er/Gd Nano-Rods. *Phys. Chem. Chem. Phys.* **2015**, *17* (24), 16170–16177. https://doi.org/10.1039/c5cp02249e.

(53) Aigouy, L.; González, M.-U.; Lin, H.-J.; Schoenauer-Sebag, M.; Billot, L.; Gredin, P.; Mortier, M.; Chen, Z.; García-Martín, A. Mapping Plasmon-Enhanced Upconversion Fluorescence of Er/Yb-Doped Nanocrystals near Gold Nanodisks. *Nanoscale* **2019**, *11* (21), 10365–10371. https://doi.org/10.1039/C9NR02113B.

(54) Feng, J.; Zhu, X.; Yang, Z.; Zhang, X.; Niu, J.; Wang, Z.; Zuo, S.; Priya, S.; Liu, S. (Frank); Yang, D. Record Efficiency Stable Flexible Perovskite Solar Cell Using Effective Additive Assistant Strategy. *Adv. Mater.* **2018**, *30* (35), 1–9. https://doi.org/10.1002/adma.201801418.

(55) Hu, W.; Zhou, W.; Lei, X.; Zhou, P.; Zhang, M.; Chen, T.; Zeng, H.; Zhu, J.; Dai, S.; Yang, S.; Yang, S. Low-Temperature In Situ Amino Functionalization of TiO 2 Nanoparticles Sharpens Electron Management Achieving over 21% Efficient Planar Perovskite Solar Cells. *Adv. Mater.* **2019**. https://doi.org/10.1002/adma.201806095.

Chapter 4. Thermal Conductivity and Diffusivity of Triple-cation Perovskite Halide Materials for Solar Cells

In this chapter, we report on the measurement of the thermal conductivity and the thermal diffusivity by the technique of modulated thermoreflectance microscopy on a mixed-cation perovskite material [$Cs_{0.05}$(formamidinium$_{0.83}$methylammonium$_{0.17}$)$_{0.95}$Pb($I_{0.83}Br_{0.17}$)$_3$] widely applied for solution-processed perovskite solar cells. Such materials are supposed to present an improved thermal stability compared to methylammonium-based single cation perovskites. We measured a thermal conductivity k_{per} of 0.26 ± 0.03 W m^{-1} K^{-1} and a thermal diffusivity D_{per} of $3.5.10^{-7}$ ± 0.5 m^2 s^{-1}. The value for the thermal diffusivity was not reported previously.

4.1. Introduction

The main drawback of perovskite materials come from their stability over time, which limits their current development. These materials are very sensitive to humidity, ultraviolet light and temperature rises.[1,2] In particular, during their operation in front of the sunlight, the temperature of the cells can increase, causing an accelerated degradation. This is very problematic for methylammonium (MA)-based perovskites which appears to be thermally unstable[3] and that can degrade above ~358 K[4]. Recently, it has been observed that formamidinium (FA)-based cells exhibit a much larger stability than MA-based ones, making this compound very promising for future developments.[2] Yet FA-based perovskite halides suffer from the formation of amorphous phases at some I/Br ratio, the tuning of which is an efficient tool to modify the bandgap of the material. The addition of Cs^+ cation into the formulation and the formation of the triple mixed cation (MA-FA-Cs) perovskite halides can largely overcome the formation of amorphous phases facilitating a continuous tuning of bandgap by tuning the I/Br ratio while keeping the interesting thermal stability.[4]

In this chapter, we decided to study the thermal properties of triple mixed cation FA-MA-Cs-based perovskite solar cells.[1,5,6] More specifically, we have measured both their thermal conductivity and thermal diffusivity which are crucial parameters to predict how fast and how efficiently heat will dissipate in the active layer and toward the substrate. While several thermal conductivity measurements have already been performed on MA-based

compounds, very little data is available on triple-cation-based ones. Our measurements indicate that the thermal conductivity of such compounds is only slightly smaller than the one of MA-based perovskites found in literature, showing that the substitution of MA^+ by FA^+ and Cs^+ has a very limited influence on the thermal properties of these compounds. The experiments were carried out by modulated thermoreflectance microscopy (MTRM) on $Cs_{0.05}(FA_{0.83}MA_{0.17})_{0.95}Pb(I_{0.83}Br_{0.17})_3$ layers of different thicknesses and directly grown on a TiO_2/SnO_2:F/SiO_2 substrate, in a real solar cell configuration. The relative concentration of FA, MA and Cs was chosen to optimize the power conversion efficiency, the morphology of the grains and their stability.

4.2. Results and Discussion

4.2.1. Morphology, XRD and EDS Measurements of Perovskite Films

The structure of the cells is illustrated in **Fig. 1(a)**. A 50 nm-thick planar compact TiO_2 electron transport layer (ETL) was deposited by spin coating on fluorine-doped tin oxide (SnO_2:F or FTO) coated SiO_2 substrates of 500 nm thickness. We show in **Fig. 1(b)** a cross-sectional and in-plane scanning electron microscope (SEM) images of the 540 nm-thick perovskite surface. The crystalline $Cs_{0.05}(FA_{0.83}MA_{0.17})_{0.95}Pb(I_{0.83}Br_{0.17})_3$ was deposited by spin-coating on the substrate under different concentration and speed and five films were grown with perovskite thicknesses t_{per} equal to 250, 310, 400, 540 and 1000 nm respectively (the specific preparation details can be found in experimental chapter). The morphology of the perovskite layer based on corresponding thickness are shown in **Fig.2**. The size of the grains lies in the 100-300 nm range, in agreement with previous measurements performed on FA- and MA-based structures.[4,7,8] Finally, a 150 nm-thick gold film was then deposited on the perovskite layers for the thermal measurements.

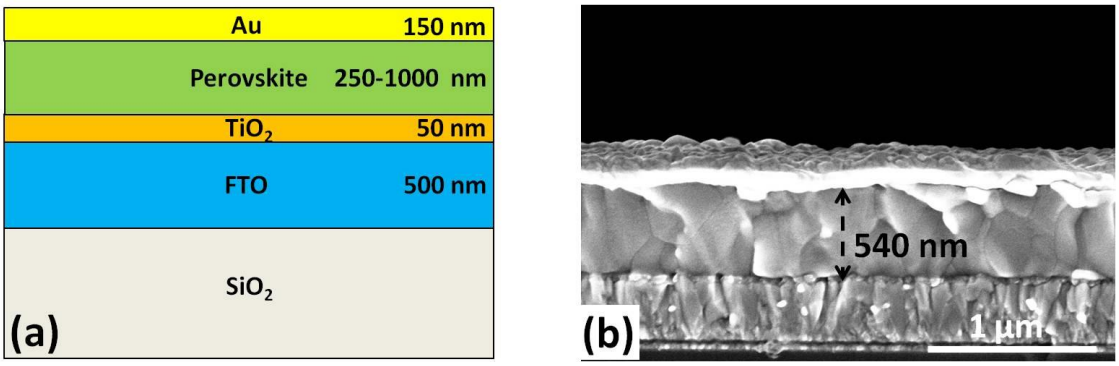

Figure 1: *Sketch of the solar cell structure (a), cross-sectional SEM image of the 540-nm thick perovskite structure (b).*

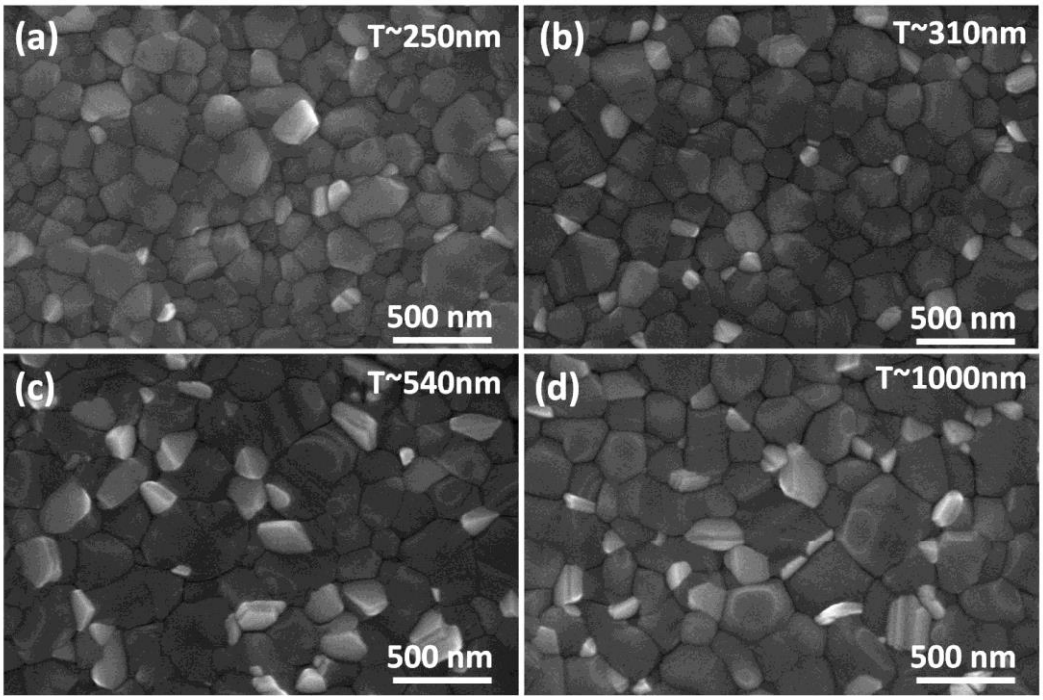

Figure 2*: SEM image of the surface of perovskite based on various thicknesses prior to Au deposition.*

To confirm the crystal structure of the perovskite layer, powder X-ray diffraction (XRD) spectra were obtained by a PANalytical X'Pert X-ray diffractometer using Cu-Kα radiation. The XRD pattern of the perovskite compound is shown in **Fig. 3**. The observed peaks are in agreement with XRD patterns observed in ref 9, 10 and 11 on a similar compound.[9–11]

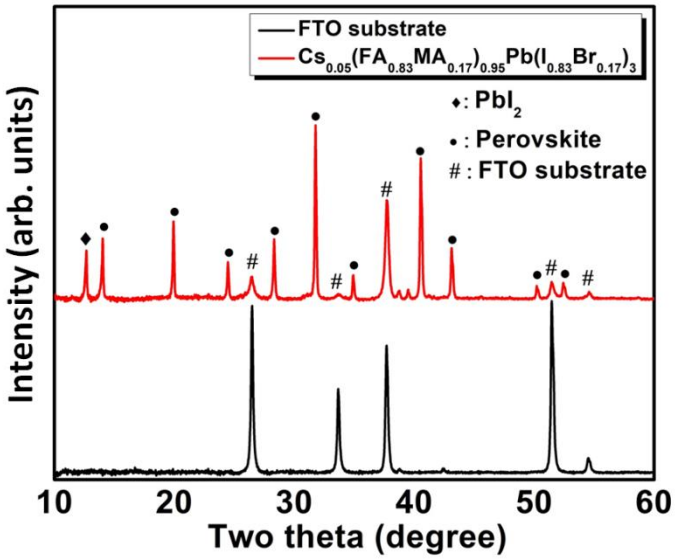

Figure 3: *X-ray diffraction (XRD) patterns of the perovskite film deposited on FTO glass substrate.*

In order to confirm the composition of perovskite films, energy dispersive X-ray spectroscopy (EDX) was used to detect and analyze the distribution and content of various elements. To perform EDX, the perovskite film was grown on a Si substrate which limits the number of unwanted elements compared to SiO_2/FTO/TiO_2. The results are shown in **Fig. 4.** The top-view SEM of the perovskite film is shown in **Fig. 4(a)**. In the EDX spectra analysis, shown in **Fig. 4(b)**, we observe clear signals that belong to I, Pb, Br, C, N and Cs elements. The Si element signal comes from the silicon substrate. The corresponding elemental mappings of the perovskite film and silicon substrate are presented in **Fig. 4(c-h)**. As we can see, the distribution of all the elements is homogenous on the substrate. The experimental weight percent of I, Pb, Br, and Cs elements (listed in **Table 1**) were normalized on the sum of the wt% from all elements in the perovskite formula except that from H (*i.e.* sum = I% + Br% + Pb% + C% + N% + Cs%). Please note that the wt% of H was not able to be measured accurately in EDX and the fact of ignoring the wt% of H may contribute to the difference observed in **Table 1** between the experimental and the theoretical values. Nevertheless, as indicated in **Table 1**, the obtained experimental wt% of these elements were reasonably close to the theoretical values calculated from the perovskite formula. We therefore conclude that the composition of the perovskite film prepared in this work is consistent with the $Cs_{0.05}(FA_{0.83}MA_{0.17})_{0.95}Pb(I_{0.83}Br_{0.17})_3$ formula assumed from the its synthesis method.

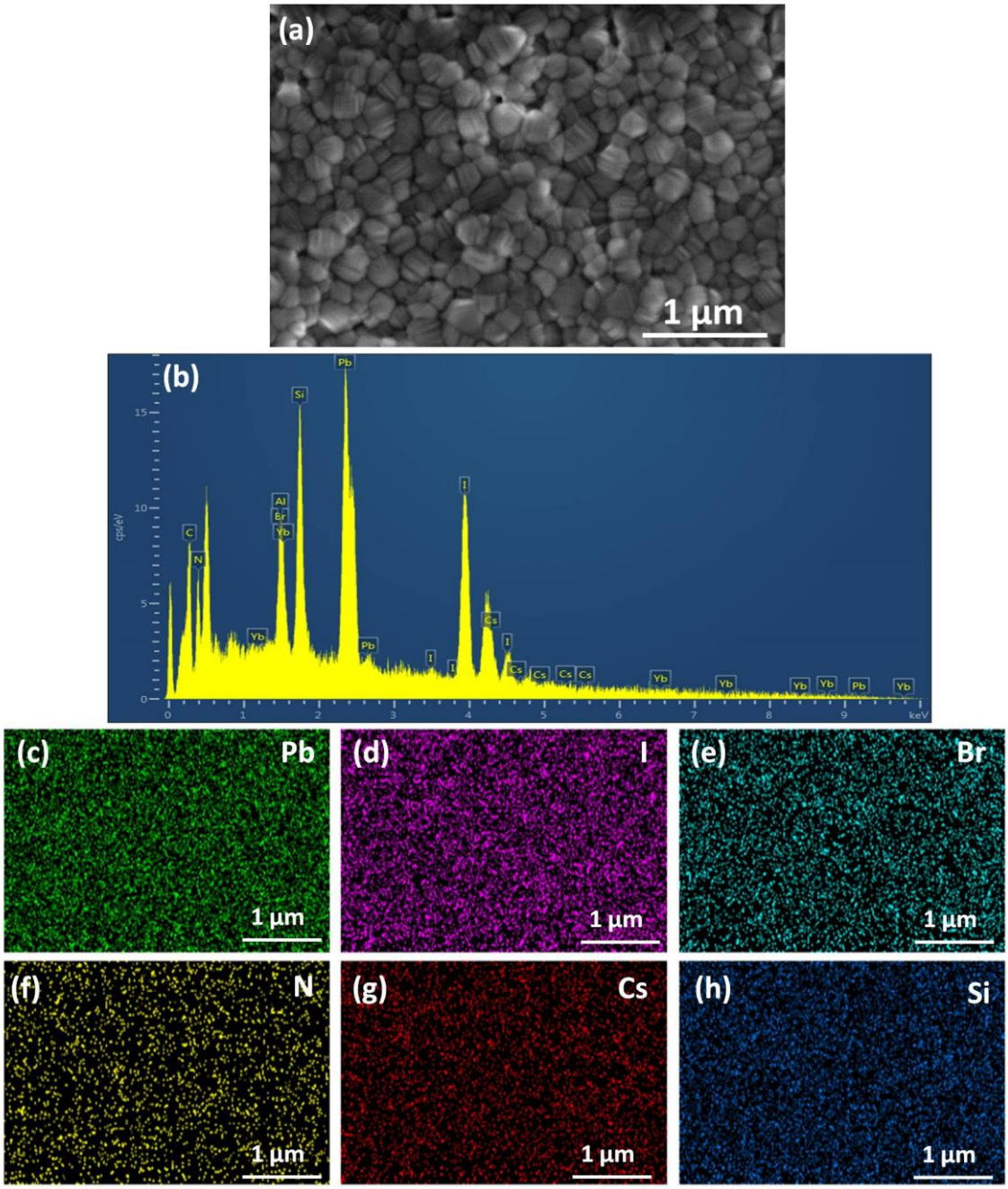

Figure 4: *SEM image (a) of a perovskite film together with EDS spectra (b) and elemental mappings of (c) Pb, (d) I, (e) Br, (f) N, (g) Cs, (h) Si on the same sample area, respectively.*

Table 1. *The weight percentages of I, Pb, Br and Cs elements obtained from the EDS spectra and from the formula.*

Sample	$I_{(wt\%)}/Br_{(wt\%)}$	$I_{(wt\%)}/Pb_{(wt\%)}$	$I_{(wt\%)}/N_{(wt\%)}$	$I_{(wt\%)}/Cs_{(wt\%)}$
Theory	7.75	1.53	12.98	47.56
EDS spectra	8.00	1.45	10.67	32.00

4.2.2. The Principle of Modulated Thermoreflectance Microscopy (MTRM) Measurement

MTRM measurements were carried out in a homemade optical microscope[12,13] whose principle is described in **Fig. 5**. A modulated pump beam (λ = 532 nm, P = 2 mW/μm^2) is focused on the sample surface on a ~1 µm size spot and heats the Au film locally and periodically (frequency f = 50-800 kHz). A CW probe beam (λ = 488 nm, P = 100 µW/μm^2) is also focused on the surface in a similar way. The heat created by the pump beam then diffuses laterally on the surface (r direction) and inside the different layers (z direction). This induces a periodic modulation of the surface temperature of the Au layer and then a periodic modulation of the Au reflection coefficient ΔR. The probe beam is detected by a silicon detector whose output is sent to a lock-in amplifier which can extract the amplitude ΔR and the phase $\Delta\phi$ of the modulated photoreflectance signal. During an experiment, the pump beam is progressively moved away from the probe beam, and ΔR and $\Delta\phi$ are measured as a function of their separation distance. These experiments were performed in the laboratory of Daniele Fournier (Institut des Nanosciences de Paris, Jussieu).

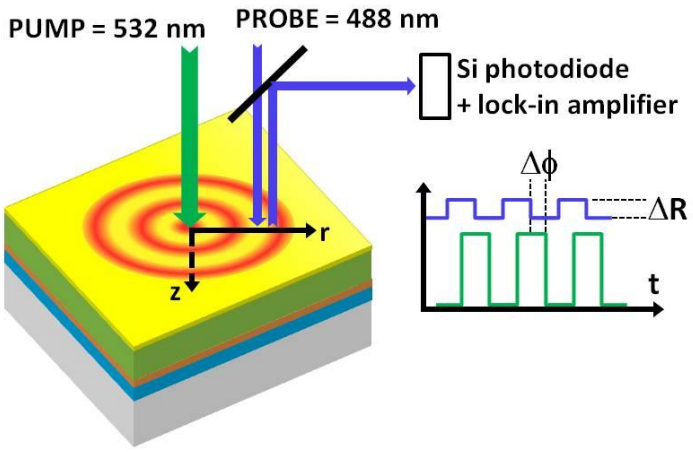

***Figure 5**: Sketch of the modulated photoreflectance experimental set-up.*

4.2.3. Thermal Diffusivity and Conductivity Computation upon Perovskite Films

To extract the thermal conductivity *k* and diffusivity *D* of the different layers in the structure, we used a thermal model similar to the one described in ref. 13. Both ΔR and Δϕ decrease as the distance between the two beams increases and the slopes of the curves are a function of *k* and *D* of the stack. Due to the circular symmetry of the pump laser spot on the surface, the heat diffusion equation is solved in cylindrical geometry using a Hankel transformation method. Here, we have to deal with several intermediate materials and layers (SiO_2, FTO, TiO_2, Au) whose thermal properties are usually known in the absolute in their bulk form but are in fact strongly dependent on the deposition conditions. We therefore performed a progressive analysis and first characterized the properties of the Au layer on the raw SiO_2 substrate by removing the FTO. Then, we successively studied the SiO_2/FTO/Au and the SiO_2/FTO/TiO_2/Au structures to extract the FTO and the TiO_2 thermal properties respectively. This layer by layer procedure minimizes the uncertainty on each material. The measured thermal conductivity *k* and thermal diffusivity *D* of Au, FTO and TiO_2 are summarized in Table I. No dependence on the excitation power was observed for these parameters during the experiments. The values are in reasonable agreement with the ones found in literature.[14–17]

Table 2. *Thermal parameters of the different underlying materials involved.*

Material	SiO_2	Au	FTO	TiO_2
k ($W.m^{-1}.K^{-1}$)	1.12	220	39	10
D ($10^{-7}\times m^2.s^{-1}$)	6.13	880	150	36

For TiO_2, we found a thermal conductivity value close to the one of the bulk. In fact, due to its small thickness, the influence of the TiO_2 layer is very weak and smaller values could have been used for fitting the data. Once all the sublayers were characterized, we then studied the entire cells which contain the mixed FA-MA perovskite. We followed the approach described in ref 12 in the case of lithium phosphorous oxynitrile films grown on a Si substrate. This methodology consists to first study the structures at high frequency (800 kHz) and then at low frequency (100 kHz). By varying the modulation frequency we change the thermal penetration depth. In that case, at 800 kHz, we can fit the experiment without taking into account the thickness of the perovskite layer which can be considered as infinite from a thermal point of view. When lowering the frequency and/or the thickness of the layer, the lower interface is reached by heat and the simulations have to take into account the interface perovskite/TiO_2.

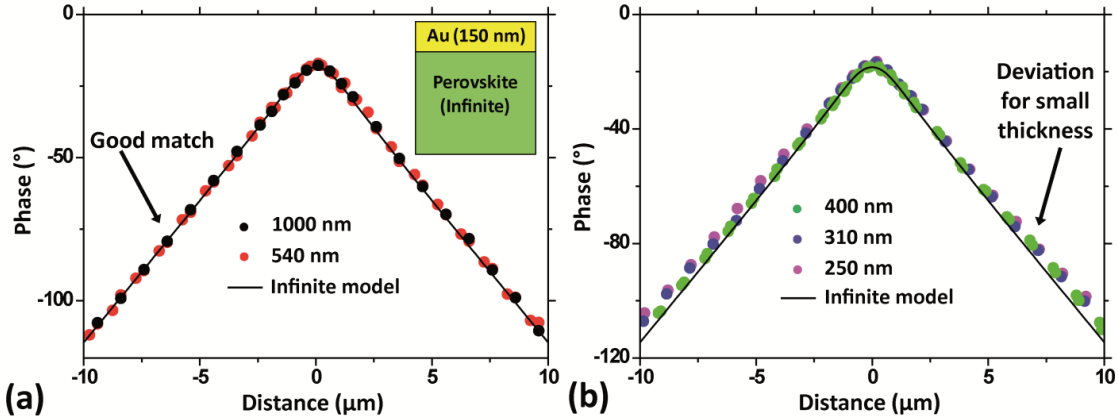

Figure 6: *Phase of the MTRM signal for t_{per} = 1000 nm and 540 nm (a) and for t_{per} = 400 nm, 310 nm, and 250 nm (b). On both graphs, the black curve represents a simulation with an infinite model.*

We show in **Fig. 6** the phase of the MTRM signal measured at high frequency (800 kHz) for all five thicknesses. Same curves were measured at different positions on the surface and in different directions, which shows a good uniformity and a weak sensitivity to an eventual anisotropy of the films. Note that the crystallites may be oriented differently from each other, but the measurement is averaged over the size of the laser spot. As seen in **Fig. 6(a)**, the experimental curves for t_{per} = 1 µm and t_{per} = 540 nm are superimposed. For this thickness range, this means that, at this frequency, the thickness of perovskite is not a parameter that influences heat diffusion. Perovskite is not a very good thermal conductor and heat does not reach the lower interface, and the structure behaves like an infinite material. Using an infinite model, we fitted the experimental data and found approximate values for the thermal conductivity and diffusivity of the perovskite layer: k_{per} = 0.22 W m^{-1} K^{-1} and D_{per} = 3.10^{-7} m^2 s^{-1}. Interestingly, for smaller thicknesses [see **Fig. 6(b)**], the infinite model does not fit anymore the experimental data. For these structures, heat reaches the interface between the perovskite and TiO_2, and the substrate cannot be neglected anymore. This enables us to have an idea of the thermal diffusion length μ which is given by $\mu = \sqrt{D/\pi f}$ where D and f are the thermal diffusivity and the frequency respectively. For D = 3.10^{-7} m^2 s^{-1} and f = 800 kHz, we find μ = 345 nm, a value which is consistent with the thickness of the perovskite layer below which the substrate cannot be ignored anymore. Another parameter we can extract from the fit of **Fig. 6(a)** is the thermal effusivity e of the perovskite layer which characterizes its ability to exchange thermal energy with its surroundings. Knowing that $e = k/\sqrt{D}$, we find e = 400 W m^{-2} K^{-1} s$^{1/2}$ which is a value similar to the one of a thermal insulator like wood and much smaller than the ones of metals.

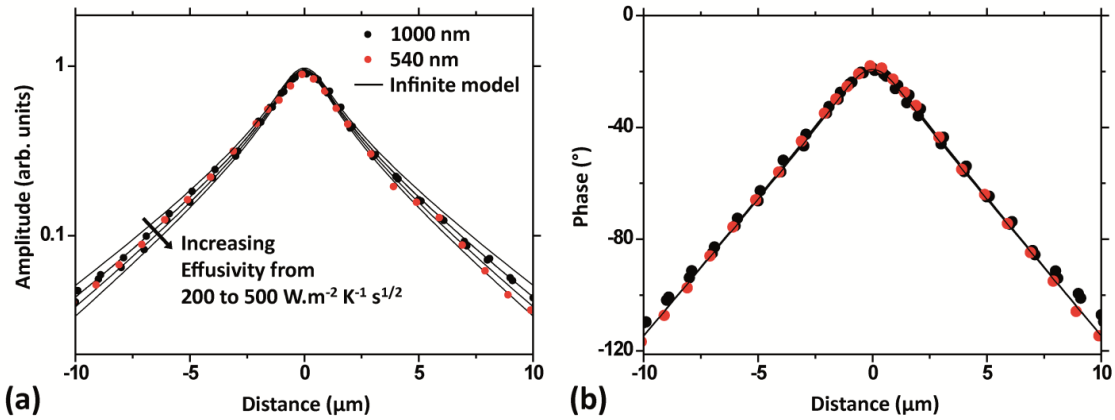

***Figure 7**: Amplitude (a) and Phase (b) of the MTRM signal for t_{per} = 1000 nm and 540 nm for different values of the effusivity. Circles: experimental values; lines: simulations considering an infinite model with e = 200, 300, 400, 500 W m^{-2} K^{-1} $s^{1/2}$.*

However, knowing the thermal effusivity does not allow to find *D* and *k*. The coupled parameters *D* and *k* are unfortunately not unique and good fits can also be obtained for slightly different values. An example showing the influence of *k* on the phase of the simulated curves for t_{per} = 1 µm and t_{per} = 540 nm is presented in **Fig.7.** Setting $D = 4.10^{-7}$ m^2 s^{-1} and varying *k* from 0.12 to 0.31 W m^{-1} K^{-1}, which corresponds to a variation of the effusivity between 200 and 500 W m^{-2} $K^{-1}s^{1/2}$, does not modify the simulated phase. The corresponding simulated amplitude ΔR slightly differs but the changes are not important enough to diminish the uncertainty of this measurement. To accurately determine the best values of *D* and *k*, we need to fit the data at smaller frequencies and on all the structures simultaneously. The thermal diffusion length μ increases with decreasing frequency (it varies like the square root of 1/*f*). For instance, μ is supposed to be a factor $\sqrt{8}$ larger at 100 kHz than at 800 kHz. In that case, the lower interfaces influence the MTRM signals and we cannot use anymore the semi-infinite model, we need to take into account the interfaces of all the materials present in the cell.

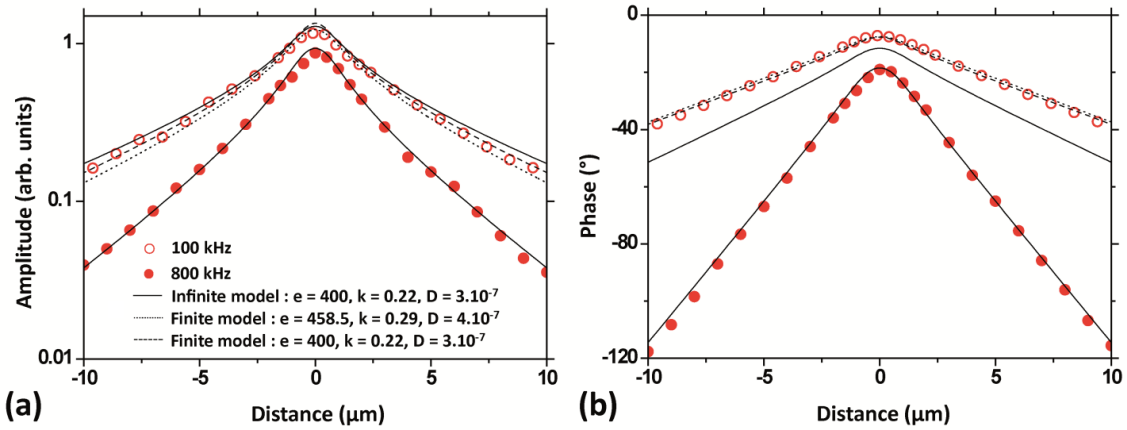

Figure 8: *Amplitude (a) and Phase (b) of the MTRM signal for t_{per} = 540 nm at 100 kHz and 800 kHz. Circles: experimental data. Lines: simulation with an infinite model (full lines) or with a finite model (dashed and dotted lines).*

We first focused on the sample of intermediate thickness (t_{per} = 540 nm). The experimentally measured amplitude and phase of the MTRM signal are represented in **Fig. 8** for two frequencies: 800 kHz (full red circles) and 100 kHz (thin red circles). Due to the larger diffusion length, the amplitude and phase measured at 100 kHz decrease more slowly than the 800 kHz ones. The infinite model (full lines), which describes well the experimental data at 800 kHz is no more accurate at 100 kHz, in particular on the phase which decreases too fast. A much better agreement is obtained with a model which takes into account the thickness of the layer, the interfaces and the different materials of the structure.[15] Good fits can be obtained for the couples of values k_{per} = 0.29 W m^{-1} K^{-1} / D_{per} = 4.10^{-7} m^2 s^{-1} which gives an effusivity e = 400 W m^{-2} K^{-1} s$^{1/2}$ and k_{per} = 0.22 W m^{-1} K^{-1} / D_{per} = 3.10^{-7} m^2 s^{-1} which gives e = 458.5 W m^{-2} K^{-1} s$^{1/2}$. For both couples of values, the phase variations are the same, but the amplitude is slightly different. From these fits, we now have a reasonable approximation of the value of the thermal conductivity and diffusivity of the perovskite material. In addition to the experiment on the 540 nm-thick sample, we checked and improved the accuracy of these values on thinner samples and at several frequencies between 50 kHz and 800 kHz.

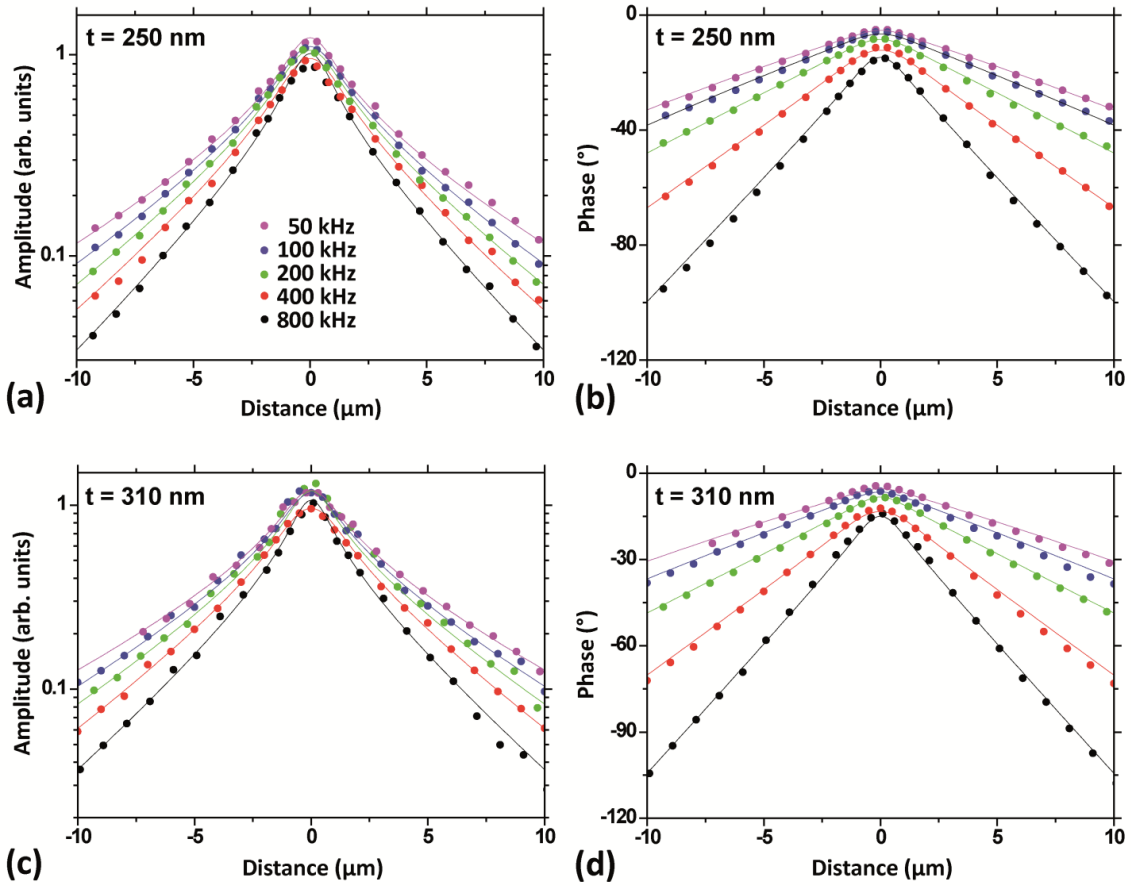

Figure 9: *Amplitude (a,c) and phase (b,d) of the MTRM signal for t_{per} = 250 nm and 310 nm, at 5 different frequencies. Full circles: experimental data, full lines: simulations with a finite model (k_{per} = 0.26 W m^{-1} K^{-1} D_{per} = 3.5.10^{-7} m^2 s^{-1} e = 439 W m^{-2} K^{-1} s$^{1/2}$).*

We show in **Fig. 9** the MTRM experiments carried out on 250 nm and 310 nm thick samples at five frequencies from 50 kHz to 800 kHz. The best agreement was found for k_{per} = 0.26 W m^{-1} K^{-1} and D_{per} = 3.5.10^{-7} m^2 s^{-1} which gives an effusivity e = 439 W m^{-2} K^{-1} s$^{1/2}$. The uncertainty was estimated to 0.03 W.m^{-1}.K^{-1} for k and 0.5.10^{-7} m^2 s^{-1} for D. Let us now compare the measured thermal conductivity to the values found in literature on similar thin film or bulk samples. As summarized in Table 3, most of the available data concern MA-based perovskites, not the mixed cation ones.[18–24] Apart from the results given in ref. 23, all thermal conductivities are found to be between 0.2 and 0.7. In our case, we find a value in the same range, showing that the incorporation of Cs and FA does not change the thermal properties compared to MA-based compounds.

Our measurements were performed on a series of samples of variable thickness without considering that *k* was thickness-dependent. We think this assumption is valid because the thinnest perovskite layer (250 nm) is not small enough to influence the scattering of phonons, whose mean free path is much smaller than the thickness of the polycrystalline perovskite layer.[25] In addition, Heiderhoff et al[22], observed that the thermal conductivity of several perovskite materials was nearly identical between the bulk and a 200 nm thin film. Finally, we observed by SEM that the perovskite layers were very similar for all samples, the size of the grains being nearly identical, which presumably discard the influence of the morphology on the materials thermal properties (see supplementary materials). Regarding the thermal diffusivity, we could not find a value for similar compounds in the literature to make a comparison. However, *k* and *D* are linked through the simple relation $k/D = \rho C$ where ρ is the density and *C* is the specific heat. The density of our material is not well known but since its molar mass (611.23 g/mol) is approximately the same than the one of $CH_3NH_3PbI_3$ (619.9 g/mol) we can speculate reasonably both materials have similar densities $\rho \sim 4000$ kg/m.[3, 26] From the previous relation, we can deduce the specific heat $C = 113.5$ J.K^{-1}.mol^{-1}, which is of the same order of magnitude than the one found in literature for many similar compounds ($C = 170 – 190$ J K^{-1} mol^{-1} for (MA)$PbBr_3$ and (MA)PbI_3 in ref. 27) thus confirming the accuracy of our values for *k* and *D*.[27]

Table 3*. Room temperature thermal conductivities of some MA- and FA-based perovskite materials.*

Material		k (W m^{-1} K^{-1})	Reference
Cs(FA,MA)Pb(IBr)$_3$	Thin film	0.26 ± 0.03	This work
$CH_3NH_3PbI_3$	Polycrystalline	0.3	Pisoni et al. [19]
$CH_3NH_3PbI_3$	Thin film	0.2-0.5	Guo et al. [18]
$CH_3NH_3PbI_3$	Thin film	0.33 ± 0.12	Heiderhoff et al. [24]
$CH_3NH_3PbBr_3$	Thin film	0.39 ± 0.05	Heiderhoff et al. [24]
$CH_3NH_3PbCl_3$	Thin film	0.50 ± 0.12	Heiderhoff et al. [24]
$CH_3NH_3PbI_3$	Thin film	11.2 ± 0.8	Chen et al. [23]
$CH_3NH_3PbI_3$	Polycrystalline	0.6	Kovalsky et al. [21]

$CH_3NH_3PbI_3$	Polycrystalline	0.6-0.7	Kovalsky et al. [22]
$CH_3NH_3PbI_3$	Nanowire	0.23	Wang et al. [25]
$CH_3NH_3PbBr_3$	Nanowire	0.3-0.35	Wang et al. [25]

4.3. Conclusion

In summary, we have measured by modulated thermoreflectance microscopy the thermal conductivity and thermal diffusivity of a recently developed mixed cation perovskite material, whose thermal stability is supposed to be improved compared to MA-based single cation perovskites. Our measurements were performed on a series of structures of variable thicknesses, of same morphologies, which strengthen the validity of our study. The value found for the thermal conductivity (k_{per} = 0.26 W m^{-1} K^{-1}) is of the same order than the one measured on MA-based perovskite materials. This shows that the thermal properties of such materials are almost the same whatever the nature of the cation. Therefore, the recently observed enhanced thermal stability of these triple-cation perovskites cannot be explained by a different value of their thermal conductivity or thermal diffusivity. The enhanced thermal stability of these perovskites may rather come from a chemical origin.

4.4. References

1. Wang, Z. *et al.* Efficient ambient-air-stable solar cells with 2D-3D heterostructured butylammonium-caesium-formamidinium lead halide perovskites. *Nat. Energy* **2**, 1–10 (2017).
2. Berhe, T. A. *et al.* Organometal halide perovskite solar cells: Degradation and stability. *Energy Environ. Sci.* **9**, 323–356 (2016).
3. Ava, T. T., Al Mamun, A., Marsillac, S. & Namkoong, G. A review: Thermal stability of methylammonium lead halide based perovskite solar cells. *Appl. Sci.* **9**, (2019).
4. McMeekin, D. P. *et al.* A mixed-cation lead mixed-halide perovskite absorber for tandem solar cells. *Science (80-.).* **351**, 151–155 (2016).
5. Yang, W. S., Park, B., Jung, E. H. & Jeon, N. J. Iodide management in formamidinium-lead-halide – based perovskite layers for efficient solar cells. **1379**, 1376–1379 (2017).
6. Yang, D. *et al.* High efficiency planar-type perovskite solar cells with negligible hysteresis using EDTA-complexed SnO2. *Nat. Commun.* **9**, (2018).

7. Cao, J., Tao, S. X., Bobbert, P. A., Wong, C. P. & Zhao, N. Interstitial Occupancy by Extrinsic Alkali Cations in Perovskites and Its Impact on Ion Migration. *Adv. Mater.* **30**, 1–9 (2018).

8. Schalkwijk, W. Van & Mater, N. High-performance photovoltaic perovskite layers fabricated through intramolecular exchange. **348**, 2013–2017 (2015).

9. Peng, J. *et al.* Efficient Indium-Doped TiOx Electron Transport Layers for High-Performance Perovskite Solar Cells and Perovskite-Silicon Tandems. *Adv. Energy Mater.* **7**, 1–10 (2017).

10. Saliba, M. *et al.* Cesium-containing triple cation perovskite solar cells: Improved stability, reproducibility and high efficiency. *Energy Environ. Sci.* **9**, 1989–1997 (2016).

11. Dong, J. *et al.* Annealing-Free Cr2O3 Electron-Selective Layer for Efficient Hybrid Perovskite Solar Cells. *ChemSusChem* **11**, 619–628 (2018).

12. Xu, F. *et al.* Lateral heat diffusion investigation of a layered structure: Application to the complete thermal characterization of a lithium phosphorous oxynitride film. *J. Appl. Phys.* **113**, (2013).

13. Frétigny, C., Roger, J. P., Reita, V. & Fournier, D. Analytical inversion of photothermal measurements: Independent determination of the thermal conductivity and diffusivity of a conductive layer deposited on an insulating substrate. *J. Appl. Phys.* **102**, (2007).

14. Qu, J., Wu, H., Cheng, P., Wang, Q. & Sun, Q. Recent advances in MEMS-based micro heat pipes. *Int. J. Heat Mass Transf.* **110**, 294–313 (2017).

15. Scott, E. A., Gaskins, J. T., King, S. W. & Hopkins, P. E. Thermal conductivity and thermal boundary resistance of atomic layer deposited high- k dielectric aluminum oxide, hafnium oxide, and titanium oxide thin films on silicon. *APL Mater.* **6**, (2018).

16. Hudaya, C., Jeon, B. J. & Lee, J. K. High thermal performance of SnO2:F thin transparent heaters with scattered metal nanodots. *ACS Appl. Mater. Interfaces* **7**, 57–61 (2015).

17. Jimenez-Olarte, D., Vigil-Galan, O., De la Rosa, J., Seuret-Jiménez, D. & Contreras-Puente, G. Laser scribing of fluorine doped tin oxide for serial interconnection of CdS/CdTe solar cells. *Rev. Mex. Fis.* **61**, 160–165 (2015).

18. Guo, Z., Yoon, S. J., Manser, J. S., Kamat, P. V. & Luo, T. Structural Phase- and Degradation-Dependent Thermal Conductivity of CH3NH3PbI3 Perovskite Thin Films. *J. Phys. Chem. C* **120**, 6394–6401 (2016).

19. Pisoni, A. *et al.* Ultra-low thermal conductivity in organic-inorganic hybrid perovskite CH3NH3PbI3. *J. Phys. Chem. Lett.* **5**, 2488–2492 (2014).

20. Wang, Y. *et al.* Cation Dynamics Governed Thermal Properties of Lead Halide Perovskite Nanowires. *Nano Lett.* **18**, 2772–2779 (2018).

21. Kovalsky, A., Wang, L., Guo, X., Dyck, J. S. & Burda, C. Temperature-dependent thermal conductivity study of MAPbI3: Using mild aging to reach a thermal percolation threshold for greatly improved heat transport. *J. Phys. Chem. C* **121**, (2017).

22. Kovalsky, A., Wang, L., Marek, G. T., Burda, C. & Dyck, J. S. Thermal Conductivity of CH3NH3PbI3 and CsPbI3: Measuring the Effect of the Methylammonium Ion on Phonon Scattering. *J. Phys. Chem. C* **121**, 3228–3233 (2017).

23. Chen, Q. *et al.* Efficient thermal conductance in organometallic perovskite CH3NH3PbI3 films. *Appl. Phys. Lett.* **108**, (2016).

24. Heiderhoff, R. *et al.* Thermal Conductivity of Methylammonium Lead Halide Perovskite Single Crystals and Thin Films: A Comparative Study. *J. Phys. Chem. C* **121**, 28306–28311 (2017).

25. Wang, M. & Lin, S. Anisotropic and Ultralow Phonon Thermal Transport in Organic–Inorganic Hybrid Perovskites: Atomistic Insights into Solar Cell Thermal Management and Thermoelectric Energy Conversion Efficiency. *Adv. Funct. Mater.* **26**, 5297–5306 (2016).

26. Stoumpos, C. C., Malliakas, C. D. & Kanatzidis, M. G. Semiconducting tin and lead iodide perovskites with organic cations: Phase transitions, high mobilities, and near-infrared photoluminescent properties. *Inorg. Chem.* **52**, 9019–9038 (2013).

27. Onoda-Yamamuro, N., Matsuo, T. & Suga, H. Calorimetric and IR spectroscopic studies of phase transitions in methylammonium trihalogenoplumbates (II)†. *J. Phys. Chem. Solids* **51**, 1383–1395 (1990).

Chapter 5. Optimizing Triple-cation Perovskite Solar Cells by Eliminating Excess PbI_2 from the Perovskite/Hole-transport-layer Interface

In this chapter, we investigate the effect of removing the excess PbI_2 from the surface of a triple-cation mixed-halide $Cs_{0.05}(FA_{0.83}MA_{0.17})_{0.95}Pb(I_{0.83}Br_{0.17})_3$ perovskite layer by four different organic salts on their photovoltaic performance and stability. We show that treatments with iodide salts such as methylammonium iodide (MAI) and formamidinium iodide (FAI) can lead to the strongest beneficial effects on solar cell efficiency, charge recombination suppression, and stability while non-iodide salts such as MABr and MACl can also provide improvements in terms of charge recombination suppression and stability to a moderate extent by comparison to the non-treated sample. In the most optimized cases, under continuous solar illumination, the MAI and FAI-treated devices maintained respectively 81% and 86% of their initial PCEs after 100 hours of continuous illumination (*v.s.* 64% for the non-treated solar cell with excess PbI_2). Our study demonstrates that eliminating the PbI_2 excess at the perovskite/HTL interface by treating the perovskite surface with organic salts is a simple and efficient route to enhance the efficiency and in particular the stability of perovskite solar cells.

5.1. Introduction

Various strategies are currently under extensive investigation in order to precisely control the crystallinity and the morphology of the perovskite layer and its interfaces with the transport layers aiming to obtain a highly crystalline, compact and smooth layer with large crystalline grains.[1] Very commonly, a slight increase in the PbI_2/methylammonium iodide (MAI) concentration ratio above the stoichiometric ratio of 1 was found to be beneficial for the photovoltaic performance.[2–5] The origin of this increase has been proposed to arise from various factors. For example, supported by computations,[6] the excess PbI_2 in perovskite films were believed to passivate defects at the perovskite grain boundaries and thus contribute to a lower carrier recombination.[7] Alternatively, the excess PbI_2 at the perovskite/electron-transport-layer (ETL) interface (e.g. TiO_2) was claimed to lead to lower carrier recombination at this interface,[2,8,9] facilitating electron injection into TiO_2[4,10] possibly

due to TiO_2 surface passivation and/or band-edge matching between TiO_2, PbI_2, and the perovskite. Similarly, at the perovskite/hole-transport-layer (HTL) interface, excess PbI_2 was proposed to facilitate hole injection, block electrons and reduce carrier recombination.[2,11]

Nevertheless, the beneficial effect of the excess PbI_2 remains controversial. By comparison to PbI_2-deficient perovskite samples, samples with excess PbI_2 exhibited more pronounced current-voltage hysteresis and significantly lower photostability.[12,13] Recently, it was identified that the excess PbI_2 is the culprit for the solar cell's accelerated degradation due to the photodecomposition of PbI_2 to metallic lead and volatile I_2 under continuous solar illumination.[14] Moreover, some reports show that excess in MAI, rather than PbI_2, is beneficial for device performance.[15,16] Following these reports several groups investigated a post-treatment process in which an MAI is introduced to the surface of the perovskite active layer, either by thermal evaporation[17] or spin-coated from solution[18] onto the surface of the perovskite layer generally resulting in an improvement of the photovoltaic performance. In light of these seemingly contradicting results, further understanding on the controversial role of the excess PbI_2 in perovskite solar cells is needed, particularly if one can decouple its effect in the bulk and at the interface.

In this work, based on mixed-cation and mixed-halide $Cs_{0.05}(FA_{0.83}MA_{0.17})_{0.95}Pb(I_{0.83}Br_{0.17})_3$ perovskite solar cells, we provide an experimental comparison on the photovoltaic behavior and the solar cell stability under continuous solar illumination between samples with a slight excess of unreacted PbI_2 (in the bulk and at the interface) and samples with the excess PbI_2 intentionally removed at the perovskite/HTL interface. Four different organic salts including iodide salts and non-iodide salts are applied to treat the perovskite film surfaces in order to remove the excess PbI_2. The resultant solar cell parameters and stability are compared by combining a series of structural, optical, and photovoltaic characterization methods. By simultaneously removing the surface excess PbI_2 and passivating surface iodide defects, treatments with iodide salts such as MAI and formamidinium iodide (FAI) lead to the strongest improvements on charge recombination reduction, solar cell efficiency and stability under continuous illumination by comparison to the non-treated sample. For treatments involving non-iodide salts such as MABr and MACl, which in principle remove surface excess PbI_2 without passivating surface iodide defects, the resultant perovskite solar cells exhibit also reduced charge recombination as well as clear improvements in terms of stability.

Our study indicates that, at the perovskite/HTL interface, the existence of excess PbI_2 is not beneficial for charge recombination suppression and the stability of the photovoltaic devices.

5.2. Results and Discussion

5.2.1. Top-View and Cross-Section SEM Measurements of Perovskite Films

Mixed-cation mixed-halide $Cs_{0.05}(FA_{0.83}MA_{0.17})_{0.95}Pb(I_{0.83}Br_{0.17})_3$ thin films were first prepared according to the procedure reported by Saliba et al.[19] According to this method, a precursor solution, where the sum of FA^+, MA^+, and Cs^+ is 1.26 mmol and the sum of Pb^{2+} is 1.3 mmol, was prepared leading to a slight excess of Pb^{2+} (about 3%). We then optimized the concentration of the precursor solutions while maintaining the proportion between each sub-constituent unchanged in order to maximize the average perovskite grain size which should offer a better endurance against degradation (details are described in the Experimental section). A 1mL precursor solution was prepared containing FAI (1 M), MABr (0.2 M), PbI_2 (1.1 M), and $PbBr_2$ (0.2 M) dissolved in a mixture of dimethylformamide (DMF) and dimethyl sulfoxide (DMSO) (4:1, v/v). 40 µL of a CsI stock solution in DMSO (1.5 M) was then added into the above precursor solution to achieve the $Cs_{0.05}(FA_{0.83}MA_{0.17})_{0.95}Pb(I_{0.83}Br_{0.17})_3$ composition. This precursor solution was defined here as concentration 1 (C1). Besides C1, more concentrated precursor solutions, representing 30%, 60%, and 90% more concentrated than C1, while maintaining the proportion between each sub-constituent unchanged, were also prepared and are defined here as C2, C3, and C4, respectively.

All prepared perovskite films were examined by X-ray diffraction (XRD), UV-Vis absorption, and scanning electron microscopy (SEM). As shown in **Figure 1** and **Figure 2**, samples fabricated from different precursor concentrations all exhibited typical perovskite diffraction peaks in agreement with previous reports. A small diffraction peak at 12.7° corresponds to the excess cubic PbI_2 residue in the perovskite film. In agreement with the measured UV-Vis absorbance (**Figure 4a**), the use of more concentrated precursor solution also leads to a thicker perovskite film and increased perovskite grain size. Functional perovskite solar cells were then fabricated based on these precursor concentrations on planar TiO_2 (cp-TiO_2)-coated fluorine doped tin oxide (FTO) glass substrates together with a layer of HTL of

2,2',7,7'-Tetrakis[N,N-di(4-methoxyphenyl)amino]-9,9'-spirobifluorene (Spiro-OMeTAD) and gold top contacts. An optimal precursor concentration was then identified from the photovoltaic characteristics of these devices (**Figure 4b** and **Table 1**) and will be applied in all the following experiments as the reference condition. In such an optimized condition, the average perovskite grain size was measured to be 376 nm (**Figure 2b**). Clearly visible from the SEM characterizations shown in **Figure 1 (a)**, those crystals showing a brighter SEM contrast than the rest of the film (sometimes referred as the "white phases" previously[20]) and often precipitated at perovskite grain boundaries are assigned as PbI_2 crystals according to previous studies.[20,21] The higher lead content in PbI_2 than in the perovskite phase leads to the brighter SEM contrast observed. Cross-section SEM characterizations on a typical perovskite solar cell by the optimized condition exhibited smooth interfaces with a majority of large perovskite grains protruding throughout the entire film thickness (**Figure 1(b)**).

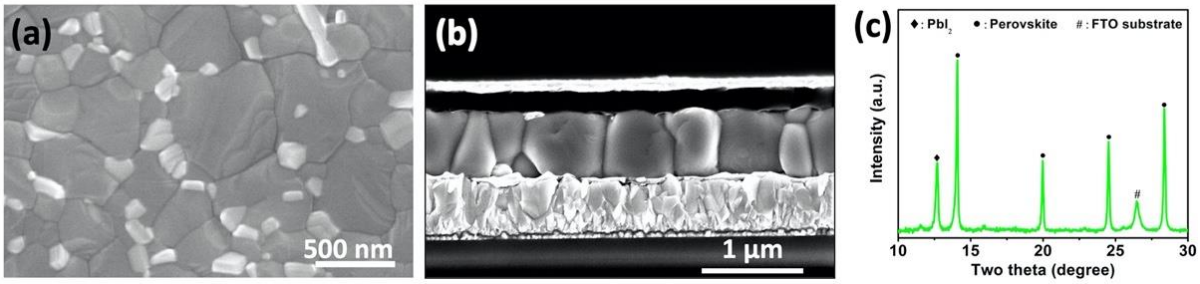

Figure 1. *(a) Morphologies revealed by SEM on the* $Cs_{0.05}(FA_{0.83}MA_{0.17})_{0.95}Pb(I_{0.83}Br_{0.17})_3$ *perovskite thin film on a FTO/glass substrate fabricated by the optimized precursor concentration (which will be used as the reference condition for the following experiments). (b) Cross-section SEM characterization of a completed perovskite solar cell. (c) XRD patterns of the perovskite thin film shown in (a).*

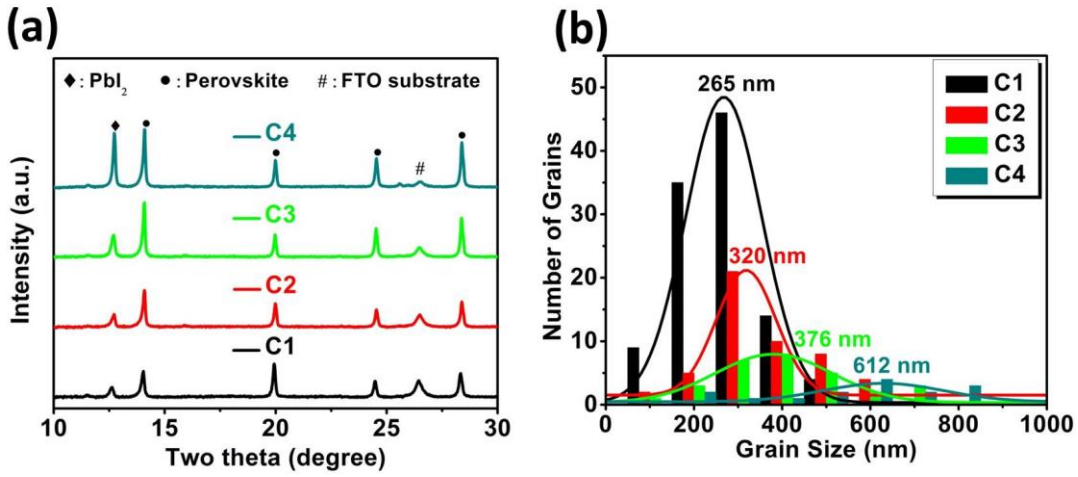

Figure 2. *(a) XRD patterns of the four* $Cs_{0.05}(FA_{0.83}MA_{0.17})_{0.95}Pb(I_{0.83}Br_{0.17})_3$ *perovskite thin films on FTO/glass substrates fabricated by the C1, C2, C3, and C4 precursor concentration. (b) The average grain size measured by scanning electron microscopy (SEM) on the four perovskite thin films fabricated by these conditions.*

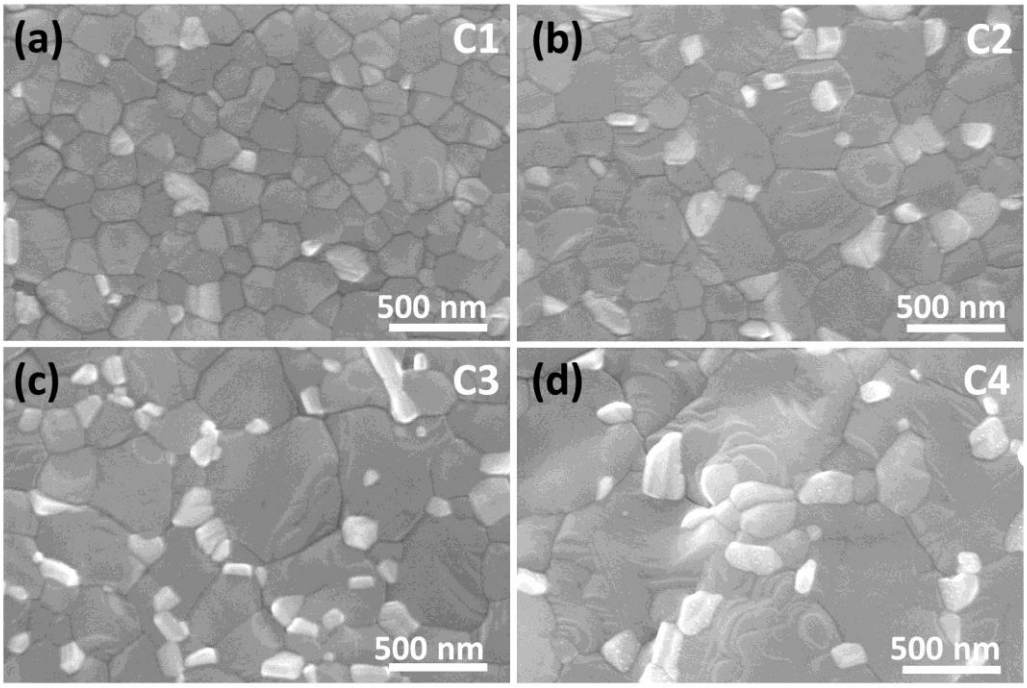

Figure 3. *(a, b, c, d) Morphologies revealed by SEM on the four perovskite thin films fabricated by these conditions.*

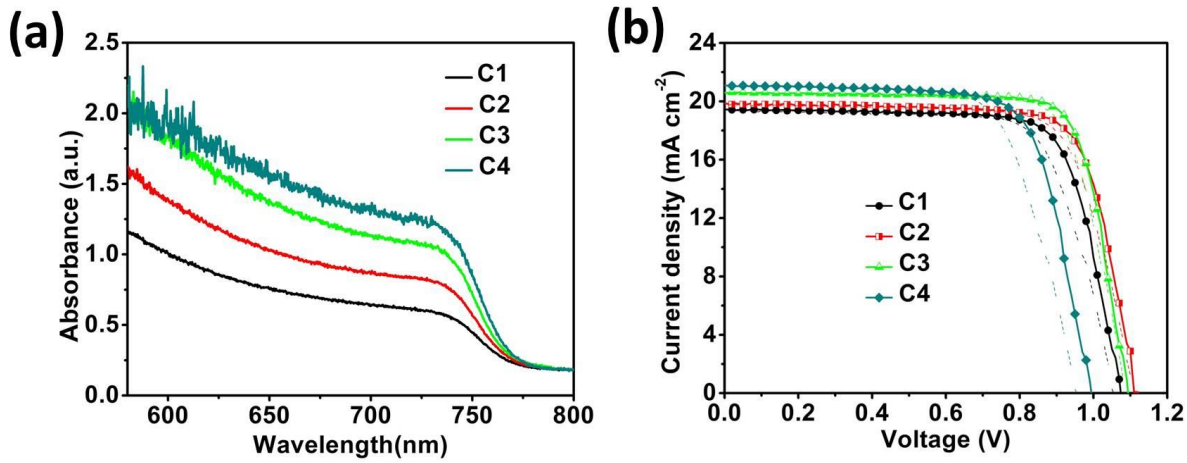

Figure 4. *(a) UV-Vis absorbance of the four perovskite thin films fabricated by these conditions. (b) Current-voltage (J-V) characteristics under simulated AM1.5G solar illumination (at 100 mW cm^{-2}) of four representative perovskite solar cells with their active layer fabricated by the C1, C2, C3, and C4 condition. Data from reverse scans (V_{oc} to 0V) are indicated by solid lines and symbols and those from forward scans (0V to V_{oc}) are indicated by dash lines.*

Table 1*. Summary of the Photovoltaic Characteristics of the Perovskite Solar Cells Fabricated by Different Precursor Concentrations*

Precursor Concentration	J_{sc} (mA cm^{-2})	V_{oc} (V)	FF (%)	PCE (%)
C1	19.44	1.08	74.48	15.64
C2	19.84	1.13	74.51	16.71
C3	20.60	1.10	77.50	17.56
C4	21.10	1.00	71.77	15.14

5.2.2. Morphology and Optical Properties of Absorber Layer after Post-Treatment

To selectively investigate the effect of eliminating PbI_2 from the perovskite/HTL interface and in contrast to the report by Kogo et al,[18] we used a dilute methylammonium halide (MAX) or FAI solution (1 to 4 mg/mL in isopropanol) that was spin-coated onto the perovskite surface, followed by a five-minute annealing at 100 °C (**Figure 5(a)**). Here, four different organic salts, including MAI, MABr, MACl, and FAI, were chosen in our experiments in order to distinguish the effect of surface iodide defect passivation from the effect of removing

the surface excess PbI_2. While we expect that the treatments of all these four salts on the perovskite film surface can lead to the removal of the excess PbI_2 crystals on the film surface, non-iodide salts were previously shown to be non-effective to passivate the iodide defects on perovskite surface.[22] SEM characterizations, after the treatments of these salt solutions at different concentrations, revealed a clear morphological change (**Figure 5 (b) to (m)**) by comparison to the reference sample (SEM image shown in **Figure 1(a)**). The excess PbI_2 crystals, which have a brighter SEM contrast than the rest of the film were completely eliminated from the perovskite surface after the samples were treated by a MAI or FAI solution with a minimum concentration of 2 mg/mL, or by a MABr or MACl solution with a minimum concentration of 4 mg/mL. As the objective here is to remove the surface excess PbI_2, these minimum salt concentrations were then applied in the experiments described below. Revealed by XRD, only a very small reduction of diffraction peak intensity for the PbI_2 phase (for example, 8929 counts by comparison to 9237 counts for the case of MAI treatment) was found when comparing samples before and after the treatments of salt solutions (**Figure 6**). This indicates that our treatment procedure by these four salts only removed the excess PbI_2 crystals on the surface of the perovskite film but not those in the bulk or at the bottom interface. UV-Vis absorbance spectrum was measured on the perovskite films before and after these surface treatments (**Figure 7**). FAI and MAI-treated perovskite films exhibited identical optical bandgaps by comparison to the reference sample (without any salt treatment). In contrast, the MABr and MACl surface treatments led to respectively a ~ 0.01 eV and 0.02 eV increase of optical bandgap of the perovskite film (**Figure 7** and **Figure 8**). This can be understood as result of the MABr and MACl surface treatments which transform the surface excess PbI_2 respectively into larger bandgap perovskites such as $MAPb(Br_xI_{3-x})$ and $MAPb(Cl_xI_{3-x})$ on the surface of the film. Atomic force microscopy (AFM) characterizations were also performed before and after these four organic salt surface treatments. Results reveal the same order-of-magnitude surface roughness on perovskite films before and after treatments (**Figure 9**). A slight reduction of surface roughness, from 18 nm on non-treated samples to 12 - 13 nm on treated samples, can be associated to the removal of the excess PbI_2 crystals on the film surface. Such a surface roughness change is however rather small when considering the total film thickness of about 640 nm. Perovskite films with their surfaces treated by these four organic salts revealed an enhanced photoluminescence (PL) intensity by comparison to the non-treated sample, with the FAI and MAI treatments

exhibiting the strongest effect (**Figure 10**). A slight shift of PL peak wavelength was observed on MABr and MACl-treated samples, which is coherent with the results of the slight bandgap changes on these samples observed in UV-Vis absorbance. These results suggest that, among the four organic salts, the dual functions provided by FAI and MAI treatments in terms of surface excess PbI_2 removal and surface iodide defect passivation likely have the strongest effect suppressing non-radiative recombination centers. By comparison, the MABr and MACl treatments, only removing the surface PbI_2, can also provide an intermediate PL intensity enhancement. This corroborates with recent calculations[23] which suggested that PbI_2-terminated perovskite surface is sensitive to surface defects which act as recombination centers and it is coherent with the device characteristics and stability results that will be discussed below.

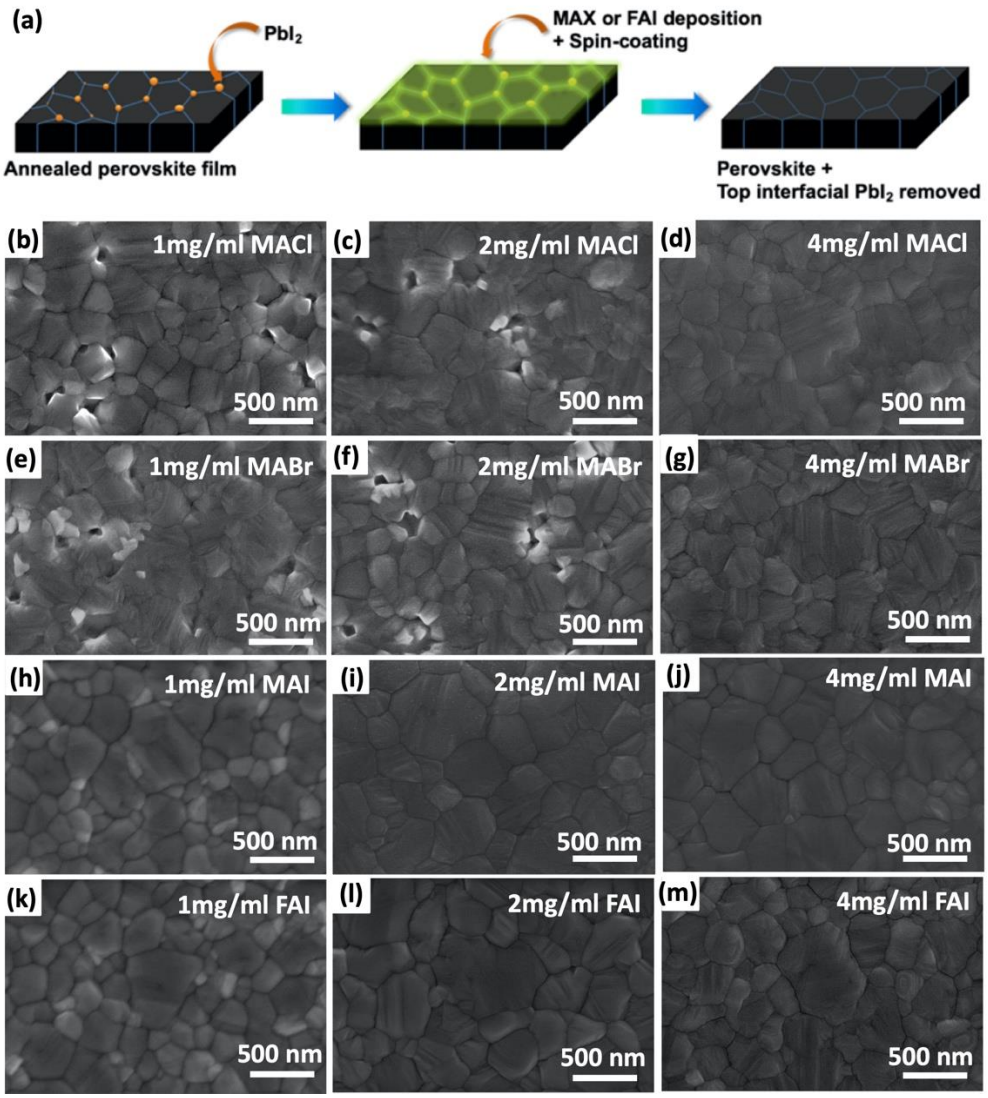

***Figure 5**. (a) Schematic illustration of treating the surface of perovskite films by methylammonium halide (MAX) or formamidinium iodide (FAI) solution in isopropanol and subsequent spin-coating to remove the excess PbI_2 at the top interface. (b - m) SEM characterizations of the $Cs_{0.05}(FA_{0.83}MA_{0.17})_{0.95}Pb(I_{0.83}Br_{0.17})_3$ perovskite film after (b, c, d) MACl, (e, f, g) MABr, (h, i, j) MAI, and (k, l, m) FAI isopropanol solution treatments with the organic salt concentration fixed at 1 mg/mL, 2 mg/mL, and 4 mg/mL.*

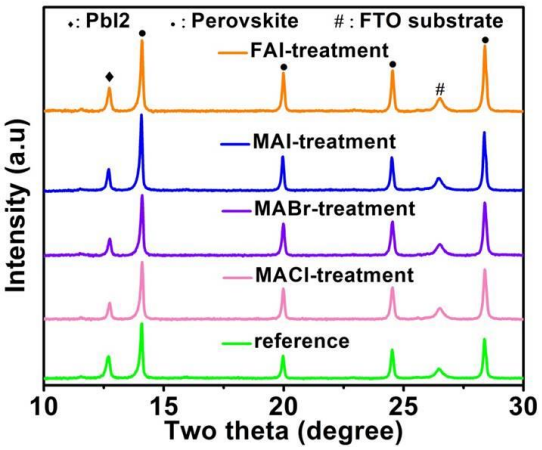

***Figure 6.** XRD spectrum of the $Cs_{0.05}(FA_{0.83}MA_{0.17})_{0.95}Pb(I_{0.83}Br_{0.17})_3$ perovskite thin films without (reference) and with the different organic salt solution surface treatments.*

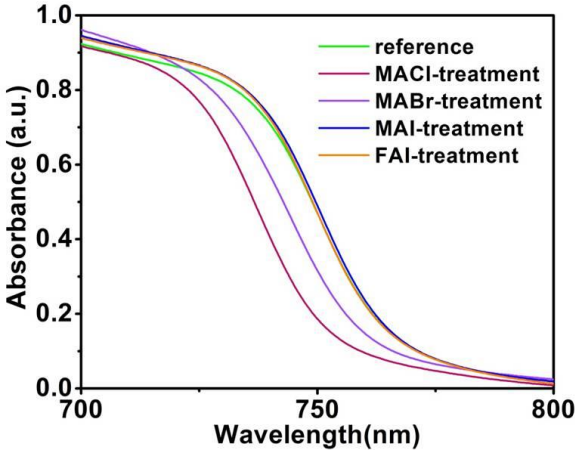

***Figure 7.** UV-Visible absorbanceof the $Cs_{0.05}(FA_{0.83}MA_{0.17})_{0.95}Pb(I_{0.83}Br_{0.17})_3$ perovskite thin films without (reference) and with the different organic salt solution surface treatments.*

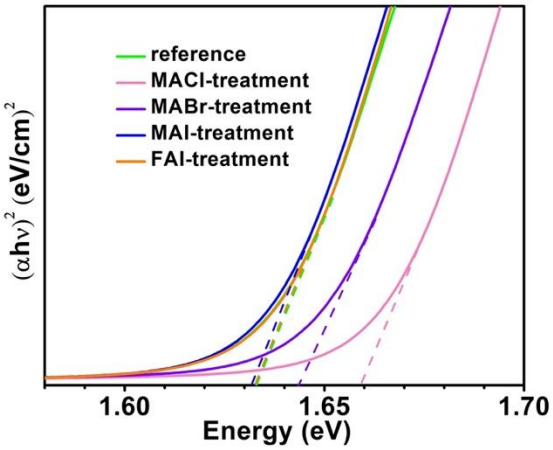

Figure 8*. Tauc plots obtained from UV-Vis absorbance data displayed in the* ***Figure 7*** *of the main text. These plots reveal a near identical optical bandgap for the perovskite films treated by MAI or FAI, and a 0.01 eV and 0.02 eV increase of optical bandgap associated with the MABr and the MACl treatment, respectively.*

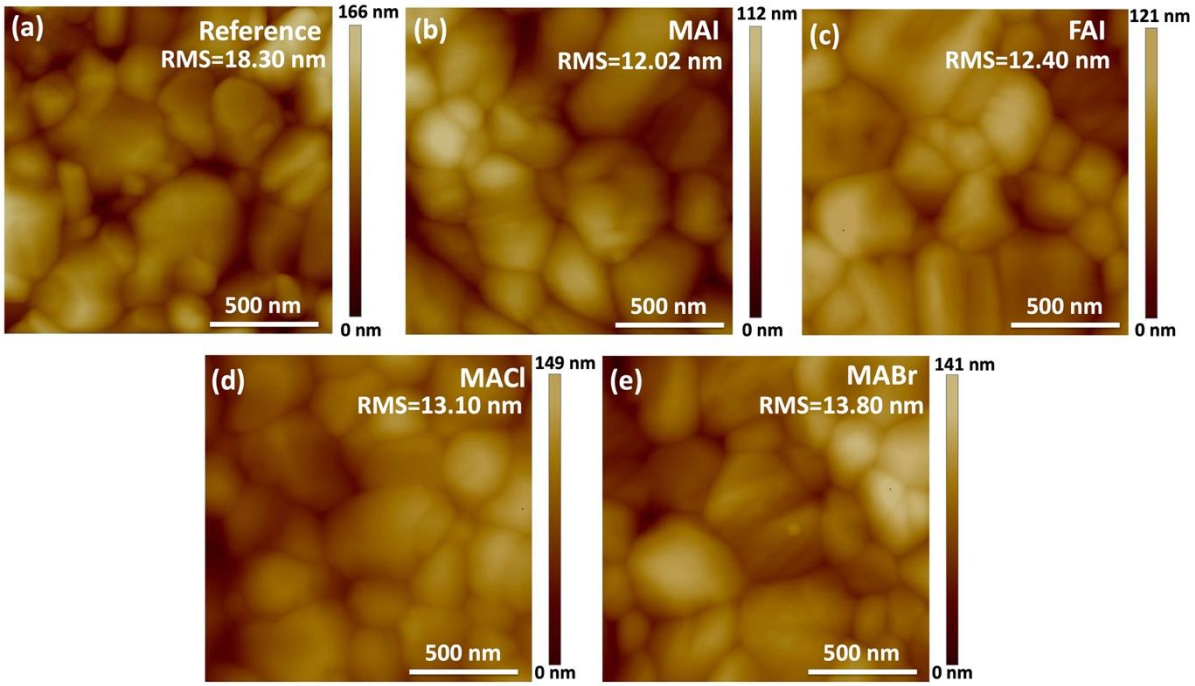

Figure 9*. Atomic force microscopy (AFM) characterizations on the same* $Cs_{0.05}(FA_{0.83}MA_{0.17})_{0.95}Pb(I_{0.83}Br_{0.17})_3$ *perovskite thin film before (a) and after (b) the MAI, (c) the FAI, (d) the MACl, and (e) the MABr surface treatment.*

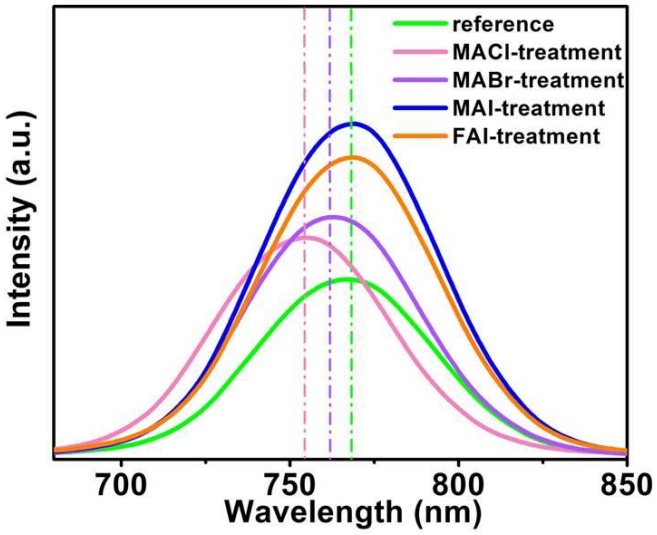

Figure 10. *photoluminescence (PL) (excitation λ = 365 nm) of the $Cs_{0.05}(FA_{0.83}MA_{0.17})_{0.95}Pb(I_{0.83}Br_{0.17})_3$ perovskite thin films without (reference) and with the different organic salt solution surface treatments. Dotted lines indicate the slight shift of PL peak wavelength.*

5.2.3. Photovoltaic Performance of the Devices with Small Molecular Modification

After removing the excess PbI_2 crystals from the surface of the perovskite film by these organic salt treatments, we completed the solar cell fabrication by depositing a layer of Spiro-OMeTAD as the HTL and a layer of gold as the top electrode. The current-voltage ($J-V$) characteristics, measured under 100 mW cm^{-2} AM 1.5G simulated illumination, of the best-performing perovskite solar cells with and without different organic salt treatments are shown in **Figure 11** and **Table 2**, with the statistics of the photovoltaic parameters shown in **Figure 12**. By comparison to the reference sample without salt treatments, the MAI and FAI-treated solar cells exhibit a clear improvement of photovoltaic performance. Specifically, there is an increase of the solar cell J_{sc}, from 20.60 mA cm^{-2} for the reference sample to 21.12 mA cm^{-2} for MAI-treated and 21.16 mA cm^{-2} for the FAI-treated sample, as well as an increase of FF from 77.50% to 79.29% for the MAI-treated and 78.60% for the FAI-treated sample. A combination of both leads to respectively a 7% and 5% increase of PCE for the MAI and FAI-treated solar cell compared to the reference sample. As there was no change of optical bandgap in the perovskite film associated with the MAI and FAI treatment (**Figure 7**),

the increase of J_{sc} observed likely originates from a slightly enhanced absorption due to the transformation of the surface excess PbI_2 into a perovskite phase and/or more charges being able to make their way to the electrodes due to reduced recombination loss. For MABr and MACl-treated samples, they exhibit a similar PCE by comparison to the reference sample. Specifically, there is a slight reduction of J_{sc}, from 20.60 mA cm^{-2} for the reference sample to 20.19 mA cm^{-2} for the MACl-treated and 20.32 mA cm^{-2} for the MABr-treated sample, together with a slight increase of V_{oc} from 1.10 V to 1.14 V for the MACl-treated and 1.13 V for the MABr-treated sample. These observations are coherent with the slight increase of perovskite optical bandgap associated with the treatments with these two salts (**Figure 7**). The external quantum efficiency (EQE) spectra measured on the optimal devices treated by different organic salts are shown in **Figure 11b**. The short-circuit current densities obtained from integrating their EQE spectra with the AM 1.5G spectrum are in good agreement (with < ± 0.2 mA cm^{-2} of difference) by comparison to the J_{sc} measured in the $J-V$ curves.

To gather further insights into the charge transfer and recombination processes in these devices, they were investigated via electrochemical impedance spectroscopy (EIS) and light-intensity-dependent measurements. **Figure 13a** shows the Nyquist plots of the perovskite solar cells with and without different organic salt treatments, measured in dark with an external bias holding at their respective V_{oc}. The measured EIS spectra can be fitted well using an equivalent circuit model previously applied on perovskite solar cells (shown in the inset of **Figure 13(a)**).[24,25] The inner series resistance (R_s), charge transport resistance (R_{tr}), and the recombination resistance (R_{rec}) obtained from fitting the experimental data are listed in **Table 2**. By comparison to the non-treated sample, one can observe that there is a clear increase of recombination resistance together with a decrease of charge transport resistance associated with the treatments of different organic salts. Among the four salts applied, MAI and FAI lead to the most significant effects with the recombination resistance of the solar cell increased from 1590 Ω (non-treated) to 3665 Ω for the MAI-treated and 3410 Ω for the FAI-treated sample, and with the charge transport resistance reduced from 115.9 Ω to 50.9 Ω for the MAI-treated and 68.8 Ω for the FAI-treated sample. For the MABr and MACl treated samples, similar trends of increased recombination resistance and decreased transport resistance are also observed by comparison to the non-treated sample but their effects are not as important as the treatment of MAI and FAI. These EIS results are coherent with the light-intensity-dependent V_{oc} measurement results shown in **Figure 13(b)**. Such

light-intensity-dependent V_{oc} measurements have been applied previously to reveal the dominant recombination mechanisms in perovskite solar cells.[26,27] The slope of V_{oc} over the natural logarithm of light intensity ($\frac{\delta V_{oc}}{\delta \ln(I_{light})}$) being kT/q indicates the dominant bimolecular recombination, whereas such slope being 2kT/q indicates the dominant trap-assisted recombination. Our results exhibit a decrease of such a slope associated with the application of any of these four salt treatments on the perovskite film surface, with the MAI and FAI treatments leading to the strongest effect decreasing the slope from 2.05 kT/q to 1.65 kT/q for the MAI treatment and 1.68 kT/q for the FAI treatment. A strong reduction of trap-assisted recombination in these MAI and FAI-treated samples should originate from their dual roles, which removes the excess surface PbI_2 and at the same time passivate surface iodide defects. Interestingly, the MABr and MACl-treated samples also exhibit a moderate decrease of ($\frac{\delta V_{oc}}{\delta \ln(I_{light})}$), from 2.05 kT/q to 1.80 kT/q for the MABr treatment and 1.82 kT/q for the MACl treatment. As these non-iodide salts could not passivate surface iodide defects which were considered as the dominating defects of the perovskite surfaces,[22] our observation suggests that the removal of the surface excess PbI_2 alone can help to alleviate trap-assisted recombination. Indeed, such PbI_2 crystallites might hinder charge transport at that interface due to the formation of charge transport barriers[12] and recent calculations[23] even suggested that PbI_2-terminated perovskite surface being recombination centers. Consequently, the removal of the surface excess PbI_2 can result in the formation of a more intimate perovskite interface with the HTL reducing charge recombination and improving charge transfer to the transport layer.

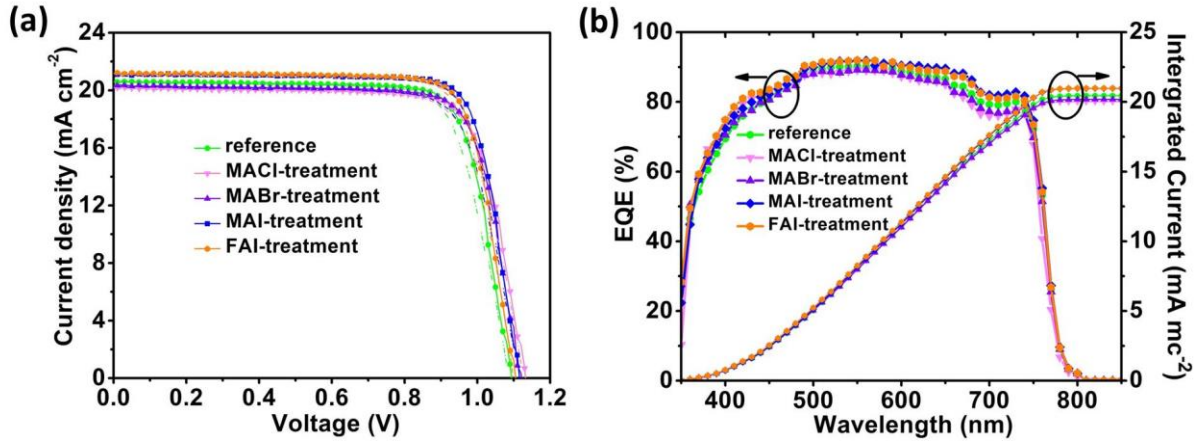

Figure 11. ***(a)*** *Current density−voltage (J−V) photovoltaic characteristics measured on the* $Cs_{0.05}(FA_{0.83}MA_{0.17})_{0.95}Pb(I_{0.83}Br_{0.17})_3$ *perovskite solar cells, with the device architecture shown in* ***Figure 1(b)****, fabricated with MACl, MABr, MAI, or FAI surface treatment by comparison to the reference sample (without treatment), under 100 mW* cm^{-2} *AM 1.5G illumination. The solid dots and lines indicate results from the reverse scan (from* V_{oc} *to* J_{sc}*), and the dash lines indicate results from forward scan (from* J_{sc} *to* V_{oc}*).* ***(b)*** *EQE spectra for the perovskite solar cells shown in (a) and the corresponding integrated* J_{sc} *of the devices.*

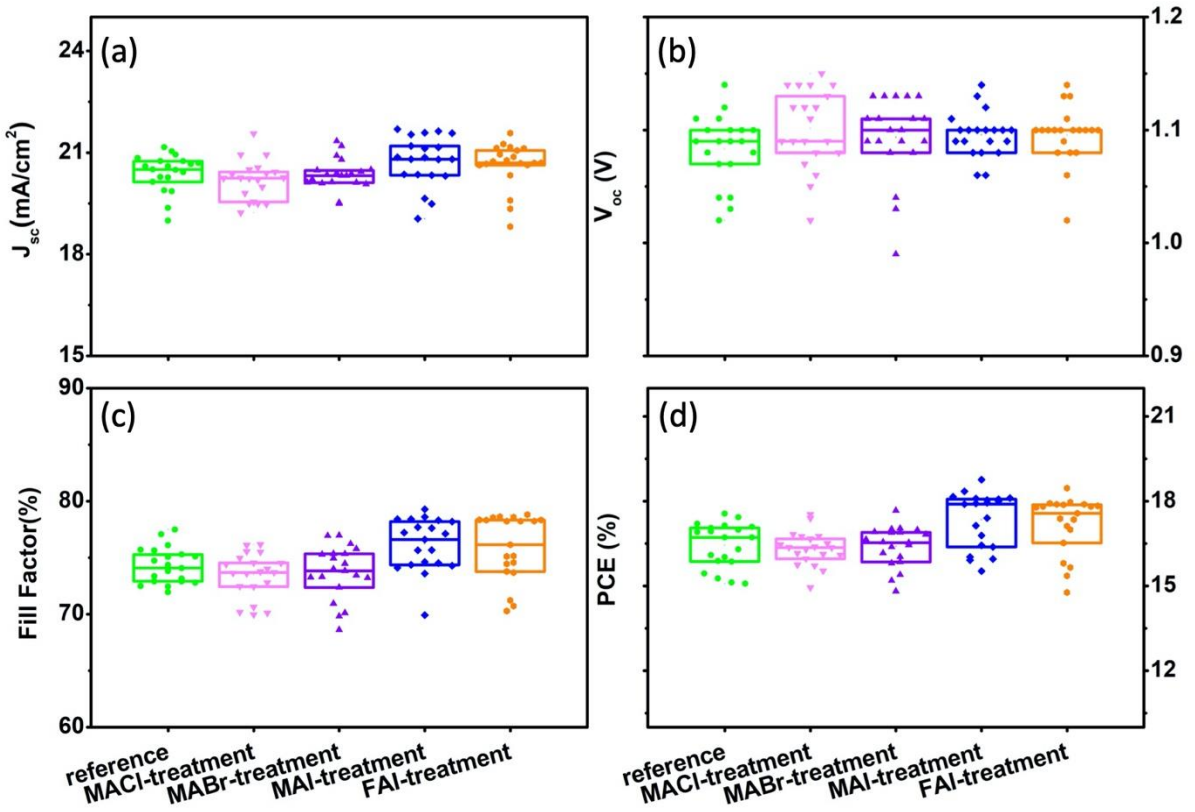

Figure 12. *Photovoltaic parameters of the* $Cs_{0.05}(FA_{0.83}MA_{0.17})_{0.95}Pb(I_{0.83}Br_{0.17})_3$ *Perovskite Solar Cells Fabricated with and without the Surface Treatments of Different Organic Salts.*

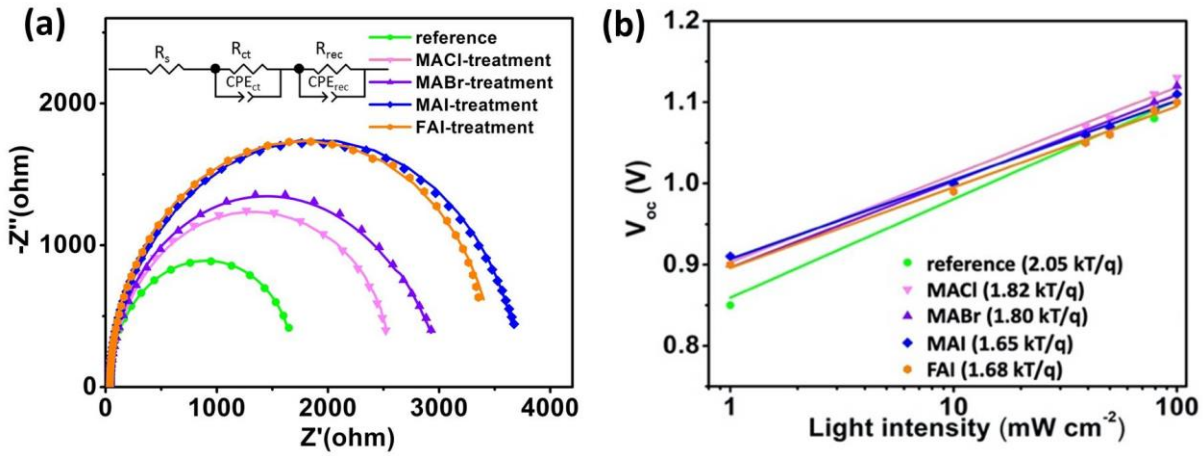

Figure 13*. (a) Typical Nyquist plots (symbols) obtained from the perovskite solar cells shown in (**Figure 11**a) tested in the dark and at their V_{oc}. The solid lines represent the fits obtained by applying the equivalent circuit shown in the inset. (b) Light intensity dependence of V_{oc} for these solar cells. The filled symbols and lines represent experimental data and numerical fits, respectively. Fitted values of the slope of V_{oc} over the natural logarithm of light intensity ($\frac{\delta V_{oc}}{\delta ln(I_{light})}$) are indicated inside the bracket of the label for each curve.*

Table 2. Summary of the Photovoltaic Characteristics of the $Cs_{0.05}(FA_{0.83}MA_{0.17})_{0.95}Pb(I_{0.83}Br_{0.17})_3$ Perovskite Solar Cells, with the Device Architecture Shown in Figure 1(b), Fabricated with and without the Surface Treatments of Different Organic Salts.[a]

Sample	J_{sc} (mA cm^{-2})	V_{oc} (V)	FF (%)	PCE (%)	R_s (Ω)	R_{tr} (Ω)	R_{rec} (Ω)
Reference	20.60	1.10	77.50	17.56	30.77	115.94	1590
MACl	20.19	1.14	76.17	17.53	28.34	75.93	2475
MABr	20.32	1.13	76.97	17.67	27.12	70.96	2895
MAI	21.12	1.12	79.29	18.76	26.76	50.89	3665
FAI	21.16	1.11	78.60	18.46	27.81	68.79	3410

[a]Results are presented together with the parameters (inner series resistance R_s, charge transport resistance R_{tr}, and recombination resistance R_{rec}) obtained from fitting the electrochemical impedance spectroscopy results. J_{sc}: short-circuit current density; V_{oc}: open-circuit voltage; FF: fill factor; PCE: power conversion efficiency.

To illustrate the versatility of salt treatments, we applied the same MAI treatment described above, which led to the strongest effect on the improvement of $Cs_{0.05}(FA_{0.83}MA_{0.17})_{0.95}Pb(I_{0.83}Br_{0.17})_3$ perovskite solar cell efficiency, into the same type of triple cation perovskite solar cells but with an inverted device structure of glass/indium tin oxide (ITO)/poly[bis(4-phenyl)(2,4,6-trimethylphenyl)amine] (PTAA)/poly[(9,9-bis(3'-(N,N-dimethylamino)propyl)-2,7-fluorene)-*alt*-2,7-(9,9-dioctylfluorene)] (PFN)/perovskite/[6,6]-phenyl-C_{61}-butyric acid methyl ester (PCBM)/bathocuproine (BCP)/silver. As shown in **Figure 14a** and **Table 3**, the MAI treatment clearly improves the photovoltaic performance, leading to a maximum PCE of 20.03% for the treated sample by comparison to the PCE of the non-treated sample (19.45%). From the statistics made from the same batch of inverted solar cells (**Figure 14(b)**), one can observe a clear improvement of J_{sc} and a slight augmentation of V_{oc} associated with the MAI treatment, which is coherent with

reduced trap-assisted recombination by such a treatment observed above from the EIS and light-intensity measurements.

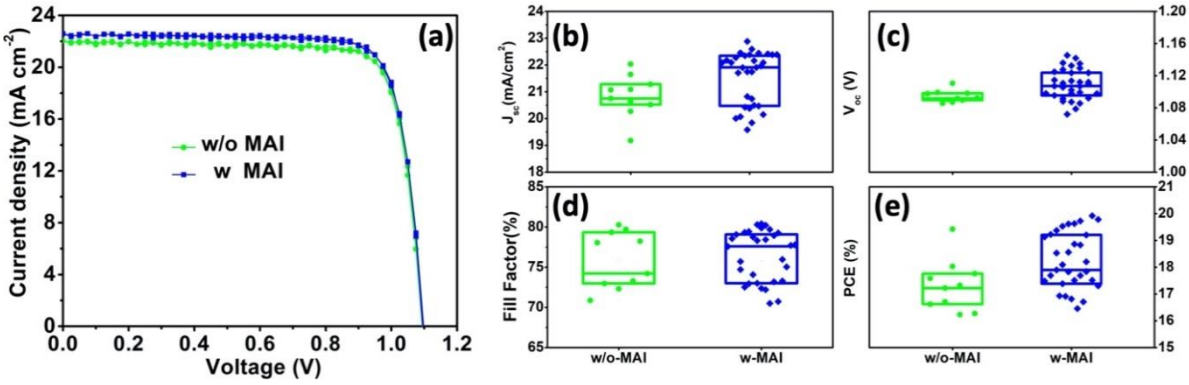

Figure 14. *(a) Current density−voltage (J−V) photovoltaic characteristics measured on the best performing* $Cs_{0.05}(FA_{0.83}MA_{0.17})_{0.95}Pb(I_{0.83}Br_{0.17})_3$ *perovskite solar cells with an inverted device architecture (glass/ITO/PTAA/PFN/perovskite/PCBM/BCP/silver) with and without the MAI treatment on the perovskite film surface, under 100 mW* cm^{-2} *AM 1.5G illumination. (b) The short-circuit current (*J_{sc}*), (c) open-circuit voltage (*V_{oc}*), (d) fill factor (FF), and (e) power conversion efficiency (PCE) of the same batch of* $Cs_{0.05}(FA_{0.83}MA_{0.17})_{0.95}Pb(I_{0.83}Br_{0.17})_3$ *perovskite solar cells with this inverted architecture with and without the MAI treatment on the perovskite film surface.*

Table 3. *Summary of the Photovoltaic Characteristics of the* $Cs_{0.05}(FA_{0.83}MA_{0.17})_{0.95}Pb(I_{0.83}Br_{0.17})_3$ *Perovskite Solar Cells Fabricated by An Inverted Architecture (glass/ITO/PTAA/PFN/perovskite/PCBM/BCP/silver) with and without the MAI Treatment on the Perovskite Film Surface.*

Samples		J_{sc} (mA cm-2)	V_{oc} (V)	FF (%)	PCE (%)
Reference (w/o. MAI)	Average	20.85 ± 0.79	1.09 ± 0.01	75.92 ± 3.53	17.32 ± 0.96
	Best (reversea)	22.03	1.10	80.27	19.45
	Best (forwardb)	22.03	1.09	80.69	19.38
w. MAI treatment	Average	21.53 ± 0.98	1.11 ± 0.02	75.81 ± 4.76	18.11 ± 1.37
	Best (reverse)	22.59	1.10	80.29	19.95
	Best (forward)	22.59	1.10	80.60	20.03

[a] Reverse scan (from V_{oc} to J_{sc}); [b] Forward scan (from J_{sc} to V_{oc})

5.2.4. Stability of the Perovskite Devices

After studying the impacts of these organic salt surface treatments on the perovskite solar cell photovoltaic parameters, we proceed to characterize their effects on solar cell stability. In recent years it has been increasingly recognized that the enhancement of the photovoltaic stability of perovskite solar cells is a critically important prerequisite to their integration into industrial applications.[28–30] Perovskite materials and solar cells have been shown to be sensitive to environmental factors such as oxygen[31] or water,[32] as well as unavoidable exposure to light and temperature.[33,34] A common point of these four organic salts is that they can all eliminate the perovskite/HTL interfacial excess PbI_2 of the solar cell, with the MAI and FAI treatments capable to passivate surface iodide defects at the same time. Unencapsulated perovskite solar cells with and without these salt surface treatments were measured under continuous AM 1.5G simulated solar illumination at 100 mW cm^{-2} inside an Ar-filled glovebox for 100 hours. A global view of these solar cell degradation characteristics under continuous illumination is shown in **Figure 15(a)**. One can notice that, for the non-treated sample, the degradation can be described roughly in two stages: (i) A fast "burn-in" degradation, resulting a PCE drop to 77.4% of its initial value, happening during the first two hours (**Figure 15(b)**); (ii) A much slower degradation after this burn-in stage until the end of the experiment when one measured a PCE of 63.5% of its initial value after 100 hours of illumination. Remarkably, by comparison to the non-treated sample, solar cells treated by these four organic salt treatments all exhibit significantly less severe burn-in degradation, with the strongest effect observed in the MAI and FAI-treated cases: For example, after the first two-hours' degradation, the MAI, FAI, MABr and MACl-treated samples exhibited only a slight PCE drop to 98.0%, 98.0%, 96.2%, and 92.1% of their initial values, respectively. Concerning the longer-term degradation after the first two-hours, the slow degradation behaviors until the end of the experiment of the salt-treated samples are similar to that of the non-treated case. Nevertheless, mainly due to the degradation improvement made during the burn-in stage, after 100 hours of degradation, the PCE of the MAI, FAI, MABr and MACl-treated solar cells still remained respectively 81.2%, 85.7%, 77.1%, and 75.1% of their initial values, which is significantly higher than the non-treated reference sample. The strong beneficial effect by the MAI and FAI surface treatments can be understood as the combined consequence of interfacial excess PbI_2 removal and surface iodide defect passivation. Interestingly, even without passivating surface iodide defects, just

by removing the interfacial excess PbI_2 through the MABr or MACl treatments, a clear improvement of perovskite solar cell degradation behavior can already be observed, in particular for the early burn-in stage. A possible origin of this enhancement can be related to the decomposition of PbI_2 under continuous illumination into iodine (gaseous phase) and metallic lead, which act as recombination centers capable to accelerate degradation.[14]

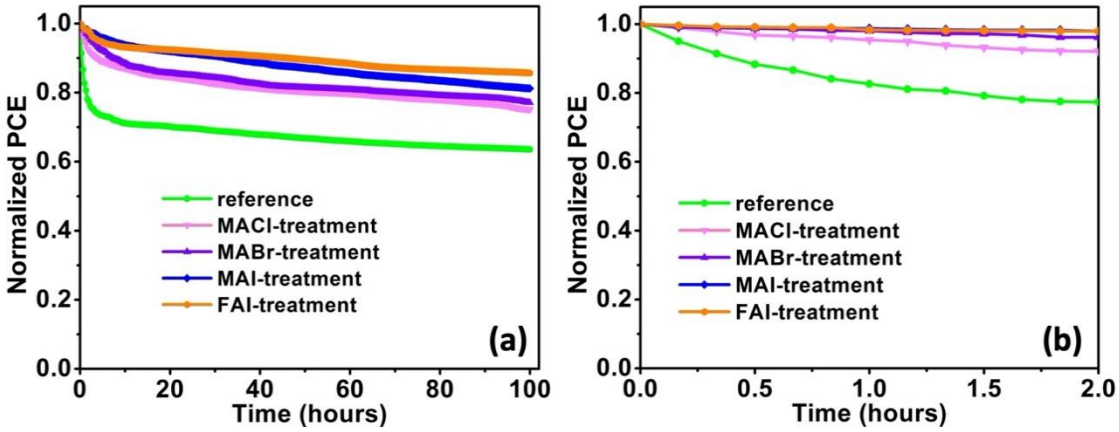

Figure 15. *(a) Efficiency evolution over 100 hours of the unencapsulated* $Cs_{0.05}(FA_{0.83}MA_{0.17})_{0.95}Pb(I_{0.83}Br_{0.17})_3$ *perovskite solar cells, fabricated with the device architecture shown in* ***Figure 1(b)****, with the MAI (blue), FAI (orange), MABr (purple), and MACl (pink) surface treatments by comparison to the reference solar cell without treatment (green) under continuous AM 1.5G illumination at 100 mW* cm^{-2} *measured inside an Ar-filled glovebox. (b) The zoom-in view of (a) for the first two hours of degradation.*

5.3. Conclusion

In summary, we investigated the role of interfacial PbI_2 excess in $Cs_{0.05}(FA_{0.83}MA_{0.17})_{0.95}Pb(I_{0.83}Br_{0.17})_3$ perovskite solar cells on their photovoltaic performance and stability. Four different organic salts, MAI, FAI, MABr, and MACl, were applied in a diluted solution to treat the perovskite film surface in order to remove the excess surface PbI_2 and the resultant device characteristics were compared. Treatments with iodide salts, such as MAI and FAI, provided the strongest improvements in terms of solar cell efficiency, charge recombination suppression, and device stability under continuous illumination by comparison to the non-treated sample, which is likely linked to their dual effects in terms of surface excess PbI_2 removal and surface iodide defect passivation. Treatments with non-iodide salts,

such as MABr and MACl, which remove surface excess PbI_2 without passivating iodide defects, can also provide a clear improvement in terms of charge recombination suppression and device stability. In the most optimized cases, under continuous solar illumination, the MAI and FAI-treated devices maintained respectively 81% and 86% of their initial PCEs after 100 hours of continuous illumination (*v.s.* 64% for the non-treated solar cell with excess PbI_2). Our results show that eliminating PbI_2 at the perovskite/HTL interface by organic salt treatments is highly beneficial for both the efficiency and stability of perovskite devices and can be easily implemented during their fabrication process.

5.4. References

1. Dubey, A. *et al.* A strategic review on processing routes towards highly efficient perovskite solar cells. *J. Mater. Chem. A* **6**, 2406–2431 (2018).
2. Chen, Q. *et al.* Controllable Self-Induced Passivation of Hybrid Lead Iodide Perovskites toward High Performance Solar Cells. *Nano Lett.* **14**, 4158–4163 (2014).
3. Kim, Y. C. *et al.* Beneficial Effects of PbI 2 Incorporated in Organo-Lead Halide Perovskite Solar Cells. *Adv. Energy Mater.* **6**, 1–8 (2016).
4. Roldán-Carmona, C. *et al.* High efficiency methylammonium lead triiodide perovskite solar cells: the relevance of non-stoichiometric precursors. *Energy Environ. Sci.* **8**, 3550–3556 (2015).
5. Jiang, Q. *et al.* Surface passivation of perovskite film for efficient solar cells. *Nat. Photonics* **13**, 460–466 (2019).
6. Haruyama, J., Sodeyama, K., Han, L. & Tateyama, Y. Termination Dependence of Tetragonal CH 3 NH 3 PbI 3 Surfaces for Perovskite Solar Cells. *J. Phys. Chem. Lett.* **5**, 2903–2909 (2014).
7. Wang, L., McCleese, C., Kovalsky, A., Zhao, Y. & Burda, C. Femtosecond Time-Resolved Transient Absorption Spectroscopy of CH 3 NH 3 PbI 3 Perovskite Films: Evidence for Passivation Effect of PbI 2. *J. Am. Chem. Soc.* **136**, 12205–12208 (2014).
8. Nakayashiki, S., Daisuke, H., Ogomi, Y. & Hayase, S. Interface structure between titania and perovskite materials observed by quartz crystal microbalance system. *J. Photonics Energy* **5**, 057410 (2015).
9. Cao, D. H. *et al.* Remnant PbI 2 , an unforeseen necessity in high-efficiency hybrid perovskite-based solar cells? *APL Mater.* **2**, 091101 (2014).
10. Somsongkul, V. *et al.* Hole blocking PbI 2 /CH 3 NH 3 PbI 3 interface. *Phys. status solidi - Rapid Res. Lett.* **08**, 763–766 (2014).
11. Calloni, A. *et al.* Stability of Organic Cations in Solution-Processed CH 3 NH 3 PbI 3 Perovskites: Formation of Modified Surface Layers. *J. Phys. Chem. C* **119**, 21329–21335 (2015).

12. Jacobsson, T. J. *et al.* Unreacted PbI2 as a Double-Edged Sword for Enhancing the Performance of Perovskite Solar Cells. *J. Am. Chem. Soc.* **138**, 10331–10343 (2016).

13. Liu, F. *et al.* Is Excess PbI 2 Beneficial for Perovskite Solar Cell Performance? *Adv. Energy Mater.* **6**, 1502206 (2016).

14. Tumen‐Ulzii, G. *et al.* Detrimental Effect of Unreacted PbI 2 on the Long‐Term Stability of Perovskite Solar Cells. *Adv. Mater.* 1905035 (2020). doi:10.1002/adma.201905035

15. Bi, D. *et al.* Morphology Engineering: A Route to Highly Reproducible and High Efficiency Perovskite Solar Cells. *ChemSusChem* **10**, 1624–1630 (2017).

16. Fassl, P. *et al.* Fractional deviations in precursor stoichiometry dictate the properties, performance and stability of perovskite photovoltaic devices. *Energy Environ. Sci.* **11**, 3380–3391 (2018).

17. Hawash, Z. *et al.* Interfacial Modification of Perovskite Solar Cells Using an Ultrathin MAI Layer Leads to Enhanced Energy Level Alignment, Efficiencies, and Reproducibility. *J. Phys. Chem. Lett.* **8**, 3947–3953 (2017).

18. Kogo, A., Miyadera, T. & Chikamatsu, M. Tuning Methylammonium Iodide Amount in Organolead Halide Perovskite Materials by Post-Treatment for High-Efficiency Solar Cells. *ACS Appl. Mater. Interfaces* **11**, 38683–38688 (2019).

19. Saliba, M. *et al.* Cesium-containing triple cation perovskite solar cells: Improved stability, reproducibility and high efficiency. *Energy Environ. Sci.* **9**, 1989–1997 (2016).

20. Jiang, Q. *et al.* Planar‐Structure Perovskite Solar Cells with Efficiency beyond 21%. *Adv. Mater.* **29**, 1703852 (2017).

21. Chen, Y. *et al.* Mechanism of PbI 2 in Situ Passivated Perovskite Films for Enhancing the Performance of Perovskite Solar Cells. *ACS Appl. Mater. Interfaces* **11**, 44101–44108 (2019).

22. Aristidou, N. *et al.* Fast oxygen diffusion and iodide defects mediate oxygen-induced degradation of perovskite solar cells. *Nat. Commun.* **8**, 1–10 (2017).

23. Ambrosio, F., Meggiolaro, D., Mosconi, E. & De Angelis, F. Charge localization and trapping at surfaces in lead-iodide perovskites: the role of polarons and defects. *J. Mater. Chem. A* **8**, 6882–6892 (2020).

24. Hu, Z. *et al.* TiO 2 Nanocolumn Arrays for More Efficient and Stable Perovskite Solar Cells. *ACS Appl. Mater. Interfaces* **12**, 5979–5989 (2020).

25. Feng, J. *et al.* Record Efficiency Stable Flexible Perovskite Solar Cell Using Effective Additive Assistant Strategy. *Adv. Mater.* **30**, 1–9 (2018).

26. Zhao, D. *et al.* High-Efficiency Solution-Processed Planar Perovskite Solar Cells with a Polymer Hole Transport Layer. *Adv. Energy Mater.* **5**, 1401855 (2015).

27. Sherkar, T. S. *et al.* Recombination in Perovskite Solar Cells: Significance of Grain Boundaries, Interface Traps, and Defect Ions. *ACS Energy Lett.* **2**, 1214–1222 (2017).

28. Bush, K. A. *et al.* Thermal and Environmental Stability of Semi-Transparent Perovskite Solar Cells for Tandems Enabled by a Solution-Processed Nanoparticle Buffer Layer and Sputtered ITO Electrode. *Adv. Mater.* **28**, 3937–3943 (2016).

29. Hoffmann, L. *et al.* Spatial Atmospheric Pressure Atomic Layer Deposition of Tin Oxide as an Impermeable Electron Extraction Layer for Perovskite Solar Cells with Enhanced Thermal Stability. *ACS Appl. Mater. Interfaces* **10**, 6006–6013 (2018).

30. Wang, R. *et al.* A Review of Perovskites Solar Cell Stability. *Adv. Funct. Mater.* **29**, 1808843 (2019).

31. Sun, Q. *et al.* Role of Microstructure in Oxygen Induced Photodegradation of Methylammonium Lead Triiodide Perovskite Films. *Adv. Energy Mater.* **7**, 1700977 (2017).

32. Wang, Q. *et al.* Scaling behavior of moisture-induced grain degradation in polycrystalline hybrid perovskite thin films. *Energy Environ. Sci.* **10**, 516–522 (2017).

33. Divitini, G. *et al.* In situ observation of heat-induced degradation of perovskite solar cells. *Nat. Energy* **1**, 15012 (2016).

34. Li, Y. *et al.* Light-Induced Degradation of CH 3 NH 3 PbI 3 Hybrid Perovskite Thin Film. *J. Phys. Chem. C* **121**, 3904–3910 (2017).

Chapter 6. Nanostructuration and Near-Field Optical Study of Perovskite Thin Films for Er/Yb Doped Solar Cells

In this chapter, we have studied the effect of nanostructuration on the local optical properties of perovskite thin films used in the fabrication of hybrid solar cells. Our aim is to incorporate up-converting fluorescent nanocrystals on the surface, to excite them at λ = 975 nm, and to boost their visible fluorescence thanks to the nanostructuration, in order to improve the solar cell absorption. The perovskite surface was engraved with a focused ion beam to form gratings of one-dimensional grooves. By scanning structures as a function of the grooves depth, ranging from 100 nm to 200 nm, we observed that a 3-fold fluorescence enhancement could be obtained for a depth of 200 nm. In addition, we also studied the influence of the inhomogeneities of the perovskite layer and we observed that the roughness tends to locally modify the intensity of the fringes and to distort their alignment.

6.1. Introduction

Thin films-based solar cells are nowadays the subject of intense research efforts due to their remarkable properties.[1,2] Compared to bulk materials, the small amount of matter involved in thin film fabrication makes them very competitive in terms of costs, waste and pollution, and regarding the amount of energy needed to produce them. In addition, the possibility of using thin films for making flexible devices opens the way to develop new applications such as curtains, backpacks, clothes and other day to day items. On the further development of perovskite solar cells, one of the strategies is based on optical optimization. For that, many approaches have been proposed using micro and nanostructures able to modify the incident plane wave by scattering within the active layer or by trapping and concentrating light in high intensity near-field zones. Among them, numerous dielectric materials, arranged to form photonic crystals[3,4], or nano-antenna[5], nanoprisms[6], microlenses[7] have been tested and showed an improvement of solar cells efficiency. In the case of PSCs[8–10], it has also been observed that the texturation of the substrate, the electron transport layer (ETL) or directly the absorbing layer also contributed to increase the efficiency of the devices. Finally, metallic nanoparticles, which support surface plasmon resonances, can also improve the cell

characteristics thanks to the enhancement of the local electromagnetic near-fields[11–13]. In addition to increasing optical absorption, it has been shown that plasmonic particles can also modify the generation of excitons, enhance the charge separation, and diminish the recombination rate, thus easing the electron and hole transport in the devices[14].

Usually, the nanostructuration is performed in order to enable light trapping and absorption in a wavelength range which is directly absorbed by the active material, typically in the visible part of the solar spectrum. In this work, our aim is different, we want to study the effect of a nanostructuration on the optical properties of a PSC but in the near-infrared (NIR) wavelength range, which is not usually absorbed. The goal is to produce intense and localized local electromagnetic fields able to boost the up-conversion fluorescence of nanocrystals embedded in the absorbing layer or situated at the interface between the absorbing layer and another adjacent material (the electron or the hole transport layers, or the metallic contact for instance)[15–17]. The principle of this effect is straightforward. Some rare-earth-doped materials like Er^{3+} can absorb the unabsorbed NIR light and reemit it by luminescence in the visible range, a wavelength which is absorbed by the PCS. However this effect is rather weak due to the low two-photon absorption cross-section efficiency of such materials[18,19] compared to organic molecules or semi-conducting quantum dots. Boosting the up-conversion absorption process and the emitted fluorescence can be done with plasmonic[15,16,19,20] or dielectric nanoparticles[21]. In the case of metallic nanoparticles, the fluorescence enhancement arises either from an increase of the local electromagnetic field[15,22,23] due to plasmonic resonances, or from an increase of the decay rate[22,24,25]. Differently, in the case of dielectric micro- and nano-structures, incident light can be trapped and concentrated in different zones due to the refractive index difference between the structures and the environment. Also, Mie resonances, which are due to the local fields and displacement currents induced by the incident wave, can produce strong electromagnetic fields both inside and outside the particles[26].

We will show here that grooves in a thin film of a perovskite material can generate strong variations of the local electromagnetic field and induce large up-conversion fluorescence enhancements compared to a flat surface. The enhancement depends on the dimensions of the structure (width, depth and period) and on the polarization direction of the incident light. Here, we paid particular attention to the influence of the grooves depth which is a parameter that strongly influences the contrast and the fluorescence enhancement. We will also show that the effect of roughness and the presence of defects generate fluctuations and ‘hot spots’ that

modifies the fluorescence. Although the structures have been fabricated by direct lithography using focused ion beam technique (FIB) on a sub-millimeter scale, they can also be created on much larger scales using, for instance, interference lithography.

6.2. Results and Discussion

6.2.1. SEM and AFM Tests Based on Perovskite Film Etched by Focused Ion Beam

The sample was introduced into the chamber of a focused ion beam system. The achieved structure of the sample is illustrated in **Fig. 1**. To calibrate the milling depth, squared patterns were created and characterized by atomic force microscopy (AFM). We show in **Fig. 2** the influence of the Ga ions dose on the etched depth. A linear variation was measured, enabling to adjust the depth with the dose in future fabrication runs. The roughness created by the FIB milling was characterized by scanning electron microscopy (SEM) and AFM. As shown on the SEM picture in **Fig. 3**, the perovskite surface looks identical between etched and un-etched zones, with alternative white and dark grains, as usually observed on this material[27]. The roughness measured by AFM is indicated on **Fig. 4** for the squares shown in **Fig. 3**. It varies between 28 nm to 60 nm and is of the same order of magnitude that on the un-etched zones (30 nm).

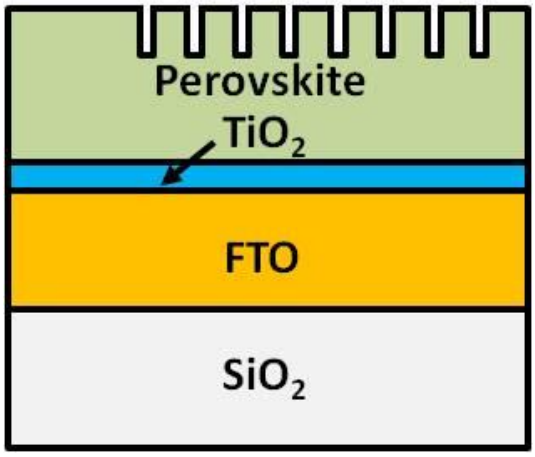

***Figure 1**: Structure of the perovskite thin film.*

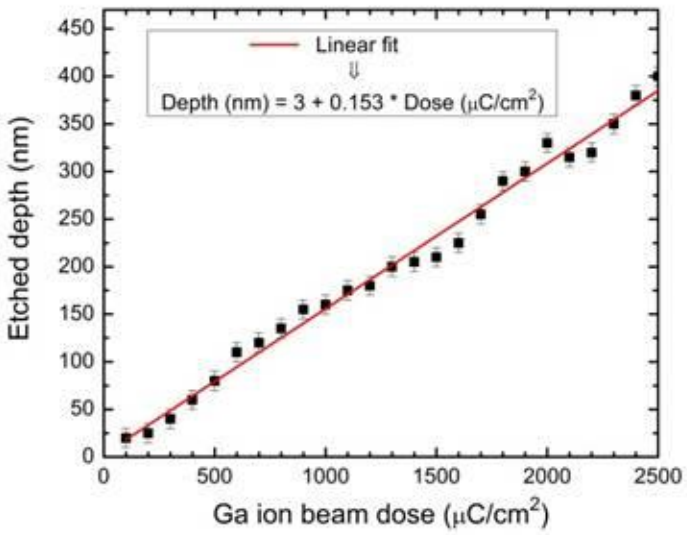

***Figure 2**: Influence of the Ga dose on the etching depth.*

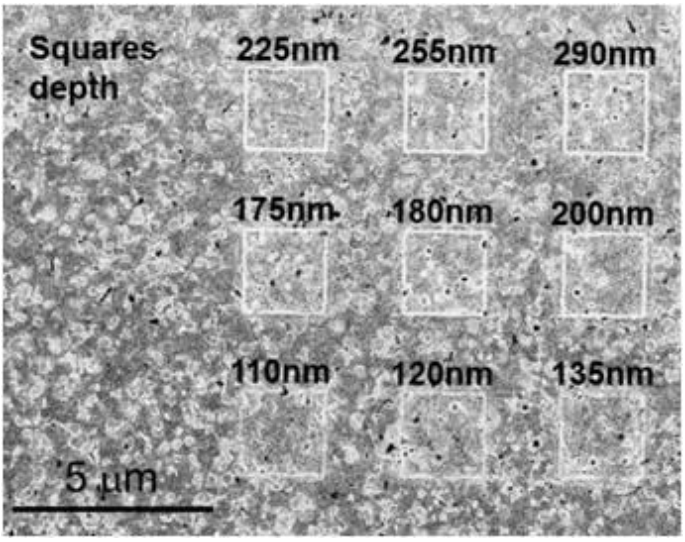

***Figure 3**: SEM picture of the perovskite surface with etched patterns of different depths. The depths are indicated near the patterns.*

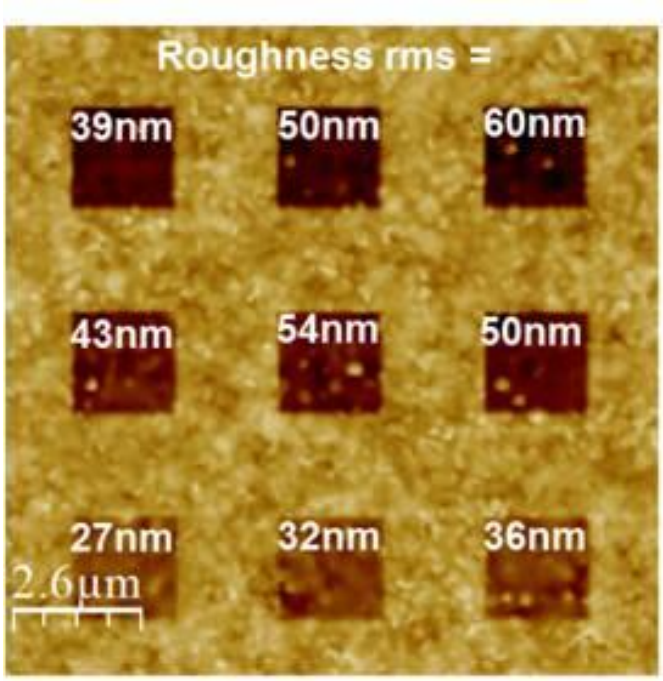

Figure 4*: AFM image of the same zone than* ***Figure 3*** *with corresponding roughnesses.*

In this work, we chose to study arrays of one-dimensional (1D) structures made of grooves with a period p equal to 500 nm and 1 µm. The patterns were made on 50 x 50 μm^2 zones. We show in **Fig. 5** a SEM picture of a groove array with a period equal to 500 nm, and a groove width and depth equal to 150 nm and 250 nm respectively. Although some grains, which are probably residues from the erosion process, remain on the surface, the grooves are regularly spaced with abrupt edges showing that the direct milling of a perovskite material with a FIB can be performed in a well-controlled and non-destructive way. The FIB experiments were performed by María Ujué González, in the laboratory of Instituto de Micro y Nanotecnología IMN-CNM, CSIC, Madrid.

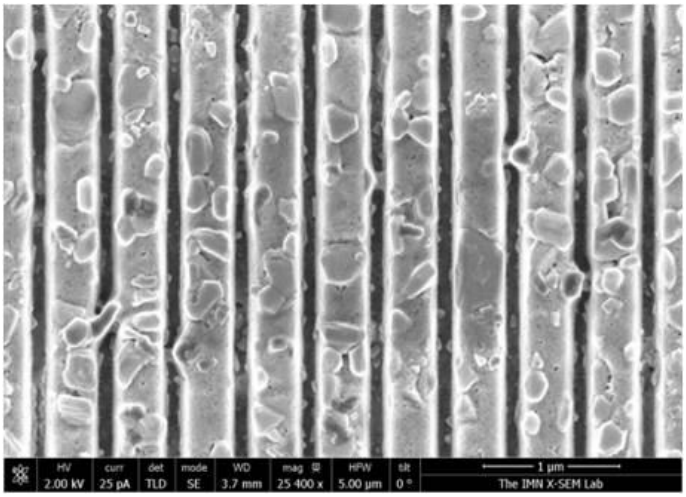

Figure 5*: SEM picture of a 500 nm period grating milled in the perovskite surface.*

6.2.2. SNOM Analysis of Treated Perovskite Films

In order to measure the localization of the electromagnetic field and to evaluate the fluorescence enhancement, we used a homemade scanning near-field optical microscope (SNOM) whose probe is a fluorescent nanocrystal. This nanocrystal is made of KY_3F_{10} codoped with Er^{3+} and Yb^{3+} ions and is glued at the end of a sharp AFM tip[21,28]. The diameter of the nanocrystal used in this study was between 100 nm and 200 nm. The principle of the experiment is described in **Fig. 6**. The sample is set on a scanning stage and illuminated in a transmission mode with a modulated focused laser beam (λ_{exc} = 975 nm, f_{mod} = 320 Hz). The tip scans the sample in the tapping mode and the nanocrystal is excited by the electromagnetic field at λ_{exc} localized on the surface. After the absorption of 2 photons, it emits light by fluorescence in the 525 - 550 nm range. The emitted light is collected with a large numerical aperture objective (N.A. = 0.8) and is sent to a photomultiplier tube connected to a lock-in amplifier. The images are recorded with a homemade Labview program that also drives the movement of the scanning stage.

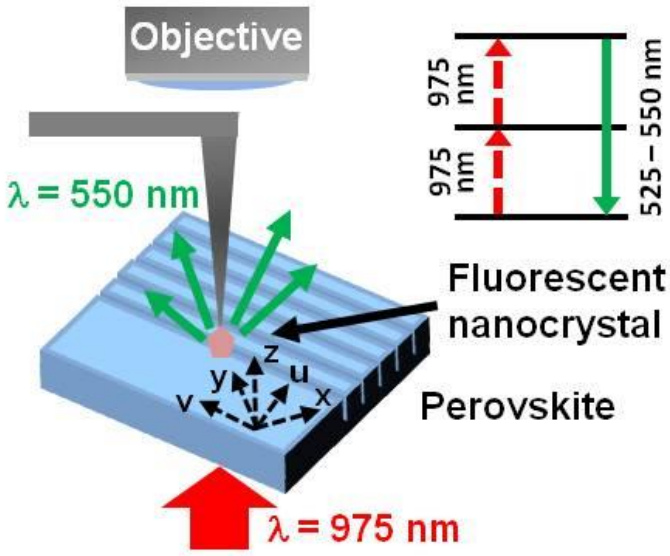

Figure 6*: Sketch of the experimental configuration.*

We show in **Fig. 7(a)** and **7(b)** two fluorescence images obtained on structures having a period of 1 µm and 500 nm. The corresponding AFM images are shown in the insets. The bare perovskite surface, with no structures, is visible on the lower left part of the images. The polarization of the incident laser beam was parallel to the grooves. As we can see, the presence of the grooves creates bright and dark lines, oriented in a direction parallel to the grooves. Although the measured quantity is the nanocrystal fluorescence, we recently observed on other structures[21,28] that it is directly linked to the intensity of the near-field on the surface, at the excitation wavelength. The observed lines are due to the refractive index difference between the air and the perovskite (n = 2.5) which perturbs the incident plane wave and tends to confine the light in some particular zones. They result from the combination of the zero order diffraction and other modes in the perovskite layer which are evanescent in the vertical z-direction. These periodic structures constitute a waveguide grating directly engraved in the perovskite. Among the different geometrical parameters that influence the intensity of the electromagnetic field and the fluorescence, we decided to study in more details the effect of the groove depth on the contrast.

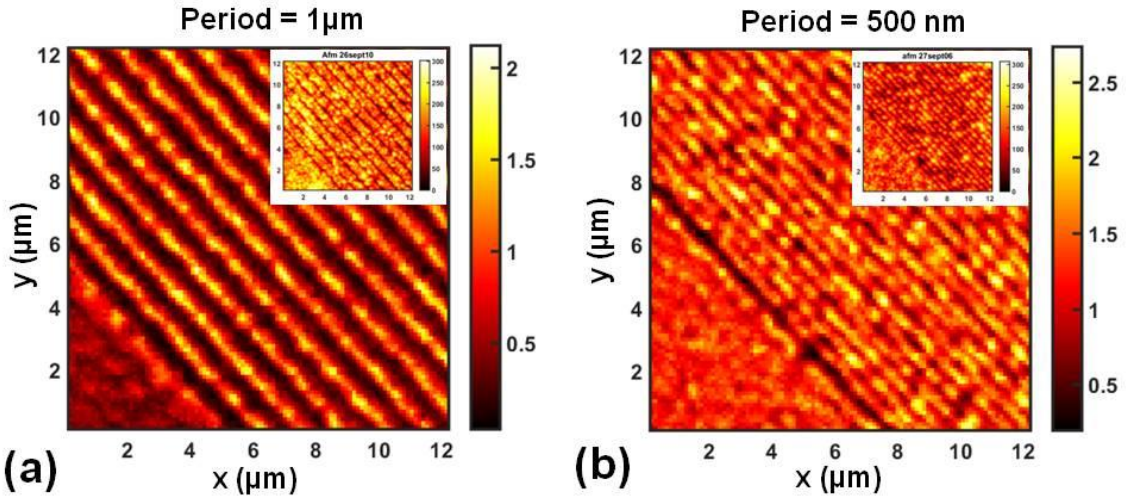

Figure 7*: (a) Fluorescence image measured on a structure with p = 1 µm, d = 200 nm and w = 250 nm; (b) same than (c) with p = 500 nm. The insets are the corresponding AFM images simultaneously acquired during scanning.*

6.2.3. Analysis of SNOM and Finite-Difference Time-Domain (FDTD) Simulation with Treated Perovskite Film

A finite difference time domain (FDTD) method has been used to calculate the near-field intensity with a proprietary code Lumerical®, which provides a robust and reliable solver for Maxwell's equations. An impinging plane wave was used, of unit amplitude everywhere, from the substrate side, and we employed scattering-like boundary conditions. The total field is then extracted to give rise to the near field intensity color maps. All are normalized to the impinging plane wave (unit amplitude for convenience).

We therefore characterized three structures having the same period (p = 1 µm), the same groove width (w = 250 nm) and three groove depths (d = 100 nm, d = 150 nm, and d = 200 nm). The incident polarization was parallel to the grooves. The fluorescence images are displayed in **Fig. 8** and the cross-sections in the direction perpendicular to the grooves are also shown in the insets. The oscillatory behavior is huge and presents very contrasted fringes. If we compare the maximum intensity of the fringes I_{max} to the intensity on the bare surface I_b, we find that the ratio I_{max} / I_b increases from 2 to 3 when the depth increases from 100 nm to 200 nm [**Fig. 11(b)**]. Similarly, the contrast, defined as (I_{max} - I_{min}) / (I_{max} + I_{min}) where I_{min} is the oscillation minimum, and plotted in **Fig 8(d)** as a function of the depth, increases from 0.45 to 0.65. Both the intensity and the contrast increase as the depth increases.

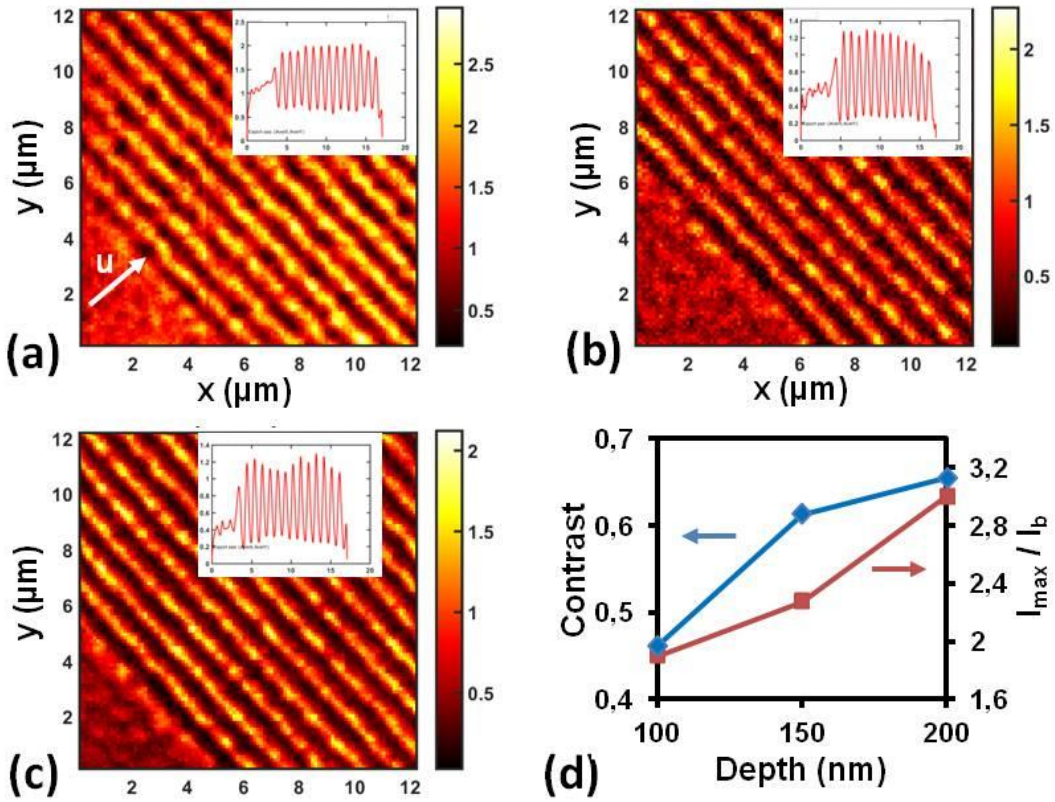

***Figure 8**: (a), (b) and (c) Fluorescence images measured by scanning the structures with p = 1 µm, w = 250 nm and d = 100 nm (a), d = 150 nm (b), and d = 200 nm (c). The insets are cross sections extracted from the images in a direction perpendicular to the grooves; (d) measured contrast as a function of the depth for three tips.*

To confirm the measured results, FDTD simulations, showing the variations of the near-field intensity, are depicted in **Fig. 9**. The maps are cuts in the plane perpendicular to the surface and to the grooves (u,z plane). As we can see, the oscillatory behavior is very similar to the one of the experiments, and the contrast also increases as the depth increases. From the cross-sections, we see that the bright lines are located between the grooves whereas the minimum is located above them. We will see later that the same result is observed experimentally by comparing fluorescence and topographic cross sections. In the simulation, two bright spots of less intensity are also visible on the sides of the grooves but they do not appear on the fluorescence images, probably because of the lack of resolution of the fluorescent nanocrystal used in the measurements and also because they are mainly located inside the perovskite material. These experiments and the simulation indicate that, if we want

to incorporate up-converting fluorescent nanocrystals in solar cells, we have to place them between the grooves, in order to get the maximum fluorescence enhancement. All the FDTD simulations were performed by Antonio García-Martín from the laboratory of Instituto de Micro y Nanotecnología IMN-CNM, CSIC, Madrid.

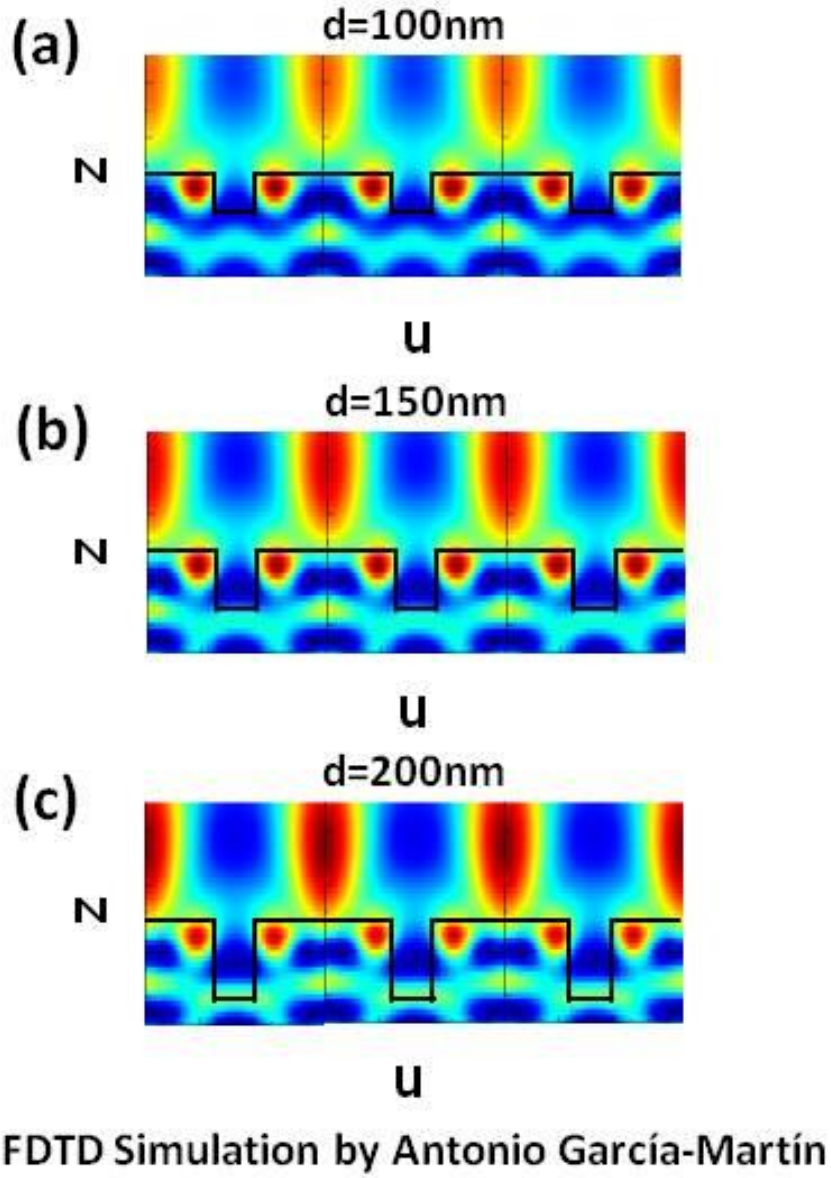

***Figure 9**: FDTD calculation of the near-field intensity for the three structures. The maps are cuts in a plane perpendicular to the surface and to the grooves (u,z) plane.*

All the previous images were measured with an illumination whose polarization was parallel to the grooves. We next studied the influence of the polarization direction on the fluorescence enhancement. We focused on the sample with the larger contrast (p = 1 µm, w = 250 nm, and d = 200 nm) and compared two images obtained with both parallel and perpendicular polarizations (see **Fig. 10 and Fig. 11**). We cannot compare the relative intensities of the two images because the excitation intensity is different for each situation, however it appears that the contrast is better in the case of the parallel polarization than for the perpendicular one. The bright line is however broader in the case of the perpendicular polarization. To understand this broadening, we calculated by FDTD the near-field intensity on the structure for both polarizations [see **Figs. 10(e)**, **10(f)**, **11e)** and **11(f)**]. In the case of the perpendicular polarization, the simulation reveals that the near-field is in fact composed of two peaks located on both sides of the grooves. These two peaks are not clearly contrasted, the intensity dropping only by ~30 % between them [**Fig. 11(f)**]. However, on the experimental image, these two peaks are merged in a single one. The reasons that can explain that are *i)* an eventual lack of resolution induced by the fluorescent nanocrystal due to its size, and *ii)* some roughness and residues that can enlarge the near-field distribution, thus impeding the separation and merging the two fringes. These two explanations are both credible and explain why we only see a broader peak. From this experiment, we can see that whatever the polarization, we observe a fluorescence enhancement between the grooves. Considering the application we described in the introduction, i.e. the incorporation of fluorescent up-converting nanocrystals inside the nanostructured solar cell, illuminated by an unpolarized solar radiation, this experiment indicates that the nanocrystals have to be placed at this exact location, between the grooves.

From the fluorescence maps shown in **Fig. 8** and **Fig. 10** and **Fig. 11**, we see that the bright lines are not perfectly lined up and that they are not of constant intensity. This may be due to some residues left from the milling but also to the roughness of the perovskite surface. Following this idea, we next tried to evaluate the effect of roughness on the near-field distribution on the surface.

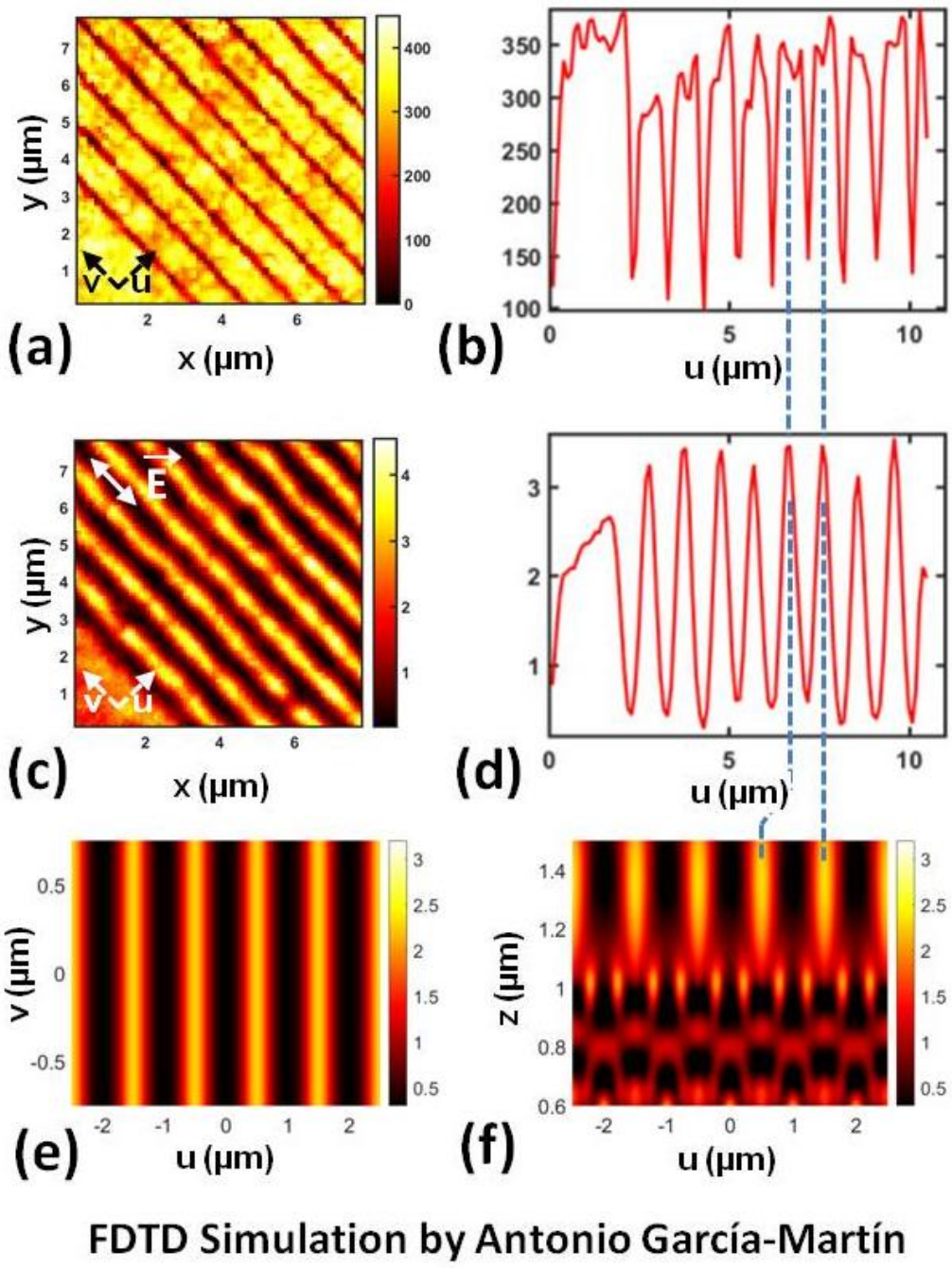

***Figure 10**: Topography (a,b) and fluorescence (c,d) measured by scanning the structure (p = 1 µm, w = 250 nm); (b,d) are cross-sections extracted from images (a,c). The polarization is parallel (c,d) to the grooves. The simulations (e), (f) are FDTD maps of the near-field intensity in different planes on the surface.*

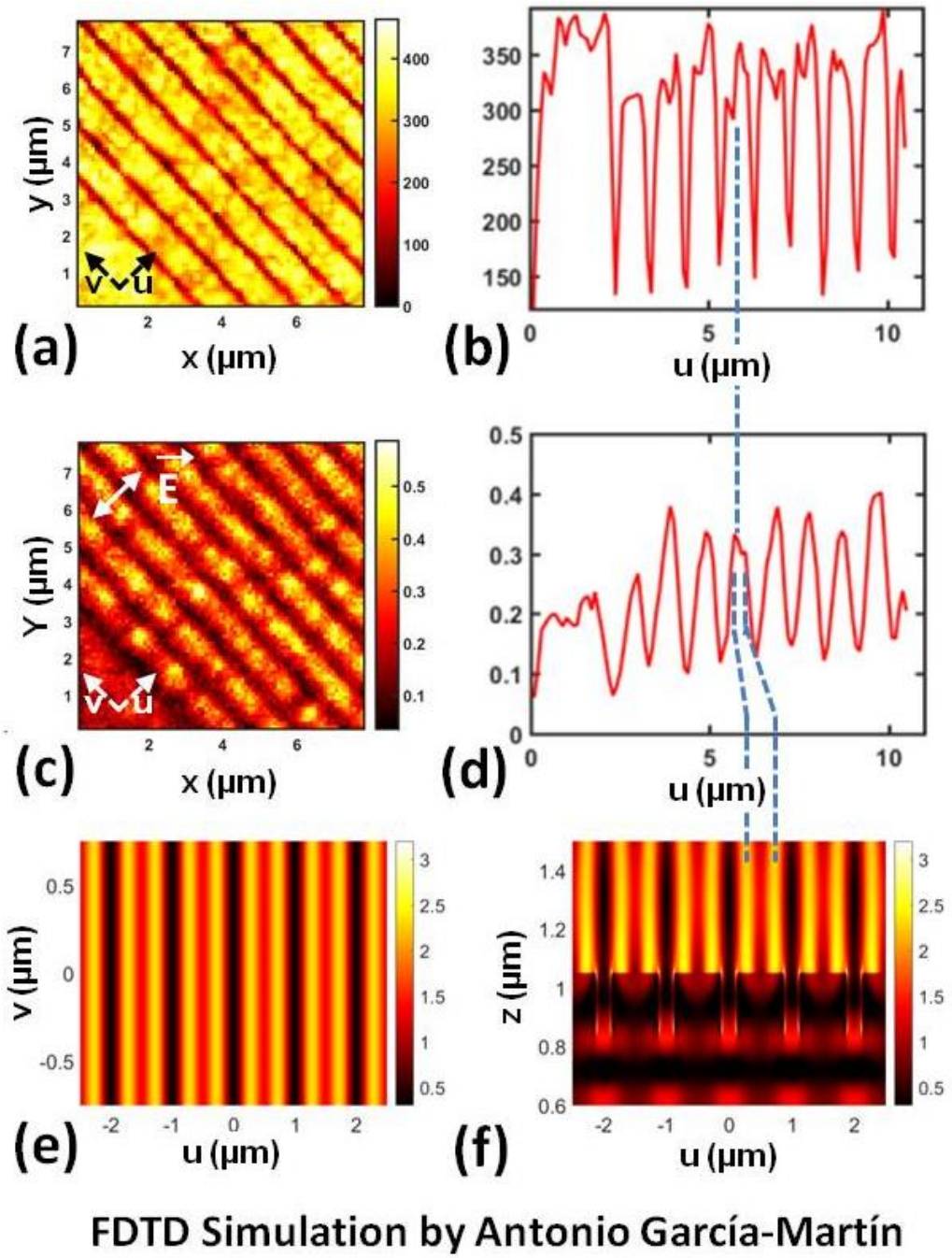

Figure 11*: Topography (a,b) and fluorescence (c,d) measured by scanning the structure (p = 1 µm, d = 100 nm); (b,d) are cross-sections extracted from images (a,c). The polarization is perpendicular to the grooves (c,d). The simulations (e), (f) are FDTD maps of the near-field intensity in different planes on the surface.*

6.2.4. The Effect of Roughness on the Near-field Distribution on the Surface by FDTD Simulation

The results are shown in **Fig. 12 and 13**. The roughness, estimated from AFM measurements [**Fig. 12**], was set to 40 nm. In **Fig. 13**, the maps in (u,z) and (u,v) planes are given for both polarization directions taking into account this roughness. Compared to the FDTD maps without roughness shown for instance in **Figs. 10(e)**, **10(f)**, **11(e)** and **11(f)**, both the intensity and the shape are modified from fringe to fringe. The intensity can be locally enhanced and forms hot spots where fluorescence is increased. In the case of the perpendicular polarization, we can see that the roughness tends to enlarge the fringes and merge them. Combined to the space-averaging due to the size of the fluorescent nanocrystal, it is not surprising that we were not able to separate the two fringes in the fluorescence experiments [see **Figs. 11(c)** and **11(d)**]. The effect of roughness is less important in the case of parallel polarization for which the fringes are more separated and contrasted [**Figs. 13(a**) and **13(c)**]. As measured experimentally [see **Fig. 10(d)**], the full width at half maximum of the fringes for this polarization is approximately 400 nm, in agreement with the FDTD simulations shown in **Fig. 10(e)** and **Fig. 13(c)**. This means that the fluorescence enhancement, compared to the bare perovskite surface, occurs in this entire large zone. For our application, this situation is very interesting because this area is wide enough to be easily covered with a large amount of fluorescent nanocrystals, thus contributing efficiently to the improvement of the solar cell efficiency. Another positive effect that could have both the nanostructuration and the presence of fluorescent nanocrystals is the improved scattering and trapping of the visible light inside the perovskite layer. It could result in an enhanced absorption of the visible light compared to the flat surface. We did not make this study here, keeping focused on the near-field effects in the NIR, but it could be interesting to couple these two distinct effects (absorbed visible light and unabsorbed NIR) of the nanostructuration and optimize the structures to maximize both of them. On the other hand, many questions could be raised on the negative effects that could have the nanocrystals on the electrical properties of the solar cells. If we refer to recent studies, it has been reported that the incorporation of plasmonic[11,14] or dielectric[28] nanoparticles improved the PCE of the devices, thus we are therefore confident that fluorescent nanocrystals would have a very limited negative effect. Finally, in this study, we only varied here the depth of the grooves, but a deeper optimization of their width as well as of the period

of the array could be done by FDTD and would probably contribute to design structures that provide larger fluorescence enhancements.

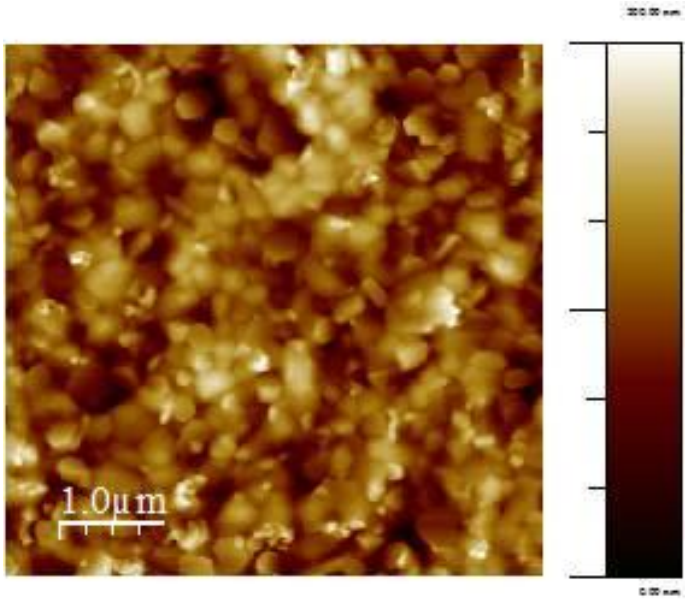

***Figure 12**: Topography of the perovskite surface.*

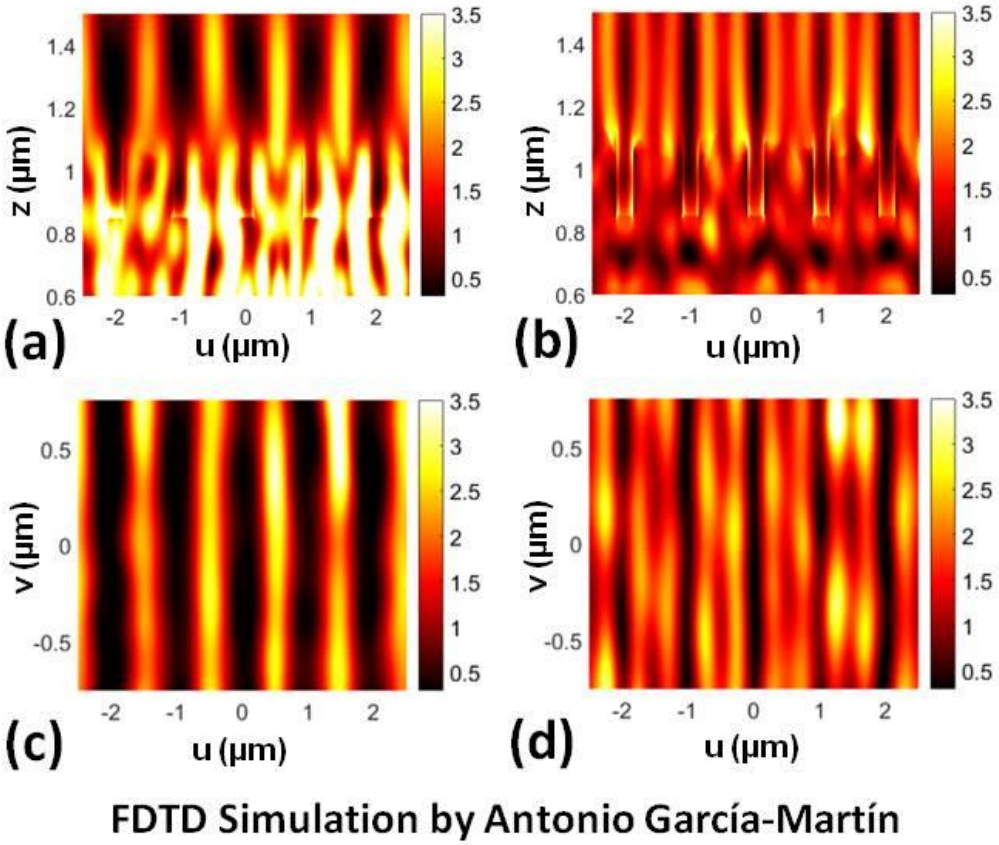

***Figure 13**: FDTD simulations with roughness in a (u,z) plane for parallel (a) et perpendicular (b) polarizations; FDTD simulations in the (u,v) plane with roughness for parallel (c) and perpendicular (d) polarizations.*

6.3. Conclusion

We fabricated perovskite thin films used in hybrid solar cells and engraved their surface with a focused ion beam. Our aim was to create zones where infrared light is both localized and enhanced to boost the fluorescence of up-converting nanocrystals situated on the material. We created arrays of grooves of variable depth and we studied them by near-field fluorescence microscopy. We observed periodic fluorescence variations and the formation of fringes oriented in a direction parallel to the grooves. A fluorescence enhancement by a factor of 2 to 3 was measured when the nanocrystals are situated between the grooves compared to the bare perovskite surface. We found that the enhancement and the intensity contrast were both larger when increasing the groove depth. The polarization of the incident light has also an effect on the electromagnetic field distribution. It is composed of either a single or two fringes when the incident polarization is parallel or perpendicular to the grooves respectively. All the results are in good agreement with numerical simulations performed by FDTD. The influence of the inhomogeneities of the perovskite layer was also studied and showed that the roughness tends to locally modify the intensity of the fringes and to distort their alignment. The measurements and simulations indicate that they can lead to additional hot spots. From our study, we showed that, whatever the polarization, which is the operating situation of solar cells under sunlight, the ideal position of the nanocrystals is between the grooves where fluorescence can be enhanced. As a prospect, further optimization could be made by changing the period, and the width of the grooves, and by improving the quality of the surface to reduce the roughness. The design of two-dimensional structures like squares or circular disks could also lead to larger enhancements, and the structures would in that case be insensitive to polarization effects.

6.4. References

1. Lee, T. D. & Ebong, A. U. A review of thin film solar cell technologies and challenges. *Renew. Sustain. Energy Rev.* **70**, 1286–1297 (2017).

2. Powalla, M. *et al.* Thin-film solar cells exceeding 22% solar cell efficiency: An overview on CdTe-, Cu(In,Ga)Se 2 -, and perovskite-based materials. *Appl. Phys. Rev.* **5**, (2018).

3. Bermel, P., Luo, C., Zeng, L., Kimerling, L. C. & Joannopoulos, J. D. Improving thin-film crystalline silicon solar cell efficiencies with photonic crystals. *Opt. Express* **15**, 16986 (2007).

4. Mallick, S. B., Agrawal, M. & Peumans, P. Optimal light trapping in ultra-thin photonic crystal crystalline silicon solar cells. *Opt. Express* **18**, 5691 (2010).

5. Yu, Y., Ferry, V. E., Alivisatos, A. P. & Cao, L. Dielectric core-shell optical antennas for strong solar absorption enhancement. *Nano Lett.* **12**, 3674–3681 (2012).

6. Wang, D.-L. *et al.* Highly efficient light management for perovskite solar cells. *Sci. Rep.* **6**, 18922 (2016).

7. Peer, A., Biswas, R., Park, J.-M., Shinar, R. & Shinar, J. Light management in perovskite solar cells and organic LEDs with microlens arrays. *Opt. Express* **25**, 10704 (2017).

8. Jošt, M. *et al.* Efficient Light Management by Textured Nanoimprinted Layers for Perovskite Solar Cells. *ACS Photonics* **4**, 1232–1239 (2017).

9. Pascoe, A. R. *et al.* Enhancing the Optoelectronic Performance of Perovskite Solar Cells via a Textured CH 3 NH 3 PbI 3 Morphology. *Adv. Funct. Mater.* **26**, 1278–1285 (2016).

10. Zheng, L. *et al.* Improved light absorption and charge transport for perovskite solar cells with rough interfaces by sequential deposition. *Nanoscale* **6**, 8171–8176 (2014).

11. Ginting, R. T. *et al.* Plasmonic Effect of Gold Nanostars in Highly Efficient Organic and Perovskite Solar Cells. *ACS Appl. Mater. Interfaces* **9**, 36111–36118 (2017).

12. Atwater, H. A. & Polman, A. Plasmonics for improved photovoltaic devices. *Nat. Mater.* **9**, 205–213 (2010).

13. Ferry, V. E., Sweatlock, L. A., Pacifici, D. & Atwater, H. A. Plasmonic nanostructure design for efficient light coupling into solar cells. *Nano Lett.* **8**, 4391–4397 (2008).

14. Luo, Q. *et al.* Plasmonic Effects of Metallic Nanoparticles on Enhancing Performance of Perovskite Solar Cells. *ACS Appl. Mater. Interfaces* **9**, 34821–34832 (2017).

15. Wu, D. M., García-Etxarri, A., Salleo, A. & Dionne, J. A. Plasmon-enhanced upconversion. *J. Phys. Chem. Lett.* **5**, 4020–4031 (2014).

16. Wang, P. H. *et al.* Surface plasmon enhanced up-conversion from NaYF4:Yb/Er/Gd nano-rods. *Phys. Chem. Chem. Phys.* **17**, 16170–16177 (2015).

17. Schoenauer Sebag, M. *et al.* Microscopic Evidence of Upconversion-Induced Near-Infrared Light Harvest in Hybrid Perovskite Solar Cells. *ACS Appl. Energy Mater.* **1**, 3537–3543 (2018).

18. Boyer, J. C. & Van Veggel, F. C. J. M. Absolute quantum yield measurements of colloidal NaYF4: Er 3+, Yb3+ upconverting nanoparticles. *Nanoscale* **2**, 1417–1419 (2010).

19. Wang, Y. L. *et al.* Tailoring plasmonic enhanced upconversion in single NaYF4: Yb3+/Er3+ nanocrystals. *Sci. Rep.* **5**, 1–7 (2015).

20. He, J. *et al.* Plasmonic enhancement and polarization dependence of nonlinear upconversion emissions from single gold nanorod@SiO2@CaF2:Yb3+, Er3+ hybrid core-shell-satellite nanostructures. *Light Sci. Appl.* **6**, e16217-11 (2017).

21. Lin, H. J. *et al.* Fluorescence enhancement near single TiO2 nanodisks. *Appl. Phys. Lett.* **111**, (2017).

22. Anger, P., Bharadwaj, P. & Novotny, L. Enhancement and quenching of single-molecule fluorescence. *Phys. Rev. Lett.* **96**, 3–6 (2006).

23. Goldschmidt, J. C. & Fischer, S. Upconversion for photovoltaics - a review of materials, devices and concepts for performance enhancement. *Adv. Opt. Mater.* **3**, 510–535 (2015).

24. Fischer, S., Kumar, D., Hallermann, F., von Plessen, G. & Goldschmidt, J. C. Enhanced upconversion quantum yield near spherical gold nanoparticles – a comprehensive simulation based analysis. *Opt. Express* **24**, A460 (2016).

25. Kühn, S., Håkanson, U., Rogobete, L. & Sandoghdar, V. Enhancement of single-molecule fluorescence using a gold nanoparticle as an optical nanoantenna. *Phys. Rev. Lett.* **97**, 1–4 (2006).

26. Albella, P. *et al.* Low-Loss Electric and Magnetic Field-Enhanced Spectroscopy with Subwavelength Silicon Dimers. *J. Phys. Chem. C* **117**, 13573–13584 (2013).

27. Nicholson, B., Verma, S., Med, P. & S, S. R es e a rc h. (2014).

28. Zhang, C. *et al.* Enhancing photovoltaic performance of perovskite solar cells utilizing germanium nanoparticles. *Sol. Energy* **188**, 839–848 (2019).

Chapter 7. Experiment and Characterizations

7.1. Experimental Section

All chemicals were purchased from Sigma-Aldrich and Alfa Aesar unless indicated otherwise and used as received.

Synthesis of methylammonium bromide (MAI): CH_3NH_3I was synthesized according to the literature published by Roldán-Carmona et al.[1] Briefly, 21.6 ml methylamine (40%wt in water, Aldrich) and 30 ml hydroiodic acid (57 wt% in water, Aldrich) were transferred into a 250-mL-volume Erlenmeyer flask to react, with stirring in an ice bath (0 °C) for 2h. A white precipitate was obtained by evaporation in a 55 °C water bath for 1 hour. The product, methylammonium iodide (CH_3NH_3I) was purified by ethanol, diethyl ether, and finally dried at 60 °C in a vacuum oven overnight.

Synthesis of methylammonium bromide (MABr): CH_3NH_3Br was prepared similarly to a previous paper.[2] In brief, 24 ml of methylamine (40 wt% in water, Aldrich) and 12 ml of hydrobromic acid were added into a 250-mL-volume Erlenmeyer flask and then immersed in an ice bath for 2h with constant stirring. The white powder was recovered by rotary evaporation at 55 °C for 1h. To further enhance the purity of the MABr precipitate, it was redissolved in ethanol, and diethyl, which was repeated for three times. Finally, the achieved white solid was collected and dried at 60 °C in a vacuum oven overnight.

Synthesis of methylammonium bromide (MACl): CH_3NH_3Cl was synthesized by reacting methylamine (33 wt % ethanol solution) and 33 wt % hydrocholoride acid with the molar ratio of 1.2:1 in an ice bath for 2 h with stirring followed by vacuum drying and cleaning with acetonitrile.[3] Last, the achieved white precipitate was collected and stored at 60 °C in a vacuum oven overnight.

Synthesis of formamidinium iodide (FAI): $HC(NH_2)_2I$ was prepared according to the method reported by McMeekin et al.[4] with minor modifications. In a typical preparation, 12.60 g of formamidinium acetate was added to 125 mL of methanol in a 250-mL-volume Erlenmeyer flask that was immersed in an ice bath. 24 mL of hydriodic acid (57 wt %) was then added dropwise. The reaction was left stirring for approximately 2 hours at room temperature. The precipitate was collected by evaporating the entire reaction product at 55 °C

for 2 hours. The obtained solid after evaporation was dissolved in isopropanol and precipitated by adding diethyl ether and subsequent centrifugation. This precipitation and centrifuge procedure was further repeated three times. The final white powder obtained was dried in a vacuum oven at 50 °C overnight before being transferred to an Ar-filled glovebox for storage and further use.

Procedure for etching FTO-coated glass substrate: Fluorine-doped tin oxide (FTO) glass substrates were etched with Zn powder and HCl acid (2M) to achieve the required glass substrate as a control sample to compare with FTO/glass substrates.

Procedure for cleaning FTO-coated glass substrates: The etched and pristine FTO slides were then rinsed by four sequential ultrasonication baths with soap (2% Hellmanex in water), deionized water, acetone and isopropanol for 15 min, respectively. Then the dried substrates treated by an oxygen plasma process for 10 min.

Preparation of TiO_2 compact layer: To prepare the compact TiO_2 (cp-TiO_2) ETL, a sol-gel precursor solution based on titanium (IV) isopropoxide was prepared according to a previously reported procedure.[5] For the synthesis of the sol−gel solution, 2.7 mL of titanium(IV) isopropoxide (Sigma-Aldrich) was dropwise to 71 mL of isopropanol and 1.0 g of diethanolamine; after stirring for 5 min at room temperature, then 70 μL of deionized water was added, finally, the sol was kept to age for an hour before being used. This precursor solution was then spin-coated (at 4000 rpm) onto cleaned FTO substrates followed by substrate annealing in an oven in the air first at 120 °C for 15 minutes and then at 450 °C for 1 hour.

Preparation of TiO_2 nanocolumn arrays: The aligned 1D TiO_2 nanocolumn arrays have been fabricated in two steps. The first step was the fabrication of Ti nanocolumns by GLAD with magnetron sputtering using the setup and methodology described in detail in previous work.[6] The sputter gas was argon and the parameters used were: pressure = 0.15 Pa, power (DC discharge) = 300 W, and tilt angle between substrate and target = 75º. The second step is the thermal oxidation of the Ti nanocolumn arrays to obtain TiO_2 nanocolumns. For this purpose, they were placed in a quartz tube inside a tubular furnace. Synthetic air was passed through the tube at a flow rate of 50 cm^3 min^{-1}. The furnace was then heated with a 10 °C min-1 ramp up to 500 ºC and kept at that temperature for 10 min, after which it was let to cool down naturally.

Perovskite thin film [$FA_{0.83}Cs_{0.17}Pb(I_{0.6}Br_{0.4})_3$]:. To prepared the perovskite precursor solution, four chemicals including FAI, CsI, $PbBr_2$ and PbI_2 were dissolved in anhydrous *N,N*-dimethylformamide (DMF) to obtain a stoichiometric solution toward the composition of $FA_{0.83}Cs_{0.17}Pb(I_{0.6}Br_{0.4})_3$ with five different molar concentrations of 0.95M, 1.10M, 1.25M, 1.40M, and 1.50M respectively. According to the method reported by McMeekin et al,[4] we added 54.7 µl of 57 wt% hydroiodic acid (HI) and 27.3 µl of 48 wt% hydrobromic acid (HBr) into 1 mL of 0.95M perovskite precursor solution. Based on these values the amounts of HI and HBr were modified linearly as the precursor concentration increases. The precursor solutions were then stirred at room temperature for at least 72 hours inside an Ar-filled glovebox. The perovskite precursor solution was spin-coated inside the glovebox on bare FTO or cp-TiO_2/FTO substrates at 2000 rpm for 45 s. After drying on a hot plate at 70 °C for 1 minute, samples were annealed in an oven at 185 °C for 90 minutes to induce the complete perovskite crystallization of $FA_{0.83}Cs_{0.17}Pb(I_{0.6}Br_{0.4})_3$.

Perovskite thin film [$Cs_{0.05}(FA_{0.83}MA_{0.17})_{0.95}Pb(I_{0.83}Br_{0.17})_3$]: To prepare the solution precursor for the $Cs_{0.05}(FA_{0.83}MA_{0.17})_{0.95}Pb(I_{0.83}Br_{0.17})_3$ perovskite layer, formamidinium iodide (FAI) and methylammonium bromide (MABr) are synthesized according to previous works.[2,4] Lead iodide (PbI_2), lead bromide ($PbBr_2$) and cesium iodide (CsI) were purchased from Sigma Aldrich. A precursor solution was formed by dissolving FAI (1 M), MABr (0.2 M), PbI_2 (1.1 M), and $PbBr_2$ (0.2 M) in a solvent mixture of dimethylformamide (DMF) and dimethyl sulfoxide (DMSO) (4:1, v/v) according to a previous report.[7] In parallel, a stock solution containing 1.5 M of CsI dissolved in DMSO was prepared. CsI stock solution was then added into the above-mentioned precursor solution to achieve the desired composition in the final precursor solution. The deposition of the perovskite precursor solution onto cp-TiO_2/TiO_2 NA-coated FTO was performed in an Ar-filled glovebox by two-step spin-coating first at 1000 rpm for 10 s and then at 5000 rpm for 45 s. During the second spin-coating step, 100 µl chlorobenzene was dropped on the spinning substrate after 30 s of spinning. After spin-coating the perovskite films were annealed inside the glovebox at 100 °C for 60 min on a hot-plate.

This above procedure led to the formation of a perovskite film of a thickness of 400 nm. For the perovskite films of a 250-nm-thickness and 310-nm-thickness, instead of the above-mentioned two-step spin-coating procedure, a one-step spin-coating method was used, at 5500 rpm for 50 s for a 250-nm-thick film and at 4500 rpm 50 s for a 310-nm-thick film,

respectively. For the preparation of perovskite films of a 540-nm-thickness and 1000-nm-thickness, the above-mentioned perovskite precursor solution was concentrated by 1.3-fold. A two-step spin-coating method was used, at 1000 rpm for 10s and then at 5000 rpm for 45 s to achieve a 540-nm-thick film, or at 1000 rpm for 10 s and then at 2000 rpm for 45 s to achieve a 1000-nm-thick film. Finally, the gold film (150 nm thickness) was thermally evaporated under high vacuum, on the top of the perovskite layer and etched FTO glass substrate to complete the device preparation, respectively. **(Chapter 4)**

Procedure of organic salts post-treatment for perovskite film: To remove the excess PbI_2 crystals on the surface of selected perovskite thin films, inside a glovebox, 50 µL of MAI, or FAI, or MABr, or MACl solution in isopropanol (1 to 4 mg/mL) was drop-cast onto the surface of the perovskite film followed by spin-coating to dry out the solution and a five-minute annealing on a hot-plate at 100 °C. **(Chapter 5)**

Fabrication of perovskite solar cells: To complete the solar cell device, on the surface of perovskites/cp-TiO_2 or TiO_2 NA structure a layer of hole transport layer (HTL), 2′-7,7′-tetrakis(N,N-di-p-methoxyphenylamine)-9,9′-spirobifluorene (Spiro-OMeTAD), was deposited by spin-coating (at 2000 rpm for 45 s) a chlorobenzene solution containing 72.3 mg/ml Spiro-OMeTAD. Additives of 32 µl of lithium bis(trifluoromethanesulfonyl)imide (170 mg/ml in 1-butanol) and 10 µl of 4-tertbutylpyridine were added into 1 mL of Spiro-OMeTAD chlorobenzene solution. The samples were then placed into a desiccator for about 12 hours in order to oxidizer the hole-transport layer. Finally, 100-nm-thick gold top contacts were thermally evaporated on the surface of the Spiro-OMeTAD HTL to complete the solar cell structure.

For perovskite solar cells with an inverted architecture, PTAA (1.5mg/ml in toluene) was spin-coated on the cleaned ITO substrates in a drybox (RH<0.5%) at 4000 rpm for 30 s with a thermal anneal of 10 min at 100 °C. After cooling down, PFN-Br (0.5mg/ml in methanol) was then spin-coated on the PTAA at 5000 rpm for 30 s. The perovskite precursor was deposited on the HTL with the same procedure as above mentioned, followed by a thermal annealing at 100 °C for 30 min. For the MAI-treated samples, the treatment procedure was identical as that mentioned above with a MAI concentration of 2mg/ml. The prepared films were then transferred to a N_2-filled glovebox. PCBM (20mg/ml in chlorobenzene) was dynamically spin-coated on the perovskite layer at 2000 rpm for 30 s, followed by a 10 min anneal at 100 °C. Sequentially, BCP (0.5mg/ml in isopropanol) was spin-coated on the PCBM at 4000

rpm for 30 s as a hole blocking layer. To complete the devices, 80 nm silver was thermally evaporated on top of the films under high vacuum. (**Chapter 5**)

7.2. Characterization Section

Structural and optical characterizations.

Scanning near-field optical microscopy (SNOM) measurements were performed by a homemade near-field optical microscope that uses a fluorescent nanocrystal as a near-field detector.[8,9] The nanocrystal is made of KY_3F_{10}/YF_3:Er/Yb, and its size is approximately 200 nm. Excitation was performed with an internally modulated laser diode ($\lambda \cong 650$ nm, f_{mod} = 320 Hz) in a transmission mode at normal incidence. The collection of the near-field signal was performed using a wide numerical aperture objective (Olympus LMPlanFl 100x 0.8) and sent to a photomultiplier tube and to a lock-in amplifier (EG&G Instruments Model 7260DSP). The sample was set on a piezo-electric 3D stage (Nanocube, Physik Instrumente) for scanning. SEM characterizations were performed with a FEI Magellan 400 system with a standard field emission gun source. XRD spectrum were obtained by a PANalytical X'Pert X-ray diffractometer using Cu-Kα radiation. UV-Visible absorption spectra were recorded in transmission mode by an Ocean Optics HL-2000 fiber-coupled tungsten halogen lamp and an Ocean Optics HR4000 spectrometer (200-1100 nm). Steady-state photoluminescence (PL) was recorded in a reflection mode by the same Ocean Optics spectrometer with an excitation source at 365 nm (Ocean Optics LLS-365). For PL decay measurements, samples are excited by a pulsed laser at λ = 376.8 nm (pulsed period = 2 µs). Time-resolved PL signal centered at 735 nm were recorded by a time-correlated single photon counting (TCSPC) setup (SPC-130-EM, Becker & Hickl GmbH). All film thicknesses were measured using a profilometer (Veeco Dektak). For the FTO/cp-TiO_2 substrate with nanocolumns covered on its half (without perovskite coating), optical absorbance spectra were recorded in a transmission mode by a V-770ST UV/VIS/NIR spectrometer with a mask (diameter of aperture = 6 mm) allowing optical transmission in only the area of interest. X-ray photoelectron spectroscopy (XPS) measurement was carried out by a KRATOS AXIS Ultra DLD apparatus at a base pressure of 3×10^{-9} Torr (X-ray Source: AlKα). Atomic Force Microscopy (AFM) was performed using a Dimension Icon from Bruker operating in non-contact mode with high-resolution probes (radius: 2nm) from Next-Tip.

Photovoltaic Characterization.

Solar cell current-voltage characteristics were measured in an Ar-filled glovebox by a computer-controlled Keithley 2612B source measurement unit (SMU). Devices were illuminated through the transparent substrate (FTO/glass) side by a class ABB (ASTM E927-10) Newport LCS-100 solar simulator with an AM 1.5G filter operated at 1 SUN. The light intensity was first calibrated by a calibrated Si reference solar cell (ReRa Solutions B.V.). For the external quantum efficiency (EQE) measurements, a monochromatic light beam was obtained from a white light source and an Oriel Cornerstone monochromator with appropriate order sorting filters. The monochromatic illumination was calibrated by a NIST-calibrated Si photodiode. The solar cell short-circuit current I_{sc} (A) at each monochromatic wavelength was measured in air by a Keithley 2634B SMU. The EQE spectrum was determined by $EQE(\%) = \frac{I_{sc}(A)}{P(W)} \times \frac{1240}{\lambda(nm)} \times 100$ where P (W) is the power of the monochromatic illumination. The electrochemical impedance spectroscopy (EIS) measurements were performed in electrochemical workstation (Agilent, E4980A) under dark and with an external applied bias holding at the open-circuit voltage of the solar cell. The frequency range of the EIS measurements was from 20 Hz to 2 MHz with a modulation amplitude of 20 mV.

7.3. References

1. Roldán-Carmona, C. *et al.* Flexible high efficiency perovskite solar cells. *Energy Environ. Sci.* **7**, 994–997 (2014).
2. Chen, H. *et al.* An amorphous precursor route to the conformable oriented crystallization of ch3nh3pbbr3 in mesoporous scaffolds: Toward efficient and thermally stable carbon-based perovskite solar cells. *J. Mater. Chem. A* **4**, 12897–12912 (2016).
3. Zhao, Y. & Zhu, K. CH3NH3Cl-assisted one-step solution growth of CH 3NH3PbI3: Structure, charge-carrier dynamics, and photovoltaic properties of perovskite solar cells. *J. Phys. Chem. C* **118**, 9412–9418 (2014).
4. McMeekin, D. P. *et al.* A mixed-cation lead mixed-halide perovskite absorber for tandem solar cells. *Science (80-.).* **351**, 151–155 (2016).
5. Edri, E., Kirmayer, S., Cahen, D. & Hodes, G. JPCL-High Open-Circuit Voltage Solar Cells Based on Organic−Inorganic Lead bromide perovskite-2012.pdf. 2–7 (2013).
6. Alvarez, R. *et al.* Nanostructured Ti thin films by magnetron sputtering at oblique angles. *J. Phys. D. Appl. Phys.* **49**, 045303 (2016).

7. Mahboubi Soufiani, A. *et al.* Impact of microstructure on the electron-hole interaction in lead halide perovskites. *Energy Environ. Sci.* **10**, 1358–1366 (2017).

8. Aigouy, L. *et al.* Mapping plasmon-enhanced upconversion fluorescence of Er/Yb-doped nanocrystals near gold nanodisks. *Nanoscale* **11**, 10365–10371 (2019).

9. Lin, H. J. *et al.* Fluorescence enhancement near single TiO2 nanodisks. *Appl. Phys. Lett.* **111**, (2017).

Chapter 8. Conclusion

Among the emerging photovoltaic materials for "third-generation" solar cells, hybrid organo-metal halide perovskites have attracted tremendous research interest recently due to their extraordinary physical properties, including large charge carrier diffusion length, high extinction coefficient, excellent charge carrier mobility, and tunable bandgap, all together leading to solar cells with promising power conversion efficiencies beyond 25%. Nevertheless, further progress is still needed before this technology can achieve wide-scale applications. In the studies involved in my thesis, we performed fundamental investigations on the roles of perovskite active layer, ETL, and the interfaces between on the performance and the stability of device. Specifically, the work performed can be summarized as follows:

In **Chapter 2**, we demonstrated a simplified planar structure of PSCs without ETL, by directly depositing the grain size- and thickness-tunable perovskite thin film onto the FTO substrates. The grain size of perovskite crystals can reach up to 12 microns through modulating the perovskite precursor concentration, which is an important pre-condition to achieve high PCE and stability of perovskite devices. The as-prepared $FA_{0.83}Cs_{0.17}Pb(I_{0.6}Br_{0.4})_3$ perovskite materials exhibited a large bandgap of ~1.74 eV which is promising to couple with silicon in a tandem solar cell configuration. In this chapter we optimized the material deposition, fabricated and characterized the functional ETL-free PSCs. Such ETL-free PSCs offer both advantages and inconveniences. While offering a simplicity in device fabrication, such ETL-free PSCs exhibit important hysteresis in the J-V characteristics of the solar cells.

To overcome the disadvantages in ETL-free PSCs, in **Chapter 3** we investigated PSCs built on a planar and a nanostructured TiO_2 ETL. For the nanostructured ETL, one-dimensional vertically aligned TiO_2 nanocolumn arrays were prepared by by glancing angle deposition with magnetron sputtering. These vertically aligned nanocolumn arrays were then applied as ETL into triple-cation lead halide perovskite solar cells based on $Cs_{0.05}(FA_{0.83}MA_{0.17})_{0.95}Pb(I_{0.83}Br_{0.17})_3$. By comparison to solar cells built on planar cp-TiO_2 of the same FTO substrate, solar cells built on a TiO_2 nanocolumn ETL exhibit a 5% increase of short-circuit current and a 7% enhancement in its power conversion efficiency together with a significantly prolonged shelf-life. Various macroscopic and microscopic characterization methods were combined to identify the physical origins of the observed enhanced photovoltaic

property. Identified from SEM characterization, SNOM, and UV-vis absorption, TiO_2 nanocolumn ETL led to enhanced perovskite optical absorption, higher solar cell short-circuit currents, and better device stability by providing numerous precursor infiltration paths, near-field light concentration, and partial UV screening. In addition to these optical advantages, electrochemical EIS analysis showed that TiO_2 nanocolumn ETL is also superior to planar cp-TiO_2 in terms of charge transport and the reduction of recombination losses. These findings thus provide mechanistic insights on how 1D TiO_2 nanocolumns affect the performance of perovskite halide solar cells in terms of the charge transport, light-harvesting, and stability, knowledge necessary for the future design of more-performing and more-stable perovskite solar cells.

In **Chapter 4**, we focus on studying the intrinsic thermal conductivity and diffusivity properties of triple-cation (Cs^+, FA^+, MA^+) perovskite materials, which are closely related to the stability behavior of PSCs. It is not know whether the enhanced thermal stability of mixed-cation PSCs by comparison to $MAPbI_3$ originates from a better thermal conductivity. Here, by modulated thermoreflectance microscopy, the value of the thermal conductivity of triple-cation perovskite ($Cs_{0.05}(FA_{0.83}MA_{0.17})_{0.95}Pb(I_{0.83}Br_{0.17})_3$) was measured to be k_{per} = 0.26 Wm^{-1} K^{-1}, which is in the same order of magnitude as $MAPbI_3$. Therefore, the enhanced thermal stability of mixed-cation perovskite materials compared to $MAPbI_3$ likely come from a chemical origin.

In **Chapter 5**, we investigated the role of interfacial PbI_2 excess in $Cs_{0.05}(FA_{0.83}MA_{0.17})_{0.95}Pb(I_{0.83}Br_{0.17})_3$ perovskite solar cells on their performance and stability. Among the various strategies to control the crystallinity and the morphology of the perovskite active layer and its interfaces with the transport layers, fabrication of perovskite solar cells from precursor solutions with a slight excess of PbI_2 has become very common. Despite this, the role of such excess in PbI_2 is still rather controversial, lacking consensus on its effect on the bulk and interface properties of the perovskite layer. In this chapter, by treating the perovskite layer with four different organic salts, the surface PbI_2 crystallites are converted into perovskite, resulting in an increase in the device efficiency. We show this increase to originate from a more efficient charge extraction and reduced carrier recombination at the perovskite/hole-transport-layer (HTL) interface. Importantly, under continuous solar illumination, the MAI and FAI-treated devices maintained respectively 81% and 86% of their initial PCEs after 100 hours of continuous illumination (*v.s.* 64% for the non-treated solar cell

with excess PbI_2). Our study demonstrates that eliminating the PbI_2 excess at the perovskite/HTL interface by treating the perovskite surface with four different organic salts is a simple and efficient route to enhance the efficiency and stability of perovskite solar cells.

In **Chapter 6**, we investigated fundamentally a light-harvesting concept by placing upconversion nanoparticles onto the surface of a nanostructured hybrid perovskite layer, engraved by a focused ion beam. By deposition of such nanoparticles capable to absorb in the near-infrared spectrum beyond 800 nm, the light absorption of hybrid perovskites can be extended. We observed periodic fluorescence variations and the formation of fringes oriented in a direction parallel to the grooves. When the upconversion nanocrystals are located between the grooves, the fluorescence signal is increased by 2 to 3 times compared to the bare perovskite surface. FDTD simulation results are consistent with the fluorescence enhancement observed by the near-field fluorescence microscopy. These results suggest the current approach a promising method leading to short-circuit current and PCE improvement in the resultant PSCs. This study provides an interesting perpective that two-dimensional structures such as squares or circular disks of the perovskite layer could also result in large light-harvesting enhancements.

In summary, the related properties of the ETL, perovskite layer, and HTL alltogether determine the final performance of performance. Every component of the device needs to be optimized. This thesis covers the multi-dimensional aspects of perovskite materials and perovskite solar cells, ranging from devices (ETL, active layer, interfaces), thermal properties, as well as light-harvesting strategies. The results obtained offer bright perspectives for the further development of this field.

Chapter 9. Outlook

Up to now, researchers have made tremendous contributions to further improve the hybrid organic-inorganic perovskite semiconductor technologies, such as solar cells, light emitting diodes, photodetectors, lasers, etc. In particular, the perovskite solar cells have achieved unprecedented progress in the last decade, involving in all the parts and aspects of the perovskite devices. Despite the excellent advances, the PSCs are still far lag behind traditional silicon solar cells in the commercial area. And, there are still many shortages of components and corresponding interfaces of PSCs, to reach large-scale applications. According to my mains topics of the thesis, the future prospects of PSCs might include the following aspects:

In **Chapter 2**, simplified the perovskite device structure with excellent photovoltaic performance is a very meaningful direction, which optimizes the preparation process and reduces the cost and increases the possibility of fabricating flexible devices. However, the efficiency of PSCs without ETLs is not as good as the perovskite devices with the completed sandwiches-structure. Moreover, the simplified perovskite device without HTL faces similar challenges. To overcome this issue, some small molecules can be used to modify the interface between bare FTO electrode and perovskite active layer, reducing serve energy loss. Therefore, modulating the FTO/perovskite layer interface energy level, increasing the quality of the perovskite layer might optimize the simplified perovskite devices.

In **chapter 3**, one-dimensional TiO_2 nanocolumn arrays are a promising candidate to replace the TiO_2 mesoporous nanoparticles via glancing angle deposition method (GLAD), presenting high efficiency and relatively stable performance. The GLAD method has been commonly used in industrial fabrication and presents excellent reproducible. Although TiO_2 ETL is widely used in PSCs, its intrinsic shortcomings also limit the development of PSCs. Many researchers have reported using other organic or inorganic n-type semiconductors to replace TiO_2 ETL. So the GLAD might be used to prepare other metal-oxide electron transport layers, like SnO_2, ZnO, WO_x, etc to further promote the performance of the perovskite devices.

As we know, investigating the factors influenced the stability of perovskite materials is very important. **In chapter 4**, the thermal conductivity and diffusivity of the triple cation perovskite materials have been tested by the modulated thermoreflectance microscopy. It can be used to efficiently supervise the thermal conductivity and diffusivity of the perovskite materials, providing some constructive information for enhancing the stability of perovskite

materials by optimizing the constitute of perovskite materials, such as doping organic or inorganic cation and anions.

In **chapter 5**, the four different organic salts precursor solution was used to modify the grain boundary and interface of perovskite materials, which resulted in the enhanced photovoltaic performance of the devices, associated with an enhanced charge extraction and reduced carrier recombination. And the stability of PSCs with four different organic salts post-treatment has been greatly improved. It is well known that the interface is a crucial part of the perovskite device and the site of negative non-radiative recombination. Therefore, applying some small molecules to passivate the interface and enhance the quality of perovskite materials is very necessary. There is still a large space for optimizing the interface of PSCs.

In **chapter 6**, the engraved perovskite structure combined with upconversion particles can extend the light absorption range, which obviously enhances the fluorescence signal compared to the planar perovskite structure. According to these results, the various nanostructures (as squares, circular disks, or honeycombs) of perovskites with upconversion nanocrystals might be a wise choice to improve the short-circuit current of the perovskite device. And the down-conversion may be also used in the above-mentioned structure to improve the performance of PSCs.